Flow and Combustion in Direct Injection Spark Ignition Engines

A thesis submitted in partial fulfilment of the requirements for the degree of Doctor of Philosophy

Blane Scott

Exeter College

University of Oxford

Trinity 2019

Flow and Combustion in Direct Injection Spark Ignition Engines

Blane Scott DPhil
Exeter College, University of Oxford Trinity 2019

Abstract

The goal of producing more efficient internal combustion engines has led to the use of more advanced technologies and operating strategies. As a result, Computational Fluid Dynamics (CFD) is now a standard tool that is used to optimise the design of new combustion systems. Validation of these numerical simulations is essential, especially for the prediction of in-cylinder flow, which is known to have a profound effect on mixture preparation and combustion. Therefore, high quality, in-cylinder flow measurements are required to aid the validation process and the design of new combustion systems.

This work outlines the development of an optical engine test facility and the installation of a high-speed Particle Image Velocimetry (PIV) system that provides in-cylinder flow measurements with high spatial and temporal resolution over a large range of crank angles. The system is capable of producing measurements at a maximum rate of 3.7 kHz at full resolution and a total of 6000 frame pairs in a single experiment. Additional improvements to the system for specific application to IC engines have been outlined, including the use of variable inter-frame delay and methods of scatter minimisation.

To aid the validation of CFD simulations, metrics known as the Weighted Relevance Index (WRI) and the Weighted Magnitude Index (WMI), have been developed to quantify differences between flow fields in terms of both alignment and magnitude. These have been combined to produce a third metric, the Combined Magnitude and Relevance Index (CMRI), that produces a single value that rates the similarity of two flow fields. The application of these metrics has been demonstrated by investigating the differences between velocity measurements and CFD RANS simulations in the central tumble plane for three test conditions. The metrics were able to determine regions of the flow field that were significantly different between simulation and experiment, which would not be highlighted by conventional metrics.

Flow field measurements were also made during the induction and compression strokes of firing cycles to investigate the effect of in-cylinder flow structures on cycle-by-cycle variations in combustion. The cycles were separated into subsets conditioned on burn rate, as indicated by in-cylinder pressure measurements. The WRI and WMI were then used to compare the conditionally averaged flow fields of fast and slow burning cycles. From this analysis, it was possible to determine regions of the flow that have a significant effect on the rate of combustion. Simultaneous combustion imaging showed that the flames for slow burning cycles tended to grow asymmetrically towards the exhaust valves. In contrast, the flames of fast burning cycles were convected away from the spark plug and grew rapidly in all directions.

Acknowledgements

First and foremost, I would like to thank Professor Richard Stone for giving me the opportunity to study at Oxford nearly 8 years ago and his continued support throughout my undergraduate degree and DPhil. His extensive knowledge, technical guidance and practical skills have been invaluable to this work, and his dedicated supervision and constant encouragement are sincerely appreciated.

The members of staff at the Department of Engineering Science have been extremely helpful during this work, especially Dave Ilsley and the maintenance team, Maurice Keeble-Smith and Cleve Williams of the student workshop, Bob Yapp and the team in Stores, and Paul Bailey of the Cryogenics group.

I would also like to extend my gratitude to both the Engines and CFD research teams at Jaguar Land Rover, with particular thanks to Dr Dave Richardson, whose technical input and endless enthusiasm have been greatly appreciated throughout this work. Further thanks must go to Dr Giuseppe Virelli and Rachel Magnanon for their CFD expertise and running countless simulations, and Dr Tom Lockyer for his valued input.

I am very appreciative of the financial support of both the EPSRC and Jaguar Land Rover, without which this project would not have been possible.

I would like to thank the members of the Combustion and Engines Group at Oxford, including Dr Martin Davy, Dr Ben Williams and Dr Felix Leach for helping me at various points throughout my DPhil. A special mention must go to Dr Chris Willman for passing on his knowledge of laser diagnostics, and his help in designing and running the PIV experiments. Also, to Dr Safwan Hanis for teaching me the subtleties of operating the optical engine. Thanks to my fellow students in the group for making it a great place to work and providing lots of happy memories, especially Nick Papaioannou, Riyaz Ismail and Leo Fang, for all the enjoyable distractions and delicious food.

Last but not least, I would like to thank my parents, family, friends, and Rachael for their unwavering support and encouragement over the last 4 years. It would not have been possible without you.

Table of Contents

Abbreviations

aTDC	After Top Dead Centre
BDC	Bottom Dead Centre
BEV	Battery Electric Vehicle
BMEP	Brake Mean Effective Pressure
bTDC	Before Top Dead Centre
CA10	Crank angle at 10% MFB
CA50	Crank angle at 50% MFB
CA90	Crank angle at 90% MFB
CA10-90	Crank angle duration from 10% MFB to 90% MFB
CCD	Charge Coupled Device
CCV	Cycle-by-Cycle Variations
CFD	Computational Fluid Dynamics
CI	Compression Ignition
CMOS	Complementary Metal-Oxide-Semiconductor
CMRI	Combined Magnitude and Relevance Index
CoV	Coefficient of Variation
CVVL	Continuously Variable Valve Lift
DAQ	Data Acquisition
DI	Direct Injection
DISI	Direct Injection Spark Ignition
DNS	Direct Numerical Simulation
ECU	Engine Control Unit
EGR	Exhaust Gas Recirculation
ETCS	Engine Timing Control System
EU	European Union
FFT	Fast Fourier Transform
GCI	Gasoline Compression Ignition
GDI	Gasoline Direct Injection
HEV	Hybrid Engine Vehicle
HWA	Hot Wire Anemometry
ICE	Internal Combustion Engine
IMEP	Indicated Mean Effective Pressure
LDA	Laser Doppler Anemometry
LED	Light Emitting Diode
LES	Large Eddy Simulation
MFB	Mass Fraction Burned
MSI	Magnitude Similarity Index
Nd:YLF	Neodymium-doped Yttrium Lithium Fluoride
NEDC	New European Drive Cycle
NMHC	Non-Methane Hydrocarbons
NO_x	Oxides of Nitrogen
OEM	Original Equipment Manufacturer
PEMS	Portable Emissions Measurement Equipment
PFI	Port Fuel Injection
PHEV	Plug-In Hybrid Engine Vehicle
PID	Proportional Integral Derivative
PIV	Particle Image Velocimetry
PLIF	Planar Laser Induced Fluorescence
PM	Particulate Matter
POD	Proper Orthogonal Decomposition
PWM	Pulse Width Modulation
RANS	Reynolds Averaged Navier-Stokes
RDE	Real Driving Emissions
RI	Relevance Index
RMS	Root Mean Square
SI	Spark Ignition
TDC	Top Dead Centre
THC	Total Hydrocarbons
TR	Tumble Ratio
TTL	Transistor-Transistor Logic
VVA	Variable Valve Actuation
WLTC	Worldwide harmonised Light vehicles Test Cycle
WLTP	Worldwide harmonised Light vehicles Test Procedure
WMI	Weighted Magnitude Index
WRI	Weighted Relevance Index

Nomenclature

°ca	Degree crank angle
μ	Fluid dynamic viscosity
ρ_f	Fluid density
ν_f	Fluid kinematic viscosity
ρ_p	Tracer fluid density
τ_p	Tracer particle time constant
Δp	Incremental increase in pressure for burn rate analysis
Δp_c	Incremental increase in pressure due to combustion
Δp_c	Incremental increase in pressure due to piston
θ_i	Crank angle at time step *i*
D	Lens aperture
d_τ	Particle image diameter
D_I	Size of interrogation window
d_p	Tracer particle diameter
d*t*	Laser pulse separation
f	Len focal length
F_τ	Particle image self-correlation
$f^\#$	Lens f-number
F_I	In-plane loss factor
F_O	Out-of-plane loss factor
I_z	Light sheet intensity
M	Image magnification
N_I	Particle image density
Q	Ratio of correlation peaks
R_D	PIV cross-correlation term
S_D	Mean particle displacement
S_L	Laminar Flame Speed
S_T	Turbulent Flame Speed
t_0	Light sheet intensity normalisation factor
T_b	Burned gas temperature
T_u	Unburnt mixture temperature
u	Velocity component in *x*-direction
w	Velocity component in z-direction
x	Position in *x*-direction
z	Position in z-direction

1 Introduction

1.1 Background

Internal combustion engines (ICE) are the main source of propulsion for ground transportation worldwide, which consists of approximately 1.5 - 2 billion motor vehicles [1]. The vast majority of these are powered by compression ignition (CI) and spark ignition (SI) engines using liquid hydrocarbon fuels, which remain popular due to their high energy density, existing infrastructure and ease of distribution. In 2017 alone, there were nearly 100 million motor vehicles produced globally, of which 20% were manufactured in the EU [2]. Of the 15 million new passenger car registrations in the EU, 94% were powered by either diesel or petrol. There are similar trends in the UK with 95% of the 2.5 million new car registrations in 2017 powered by internal combustion engines [3]. Despite the dominance of conventional engines, there are a number of challenges facing their continued development; namely stringent emissions regulation and the development of disrupting technologies such as electrification.

1.1.1 Emissions regulation

There is a constant need for improved fuel economy and reduced tailpipe emissions, driven largely by government regulation. Currently, about 80% of all light duty vehicles are subject to some kind of standards, for which the main motivation is reduction in greenhouse gas emissions and harmful air pollutants [4]. Although these types of emissions are sometimes conflated, the range of their harmful effects differ, with greenhouse gases acting on a global scale in contrast to air pollutants, which are mostly concentrated in densely

populated areas. The emission of carbon dioxide (CO_2), the major greenhouse gas associated with ground transportation, is directly related to the amount of fuel consumed, and hence the fuel efficiency of a vehicle. A recent report by the Intergovernmental Panel on Climate Change (IPCC) outlines the dangers of irreversible global warming due to anthropogenic emissions [5], and highlights the challenges faced in mitigating these effects. In the EU, road transportation is responsible for 72% of CO_2 transport emissions [6], and so ambitious targets have been introduced to reduce fleet-averaged emissions from passenger cars to 95 g/km by 2021, and then by a further 30% from the 2021 baseline by 2030, with an incremental target of 15% by 2025 [7]. Figure 1.1 shows the global CO_2 regulations for passenger vehicles from 2000 to 2030.

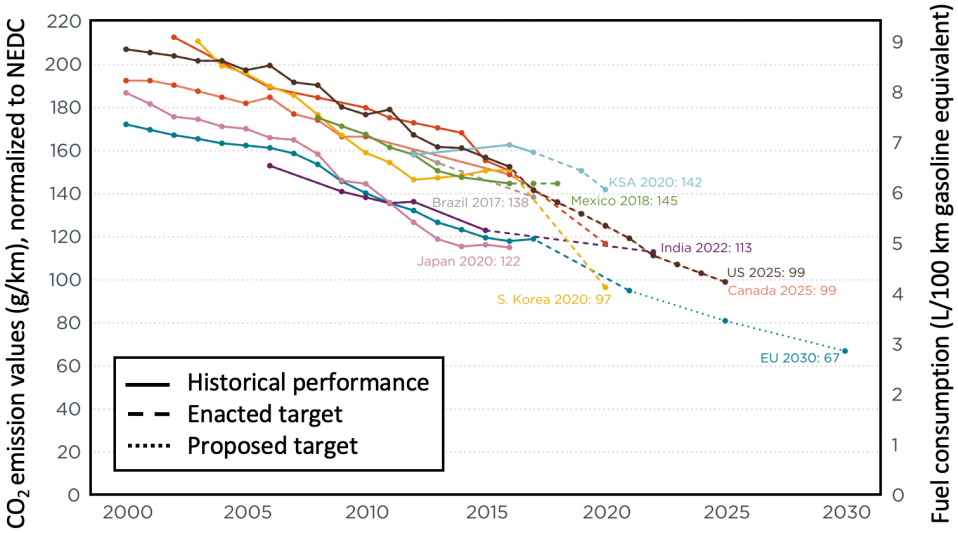

Figure 1.1 *Global CO_2 regulations for passenger vehicles until 2030 (adapted from* [8]*).*

The original 2015 EU target of 130 g/km was achieved two years in advance by manufacturers mainly through the large market penetration of light duty vehicles with direct injection diesel engines, which were aided by fiscal incentives. Although diesel engines are inherently more efficient than SI engines, concerns over the harmful effect of emissions of nitrogen oxides (NO_x) and particulate matter (PM) on local air quality have resulted in policies that target the use of diesel cars in heavily populated areas, such as the

introduction of London's Ultra Low Emissions Zone [9]. In the UK alone, uncertainty surrounding future government policy affecting diesel engines has led to a reduction in sales by 30% between 2017 and 2018 [10]. Across the EU, falling sales in diesel engines in 2017, coupled with a shift to heavier vehicles powered by spark ignition engines, has resulted in the first increase in fleet-averaged CO_2 emissions since 2000 [11], [12]. Not only does this trend highlight the need for continued development of spark ignition engines to improve fuel economy to meet the 2021 target, but it is also an example of well-intentioned policy having adverse effects.

In addition to fuel economy standards, the EU regulates air pollution by issuing directives ranging from EURO 1 in 1992 to the most recent, EURO 6d, due to be phased in by 2021. These define limits on pollutants such as NO_x, PM, total hydrocarbons (THC), carbon monoxide (CO) and non-methane hydrocarbons (NMHC). Under EURO 6, particulate matter is now regulated in terms of both particulate mass and number for direct injection spark ignition (DISI) engines. Compliance is enforced through the use of type approval tests that determine emissions by running the vehicle on a standardized drive cycle. Before 2018, the New European Drive Cycle (NEDC) was the standard test cycle for vehicles produced in the EU, however the ICCT reported that the gap between emissions produced during laboratory tests and real world driving was as great as 39% in 2017 [13], with this figure rising to around 50% by 2020 if the NEDC remained [14]. The large gap was due to the limitations of the NEDC, which was last amended in the 1990s. Furthermore, certain flexibilities in the conditions of the test allowed car manufacturers to optimise vehicles to perform well during the procedure but fall short in real world driving. This prompted the introduction of the Worldwide Harmonised Light Vehicle Test Procedure (WLTP) in 2017. The updated procedure has a more realistic, transient drive cycle (WLTC), that is longer

and has a higher mean velocity. It also tightens control of conditions at which the test is operated and takes into account optional equipment and payload of the vehicle. Figure 1.2 compares the NEDC and WLTC drive cycles.

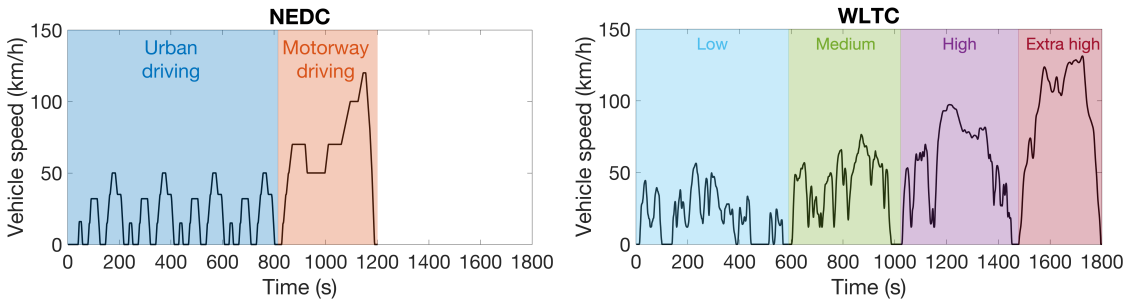

Figure 1.2 *Comparison of the NEDC and WLTC drive cycles.*

In addition to the WLTP, Real Driving Emissions (RDE) testing was also introduced in 2017. This test is carried out on public roads with a Portable Emissions Measurement System (PEMS) on-board and provides emissions measurements that are more representative of real-world driving. Manufacturers must ensure that the 'real world' emissions are within a certain conformity factor of laboratory tests, otherwise they risk substantial financial penalties.

1.1.2 Hybridisation and electrification

Of course, manufacturers must meet these ambitious targets while also offering a competitive product, which translates to improvements in fuel economy without a reduction in power output and driveability. An attractive option is the hybridisation of light duty vehicles to take advantage of the recent development of electrified powertrains in order to reach the fleet averaged CO_2 target of 95 g/km by 2021. The term 'hybridisation' covers a broad range of electrification; however, most commonly vehicles are classed as hybrid engine vehicles (HEV) and plug-in hybrid engine vehicles (PHEV). These differ in terms

of architecture and operation of the ICE and electric system, with HEVs (such as the Toyota Prius) using a combination of electric motor and internal combustion engine for propulsion. In contrast, larger batteries are used in PHEVs that can typically provide a range of about 40 km on the electric motors alone. Battery Electric Vehicles (BEV) do not possess an IC engine at all and only operate using electric motors. The Society of Motor Manufacturers and Traders (SMMT) reports that the number of new registrations of HEVs, PHEVs and BEVS in the UK have increased by 40%, 25.5% and 32.5% respectively from 2016 to 2017, making up 4.7% of the new car market [15]. The advantages of hybridisation are obvious in terms improved fuel economy with one report suggesting that hybrid powertrains can reduce fuel consumption by around 25-30% when compared with equivalent internal combustion engines [16]. Therefore, it is not surprising that many manufacturers have publicly stated their intentions of electrifying powertrains by the mid-2020s. However, despite double digit percentage increases in the number of newly registered BEVs in the UK in recent years, they only make up 0.5% of the market share. The lack of market penetration of BEVs is the result of a number of factors including relatively high prices in comparison to comparative internal combustion engines, range anxiety and the lack of an existing charging infrastructure [17]. Governmental financial incentives designed to encourage the uptake of BEVs are a key driver and vary greatly throughout Europe; this is the main reason why Norway has the largest market share of electric vehicles in the world [18]. In the UK, the maximum grant for the purchase of BEVs (vehicles that emit less than 50g/km) was reduced from £4500 to £3500 in 2018, and support for PHEVs was removed altogether. The cost premium of BEVs typically results from the relatively high costs of the battery, currently around 170$/kWh [19], although this is predicted to decrease into the mid-2020s. That said, there are concerns about the availability of the materials required for battery manufacture, such as cobalt and lithium, which are produced in a relatively limited

number of countries [20]. The range of BEVs is also predicted to increase with the improvement of battery technology, which may relieve the concerns of consumers [21]. As the costs of BEVs decrease and their price equals that of internal combustion engines, the uptake of BEVs is likely to increase. However, the installation of sufficient charging infrastructure remains a significant challenge. An increase in the number of BEVs will also result in increased load on the national power grid, especially at peak times if owners charge their vehicles at the same time. Financial incentives will be required to encourage owners to charge vehicles at off-peak times in order to distribute the load at peak times [22]. Furthermore, electric vehicles are only as clean as the energy infrastructure used to produce the electricity; therefore, to achieve the maximum benefit from a transition to electrification, significant investment must be made to ensure decarbonisation of the power sector [17].

1.1.3 Recent developments in SI engine technology

Modern engines possess a host of advanced technologies to improve fuel economy and meet the stringent emissions regulations. In a review of the current state of gasoline engine technology, Joshi [23] highlights a number of synergistic technologies that are entering the market; these include heavily downsized engines using advanced turbo-charging systems and e-boosting [24][25], exhaust gas recirculation (EGR) [26][27], homogeneous lean combustion [28][29], dynamic cylinder deactivation [30], and advanced valve control systems permitting Miller and Atkinson cycles [31][32]. Very recently, by announcing the SkyActiv-X engine, Mazda have become the first OEM to market a vehicle powered by a Gasoline Compression Ignition (GCI) combustion system [33]. This engine promises to combine the benefits of both a gasoline and diesel engine to reduce fuel consumption, without sacrificing performance.

Despite the challenges facing the internal combustion engine, it remains by far the most popular source of propulsion for ground transportation. Although a transition to electrification is highly likely in the coming decades, hybridisation will play an important role, therefore further development of IC engines is essential to improve the fuel efficiency of future vehicles. DISI (also known as gasoline direct injection (GDI)) technology is now widespread and used in modern engines to improve fuel economy. The following sections outline the main considerations of the design of such combustion systems and their advantages.

1.2 Direct Injection Spark Ignition Engines

1.2.1 Introduction

A brief summary of the basics of spark ignition engine operation is necessary before discussion of the complex nature of in-cylinder flow processes and combustion in DISI engines. The in-cylinder pressure trace of a cycle, shown in Figure 1.3, provides a simple method of explaining the processes in a 4-stroke SI engine. For each cycle, there are two revolutions of the crankshaft, and therefore the four strokes of the piston that define the main processes in a cycle: induction, compression, expansion and exhaust.

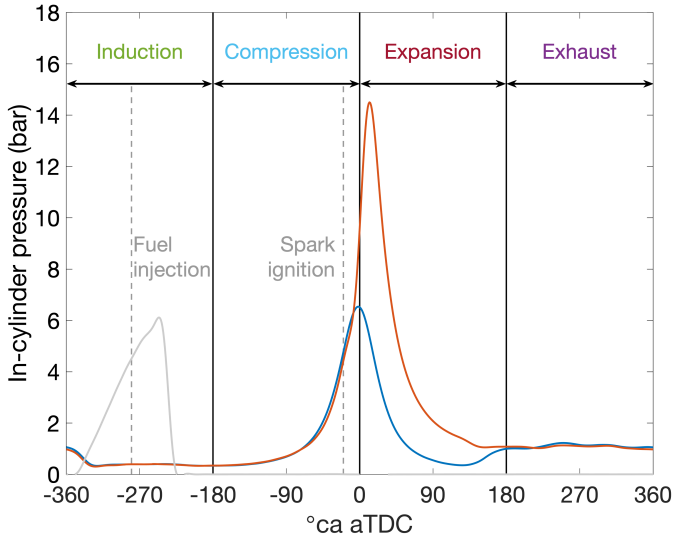

Figure 1.3 *An example of in-cylinder pressure traces for motored (blue) and fired (red) operation in a 4-stroke spark ignition engine. The inlet valve lift is also shown in light grey.*

As the piston moves downwards from top dead centre (TDC) during the induction stroke, the inlet valves open and air is drawn into the combustion chamber. Traditionally the fuel is mixed with the air before it enters the cylinder; however, in DISI engines, fuel is introduced directly into the combustion chamber. A high-speed jet of air enters the cylinder past the valves and transfers momentum to the in-cylinder charge, which results in large-scale bulk flow motion that persists throughout the cycle. After bottom dead centre (BDC), the inlet valves have closed and the piston travels towards the cylinder head, compressing the air-fuel mixture. A flame kernel is initiated by a spark plug some time before TDC, which consumes the flammable mixture and expands throughout the combustion chamber. The in-cylinder pressure increases due to the energy released by combustion of the air-fuel mixture, forcing the piston down and providing the power that drives the vehicle. During the exhaust stroke, the opening of the exhaust valves and the movement of the piston removes the combustion gases from the cylinder in preparation for the introduction of the fresh charge in the following cycle.

The work in this thesis is focussed on in-cylinder flow prior to combustion, therefore only the induction and compression processes are discussed in more detail in the following sections.

1.2.2 In-cylinder charge motion

Bulk flow

The manipulation of the in-cylinder charge motion is a key objective in the design of the induction and combustion systems in DISI engines [34]. The in-cylinder air interacts with the fuel spray to influence the distribution of the fuel throughout the combustion chamber, which dictates the homogeneity of the air-fuel mixture at the time of ignition [35]. Furthermore, the structure of the flame and its speed of propagation are dependent on both the in-cylinder motion and mixture composition; therefore optimisation of the charge motion is vital [36], [37].

The flow field set up by the induction process is three-dimensional, highly complex and turbulent. It consists of structures that range in size, from large-scale flows constrained by the geometry of the engine, to the smallest turbulent structures, only microns in length [38]. Controlling the distribution of energy throughout these scales is one of the challenges for the design of an effective induction system. Air is forced into the combustion chamber past the intake valves by the difference in pressure between the inlet manifold and the cylinder. The annular jet interacts with the cylinder walls and piston surface to setup large-scale flow structures that are typically separated into swirl and tumble, defined by their axis of rotation as shown in Figure 1.4; swirl describes a twisting motion around the axis of the cylinder and tumble refers to motion around an axis perpendicular to the cylinder.

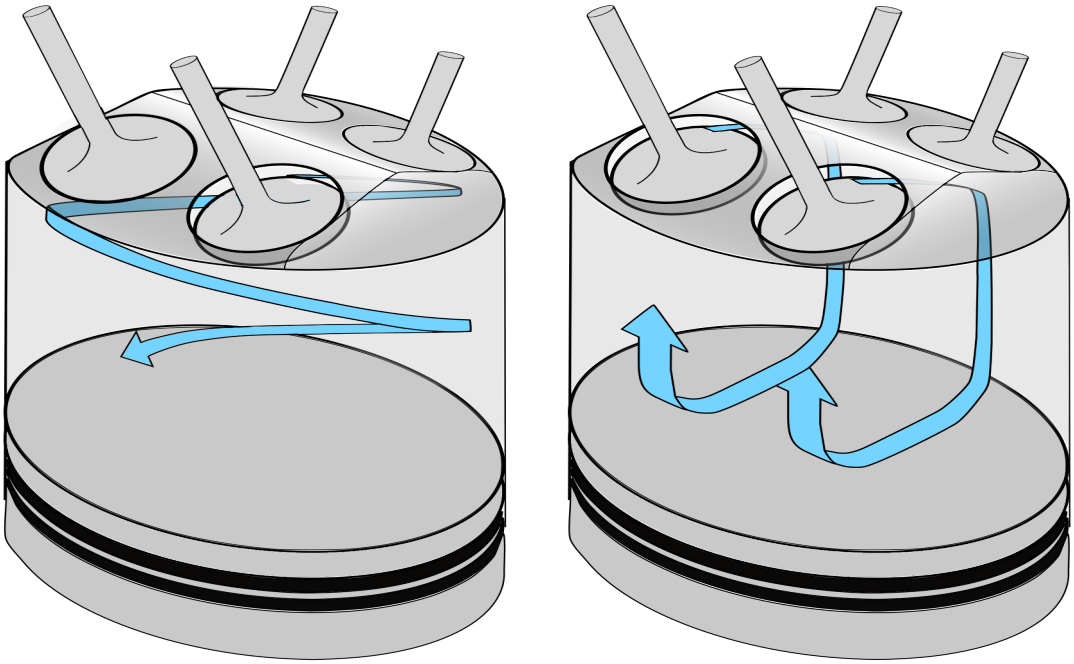

Figure 1.4 *Schematic demonstrating typical in-cylinder bulk motion - swirl (left) and tumble (right).*

After the inlet valves have closed, the bulk motion persists into the compression stroke where it is compressed by the upward motion of the piston. This causes the large-scale structures to become unstable and break down into smaller turbulent structures. By the time of ignition, there may be some residual bulk motion that interacts with the early flame kernel and dictates the direction of its displacement and early growth [36].

Variations in the large-scale flow structures from cycle to cycle are thought to be one of the main sources of cycle-by-cycle variations (CCV) observed in SI engines [39]. By analysing the differences between flow structures for directed and undirected engine flows, Reuss [40] suggests potential sources of cyclic variability: residual variability from a previous cycle, flow separation during the induction process, variation in the vortex during compression, and variation in turbulence dissipation. In addition, variations of the flow in the intake runner before the valves have also been suggested as a potential source of CCV

[41], [42]. In order to reduce cyclic variations, the induction system of modern DISI engines is typically designed to induce strong, repeatable tumble flow [43]. This is achieved by careful design of the inlet ports, tumble flaps, valve shrouding [44]–[47], and variable valve actuation (VVA) systems [48]–[50]. The flexibility of VVA systems offers the potential of new operating strategies to improve fuel economy[51], [52]; one of which is the de-throttling of the engine at part load [53], [54].

Turbulence

A major consideration in the design of the induction system is to ensure the generation of sufficient in-cylinder turbulence. The rate of air-fuel mixing and flame propagation is significantly increased by the action of turbulence, which ensures satisfactory engine operation for a large range of speeds. For example, without a turbulent flow field at ignition, laminar flames would not travel sufficiently fast to fully consume the air-fuel mixture at higher engine speeds. Enhancement of flame speed by turbulence is particularly important for engines operating under lean conditions or high levels of EGR. Therefore, one of the most important objectives of the induction system is ensure a turbulent flow field at the time of ignition.

In general, the turbulence intensity is greatest during the induction process due to the large velocity gradients between the high-speed intake jet and the relatively slow in-cylinder air. However, it is known that this turbulent motion dissipates rapidly after the inlet valves have closed, as the source of turbulence is removed [38]. For this reason, intake systems are designed to encourage the formation of large-scale flow structures, which are used to store the kinetic energy introduced in the induction process so that it can be used to generate turbulence late in the compression stroke [55]. The process by which the energy contained

in the bulk motion is transferred to smaller structures is known as the energy cascade, and occurs due to the action of shear forces [56]. The cascade continues until the turbulent energy is finally dissipated as heat on the molecular scale by diffusion. As the piston moves towards the cylinder head during the compression stroke, the tumbling structure is compressed, resulting in faster rotation due to the conservation of angular momentum. Near TDC, the rotating structure becomes unstable and breaks down into small-scale turbulent structures in time for ignition [57], [58], as demonstrated in Figure 1.5. Modern engines also use 'squish' regions, to generate more turbulence; these are regions of very small clearance between the cylinder head and piston that force jets of gas into the centre of the combustion chamber, which then break down into smaller turbulent structures. Further discussion of the methods used to analyse the effect of flow structures on combustion are provided in Chapter 7.

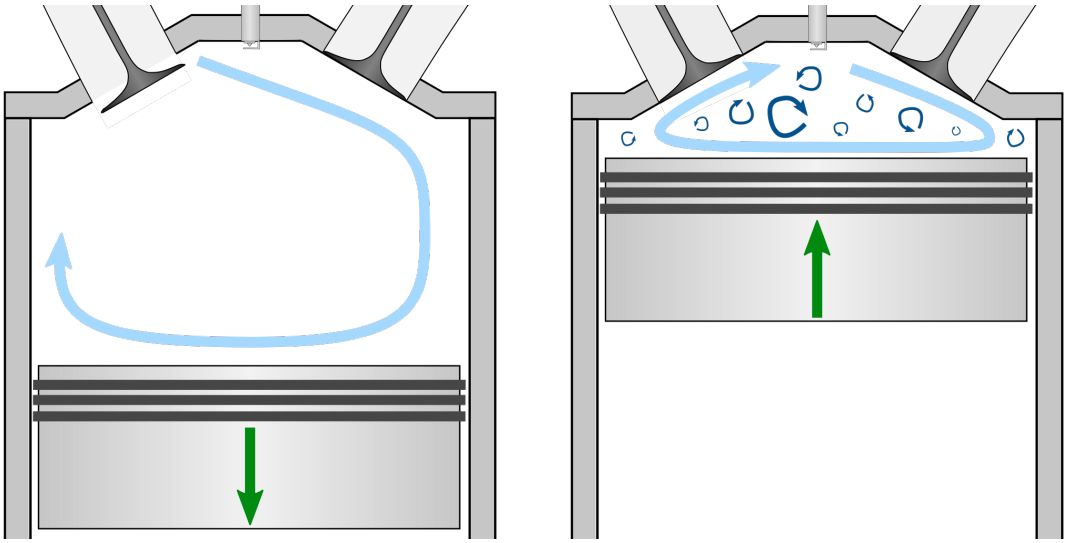

Figure 1.5 *Schematics illustrating the formation and breakdown of the tumble motion in a spark ignition engine.*

1.2.3 Fuel injection

The way in which the flammable mixture is formed before combustion has a profound effect on efficiency and emissions. Traditionally in SI engines, fuel and air was mixed

outside the combustion chamber using either a carburettor or, more recently, port fuel injection (PFI). For PFI systems, fuel is injected at low pressure onto the rear of the inlet valves, where it vaporises and mixes with the air before entering the cylinder during the induction process. These systems have been very successful as they are robust and provide good air-fuel mixing control without dedicated charge motion [37]. However, in recent decades, direct injection of fuel into the combustion chamber has become popular for high performance SI engines. Although, direct injection requires more advanced control systems and more robust fuel systems, it has been seen as a relatively inexpensive way of reducing fuel consumption by as much as 20% [59]. The images in Figure 1.6 show examples of PFI and DI fuel injection systems.

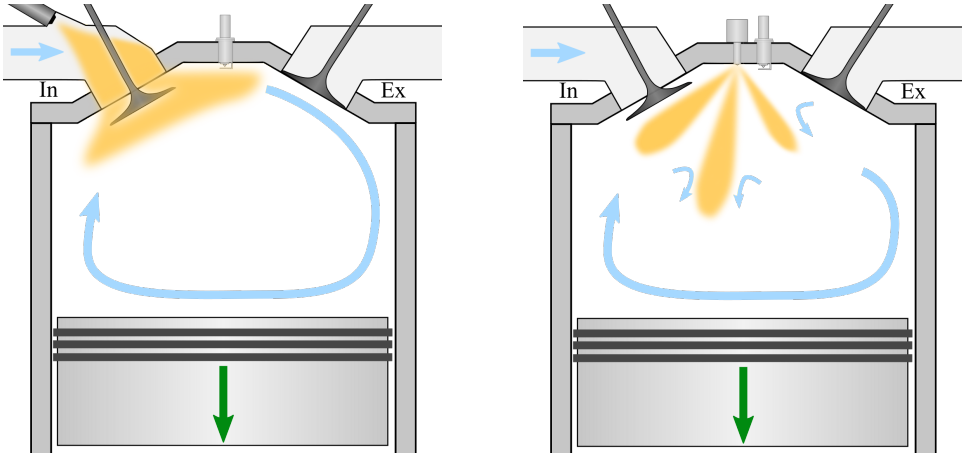

Figure 1.6 Images demonstrating PFI (left) and DI (right) fuel injection systems.

There are a number of advantages offered by direct injection; one of which is the charge cooling effect. As the liquid fuel evaporates after injection, it removes energy from the in-cylinder charge, resulting in a reduction of in-cylinder air temperature. Not only is the charge density increased, resulting in improvements in volumetric efficiency, but peak pressures are also reduced, which mitigates the onset of potentially damaging combustion knock. Therefore, direct injection allows the use of higher compression ratios, increasing cycle efficiency. Direct injection is a key technology used in engine downsizing, which has

been a major trend in modern gasoline engines [60]. This process involves replacing large, naturally aspirated (NA) engines with smaller, turbocharged engines without a significant reduction in power output. The vast majority of the newly developed engines outlined in Section 1.1.3 are downsized, direct injection engines due to the benefits of lower frictional losses, heat losses and mass. Due to the reduction in displacement, these engines commonly run at higher BMEPs than larger NA engines, which results in reduced throttling losses and lower fuel consumption.

A major issue with PFI systems is the poor transient fuelling control during acceleration. The presence of fuel films on the surfaces of the intake runner and the valves typically results in air-fuel ratio excursions during transients [36]. The combination of advanced electronic control systems and modern injectors used in direct injection systems provides much greater control of fuelling, including multiple injection events per cycle, which have been used to influence in-cylinder motion and enhance combustion [61].

The requirement of SI engines to operate under stoichiometric conditions due to the three-way catalytic converter has resulted in the use of a throttle to control the flow rate of intake air, and subsequently the power output. Increased pumping losses under part-load conditions have a significant effect on efficiency and should be mitigated. Direct injection systems provide an opportunity for significant part-load fuel economy benefits when operated in stratified mode [59]. Under this mode of operation, fuel is injected very late in the compression stroke to provide a flammable mixture in the vicinity of the spark plug, but with a globally lean air-fuel ratio. Combustion is therefore controlled by the amount of fuel injected, which enables de-throttling of the engine and reduction in pumping losses. Although this operating mode has been deployed on some production vehicles [62], its

potential has been limited by high cyclic variability and increased emissions of NO_x and particulates [63]. More commonly, engines are operated in homogeneous mode for which the fuel is injected early in the induction stroke to provide sufficient time to provide well-mixed conditions at the time of ignition. The system pressure of current injection systems is approximately 200 bar, but this is expected to increase to above 300 bar in future systems [64]. At higher fuel pressures, the spray is more finely atomised with smaller droplets that vaporise more readily, leading to a more homogeneous mixture and a subsequent reduction in particulate matter emissions [65]. However, there is a compromise between higher injection pressures for better atomisation, increased fuel pump work, and the risk of fuel impingement on the piston, which can result in 'pool fires' and increased particulate emissions [66]. The high momentum of the fuel plumes entrains air and encourages significant charge motion, which is an important factor in mixture preparation.

1.2.4 Combustion in SI engines

In SI engines, combustion typically occurs with a premixed air-fuel mixture in a turbulent flow field. By the time of ignition, the flow field near the spark plug is highly turbulent due to the breakdown of the bulk flow motion and the action of the squish regions. For DISI engines under homogeneous operation, fuel is injected early in the induction stroke to provide sufficient time for air-fuel mixing, which is also aided by the turbulent flow field. The air-fuel mixture is ignited by the electrical discharge between the electrodes of a spark plug, which is typically located centrally in the centre of the cylinder head. After initiation, the flame consumes the surrounding flammable mixture and expands rapidly to fill the combustion chamber. The growth rate of the flame and its structure are extremely important in engine performance and the production of emissions [37].

A premixed flame can be described as a thin reaction region that separates the burnt gas and unburnt mixture, shown by the temperature profile in the left-hand image of Figure 1.7. The majority of the thermal energy is produced in the reaction zone, which then heats up the unburnt mixture through conduction, resulting in further oxidation reactions and propagation of the flame front. The laminar flame speed, $\mathbf{S}_L$, is the speed at which the flame front travels through the unburnt mixture and depends on the chemical properties of the mixture and the local thermodynamic conditions. However, the flow field surrounding the spark plug is highly turbulent, which acts to significantly increase the rate of flame growth; this is known as the turbulent flame speed, $\mathbf{S}_T$. Turbulence wrinkles and distorts the smooth laminar flame front, effectively increasing its surface area, which is the cause of the increased growth rate. A schematic of a turbulent flame is provided in the right-hand image of Figure 1.7. Although globally a turbulent flame travels several times faster than a laminar flame, the local flame front travels at the laminar flame speed as the reaction chemistry is unaffected by turbulence. The scaling of turbulent flame speed with turbulence intensity is essential for the operation of SI engines as it ensures that combustion occurs sufficiently quickly over a large speed range.

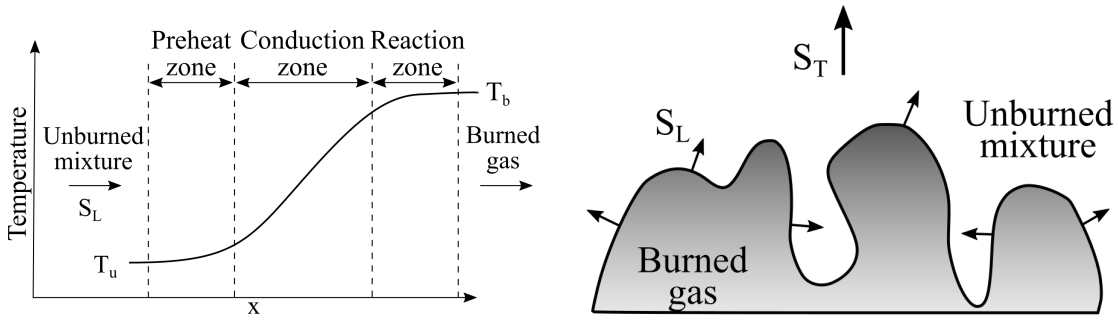

Figure 1.7 *Images demonstrating flame temperature distribution (left, adapted from* [36]*) and structure (right).*

It is clear that the in-cylinder flow field plays a crucial role in the combustion performance of an SI engine due to the requirement of sufficient generation of turbulence at the time of

ignition. Furthermore, cyclic variation in the bulk flow motion is known to be a cause of combustion cycle-by-cycle variations (CCV); the direction of the bulk flow near the spark plug dictates the movement of the early flame kernel. If the flame is convected towards the walls of the combustion chamber, or the electrodes of the spark plug, excessive heat losses can result in flame quenching, and subsequently partial burns or even misfires. DISI engines operated in stratified mode are particularly susceptible to CCV due to strong velocity gradients near the spark plug induced by the fuel spray [67].

1.3 Optical Diagnostics in Engine Research

The complex interactions between the underlying physical and chemical processes during a firing cycle in internal combustion engines have been a topic of research since they were first developed in the late 19th century [68]. Optical engines provide visualisation and quantification of these processes. The most notable early optical study was by Rassweiler and Withrow in the 1930s, who developed a side-valve engine that provided a complete view of the combustion chamber with the use of quartz plates. Modern optical engines are designed to be representative of a realistic combustion system, while providing maximum optical access. The introduction of high-speed, digital photodetectors and high-power lasers in the 1970s allowed in-cylinder phenomena to be studied in ever-greater detail [69], [70]. These technologies have advanced such that planar measurements can be acquired at rates greater than 10 kHz [71], and provide insights that would otherwise be impossible to attain. Such data are of vital importance, not only in the study of the fundamentals of combustion but also in the feasibility analysis of new combustion systems [72], [73].

Optical techniques have been developed, and often combined, to study most parts of the engine cycle in detail; in-cylinder fuel and temperature distributions have been measured

using Planar Laser Induced Fluorescence (PLIF) [74]–[78], fuel sprays have been characterised using schlieren imaging and Mie scattering [79], and combustion has been analysed using high-speed imaging [80]–[82]. For in-cylinder velocity measurements, Laser Doppler Anemometry (LDA) and Particle Image Velocimetry (PIV) have both been used, although PIV is now the most common technique for this purpose. Chapter 3 provides a more detailed discussion of in-cylinder flow measurement techniques, and PIV in particular.

In addition to fundamental studies of engine operation, optical diagnostics have also been extremely useful in providing measurements for the validation of simulations. Computational fluid dynamics (CFD) is widely used in the automotive industry to aid the design of new combustion systems and reduce the cost of engine development [73], [83]–[86]. Therefore, extensive validation of numerical models used in the simulations is essential to maximise the utility of CFD in the design process. Optical engines are necessary to provide the measurements required for validation [87]–[89]. Experimental databases, such as the those made by the Engine Combustion Network (ECN), have been setup to ensure the availability of high-quality validation data for several standard test conditions. Another example is the Transparent Combustion Engine (TCC-III) at the University of Michigan, which is a simplified 2-valve engine with a flat combustion chamber that has been specifically designed to aid the validation of LES simulations of in-cylinder processes [90].

The generation of validation data is a challenge; however, there is also the question of how that data is used to compare measurements and simulation. In some cases, well-defined criteria are used to simplify the comparison between models and experiments; an example

of this is the explicit definition of Lift-off-Length (LOL) and Ignition Delay (ID) by the ECN to quantify model validation. For the validation of in-cylinder flow simulations, this can be more difficult. The work in this thesis investigates existing methods of quantifying the differences between in-cylinder flow fields and develops a new set of metrics that separate the contributions from differences in alignment and flow speed. These metrics are also combined to provide a third metric that is able to capture the overall difference between two flow fields. The utility of these new metrics is demonstrated in the validation of RANS engine simulations and investigations of the effect of in-cylinder flow on early flame development.

1.4 Thesis Overview

A brief overview of this thesis is provided in the following section. It consists of six chapters that cover the outline of the experimental equipment (Chapters 2 and 3), the development of analysis techniques (Chapter 4), and the discussion of analysis and results (Chapters 5 and 6). Each chapter begins with a brief introduction and a discussion of the current literature.

Chapter 2 outlines the optical DISI engine test facility used throughout this thesis. The combustion system is based on Jaguar Land Rover's Ingenium family of SI engines and it offers a range of optical access, as well as boosting and a continuously variable valve lift system.

Chapter 3 provides a detailed description of the PIV technique and the current high-speed system installed on the optical engine. A summary of methods used to maximise the quality of the measurements is also provided.

Chapter 4 outlines current methods used for quantifying differences between velocity fields. A discussion of the issues with a common metric, the Relevance Index (RI), in analysing rotating structures is provided, before the development of modified metrics is presented. The Weighted Relevance Index (WRI) and the Weighted Magnitude Index (WMI) are used to quantify differences in alignment and magnitude separately. These are then combined to form the Combined Magnitude and Relevance Index (CMRI), which accounts for both differences in flow speed and alignment.

Chapter 5 demonstrates the use of the WRI, WMI and CMRI in analysing the differences between simulated and measured flow fields in a DISI engine for three test conditions. A number of different flow features are highlighted by the metrics and analysed in detail.

Chapter 6 investigates the effect of the in-cylinder flow field on cyclic variation in combustion. The metrics are used to highlight regions of the flow that are most different between subsets of fast and slow burning cycles, which are then analysed on a cycle-by-cycle basis.

Chapter 7 summarises the work presented in this thesis and suggests directions for further investigations that would improve the understanding of the effect of in-cylinder flow fields on engine operation.

2 Experimental Facilities

2.1 Single Cylinder Optical Engine

The combustion system of the optical engine is provided by Jaguar Land Rover and is based on the specification of the Ingenium family of petrol engines. The optical engine specification is shown in Table 2.1.

Table 2.1 *Optical engine specification.*

Displacement (cc)	512
Bore (mm)	85.0
Stroke (mm)	90.3
Compression Ratio	9.8*
Max. Operating Engine Speed (rpm)	2000

* Refers to operation with flat-topped piston (non-production)

The combustion system for the optical engine is designed to be as similar as possible to that of the production engine; however, some differences are necessary to provide optical access. For example, the optical engine has a bore of 85 mm, which is larger than the 83 mm bore of the production engine to accommodate the additional space required for optical components. Furthermore, the mechanical properties of the optical components are different to those of an equivalent thermal engine, which may result in different in-cylinder conditions. However, these are necessary compromises in order to obtain in-cylinder measurements. A range of optical access is offered with a choice of three different cylinder liners: a full steel barrel, a short steel barrel with transparent annulus, and a transparent quartz liner. Figure 2.1 shows annotated views of the cylinder liner and Figure 2.2 is a schematic of the test cell.

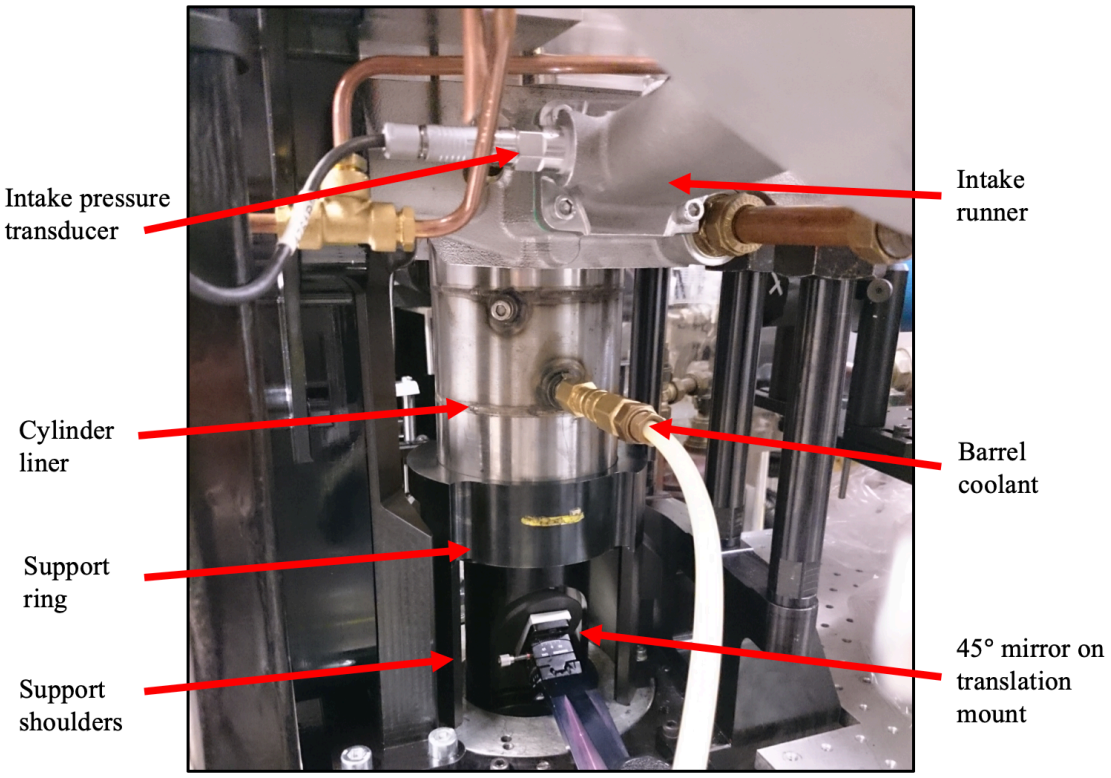

Figure 2.1 *Labelled images showing a detailed view of the cylinder liner.*

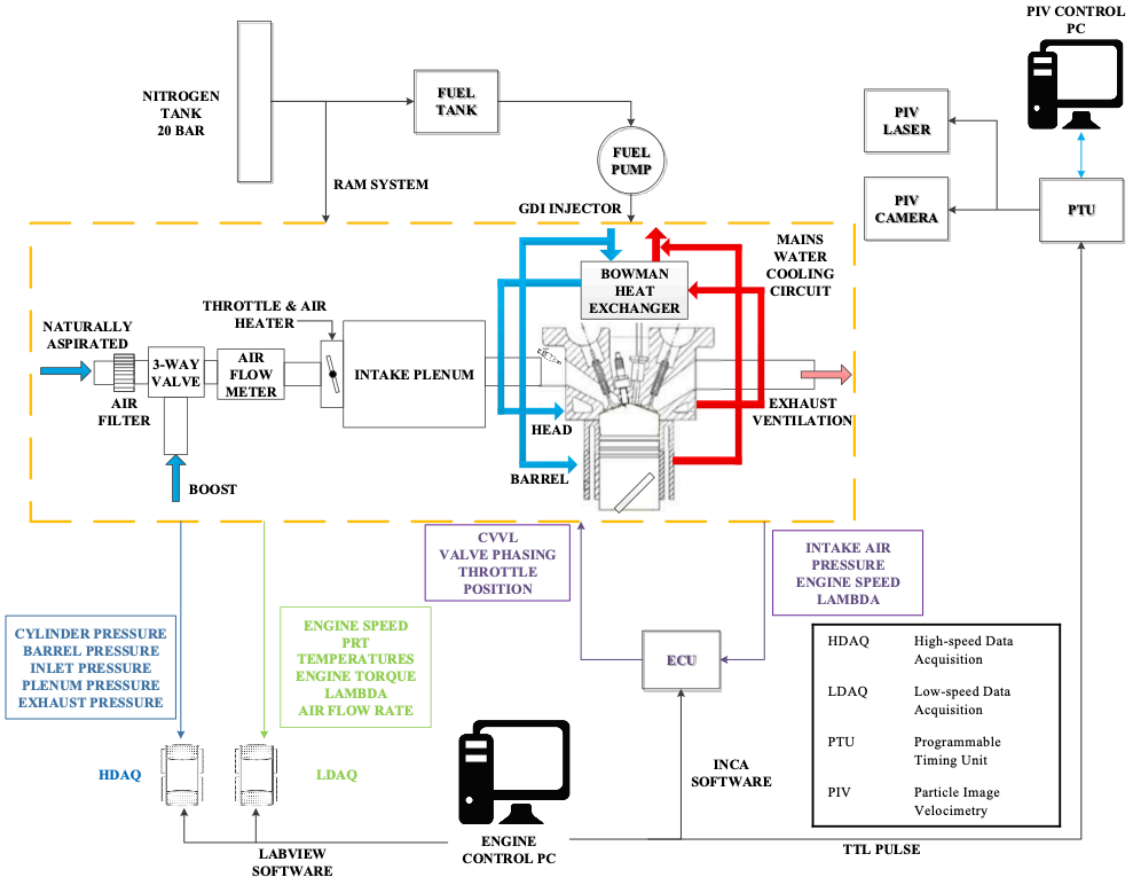

Figure 2.2 *Schematic of the engine test cell.*

2.1.1 Base engine and cylinder head support

The bottom end of the engine has a marked flywheel with crank angle resolution and is mounted on a DC dynamometer with a Control Techniques Four-Quadrant controller for speed or torque control. Engine timing signals are required for both the LabView-based Engine Timing Control System (ETCS) and data acquisition system. A shaft encoder mounted on the crankshaft at the front of the engine with a resolution of ¼ °ca provides 360 pulses per revolution for the data acquisition and ETCS systems. A bespoke toothed wheel is mounted on the flywheel to provide the timing signals for synchronisation of the Engine Control Unit (ECU).

The support structure for the cylinder head, shown in Figure 2.3, permits either the inner pair or outer pair of columns to be removed to allow greater flexibility in terms of optical access to the cylinder.

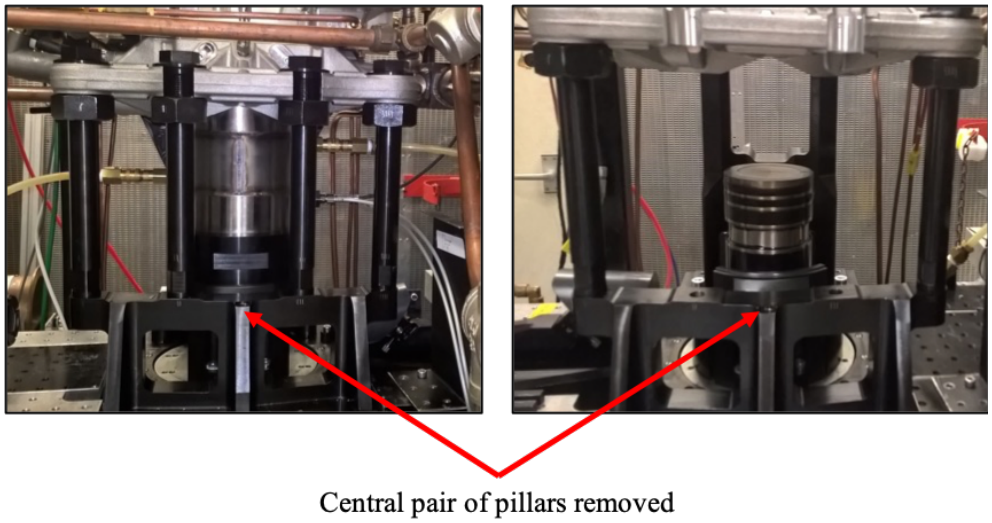

Figure 2.3 *Images showing the engine support structure with all columns in place (left) and two inner columns removed (right).*

A drop-down cylinder system [91] is used to facilitate interchangeable cylinder liners. The liner sits on a support ring that registers on two columns, which are bolted to the top surface

of an annular piston in the engine base. During engine operation, nitrogen at a pressure of 20 bar is used to lift the piston and seal the liner to the cylinder head. When a change of cylinder is required, the ram system is disengaged, and the support ring is rotated so that it drops between the two columns. An extended Bowditch piston [92] is used with a quartz piston insert and a 45° mirror to provide optical access from below the combustion chamber. The extended piston adds significant mass to the crank and slider mechanism and limits the speed of the engine to 2000 rpm. A sliding mirror bracket allows the mirror to be easily removed and cleaned during experiments. A Thor Labs goniometer provides fine control of the orientation of the mirror, allowing $\pm 15°$ in either direction.

2.1.2 Cylinder liners

The cylinder head has been designed with a curved recess to replace the pent roof windows commonly used in optical engines. This allows an uninterrupted view of the pent roof of the combustion chamber, including the spark plug and fuel injector. As a result, the cylinder liners have a matching profile, as shown in Figure 2.4. There are three liners available that offer varying degrees of optical access: full steel, short steel with annulus, and full quartz. Due to the extreme conditions in the combustion chamber during a firing cycle, there must be a compromise between optical access and realistic operation. The fully transparent liner provides full view of the cylinder; however, as it is not cooled, there is increased risk of the piston rings melting during extended operation. The combination of a short steel liner with a transparent annulus provides optical access to the spark plug and fuel injector, but also has an internal cooling jacket that allows the engine to be operated under firing conditions for extended periods. Although, the full steel liner can be run at conditions most representative of a thermal engine, it only offers optical access through the transparent piston insert.

Figure 2.4 *Photographs of the cylinder liners available for use in engine: Full steel (top left), full quartz (top right), and quartz annulus (bottom).*

2.1.3 Pistons

There are two types of titanium piston, shown in Figure 2.5, that can be used in the optical engine: a low ring-pack piston and a high ring-pack piston. If the short steel liner and annulus are in use, a low ring-pack piston must be used to prevent the compression rings crossing the boundary between the liner and the annulus. This piston has a larger crevice volume than the high ring-pack piston and so the effective compression ratio is reduced.

Torlon piston rings are used instead of metal rings due to the lack of oil lubrication. There are two sets of two compression rings and one larger ring located below that guides the

piston in the cylinder. The cooling jacket in both short and full-length steel liners prevents the temperature of the cylinder wall damaging the rings, however they have been known to melt in the full quartz liner.

Several optical techniques require optical access from below the combustion chamber through the piston crown, for which quartz piston inserts are used. A retainer is unscrewed using a custom tool allowing the metal blank to be removed and swapped with the quartz equivalent, as shown in the lower image of Figure 2.5. When using the quartz insert, a brass retainer is used to compensate for the very low coefficient of thermal expansion of fused silica (quartz).

Figure 2.5 *An exploded view of the high ring-pack piston and associated components (top), and an image of the low ring-pack piston with transparent quartz piston insert (bottom).*

The piston shown in Figure 2.5 is the standard flat-topped piston, that is commonly used in optical engines. The testing in this thesis has been completed using pistons that have shaped crown features in order to better represent those used in production engines. The three different designs, named A, B and C, are shown in Figure 2.6.

A

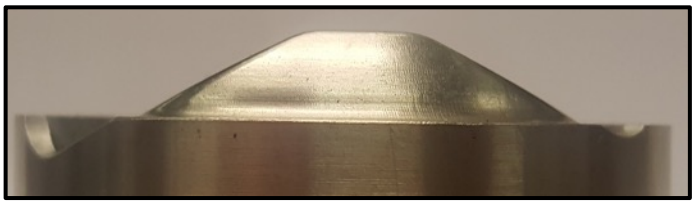

B

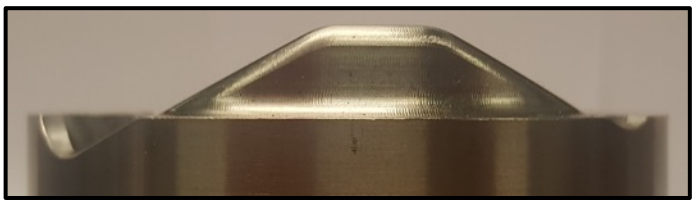

C

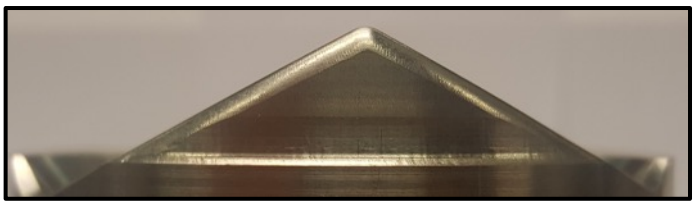

Figure 2.6 *Photographs of the pistons with shaped crown features.*

Pistons A and B are very similar in shape, with the only difference being a slight removal of material on the outer edge of the pop-up. This is to represent material that is present on the cylinder head of the production cylinder head but has been removed from the optical cylinder head due to the constraints of ensuring optical access to combustion chamber. The pop-ups on piston C have additional material that increases the effective compression ratio in comparison to pistons A and B.

It was necessary to ensure that the piston crown features were orientated such that the pop-ups were aligned with the pent-roof. For the flat-topped piston assembly, the piston is screwed directly onto the Bowditch extension, which is then clamped to the lower piston connected to the crankshaft. For the shaped piston assemblies, two spacers are required to control the clearance between the piston top-land and the cylinder head, and also the orientation of the crown features, as shown in Figure 2.7. The clearance between the cylinder head and the piston was measured using a soft, malleable material (i.e solder or 'Play-Doh') that was placed on the piston top-land, as shown in the right-hand image of Figure 2.7. The engine crank was then manually rotated, causing the piston to cross TDC, which resulted in the deformation of the malleable material. Its thickness provided the clearance between the piston and cylinder head, for which a spacer of the correct dimensions was manufactured. This spacer was then inserted between the bottom-end piston and the Bowditch extension.

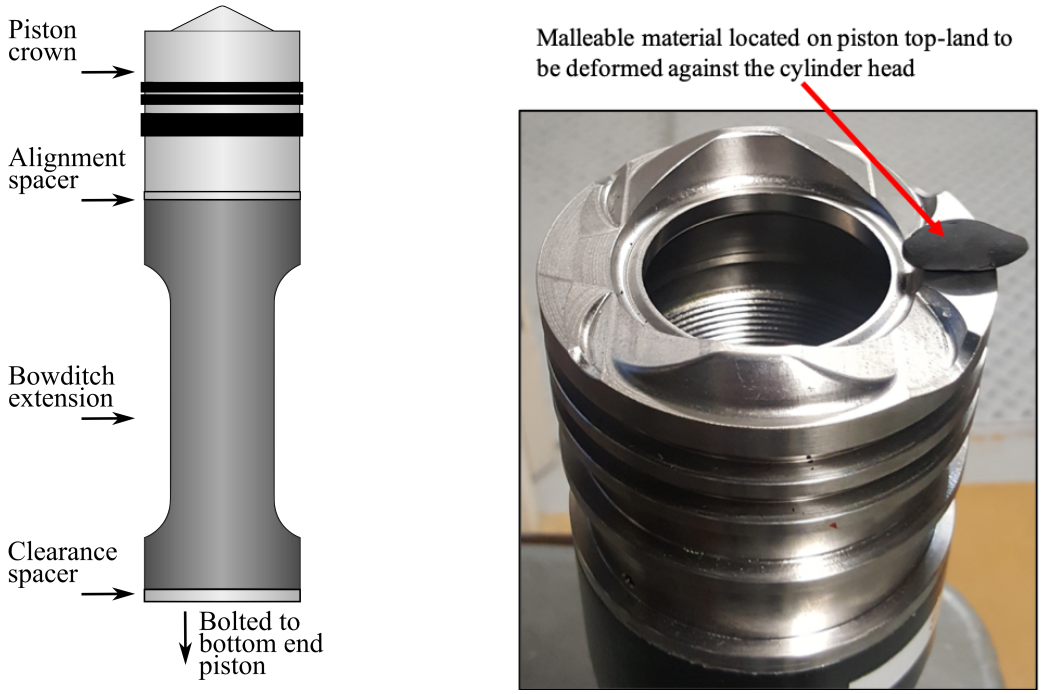

Figure 2.7 *A schematic of the Bowditch piston assembly with the required spacers for the shaped pistons (left) and a photograph showing the method used for measuring the clearance between the cylinder head and the piston (right).*

To ensure the correct orientation of the piston features, another spacer was required; this was inserted between the Bowditch extension and the piston to control its rotation. In order to calculate the thickness of spacer required to achieve the correct rotation, an aluminium block was machined to fit the piston crown features. This was then clamped to the piston surface using a bolt and a length of hollow aluminium bar, as shown in the left-hand image of Figure 2.8. The block provided a flat surface that was used to measure the required angle of rotation, from which the thickness of the spacer could be calculated. The tolerance on the thickness of the spacer was such that $\pm$ 4 μm resulted in $\pm$ 1° rotation of the piston due to the screw thread, therefore the aluminium spacers were ground. The right-hand image in Figure 2.8 shows the resulting spacer installed between the Bowditch extension and the piston crown.

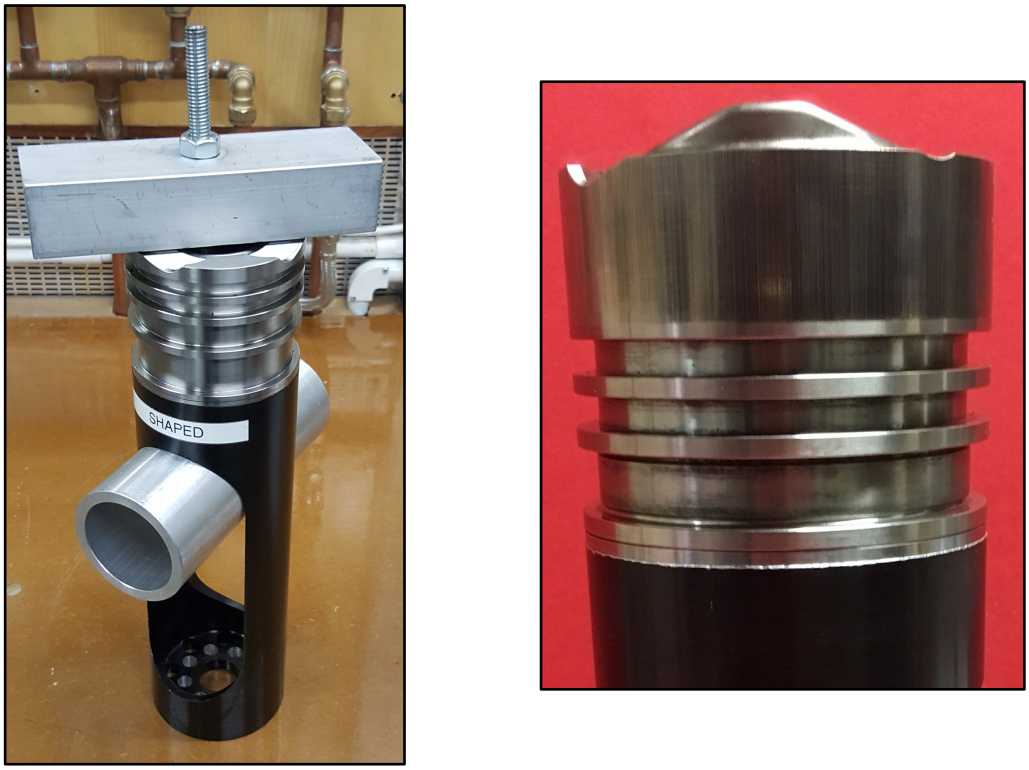

Figure 2.8 *Photographs showing the method used for measuring the required thickness of the spacer (left) and the spacer installed in the piston assembly (right).*

2.1.4 Cylinder head

The spark plug and fuel injector are located in close proximity in the centre of the chamber as shown in Figure 2.9. The in-cylinder pressure transducer is mounted flush to the cylinder head via a tapping in the chamber roof. Passages have been machined in the cylinder head to provide access to the inlet valve guides in order to measure the valve lift using Sensitec Tooth Sensor modules. The steel inlet valves have a ribbed section along the shaft that passes the tip of the sensors and interacts with the sensor element through the Giant MagnetoResistive Effect. A signal conditioning unit converts the raw signal to valve lift before it is logged by the DAQ system. These sensors have a refresh rate of 80 kHz and an absolute accuracy of $\pm$ 20 μm for a maximum valve lift of approximately 10 mm. To operate correctly, the sensors must be installed such that the tip is as close as possible to the ribbed section of the valve. Care must be taken during installation to avoid any contact between the valve stem and sensor tip as this will result in destruction of the sensor. Furthermore, thermal expansion of the sensor housing due to continual operation of the engine can result in contact and subsequent damage to the sensor.

There are three coolant ports in the cylinder head, two of which have been used as an inlet and outlet. The third is used as a vent and a thermocouple has been installed. A heater with a thermostat preheats the coolant, and temperature is controlled to within $\pm$ 1 K by a heat exchanger and proportional valve with PID control that can by-pass the heat exchanger.

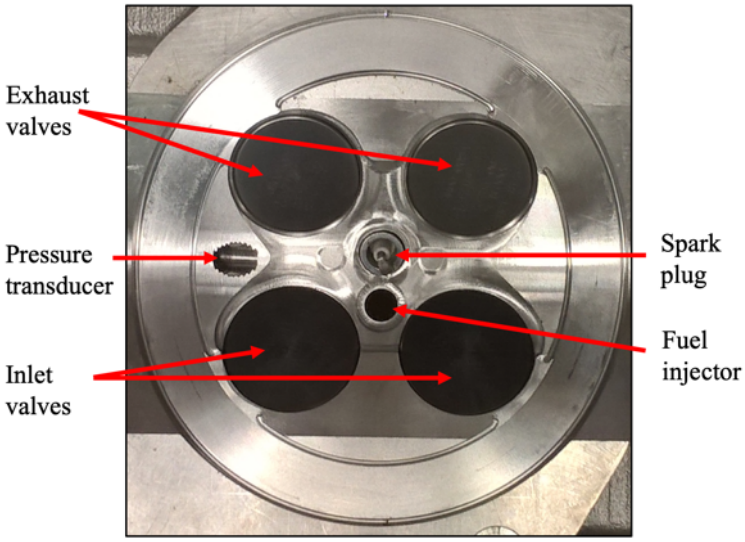

Figure 2.9 *A labelled view of the cylinder head.*

2.1.5 Gaskets

The curved profile of the top surface of the liners requires a curved gasket to provide the seal with the cylinder head. In order to shape the gaskets appropriately, plastic models of the curved surface and the corresponding cylinder head recess were fabricated in a 3D printer. PTFE-based gasket material (Garlock) is then clamped between the two pieces for a length of time and excess material removed with a scalpel. The result is a gasket that approximately matches the shape of the cylinder profile and retains its shape after use, as shown in Figure 2.10.

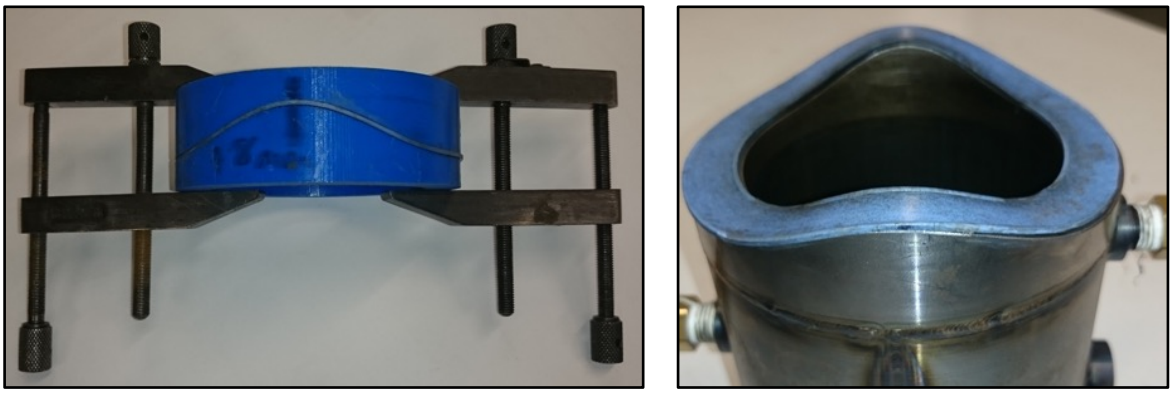

Figure 2.10 *Photographs demonstrating how clamps and 3D printed parts are used to shape the PTFE-based gaskets (left), and the resulting shape of the gasket matching the curved profile of the cylinder liner (right).*

2.1.6 Intake system

The intake system is designed to run in naturally aspirated (N/A) or boosted mode, as selected by a 3-way valve; for N/A mode, the air is taken from the test cell through a filter. For the boost system, air is supplied by a large tank of compressed air. After the 3-way valve, whether in N/A or in boosted mode, the air is drawn though a Roots type positive displacement flow meter which measures the air flow rate with an accuracy of $\pm$ 0.5%. The pressure and temperature in the air meter are also measured to allow the calculation of the air mass flow rate. A length of aluminium tube connects the air meter to a Bosch electronic throttle body, which is bolted to a 25 litre plenum. A 1.5 kW air heater is located between the throttle body and plenum so that the heating element protrudes into the plenum to provide heated intake air. An exposed junction thermocouple is inserted into the intake runner and provides the feedback signal for closed loop PID control of the intake air temperature to within $\pm$ 1 K. A Druck PDCR A20-0800 pressure transducer measures the air pressure in the plenum. There is also a Kistler type 4075A10 pressure transducer and second K-type thermocouple installed in the intake runner for monitoring the intake air pressure and temperature directly before the inlet valves.

For boosted operation, the pressure of the intake air is regulated before flowing through the air meter. This pressure regulator sets the maximum desired intake pressure and the throttle then provides closed-loop PID control of the intake air pressure. Figure 2.11 shows pressure traces for a range of boost pressures.

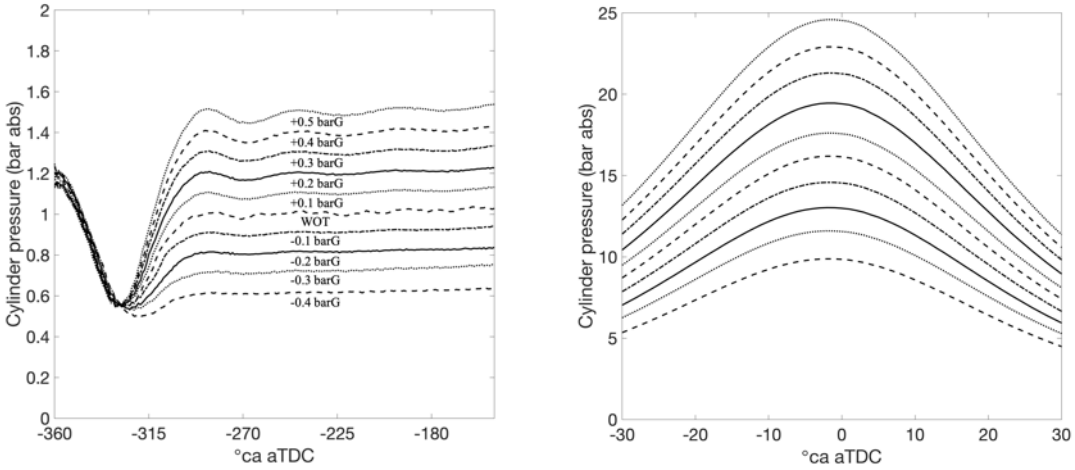

Figure 2.11 *Plots showing the pressure traces for a range of inlet pressures from -0.5 bar gauge to +0.5 bar gauge, highlighting in-cylinder pressure during induction (left) and peak pressure (right). The labels denote the intake air pressure for the pressure trace directly above.*

2.1.7 Modular cam system

The engine is designed to operate with two different cam systems; a roller finger follower (RFF) system and a continuously variable valve lift (CVVL) system. Both systems allow cam phasing with a total range of 50°ca advance for the intake and 48°ca retard for the exhaust. However, only the CVVL unit provides the flexibility of variable valve lift.

Cam Phasing System

The cam phasing system consists of a pulley with internal oil galleries that is mounted on each of the camshafts, both of which are shown in Figure 2.12. Within the pulley there are vanes that split each of the galleries and allow the pulley to rotate relative to the camshaft. A solenoid plunger valve controls the flow of oil between the galleries and the cam carrier. To vary the cam timing, the ECU sends a PWM signal to the solenoid operated spool-valve that opens the correct port, allowing oil to travel from the inlet to the correct groove in the camshaft journal, which has an internal passage that is connected to the appropriate oil gallery in the pulley. The difference in pressure across the vane in the pulley results in

rotation relative to the camshaft. The oil supply for the cam phasing system is provided by an external oil circuit to the engine in order to provide external control of oil pressure.

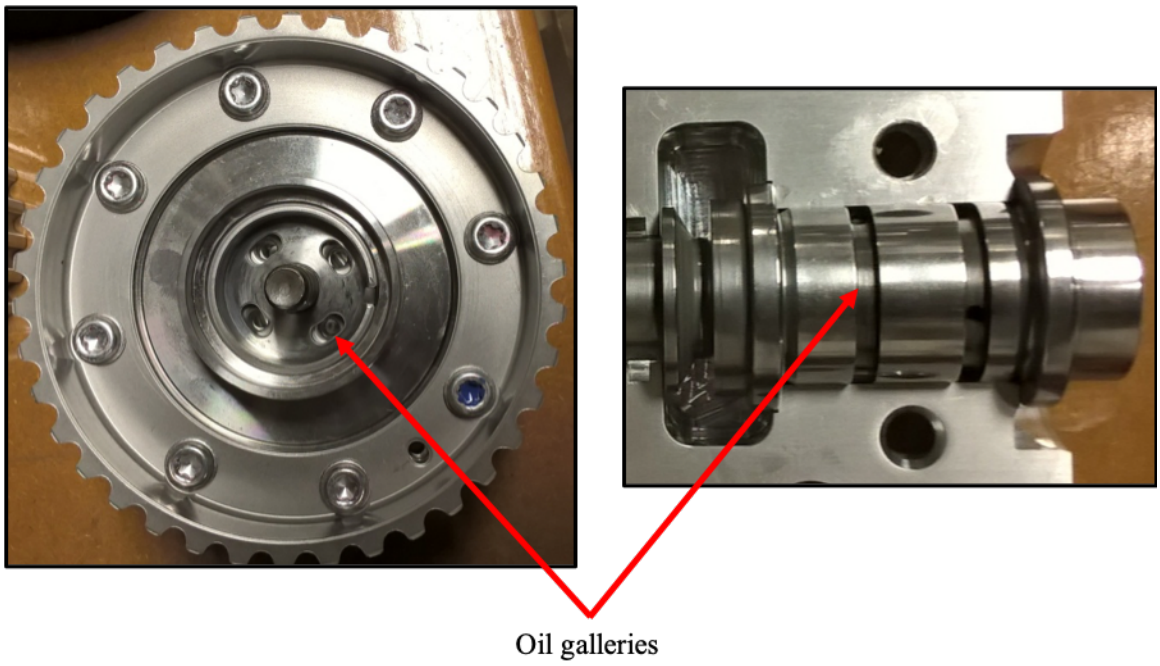

Figure 2.12 *Oil gallery ports in the pulley (left) and oil passages in the camshaft (right).*

CVVL System

The CVVL system installed on the intake system is based on the electro-hydraulic UniAir^{TM} system similar to that found on JLR's Ingenium engines and utilises pressurised volumes of oil to actuate the valve. Figure 2.13 shows a schematic of the CVVL system to aid the following description of its operation.

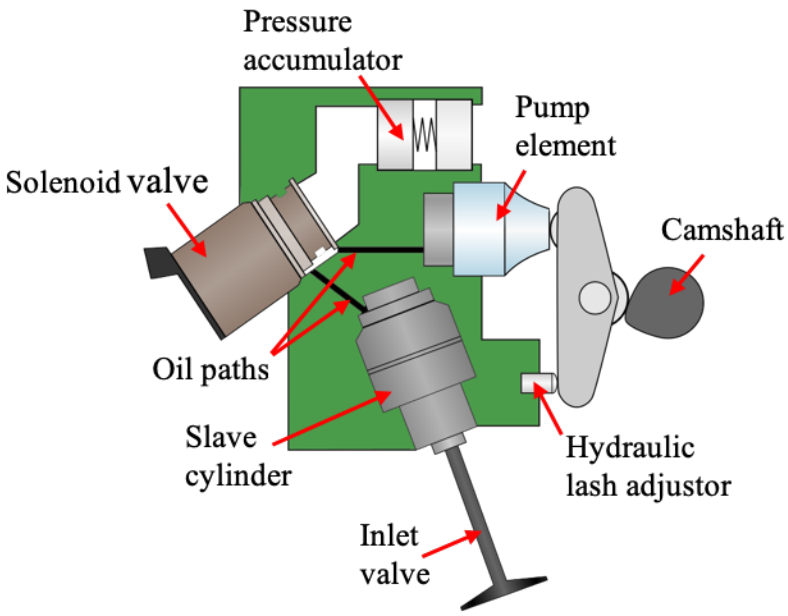

Figure 2.13 *Schematic of the CVVL system installed on the intake valvetrain.*

Oil is pressurised by a camshaft with a roller-type finger follower mechanism. The initial chamber is connected to two separate chambers through a solenoid-controlled switching valve. If the switching valve is open, oil flows through the switching valve to an intermediate-pressure chamber with a pressure accumulator, and the intake valve remains closed. When the switching valve is closed, the high-pressure chamber connected to the intake valve is filled with oil and acts as a rigid element, actuating the intake valve. In this way, by controlling the state of the switching valve and hence the volume of oil in the high-pressure chamber, the valve lift and duration can be varied in a continuous manner. Furthermore, both intake valves can be operated independently of each other. Figure 2.14 demonstrates the operation of the CVVL system when the opening time is kept constant and the closing time is varied, resulting in a range of lift durations.

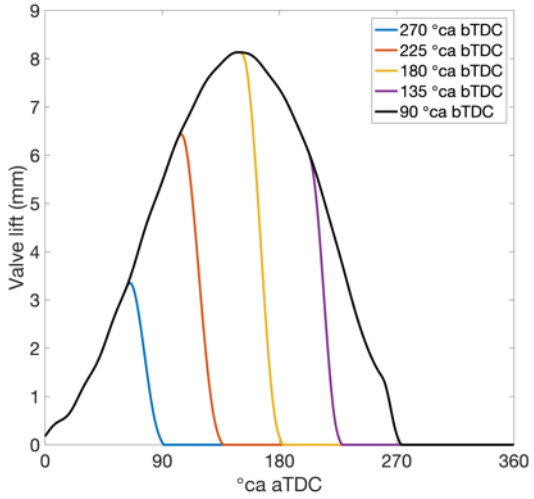

Figure 2.14 *Plots demonstrating examples of various valve lifts using the CVVL system. Each colour represents a different angle of valve closing.*

2.1.8 Oil system

The main oil circuit uses a dry sump system. Oil from the engine is drained to the sump, which is then pumped to a reservoir where it is separated from any gases. The oil is then pumped from the reservoir back to the engine. A separate circuit with an external pump is used to pressurise the oil for the cam phasing system to 3 bar and is regulated by a Sun Hydraulics high flow rate pressure regulator. For certain optical experiments, particularly those using Laser Induced Fluorescence (LIF), oil cannot be used to lubricate the cam system in case it enters the combustion chamber. Oil droplets fluoresce very strongly and produce LIF signals of greater magnitude than those of interest. For this reason, the hydraulic tappets that keep the cam in contact with the rocker have been replaced with solid tappets. The solid tappets are measured lengths of silver steel that replace the spring and piston components of the hydraulic tappet. They have been designed to provide a clearance of 250 µm.

2.1.9 Fuel system

Separate direct injection and port fuel injection systems are installed on the engine. The PFI injector is mounted in the intake runner, directly upstream of the inlet valves. The fuel tank for the PFI system is connected to a supply of nitrogen via a pressure regulator with which the fuel pressure can be set.

An external system is used to pressurise the fuel for the direct injection system to a maximum of 300 bar, which is limited by the structural design of the small reservoir located immediately before the injector. The injector itself is mounted vertically in the cylinder head, and its location in the combustion chamber can be seen in Figure 2.9. A schematic of the direct injection fuelling system is shown in Figure 2.15. The pump used in the system is a free piston, air-driven pump made by Heypac. Compressed air is supplied to the pump via a manual pressure regulator and a solenoid valve. Through the action of the pump, fuel is drawn from the tank, pressurised by a ratio of 40:1 and transferred to the injector through a short length of stainless-steel pipe. A low-pressure priming system is also installed to provide a method of purging the system when a change of fuel is required.

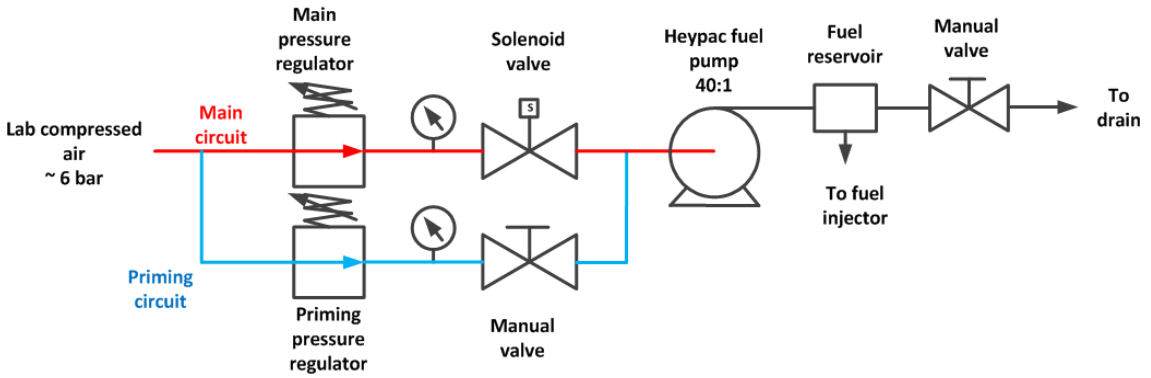

Figure 2.15 *A schematic of the main fuel system (red) and the priming circuit (blue).*

A Kistler type 4065B0500 pressure transducer is used to log fuel pressure on the high-speed DAQ system and a stock production pressure transducer provides fuel pressure for

the ECU. Two lambda sensors are mounted on the exhaust manifold; one that is logged by the LDAQ system and the other is connected to the ECU.

2.2 Pressure Measurements

A range of piezoelectric and piezoresistive transducers are used to measure pressures in the optical engine. A Kistler type 2621F pressure transducer cooling unit is used to keep the temperature of the in-cylinder, exhaust and barrel pressure transducers constant at 30 °C to prevent damage. A list of the specific sensors is provided in Table 2.2.

Table 2.2 *List of the Kistler pressure transducers installed on the optical engine.*

Type	Measuring
4075A10	Intake pressure
4075A10	Exhaust pressure with type 7533 cooled switching adaptor
4075A5	BDC reference pressure
4065B0500	Fuel pressure
6043A60	In-cylinder pressure

The signals produced by the pressure transducers are sent to an amplifier module (Kistler Type 4665) in the Signal Conditioning Platform (SCP) to be conditioned before they are transferred to the data acquisition card via BNC cables. The SCP is connected to a PC with a RS-232C serial cable in order to modify settings for the amplifier modules using the SCP software interface.

The intake, exhaust and barrel pressure transducers were calibrated with a vacuum pump and manometer, whereas the in-cylinder and fuel pressure transducers were calibrated with a dead-weight tester. The calibration plot of the exhaust pressure transducer and the resulting scatter are shown in

Figure **2.16** as an example.

.

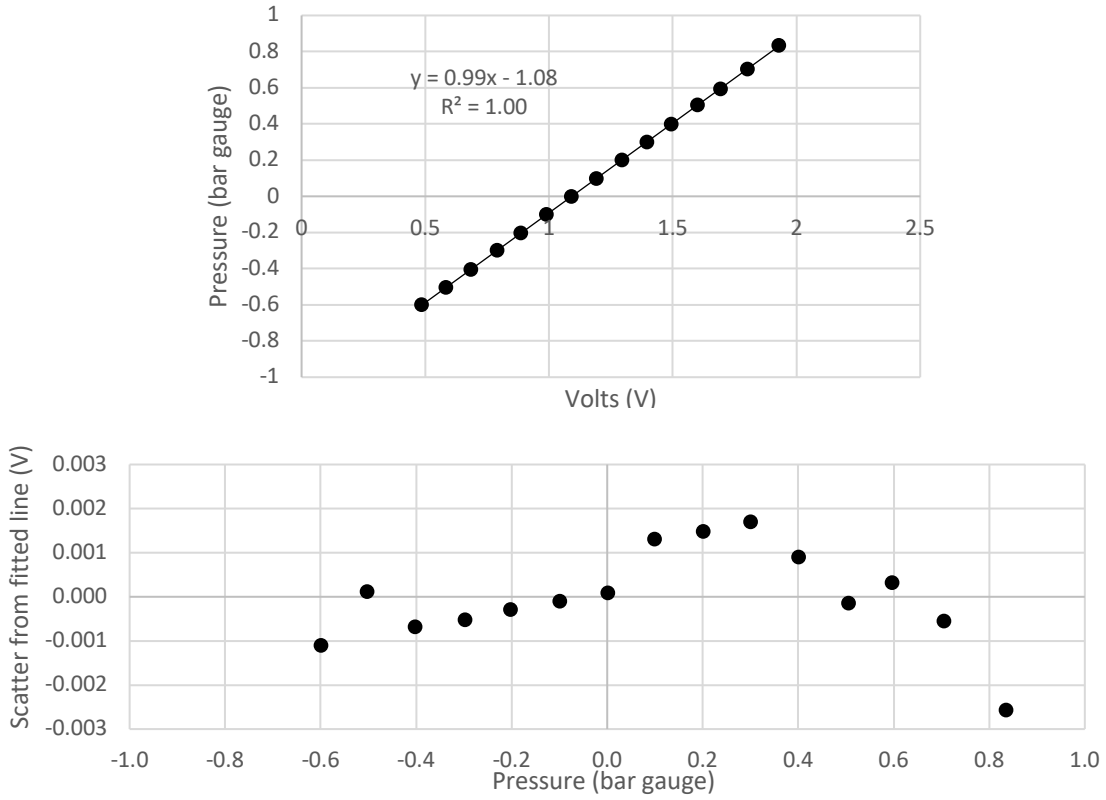

Figure 2.16 *Calibration of the exhaust pressure transducer (top) with scatter from the fitted line (bottom).*

Pressure measurements are also commonly used to derive the mass fraction of fuel burned (MFB) using the method developed by Rassweiler and Withrow. MFB has been used in the analysis in Chapter 6, therefore a brief outline is provided here; however, a more detailed description can be found in [37]. This method combines the inferred in-cylinder volume, using the crank encoder signal, and in-cylinder pressure measurements to calculate the progress of combustion. The incremental increase of pressure, Δp, as measured by the in-cylinder pressure transducer at each crank angle, θ, is assumed to be due to two processes:

- Compression due to the motion of the piston, Δp_v
- Combustion of the fuel, Δp_c

such that,

$$\Delta p = \Delta p_v + \Delta p_c \tag{2.1}$$

Hence, to find Δp_c, the pressure rise due to compression, Δp_v, is assumed to be a polytropic process with a polytropic index, n, as shown in Equation 2.2.

$$p_i V_i^n = (p_i + \Delta p_{v,i}) V_{i+1}^n \tag{2.2}$$

where V_i and V_{i+1} denote the cylinder volume between consecutive crank angles, θ_i and θ_{i+1}.

By re-arranging Equation 2.2 and substituting it into Equation 2.1, the rise in pressure due to combustion at a given crank angle, $\Delta p_{c,i}$, can be found:

$$\Delta p_{c,i} = p_{i+1} - p_i \left[\frac{V_i}{V_{i+1}}\right]^n \tag{2.3}$$

To account for the fact that combustion is not occurring at constant volume, $\Delta p_{c,i}$ is normalised at each time step by the volume at TDC, as shown in Equation 2.4.

$$\Delta p_{c,i}^* = p_{c,i} \left[\frac{V_i}{V_{TDC}}\right] \tag{2.4}$$

From this, the mass fraction burned, x, which ranges from 0 to 1, can be calculated using Equation 2.5.

$$x = \frac{\sum_{i=0}^{i} \Delta p_{c,i}^*}{\sum_{i=0}^{N} \Delta p_{c,i}^*} \tag{2.5}$$

where N is the total number of time steps over which mass fraction burned is calculated.

There are a number of assumptions that are associated with this method; for example, the analysis is sensitive to the value of the polytropic index, n. This is typically calculated from a logarithmic pressure-volume plot of a portion of the compression stroke, however this can lead to a characteristic drop in MFB due to heat losses and differences in composition

between burned and unburned gases. To account for this, the polytropic index has been calculated separately for the compression and expansion strokes, as suggested by [37].

Common indicators derived from the calculation of MFB are CA10, CA50 and CA90, which are defined as the time taken for 10%, 50% and 90% of the fuel to be burnt respectively. Another common indicator of the rate of combustion is the time taken from CA10 to CA90, defined in this work as CA10-90.

2.3 LabView DAQ and Control Systems

Currently two LabView programs are required to operate the engine and log data. The Engine Timing Control System provides control of the ignition and fuel injection systems, and also provides TTL pulses that are used to trigger optical equipment such as cameras, LEDs and the PIV system. There are two National Instruments cards for low speed (LDAQ – NI PCI 6024E) and high speed (HDAQ – NI PCI MIO 16E 1) data acquisition. The HDAQ high frequency data, such as in-cylinder pressure, are logged every crank angle degree whereas the LDAQ logs parameters such as engine torque, speed and temperatures at 10 Hz.

2.4 OpenECU and INCA Control Software

A flexible ECU has been installed in the test cell to control the cam phasing and CVVL systems. The models required by the ECU are developed in a Simulink environment and can be modified by the user. It connects to the control PC with a CAN bus interface and uses ETAS engine calibration software, INCA, as the user interface.

2.5 Summary

This chapter provides a detailed description of the optical engine and its auxiliary systems. The optical engine test cell facility developed over the course of this work offers the potential for using a range of optical diagnostic tools to measure in-cylinder phenomena. The intake system also offers variable valve lift and the option of boosting to provide a wide range of operating conditions.

The following chapter provides an overview of the particle image velocimetry (PIV) technique and a description of the system installed on the optical engine.

3 Particle Image Velocimetry

3.1 Introduction

In applied fluid mechanics, the need for quantitative flow field measurements has always been present. This chapter provides a brief overview of the techniques traditionally used to measure fluid velocities and introduces particle image velocimetry (PIV); a technique that can provide multi-dimensional, non-intrusive velocity measurements over a large region of interest. The theory behind PIV and its practical setup are then discussed in detail. This is followed by a comprehensive description of the PIV system used to measure flow fields in the optical engine used in this work. Practical difficulties that are specific to the application of PIV to optical engines are discussed and improvements to the experimental setup are presented.

3.2 Velocity Measurements in Fluids

In the study of fluids, qualitative flow visualisation techniques, such as the addition of dyes, particles and smoke to fluids, have been commonly used in the past and provide useful insights into flow behaviour over the whole domain. However, quantitative flow measurements are essential in both research and industrial applications. In internal combustion engines, the air motion generated by the induction process has a significant effect on fuel-air mixing and combustion, which dictate engine performance and emissions [37]. Quantitative flow measurements provide valuable information required to optimise the design of the cylinder head and intake system. The use of Computational Fluid Dynamics (CFD) in the design process is now widespread, hence there is a need for

quantitative measurements to validate the underlying models and provide direction for improvements.

Three techniques used for measuring velocity fields in fluids are hot wire anemometry (HWA), laser Doppler anemometry (LDA) and particle image velocimetry (PIV). A brief discussion of the two former methods is given before a thorough description of PIV is provided.

3.2.1 Hot wire anemometry

Hot wire anemometry is a flow measurement technique that infers the velocity of a flow by measuring the heat transfer from a small length of wire to the surrounding fluid. The relationship between the fluid velocity and heat lost from the wire can be found with careful calibration under known conditions. Using a probe with a single wire nominally provides a measurement of a single component of the fluid velocity in a measurement volume defined by the dimensions of the probe. However, there will be contributions from the two orthogonal flow velocities. Therefore, a probe with multiple sensing elements orientated perpendicular to each other is required to obtain multi-component measurements. Examples of HWA probes are shown in Figure 3.1. Arrays of sensing elements have also been used to take simultaneous measurements at more than one location. However, the increased size of the probe and its complex configuration can significantly disturb the flow of interest and introduce errors in the measurement.

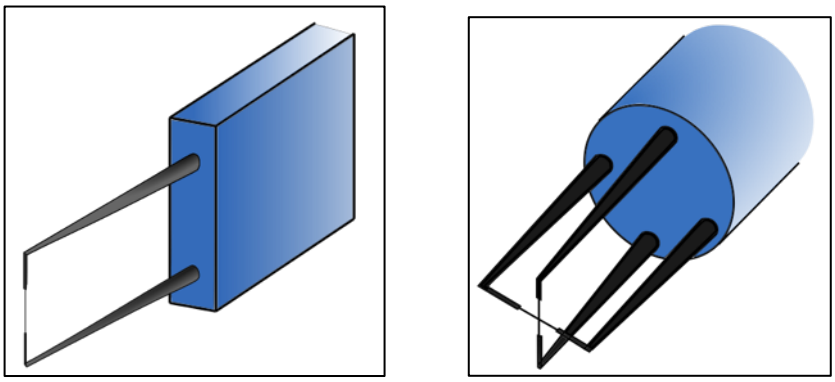

Figure 3.1 *HWA probes measuring one (left) and two (right) components of velocity.*

One of the main advantages of this technique is that the output from the sensor is an analogue signal, therefore measurements can be recorded with very high temporal resolution. This is extremely useful in studies of turbulent flows that are characterised by a mean component and superimposed high-frequency, fluctuating components [93] [94]. The diameter of the wire is typically in the order of 5 μm and its length is in the order of several millimetres, which defines the measurement volume.

HWA has been used successfully to study turbulence in flow fields due to its relatively low cost and simplicity. However, the development of high-power lasers in the 1970s provided a non-intrusive method of quantifying the flow field. Although laser-based techniques lack the high temporal resolution of HWA, they provide a spatially resolved measurement that does not disturb the flow and cannot be contaminated or damaged by harsh environments. Laser Doppler anemometry (LDA) is one of the most common laser-based methods for point-wise velocity measurements and has been extensively used in applied fluid mechanics research [95].

3.2.2 Laser Doppler anemometry

Laser Doppler anemometry, or alternatively laser Doppler velocimetry (LDV), uses the scattered light from a particle moving through an interference fringe to infer the velocity of a fluid. The most common setup of LDA uses two coherent laser beams to create an interference pattern in the measurement region. The fluid is seeded with particles that randomly pass through the set of fringes and scatter light, which is then recorded by a photodetector. The frequency of the scattered light is a function of the fringe spacing, which is dependent on the frequency of the incident laser light and the beam angle, and the velocity of the particle. The optical layout required for LDA measurements and the form of the recorded signal are shown in Figure 3.2.

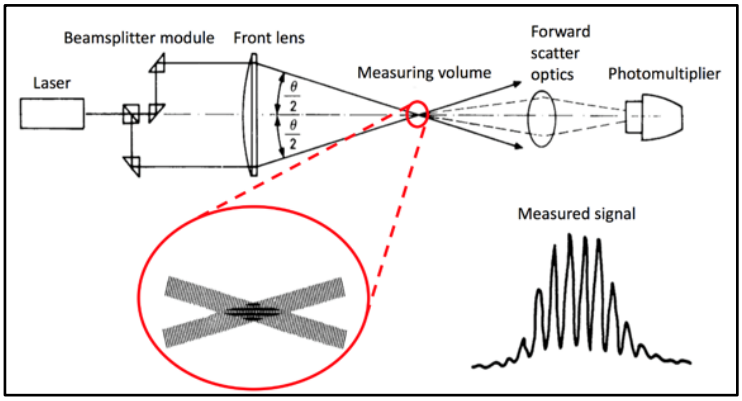

Figure 3.2 *General schematic of the optical setup required for LDA measurements (adapted with permission from* [37]*).*

Similar to HWA, LDA is a point measurement technique as a single fringe pattern nominally produces a single component of velocity in the measurement volume defined by the crossing laser beams. However, realistically, there are contributions from the whole flow field. To obtain measurements of multiple velocity components, the orientation of the fringe pattern must be changed, which may not be practical due to the limitations of optical access. Unlike HWA, LDA produces intermittent measurements as signals are produced only when a particle happens to pass through the probe volume.

Both LDA and HWA have been used extensively for velocity measurements in flow fields [96]. The non-intrusive nature of LDA provided an advantage over HWA, however this came with a substantial increase in cost due to the laser equipment and necessary optical access. The main disadvantage of both techniques is the lack of simultaneous information over the whole flow domain. Particle Image Velocimetry (PIV) is a flow measurement technique that is capable of capturing instantaneous, multi-component velocities within a plane or volume with high spatial and temporal resolution. This technique is described in detail in the following section.

3.3 Theory of Particle Image Velocimetry

3.3.1 Background

Particle image velocimetry derives the velocity of a fluid, $\boldsymbol{u}$, by measuring the displacement of a fluid, $\Delta\boldsymbol{x}$, in a known time, Δt, according to the relation $\boldsymbol{u} = \frac{\Delta \boldsymbol{x}}{\Delta t}$. The fluid is seeded with particles that are carefully chosen to faithfully follow the flow. These particles are illuminated by a pulsed light source, most commonly a laser, that has been formed into a sheet. In modern systems, the scattered light is then imaged onto a digital sensor that is positioned perpendicular to the sheet. Statistical interrogation methods are then used to calculate the displacement of groups of particles between a pair of images, from which the velocity is deduced.

PIV is a remarkably diverse technique that has found applications in a large range of scientific fields, from visualising the blood flow through a mosquito's proboscis [97] to quantifying convective flows in airplane cabins [98]. The most common setup is two-dimensional, two component (2D2C) PIV that produces planar measurements of velocity

fields. However, it is possible to measure three velocity components in a single plane using stereoscopic PIV [99] or in a volume using volumetric PIV [100]. With each added velocity component and dimension, the complexity of the experimental setup and cost of the additional equipment increases substantially.

Planar PIV has been used in this work, therefore the theory behind this variant of PIV will be described in detail in the following section.

3.3.2 Practical overview of PIV

The layout for a typical planar PIV experiment is shown in Figure 3.3.

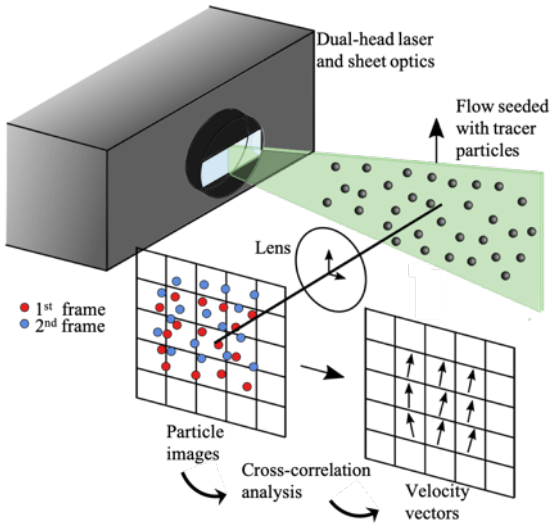

Figure 3.3 *Layout of a general planar PIV system.*

The main sub-systems that will be covered in this section are listed below:

- Seeding system
- Illumination and beam delivery
- Imaging system
- Synchronisation and data acquisition
- Image analysis, validation and post-processing

Seeding

The seeding system plays a crucial role in a PIV experiment. It is important to remember that the velocity of the fluid is not measured directly; it is inferred by the measurement of the displacement of groups of particles. Therefore, the accuracy of the measurements relies on an appropriate choice of tracer and its delivery to the fluid. The ideal seeding particle should:

- perfectly follow the flow
- remain inert
- withstand the conditions in the measurement environment
- scatter sufficient light to produce bright images
- allow stable and repeatable production in large quantities

The main consideration is the balance between light scattering properties and particle size. For example, the first criterion suggests that the particle should be small so that it faithfully follows the flow. However, the particle must also be large enough to sufficiently scatter light to form bright images on the sensor. The size of the seeding particle and its light scattering properties also influence the power requirement of the illumination source.

To investigate the ability of a particle to follow the flow, it is necessary to understand its dynamic response to variations in the fluid motion. The motion of a sphere in an unsteady flow field for high Reynolds number is complex and has been described by Maxey and Riley [101], and modified by Mei [102]. The equation of motion is derived using Stokes' Law and takes into account the properties of the particle and the fluid, body forces, momentum history effects and stresses in the surrounding fluid. An important outcome from this analysis is the time constant of the tracer particle, τ_p, which dictates the frequency

at which it can follow the underlying fluid flow. The particle time constant is defined by Adrian and Westerweel [103] as:

$$\tau_p = \frac{(\rho_p - \rho_f)\, {d_p}^2}{18\, \rho_f\, \nu_f\, \phi} \tag{3.1}$$

where ρ_f is the density of the fluid, ρ_p is the density of the particle, d_p is the diameter of the particle, υ_f is the kinematic viscosity of the fluid, and ϕ is an empirical function that accounts for the particle Reynolds number.

The particle time constant places a limit on the scales of flows that can measured with that tracer. However, Melling calculates that an oil particle of 1 μm has a frequency response of 10 kHz, which is suitable for engine flows [104].

The choice of seeding particle depends on the fluid that is being investigated and conditions of the experiment. In a review of tracer particles for PIV, Melling provides a list of seeding particles commonly used for various PIV experiments in liquids and gases [104]. Modern PIV experiments in engine-related research are almost exclusively conducted in gaseous flows, for which tracer particles typically have diameters of around 1 – 2 μm. Under motoring conditions, liquid particles such as silicone oil and vegetable oil are preferred to solid particles as they are cheap, non-abrasive to optical surfaces, and can be reliably produced in large quantities.

Multi-jet atomisers, such as the Laskin nozzle, are widely used to produce liquid droplets as seeding particles for PIV. The action of forcing air through small holes into a reservoir of seeding liquid results in small droplets, typically 1 μm in diameter, to be formed. A more thorough description of their operation can be found in [104].

Illumination and beam delivery

The power requirement of the light source is dictated by the scattering properties of the seeding particles. The seeding particles used for gaseous flows typically have a mean diameter of 1 μm , which require a light source that can produce energies in the range of 1-100 mJ per pulse to produce bright enough particle images [103] [105]. High-power, dual-head, pulsed lasers are well suited to this task and are the most common source of illumination in planar PIV experiments. That being said, in recent years, the development of high-power LEDs has led to their use as a light source [106]–[108]. They are relatively cheap in comparison to laser systems and avoid the stringent safety requirements associated with Class 4 laser installation. However, one of the main advantages of lasers is low beam divergence, which allows easy collimation. In contrast, LEDs have a relatively large beam divergence and so forming a sheet with sufficient energy density can be difficult. A schematic of a typical dual-head laser is shown in Figure 3.4.

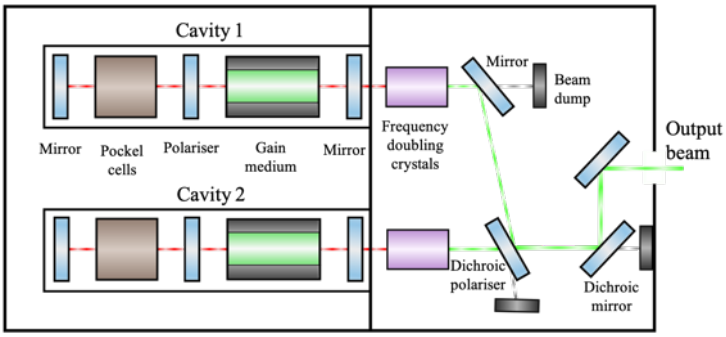

Figure 3.4 *Simplified schematic of a dual-head laser typically used in PIV experiments.*

In recent years, diode-pumped Nd:YAG or Nd:YLF (Neodymium-doped Yttrium Lithium Fluoride) lasers have replaced copper-vapour lasers as the most popular option for high speed, planar PIV due to their compactness and efficiency [69]. Nd:YLF lasers produce a beam of light at 1053 nm with a diameter in the order of 10 mm. This beam is then

frequency doubled using non-linear optical crystals to produce green light at 527 nm before it is formed into a sheet.

A combination of spherical lenses is used to focus the beam to provide the appropriate sheet thickness. A cylindrical lens is used to expand the beam in a single direction, forming a sheet. A typical arrangement of lenses for sheet formation is shown in Figure 3.5

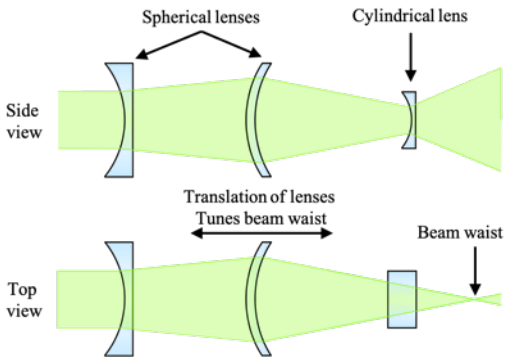

Figure 3.5 *An example of sheet forming optics.*

Imaging

The imaging setup defines the size of the of the particle images, which can have a significant effect on the error in the final measurement (see Section 3.3.3). Therefore, it is important to design the correct system to achieve the optimum particle image diameter, which is typically at least 2 - 3 pixels [109].

A lens is required to focus the particle images onto a digital sensor for image acquisition. An important property of the lens is the f-number, defined as:

$$f^{\#} = \frac{f}{D} \tag{3.2}$$

where f is the focal length of the lens and D is the diameter of the aperture.

For commercial lenses, there are typically a number of discrete f-numbers available; each 'stop' results in a factor of 2 difference in intensity from the previous stop. To produce brighter images, the f-number is decreased, which results in a larger aperture diameter and increased exposure for the sensor. However, the f-number also has an effect on the depth of field of the image, with higher f-numbers resulting in a greater depth of field. This can lead to additional background scatter being focussed onto the sensor, degrading the quality of the image. When optimising the imaging system, a compromise must be found between the intensity of the particle images, their effective image diameter and the depth of field.

For high-speed applications, the most common methods of image acquisition are CMOS (Complementary Metal-Oxide-Semiconductor) and CCD (Charge Coupled Device) cameras. The main differences between the sensors are their structure, manufacture and the method by which the electrical charge is read out. Although, CCD sensors are generally more sensitive, CMOS sensors have become the popular choice for high-speed applications due to advances in their manufacture leading to lower costs, while retaining image quality [110].

Synchronisation & Acquisition

A system is required to ensure that the laser and cameras are triggered at the correct instant. A general timing scheme is shown in Figure 3.6.

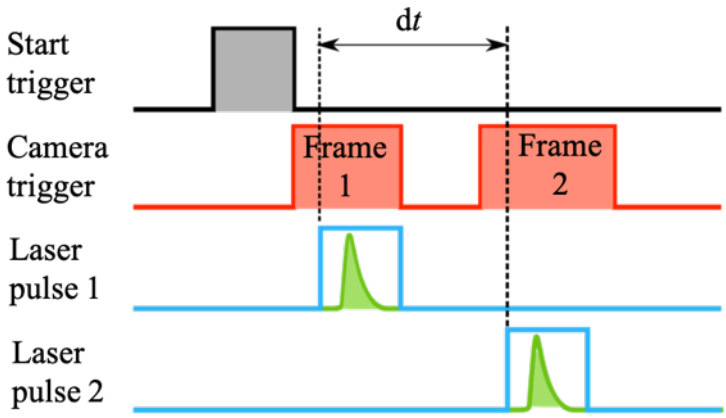

Figure 3.6 *General timing diagram for the synchronisation of the camera and laser cavities. The black line is the start trigger from the user and the red line denotes when the camera is active. The blue line denotes the laser trigger, which results in the light output, shown in green.*

This usually requires a timing unit that can trigger the laser and camera with an internal clock or by taking an external trigger as an input. This allows the PIV measurements to be synchronised to other experimental facilities, for example, the crank encoder mounted on an engine.

Correlation analysis

The method used to calculate the displacements of the tracer particles between two frames is dependent on the density of tracer particles in the experiment. Low seeding density allows particles to be tracked individually; this is known as Particle Tracking Velocimetry. For PIV, the seeding density is increased to improve the spatial resolution of the measurements. Therefore, individual particle tracking is no longer possible, and techniques are required to estimate the average displacement of groups of particles. A brief overview of the theory used for the calculation of velocity fields from multi-frame, single exposure PIV is provided here. However, a detailed treatment of the fundamental theory and historical development of PIV evaluation methods can be found in [103][109][111].

The general procedure for calculating a velocity field from a pair of recorded frames is shown in Figure 3.7.

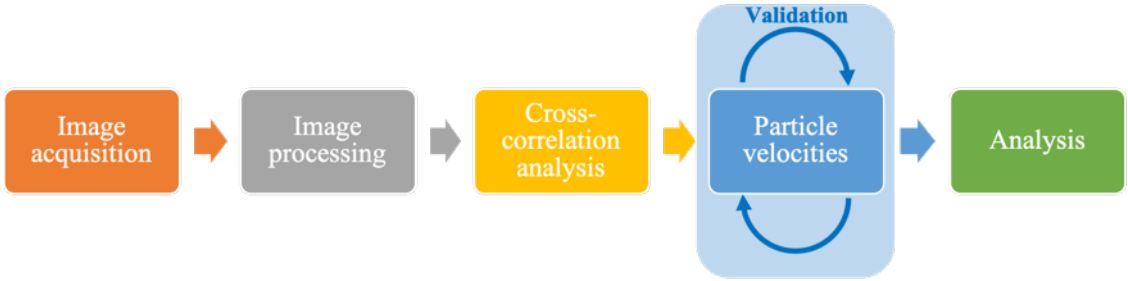

Figure 3.7 *Procedure for extracting velocity fields from particle images.*

The images are first divided into discrete regions, known as interrogation windows that typically contain 32 × 32 pixel. The implementation of the size and shape of the windows has a significant effect on the reliability and accuracy of the resulting vector field. Advanced interrogation techniques have been developed to manipulate their size and shape to minimise errors as discussed in Section 3.3.3. It is also common to overlap the interrogation windows to increase the number of vectors in the flow field. The spatial cross-correlation of corresponding interrogation windows from two frames produces a correlation map with a distinct peak located at the mean displacement of the particles in the interrogation window. Although it is possible to perform the cross-correlation directly in the spatial domain, it is common to transform the images into the Fourier domain using the Fast Fourier Transform (FFT) for the calculation. For a square interrogation window of length, N pixels, using the FFT method results in a reduction in the number of operations from N^4 to $N^2 \ln N$ [112]. Examples of good correlation and poor correlation are shown in the maps of correlation value for 64 × 64 pixel interrogation windows in Figure 3.8.

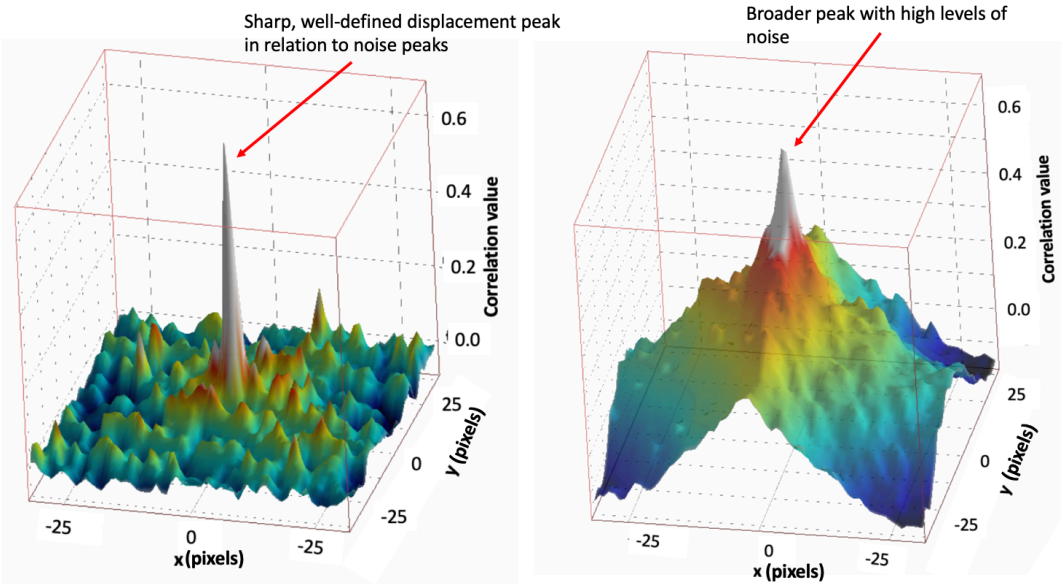

Figure 3.8 *Maps of correlation value between two 64 × 64 pixel interrogation window, demonstrating examples of good correlation (left) and poor correlation (right) - correlation maps are taken from experiments in the optical engine.*

The size, shape and location of the dominant peak provide information about the displacement of the particles. An expression for the conditional average of the correlation term, $R_D(\boldsymbol{s})$, for a given flow field is [113]:

$$\langle R_D(\boldsymbol{s})|\boldsymbol{u}\rangle = {I_z}^2\, {t_0}^2\, N_I\, F_I(\boldsymbol{s})\, F_O(\Delta Z)\, F_\tau(\boldsymbol{s} - s_D) \tag{3.3}$$

where $\boldsymbol{s}$ denotes the displacement in correlation space, I_Z is the light sheet intensity, t_0 is a normalisation factor for F_τ, $N_I$is the mean number of particle images in an interrogation window (particle image density), F_I and F_O represent the in-plane and out-of-plane loss of correlation, and F_τ is the particle image self-correlation.

The location of the peak provides the estimate of the mean displacement of the particle images, s_D, in the interrogation window. The amplitude of the peak is proportional to the particle image density, N_I, and the loss of correlation terms F_I and F_O. These terms represent the fraction of particles that remain within the interrogation volume and should

be maximised to unity for optimal results. The shape of the peak is related to the convolution of the particle image self-correlation, ${t_0}^2 F_\tau$, and the particle displacement distribution. Hence, it is affected by the presence of displacement gradients in the interrogation region.

In order to determine the mean displacement of the particle images, the location of the displacement-correlation peak must be found. A considerable effort has been made to develop methods that locate the particle image displacement with sub-pixel resolution, otherwise the accuracy of the technique is severely limited [114]. The most common method is a three-point estimator that fits either a parabolic or Gaussian curve to the three largest peaks in both directions, as shown in Figure 3.9. A Gaussian curve tends to be the most popular as ideal particle images are approximated by Gaussian distributions and it performs well [109], [111].

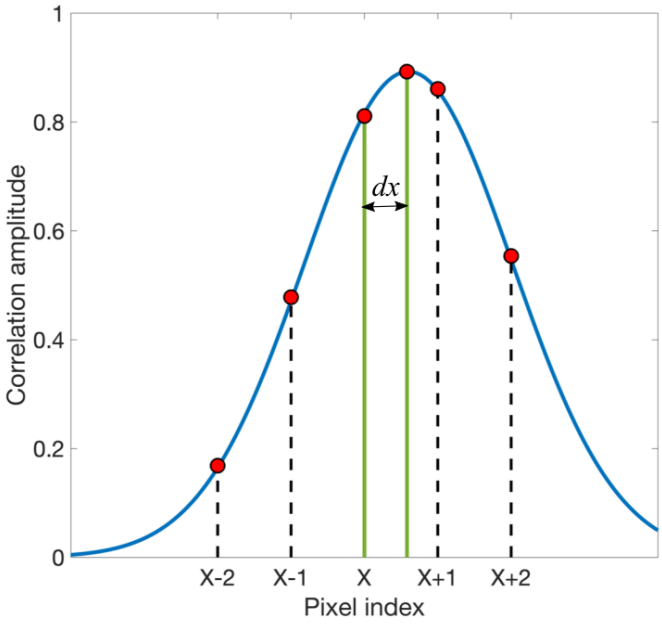

Figure 3.9 *An example of a Gaussian 3-point estimator used to determine sub-pixel displacements (adapted from* [105]*).*

Data validation and post-processing

The interrogation analysis produces a spurious vector when the amplitude of the displacement-correlation peak is relatively small and lost among the random noise peaks (see Figure 3.8). This can occur for a number of reasons including strong spatial velocity gradients within an interrogation window, large amounts of background noise and regions of high out-of-plane velocities. A robust method of vector validation is therefore necessary to remove spurious data and maximise the reliability of the measurement.

One method simply compares the amplitude of the correlation peak with a threshold value; if the peak is below the threshold, the result is discarded. A more commonly used method of validation, known as the peak detectability, Q, is the ratio between the amplitudes of the two highest correlation peaks ($C_1$and C_2), as defined in Equation 3.4.

$$Q = \frac{C_1}{C_2} \tag{3.4}$$

The higher the value of Q, the more certain the first peak is the correct estimate of the displacement. A value close to unity implies that the highest correlation peak is almost indistinguishable from the noise. These methods alone are not robust and should not be the only method of validation applied [103].

More robust methods such as histogram analysis and median testing consider more than a single interrogation result. Median testing involves the comparison of each velocity vector to the median of the surrounding velocities [115]. The median is preferred to the mean in this case as the mean is strongly skewed by spurious velocities, whereas the median is less affected. The deviation of a measured velocity from the median of the neighbouring eight velocities is calculated and normalised [116]:

$$\boldsymbol{r} = \frac{|\boldsymbol{u}_0 - \boldsymbol{u}_m|}{\boldsymbol{r}_m + \sigma} \tag{3.5}$$

where $\boldsymbol{u}_0$ is the measured velocity vector under investigation, $\boldsymbol{u}_m$ is the median of the neighbouring vectors, $\boldsymbol{r}_m$ is the median of the deviations of all the neighbouring vectors, $\boldsymbol{r}_i$ such that $\boldsymbol{r_i} = |\boldsymbol{u_i} - \boldsymbol{u_m}|$, and σ is an offset to improve the performance for low levels of fluctuation.

The disadvantage of this method is that an appropriate threshold must be selected to remove spurious vectors. However, the normalisation has been shown to make the value of $\boldsymbol{r}$ relatively insensitive to experimental conditions and so a universal value of 2 is suggested [116].

The validation process is iterative; if a vector is rejected by the methods described above, it is possible to replace it using alternative correlation information (2nd, 3rd or 4th highest correlation peaks) or interpolation of the surrounding vectors.

3.3.3 System design and minimisation of error

The measurement accuracy of the PIV technique is dependent on a number of factors that range from experimental limitations to the statistical evaluation of the particle images. Calculating velocity $\boldsymbol{u}$ using the simple relation, $\boldsymbol{u} = \frac{\Delta \boldsymbol{x}}{\Delta t}$, requires measurement of the displacement, $\Delta \boldsymbol{x}$, and control of the time separation between illumination pulses, Δt. The error in the time delay is dictated by hardware limitations associated with the laser and can be reduced to as little as 50 ns [117]. For engine experiments, a typical value of Δt is 20 μs, therefore the error in the time delay can be as low as 0.25%. Similarly, the error in the

measurement of the displacement, $\Delta \boldsymbol{x}$, must also be minimised for accurate and reliable velocity measurements. The main sources of uncertainty in the measurement are:

- Loss of particles from an interrogation volume
    - In-plane
    - Out-of-plane
- Velocity gradients in an interrogation volume
- Particle image diameter, d_τ
- Particle image density, N_I
- Background noise in particle images

Minimisation of these sources of uncertainty can be achieved by optimising experimental parameters for a given experiment. In order to define optimal experimental parameters for the interrogation analysis, Monte Carlo methods have been used to simulate the displacement particle images for a large range of different conditions, such as varying particle image density, particle image diameter and local particle displacement gradients. By analysing the results of the interrogation analysis for these simulated tests, a general set of design rules for PIV experiments have been laid out by Keane and Adrian to minimise errors in the calculation of real particle displacements [118]:

$$N_I > 10 \qquad M\,|\Delta \boldsymbol{u}|\Delta t < d_\tau \qquad |\Delta \boldsymbol{X}| < \frac{1}{4} D_{\boldsymbol{I}} \qquad |\Delta \boldsymbol{z}| < \frac{1}{4} z_{\boldsymbol{0}} \qquad (3.6)$$

where M is the magnification of the imaging setup, d_τ is the particle image diameter, $\Delta \boldsymbol{X}$ is the particle image displacement (in the image plane), D_I is the width of the interrogation window, Δz_o is the laser sheet thickness, and Δz is the out-of-plane particle displacement. It should be noted that upper-case letters (***X, Y, Z***) for displacements refer to the image plane, and lower-case letter (***x, y, z***) refer to the object plane (measurement region).

In addition to these design rules, advanced interrogation methods have been developed to minimise the error in calculating the particle displacements. In the following sections, each source of error and its minimisation are discussed.

Loss of particles from an interrogation volume

The interrogation volume is the volume defined by the interrogation window projected onto the object plane and the laser sheet thickness. Seeding particles leaving the interrogation volume between frames, both in-plane and out-of-plane, result in a reduction in the amplitude of the displacement-correlation peak. This directly affects the detectability of the displacement peak as the amplitude is proportional to both F_I and F_O (see Equation 3.3). The value of F_O represents the loss of particles from the laser sheet, therefore the design rule outlined in Equation 3.6 suggests that out-of-plane particle displacements should be less than a quarter of the laser sheet thickness, Δz_o. This can be achieved by increasing the thickness of the laser sheet to minimise the number of particles that leave the sheet. However, the energy density of the laser sheet is reduced, which results in dimmer particle images.

It is also essential to maximise F_{I}, which represents the in-plane loss of particle images. The design rule in Equation 3.6 suggests that the in-plane particle displacement should be less than a quarter of the size of the interrogation window, which places a limit on the value of Δt for a given flow velocity. Another method of ensuring that the value of F_{I} is unity is by performing multiple passes of the correlation analysis with refinement of the interrogation windows [103] [119] [120]. The advantage of using multiple passes is that for each iteration, the displacement vector can be estimated and the location of the interrogation window can be shifted in that direction. Therefore, for each subsequent pass,

it is more likely that the same particles remain in the interrogation window [121]. A visual description of this process is shown in Figure 3.10.

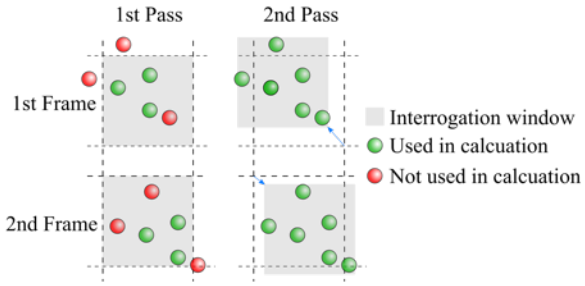

Figure 3.10 *The effect of introducing a shift in the location of interrogation windows in the correlation analysis.*

In addition to pre-shifting the interrogation windows, it is also common to decrease the size with each iteration. For example, for the first pass, the interrogation window may be 128 ×128 pixel to ensure that all the particle images from the first frame also appear in the second frame. The reduction in size continues for each pass until the final dimension is reached, which is typically 32 × 32 pixel. Due to the difficulty of reaching the required levels of seeding density without causing speckle patterns to form, 32 × 32 pixel is generally the size of the smallest interrogation window.

Velocity gradients

In the correlation analysis, it is assumed that the particle images in each interrogation window are displaced by the same amount between the two frames. However, in complex flows where strong velocity gradients are present, this may not be the case. The particle image pattern becomes deformed, which leads to the loss of particles between frames, reducing the value of F_1. Using conventional PIV interrogation analysis, the displacement-correlation peak for non-uniform displacement fields is reduced in amplitude and

broadened, sometimes splitting into multiple peaks. Therefore, its detectability is reduced and spurious vectors are more likely [122], [123].

In order to reduce the effect of velocity gradients, advanced methods that deform the shape of the interrogation window in order to minimise the loss of particle image pairs have been developed [124]. More recently, iterative schemes have been developed that apply window deformation at every pass of the interrogation analysis [125], [126].

Particle image diameter

If particle images are less than a pixel in diameter, the particle displacements can become biased towards integer values. This is commonly known as the peak-locking effect and can be a dominating source of error [114]. If the displacement-correlation peak is less than a pixel wide, the three-point estimator used to infer its location does not perform well. As a result, the location of the peak can only be calculated to the nearest pixel, which for a maximum displacement of 8 pixels in a 32 × 32 pixel interrogation window, leads to an error of approximately 6%.

As the type of seeding particle is usually constrained by the experimental conditions, the peak-locking effect can only be reduced by changing the imaging system to increase the effective particle image diameter. This can be achieved by a using different lens to increase the effective diameter at the cost of reduced field-of-view. Another possible solution is to change the location or focus of the camera in order to de-focus the particles images and increase their effective diameter [103], [105].

Particle image density

The design rules outlined in Equation 3.6 suggest that the number of particles in an interrogation window should be greater than ten. For the correlation analysis, more particle image pairs increase the amplitude of the displacement-correlation peak according to Equation 3.3. This results in a more reliable estimation of the mean particle displacement. However, increased seeding density for a given interrogation window can lead to the formation of speckle patterns and degradation of image quality due to layers of oil on optical surfaces.

3.4 Experimental Setup

The following section describes the PIV system used for the work in this thesis. Figure 3.11 shows a CAD model and schematic of the PIV setup on the engine.

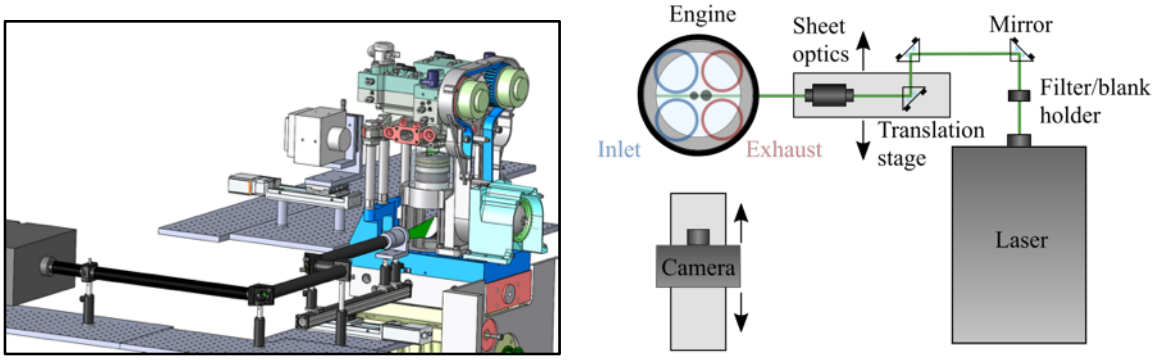

Figure 3.11 *CAD model (left) and schematic (right) of the optical setup for PIV measurements in the tumble plane.*

All velocity measurements are made in the central tumble plane, which bisects both sets of valves, the spark plug and the fuel injector, as shown in Figure 3.12.

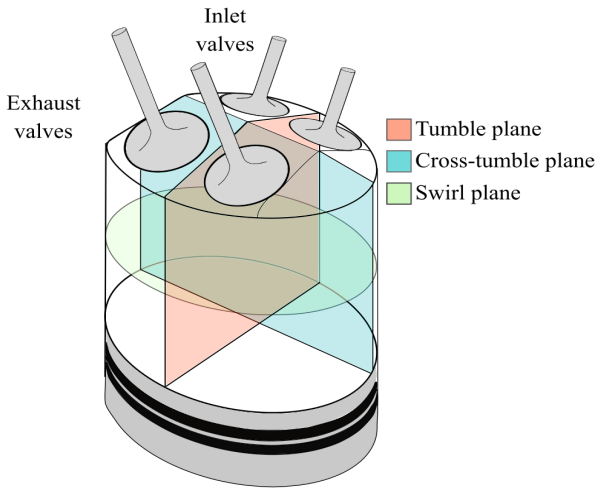

Figure 3.12 *Schematic defining the orientations of the tumble, swirl and cross-tumble planes in the engine.*

3.4.1 Seeding

A schematic of the seeding system is shown in Figure 3.13. The system consists of a supply of lab compressed air that is regulated with a manual valve to 4 bar before flowing through a mass flow controller (MKS Mass-Flo Controller). This unit provides control of the mass flow of air that enters the atomiser and the resulting seeding density for the PIV measurements. After the mass flow controller, the circuit splits into two branches, each with its own solenoid valve; one path is connected directly to the intake plenum, and the other flows through the atomiser before re-joining the path to the plenum. Initially the solenoid valve for the branch with air only is open, and the other is closed, which allows air to combine with the main engine air path in the plenum. When seeding is required, the states of the solenoid valves are switched, so that air flows through the atomiser and seeding particles are produced and enter the main air path. Without the branched system, a sudden introduction of seeded air into the intake plenum disturbs the main air path, resulting in oscillations in the throttle control and intake air pressure.

A LaVision Aerosol Generator produces oil droplets with a nominal diameter of 1 μm. As the diameter of the oil droplets is largely independent of the type of oil [127], regular olive oil is used. The oil droplets are introduced to the intake air in the intake plenum through a swan-neck pipe, as shown in Figure 3.20.

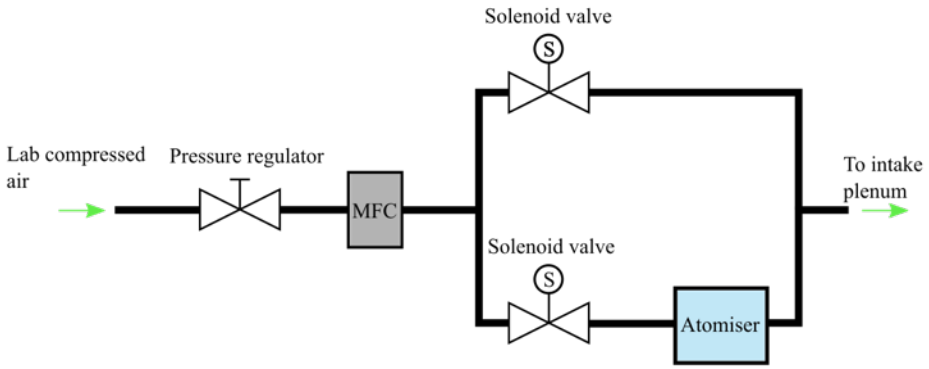

Figure 3.13 *Schematic of the seeding system.*

The optimal seeding density is largely dependent on the conditions of the flow. Hence, for each experiment, the seeding density was set using trial and error by analysing the resulting images.

3.4.2 Illumination and beam delivery

A diode-pumped, double cavity Nd:YLF laser was used as the light source. Its specification is provided in Table 3.1.

Table 3.1 *Laser specification.*

Model	Photonics Industries DM20-527 DH
Pulse energy @ 1 kHz (mJ)	20
Beam diameter (mm)	Nominally 10
Divergence (mrad)	8 ± 15%
Maximum repetition rate (kHz)	10 kHz
Pulse width (ns)	150 - 200

The LaVision DaVis system is capable of providing variable pulse separations during a single cycle. This allows the pulse separations to be tailored to the range of flow velocities within a cycle, which depends on the operating conditions and which part of the cycle is being investigated. Thus the particle image shift can be optimised throughout the cycle, minimising the loss of a particle images from interrogation windows and improving the dynamic range of the measurements [128]. A typical range of pulse separations for velocity measurements in the induction and compression strokes is from 3 μs to 50 μs.

For safety, the beam is completely enclosed in 1-inch black anodised tubes along the path from the laser head to the sheet-forming optics. A 1000 mm focal length convex lens is used to reduce the divergence of the beam. The final steering mirror and sheet optics are mounted on a rail that is bolted to a motorised translation stage (ZABER T-LSR150B). The stage can be controlled both manually or by software and provides positioning with an accuracy of 15 μm and repeatability of 2.5 μm. A telescope arrangement of spherical lenses controls the location of the beam waist and a concave cylindrical lens with focal length of -20 mm is mounted on the exit aperture (see Figure 3.5) to form an approximately 1 mm thick sheet in the measurement region. The cylindrical lens can be rotated to adjust the orientation of the sheet.

3.4.3 Imaging

A high-speed, 12-bit digital CMOS camera was used to image the tracer particles. Its specification is provided in Table 3.2. The imaging setup resulted in a magnification of 0.32 and a spatial resolution of 0.061mm/pixel (1.96 mm per 32 × 32 pixel interrogation window).

Table 3.2 *Camera specification.*

Model	Vision Research Phantom VEO 710L
Full resolution (px)	1280 × 800
Sensor dimensions (mm)	25.6 × 16
Pixel dimensions (μm)	20 × 20
Frame rate @ full resolution	7.4 kHz
On-board memory	18 GB
Maximum number of image pairs @ full resolution	6000

The camera is also mounted on a motorised translation stage so that the laser sheet remains in the focal plane of the camera when it is translated. A Nikon Nikkor 50 mm f/1.4 lens was used at $f^{\#}/4$ for the all of the work presented in this thesis. Imaging through a curved cylinder leads to image distortion, therefore the camera must be calibrated. This is achieved by imaging a uniform grid of dots placed inside the cylinder. The grid was glued onto a Perspex base that also allowed a visual check of the location of the laser sheet in relation to the imaging plane. An example of the calibration grid and a typical calibration image are shown in Figure 3.14. LaVision DaVis 8.0 software was used for calibration, image acquisition and correlation analysis.

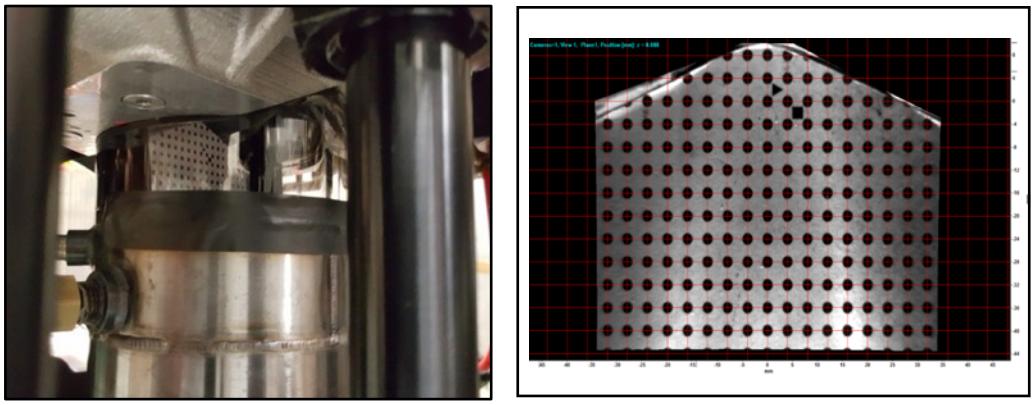

Figure 3.14 *Image of the calibration grid in the cylinder during calibration (left) and an example of the output from the calibration and distortion correction procedure using DaVis 8.0 (right).*

3.4.4 Synchronisation and acquisition

A LaVision Programmable Timing Unit (PTU X v10) monitors the synchronisation of the laser and camera with the engine. This system includes a Rotary Decoder add-on that is specifically designed for engine applications and crank-angle resolved measurements. The engine crank encoder provides the PTU with TTL signals every cycle and every crank angle. A 'start' trigger can either be triggered internally with the DaVis software or, if synchronous pressure data is required, externally with a TTL pulse from the engine ETCS system.

3.4.5 Analysis procedure

Image processing and vector calculation is performed using LaVision DaVis 8.0 software. The analysis procedure is as follows:

1. Image pre-processing
    a. Subtract moving average – 10 pixel square window.
    b. Image normalisation – Min/max filter – 10 pixel square window.
    c. Image correction applied from calibration grid
    d. Static mask applied to remove regions outside of the laser sheet.
2. Vector calculation
    a. Multi-pass, decreasing size - 128 × 128 pixel square window reduced to 32 × 32 pixel gaussian window with 50% overlap and 3 passes at the final size, with adaptive window deformation and offset.
3. Validation
    a. Universal outlier detection with a threshold of $Q < 1.8$.
    b. Median filter with 2 passes – 7 × 7 pixel window.
    c. No interpolation or smoothing applied to the final result.

4. Post-processing
    a. Remove all vectors that are not first-choice after the correlation procedure.
    b. Apply dynamic mask that removes regions that obstruct the field of view during the cycle, such as the inlet valves and the piston.

Matlab is used for all subsequent analysis of the vector fields produced by DaVis; this includes digitally masking the velocity fields to remove regions of the image where the inlet valves and piston block the scattered light. All the velocity fields from a single test are compiled into a single Matlab structure, which also contains statistics and flow quantities such as vorticity and strain rate. Figure 3.15 shows an example of a processed vector field.

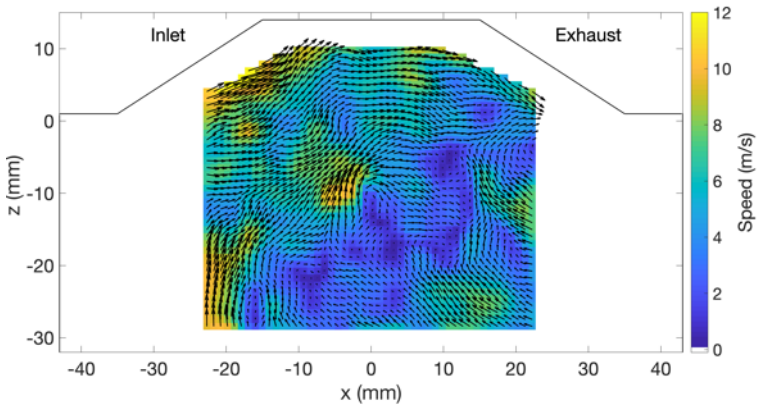

Figure 3.15 *An example of a processed vector field using Matlab.*

3.4.6 Experimental repeatability and error minimisation

Experimental repeatability

It is vital that experiments are repeatable in order to have confidence in the results. This is especially the case for in-cylinder flow measurements due to the inherent cyclic variation of in-cylinder flow operation and stochastic nature of turbulence. To ensure repeatable experiments in this work, the inlet boundary conditions were tightly controlled with closed-

loop throttle control and repeatable valve operation. Examples of this are shown in Figure 3.16, which presents ensemble averaged inlet pressure traces and inlet valve lifts for three consecutive test runs of 100 cycles each for a single condition (T8, defined in Table 5.1). It is worth highlighting that there are three lines plotted, but they are difficult to differentiate as there is little difference between the test runs. The mean of all 300 cycles is also shown with a black dashed line.

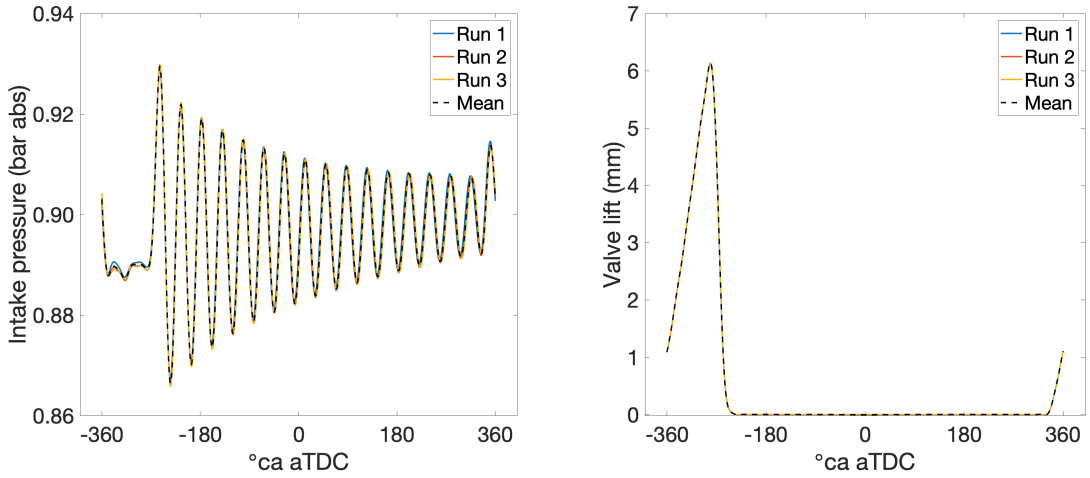

Figure 3.16 *Plots of ensemble averaged inlet pressure traces (left) and inlet valve lifts for three test runs of the same engine condition. The mean of all test runs is shown with a black dashed line.*

For this test condition, it is clear that there is very little difference between the mean inlet pressure and mean valve lifts for each run. In general, after each experimental run, the inlet conditions are checked to ensure that there is no anomalous variation within a single test run, and also between experimental runs.

The in-cylinder pressure also provides an indicator of variability between test runs; Figure 3.17 shows plots of in-cylinder pressure, with a detailed view demonstrating the variation within a single test run with markers indicating $\pm$ 1 standard deviation of the mean.

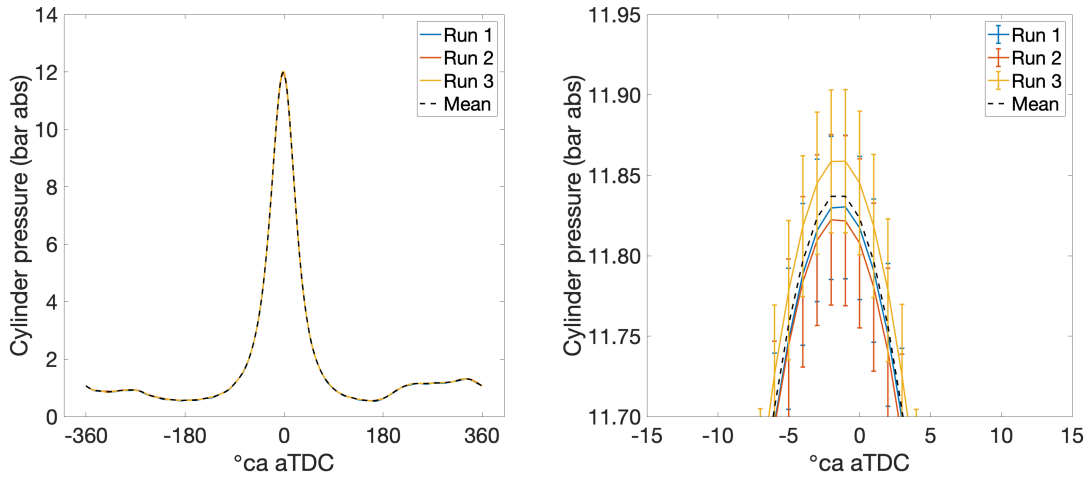

Figure 3.17 *Plots of ensemble averaged in-cylinder pressure traces (zoomed, right) for three test runs under identical conditions shown in Figure 3.16. Markers indicate ± 1 standard deviation of the mean for each run, and the mean of all test runs is shown with a black dashed line.*

Similar to Figure 3.16, it is difficult to differentiate the individual traces on the left-hand plot in Figure 3.17. However, in the zoomed view, it is possible to observe the differences between each test run. As is common for motored operation, there is very little variation in peak pressure within a single test run; for each test shown here, the standard deviation is within 1% of the mean for these tests. For this condition, the variation between the means is also within 1%, highlighting the repeatability of the operation of the engine. For other conditions, variation in boundary conditions between test runs may be greater than this example; however, if the variation in mean peak pressure between test runs was greater than 3%, the results were discarded and the test was repeated.

As well as the repeatability of engine operation, it is also worth investigating the repeatability of the in-cylinder flow velocity measurements. Figure 3.18 shows plots of ensemble averaged, spatially averaged flow speeds for the same three tests as discussed previously, as well as the mean of the whole 300 cycle dataset.

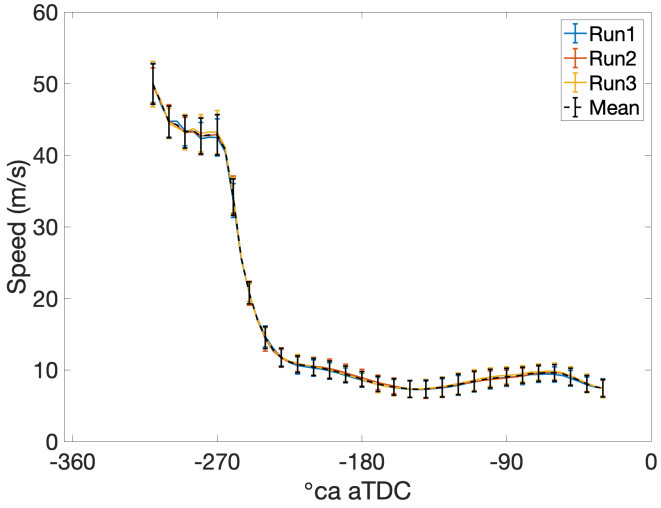

Figure 3.18 *Plots of ensemble averaged, spatially averaged flow speed for the three test conditions shown in Figure 3.16 and Figure 3.17. Markers indicate ± 1 standard deviation of the mean for each test run, and the mean of all cycles is shown with a black dashed line.*

Similar to the plots shown in Figure 3.16 and Figure 3.17, it is difficult to differentiate between the lines for each test run, with the variation in mean flow speed from run to run within approximately 2%. However, this is considerably smaller than the cyclic variation of approximately 10% for each test run, as indicated by the markers. Therefore, the tests are indeed repeatable and the three subsets of 100 cycles can be combined to form a set of 300 cycles, which can be used for further analysis.

Error minimisation

As discussed in Section 3.3.3, there are several errors associated with the PIV technique that must be minimised. LaVision DaVis 8.0 offers sophisticated algorithms that apply adaptive window deformation and offsetting during the cross-correlation analysis. This maximises the number of particle images that are correlated between each frame pair and attempts to improve the correlation when strong velocity gradients are present. To optimise the experimental setup, the rules listed in Equation 3.6 have been followed whenever possible. The seeding density was optimised for each test condition to maximise the number

of particle images without forming speckle patterns. However, as the volume in the cylinder varies throughout the cycle, the seeding density also varies. Therefore, a compromise was required to ensure there is sufficient seeding throughout the cycle.

The timing between laser pulses, d*t*, also varied throughout the cycle to account for the variation in flow speeds. In order to minimise the number of particles that leave an interrogation window between frames, it is recommended that the maximum particle image displacement is less than a quarter of the length of an interrogation window. With the current optical setup, a 32-pixel wide interrogation window corresponds to 1.96 mm in the engine. Therefore, no particle image should translate more than 0.49 mm between laser pulses. This condition places an upper limit on the measured flow speed for a given laser pulse separation. Figure 3.19 shows an example of the variable laser pulse separation, d*t*, and the corresponding maximum velocity for a single test condition to ensure that a particle does not move greater than one quarter of the interrogation window.

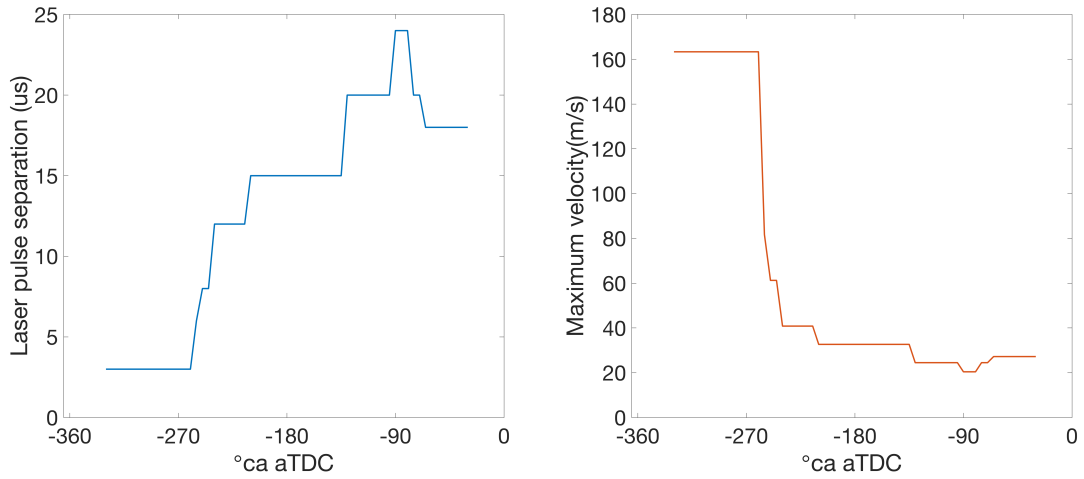

Figure 3.19 *Plots demonstrating the variable laser pulse separation, dt, (left) and the corresponding maximum velocity if a particle displacement is to be less than a quarter of an interrogation window (right).*

The initial pulse separation of 3 μs is the shortest allowed for the operation of the camera, and so is used during the induction process where the inlet jet velocities are highest. The value of dt increases as the valve closes to account for the lower gas velocities. During the compression stroke, the value of dt varies from approximately 16 μs to 24 μs, corresponding to about 20 m/s to 40 m/s. Without the variable dt, a fixed pulse separation would be used for the whole cycle, and a compromise must be made between the induction or compression processes, leading to increased errors throughout the cycle.

3.5 Flow-Derived Quantities

In order to extract as much information as possible from the spatially-resolved velocity measurements, additional quantities can be derived from the velocity fields. This section defines derived quantities that are used in this thesis, such as the specific kinetic energy and tumble ratio. However, first it is useful to define the spatial average, $\bar{Q}$, of a field, $\boldsymbol{Q}$, using Equation 3.7.

$$\bar{Q} = \frac{1}{N}\sum_{i=1}^{N} \boldsymbol{Q}_i \tag{3.7}$$

where N is the number of values contained in the column vector of $\boldsymbol{Q}_i$.

Equation 3.7 is used to calculate all spatial averages presented in this work, including the spatially averaged flow speed.

The mass-specific kinetic energy is a commonly used indicator of the amount of energy in a planar flow field at a given crank angle. This is defined in Equation 3.8 for a velocity field, $\boldsymbol{U}$, with $\boldsymbol{u}$ and $\boldsymbol{w}$ components.

$$\boldsymbol{KE} = \frac{1}{2} * (\boldsymbol{u}^2 + \boldsymbol{w}^2) \tag{3.8}$$

This quantity can also be spatially averaged using Equation 3.7 to provide an indicator of flow energy on a crank-angle basis.

Another flow-derived metric that is commonly used to assess the performance of engines is the tumble ratio (TR). This can be defined in a number of ways, but for this study, the method defined by StarCD [129] has been adopted:

$$TR = \frac{\sum_N [(Z_i - Z_m)u_i - (X_i - X_m)w_i]}{\sum_N \sqrt{(Z_i - Z_m)^2 + (X_i - X_m)^2}} \tag{3.9}$$

where N is the number of vectors in the velocity field, X_i and Z_i define the spatial location of the velocity vector of two components, u_i and w_i, and X_m and Z_m define the spatial location of the centre of mass (which is equivalent to the centre of volume as density is assumed to be constant throughout the cylinder).

This definition produces a single positive value for a velocity field that has a clockwise rotational direction for the coordinate system used in this study. The tumble ratio is dependent on the magnitude of the velocity vectors, their direction and their location in relation to the centre of mass.

3.6 Optimisation of PIV in Internal Combustion Engines

Section 3.3 outlines the general details of the planar PIV technique and the considerations that are necessary to produce accurate and reliable PIV measurements. However, the application of PIV to internal combustion engines adds extra complexity in the experimental setup. This section discusses certain difficulties that are relevant to the application of PIV in an optical engine.

3.6.1 Introduction of seeding particles to the intake system

In an ideal experiment, the seeding particles are uniformly distributed throughout the flow of interest and no structures should be present in the images [105]. In this experimental setup, the seeding particles enter the combustion chamber with the intake air flow through the valves during the induction stroke. This inevitably leads to an inhomogeneous distribution of seeding as the particles are entrained in the intake jet. However, the way in which the seeding particles are introduced to the upstream air flow has a significant effect on the uniformity of the seeding distribution later in the cycle.

As described in Section 3.4, the oil droplets are introduced to the intake air flow in the plenum, through a swan-neck pipe. The orientation of this pipe with respect to the inlet runner affects the evolution of the seeding distribution. The two orientations and corresponding particle images taken during the induction process are shown in Figure 3.20.

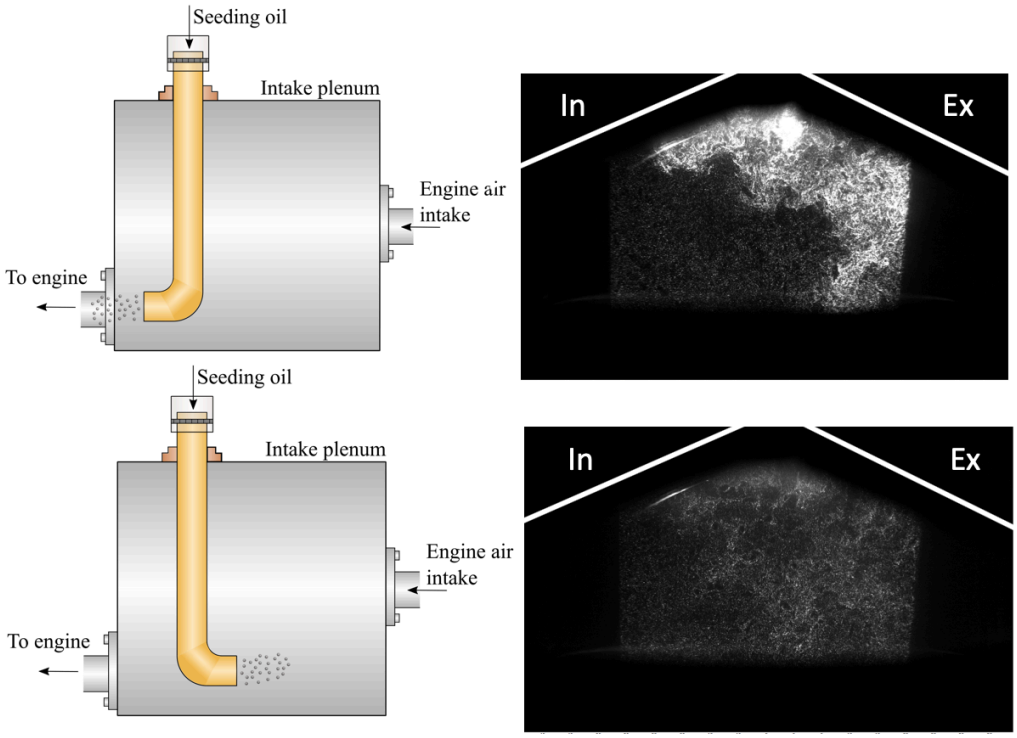

Figure 3.20 *Images demonstrating the effect of the orientation of the swan-neck pipe on the distribution of seeding particles during induction.*

When the exit of the pipe is directed away from the inlet runner, the seeding particles have more time to mix with the air in the plenum, which encourages a more uniform distribution of particles on entry to the combustion chamber. It should be noted that for this orientation, seeding particles must be introduced to the flow for approximately five seconds before data acquisition starts. Otherwise, the seeding density in the combustion chamber is too low. For the opposite orientation, the stream of seeding particles is directed towards the inlet runner, which results in large clusters of oil droplets in the intake jet. As shown Figure 3.20, there is a large region in the intake side of the cylinder where there are no seeding particles present and therefore no measurements are possible. Furthermore, the clusters of particles tend to remain grouped together throughout the remainder of the intake and compression strokes resulting in a non-uniform seeding distribution.

3.6.2 Imaging through a transparent cylindrical liner

Velocity measurements in the tumble plane requires imaging through a curved, transparent surface. The curved surface causes distortion of the images, which has a greater effect with increasing distance from the centreline of the cylinder. As described in Section 3.4, this distortion is corrected during calibration of the camera by using a plate with a regular pattern of dots. Although the camera is calibrated and focussed using a calibration plate, the particle images can appear defocussed in the horizontal and vertical directions, changing shape from points of light to ‘stripes’ as shown in Figure 3.21. The curved liner introduces an astigmatism, which results in the focal plane being different in the horizontal and vertical directions. The irregular shapes of the particle images may affect the interrogation process as the sub-pixel peak finding algorithm performs best when the shape of the particle image is close to a Gaussian distribution.

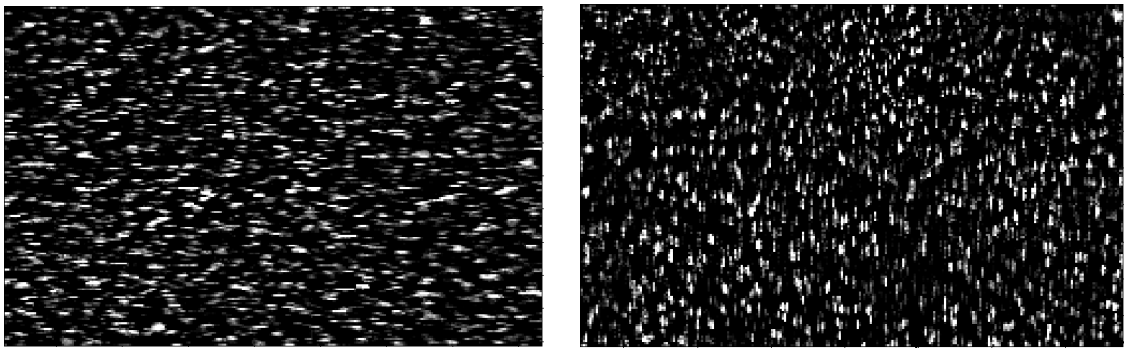

Figure 3.21 *Example of particle images that have been warped into horizontal (left) and vertical (right) stripes by the curved surface of the transparent annulus.*

To correct this, the position or focus of the camera must be moved to vary the focus of the particle images in the horizontal and vertical directions. In this way, the distortion can be minimised by trial and error. This procedure is suggested by Reuss *et al.* [130], who investigated the errors introduced to PIV measurements by imaging through a curved surface.

3.6.3 Scatter minimisation

A major issue of applying PIV to an optical engine is the high intensity of the scattered laser light reflected from the surfaces of the cylinder head and liner walls. The scattered light limits the f-number of the lens that can be used, directly affecting the brightness of the particle images. Therefore, minimising background scatter is essential to producing high-contrast particle images required for the interrogation analysis [111]. Not only does the scattered light reduce the quality of the images and hence the accuracy of the measurements, it also poses a risk to experimental equipment. The photo-sensitive elements in the camera can be damaged if overexposed, which is possible due to the high-power lasers used in PIV experiments. Due to the cost of high-speed cameras (~£40 000), the risk of damage must be minimised.

When imaging the tumble plane, the laser sheet directly impacts the cylinder head, which leads to a bright strip of scattered light as shown in Figure 3.22.

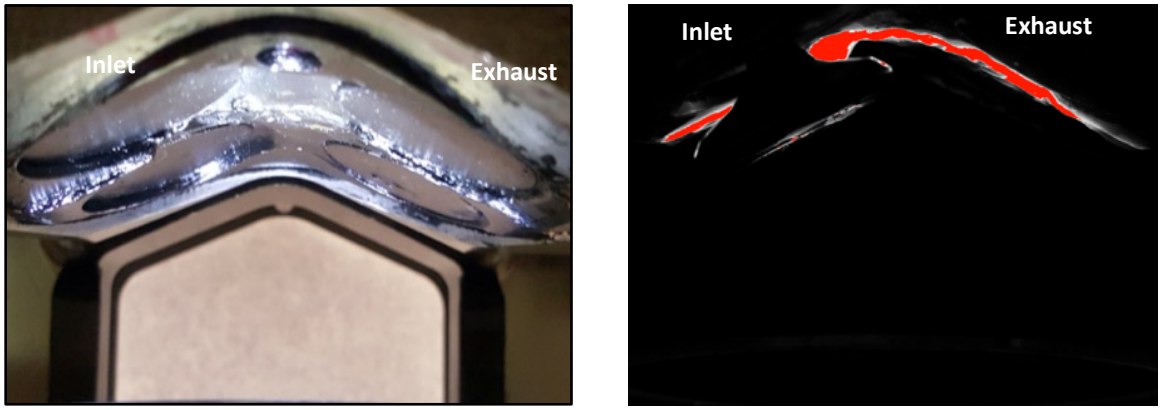

Figure 3.22 *Reference image of the cylinder head (left) and an example of scattered light from the impact of the laser sheet on the cylinder head without masking (right). The red indicates pixels of the camera sensor that are saturated (>4096 counts).*

The right-hand image of Figure 3.22 was captured with the highest f-number of the lens ($f^{\#}/16$) and is saturated at 4096 counts, shown by red pixels. At this f-number, the seeding particles are not visible and so the aperture must be opened. However, this is not possible due to the high intensity of the scattered light from the cylinder, which will dominate the light from the seeding particles. The scattered light from the pent-roof also results in bright flares from the spark plug, fuel injector, cylinder wall and the leading edge of the valves. A number of methods to minimise the background scatter have been investigated:

- Physical masking
- Black paint
- Fluorescent paint with optical filters
- Light polarisation

Physical masking

Masking involves physically preventing laser light scattered by the boundaries of the test equipment reaching the camera sensor. If the masking material is not in the direct path of the laser sheet, then black tape, paper or card may be used. Moving surfaces that enter and exit the field-of-view during a single experiment are more difficult to mask. For example, the leading edge of the valves is a significant source of scattered light that is only present during the intake process. Using a physical mask, such as tape, to block the scattered light would result in a loss of field-of-view for the duration of the cycle when the valves are not open. In these cases, the scatter must be minimised by alternative methods such as black paint.

Scatter reduction using black paint

An alternative to blocking the scattered light is to reduce its intensity at the scattering surface. This can be achieved by painting the surface with matt black paint. The black paint replaces the reflective, metal surface of the cylinder head with a black surface that absorbs and diffuses some of the incident laser light. The rear wall of the transparent annulus also has a coat of matt black paint to reduce secondary scattered light. As shown in Figure 3.23, without black paint on the rear surface of the annulus, the scattered light forms sharp, bright flares. The black paint diffuses the light, which reduces the intensity from around 3000 counts to 200 counts in the brightest region and removes the definition of the flares.

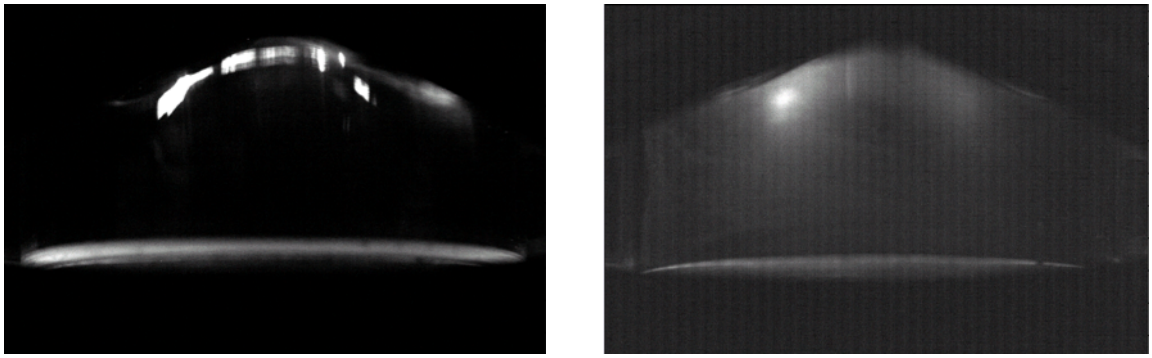

Figure 3.23 *Examples of background scatter due to the rear wall of the liner with (right) and without black paint (left).*

The only practical method of reducing the scattered light from the leading edge of the valves is by using black paint. By carefully coating the rim of the valve head, the scatter can be reduced. Due to the motion of the valves, the paint can be removed from the valve edges during engine operation and must be reapplied. Furthermore, care must be taken not to coat the valve seat with paint as this can lead to poor sealing and lack of compression.

Scatter reduction using fluorescent paint and optical filter

An alternative method to reducing the intensity of the scattered light is to use fluorescent paint to shift the wavelength of the incident laser light scattered by the cylinder head to longer wavelengths and then remove it with an optical filter. In this way, the undesired scattered light from the pent roof is removed, leaving the useful light scattered by the seeding particles. A further advantage is that measurements very close to the cylinder head would also be possible.

To investigate the potential of this method, a low-power laser pointer and spectrometer were used to measure the fluorescence spectra of various fluorescent paints. Fluorescent pink acrylic paint was found to be the most effective at absorbing the incident green light

and shifting it to longer wavelengths. An example of the fluorescence spectrum with and without a green filter is shown in Figure 3.24.

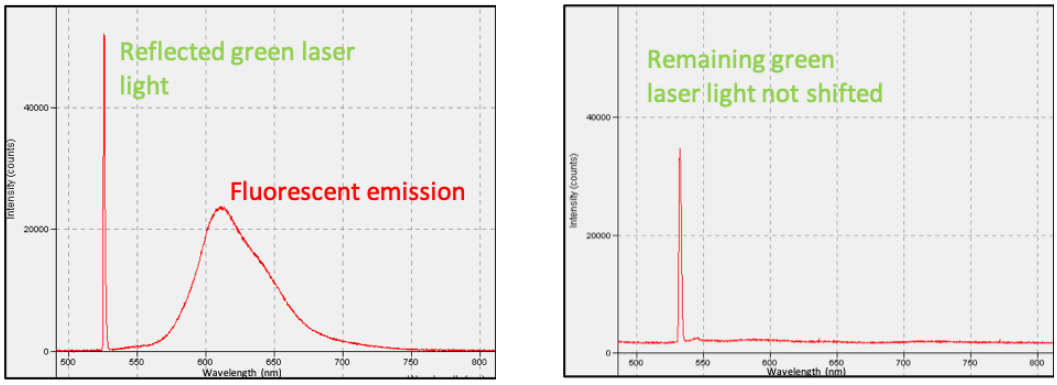

Figure 3.24 *Fluorescence spectra without a green filter (left) and with a green filter (right).*

The peak at 527 nm is due to the reflected green light that is not shifted due to the finite fluorescence efficiency of the paint molecules. The maximum of the broad fluorescence peak is located around 615 nm, which is sufficiently shifted so that most of the fluorescence can be removed using a band-pass green filter (UQG dichroic green filter).

To test this method on the engine, a fluorescent pink strip was painted on the cylinder head in the same plane as the laser sheet, as shown in Figure 3.25.

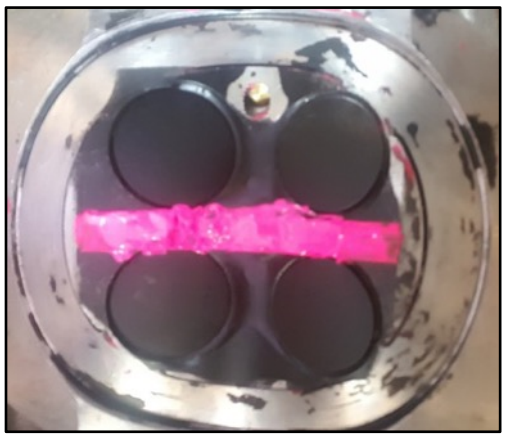

Figure 3.25 *A photograph of the cylinder head painted with matt black paint and a strip of fluorescent pink for scatter minimisation (inlet valves are on the right of the image).*

Due to the high pulse energy of the laser, all the green laser light is not absorbed by the paint and enough is reflected at the cylinder head to saturate the camera even with the green filter. However, this method does provide benefits of reduction in general background scatter, shown clearly in Figure 3.26.

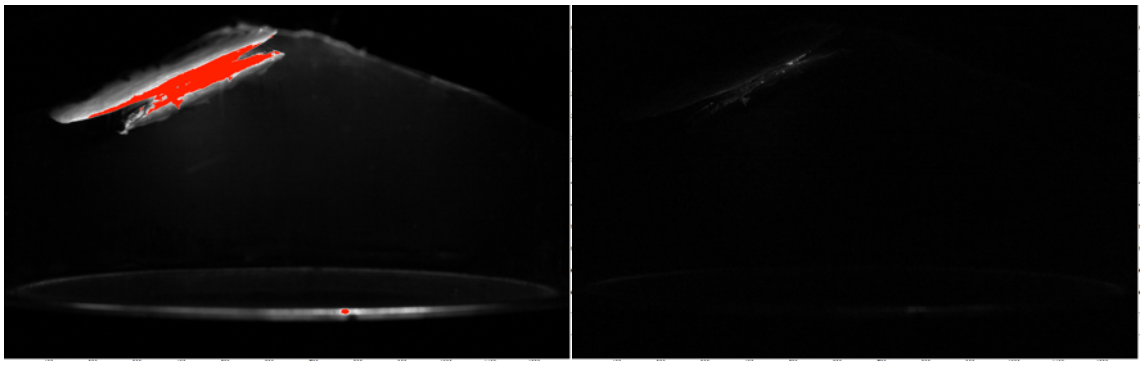

Figure 3.26 *The scattered light from the pent roof with (right) and without a green filter (left).*

The background scatter without a filter has a maximum intensity of approximately 2000 counts on the edge of the inlet valves, whereas the scatter from the inlet valves is barely visible in the filtered image. This reduction of the background scatter comes at no cost to useful scattered light from the seeding particles and increases the contrast of the particle images.

The main challenge of this method is finding a durable fluorescent paint that can withstand the high energy laser pulses at high repetition rates. The example shown in Figure 3.26 demonstrates the potential of acrylic paint, however this image is only for a single shot. For any given experimental run, there are typically thousands of shots over a period of seconds, and this degrades the paint, causing it to melt and peel off the cylinder head. Therefore, for this method to work robustly, paint with the appropriate fluorescent properties that can withstand repeated shots must be used. Paterna *et al.* [131] systematically tested several methods of scatter reduction for PIV experiments, including black paints, fluorescent paints

and reflective materials. They found that paint containing the fluorescent dye Rhodamine-6G results in the largest scatter reduction. The paint, first used by Lee [132], is prepared by mixing 3 grams of Rhodamine 6G with 100 ml of ethanol and 500 ml of water soluble, transparent acrylic paint. This mixture was prepared and tested in the same way as the acrylic paint, however only a small fraction of the green light was absorbed and emitted as fluorescence. Further work is required to optimise this mixture to produce a durable paint that can absorb enough incident laser light to remove the large scatter from the engine surfaces.

Improvement of image quality using laser light polarisation

The scattering properties of light are dependent on its polarisation. In a dual-head laser, each beam is linearly polarised in orthogonal directions to allow the use of beam combining optics with very high efficiencies. However, beams with different polarisations may scatter off the same surface in different ways. This can lead to differences in the intensity of the backgrounds and particle images in a single frame pair. To minimise the error in the velocity measurement, variations in the brightness between frame pairs should be minimised [133].

A solution to this problem is to convert the polarisation of the light from linear to circular. For circularly polarised light, the electric field has a constant magnitude and rotates in time in a direction perpendicular to the direction of motion. For linearly polarised light, the magnitude of the electric field varies with time and its direction remains constant. In practice, the polarisation of light can be converted from linear to circular by using a quarter-wave plate. The effect of the quarter-wave plate on the background scatter is shown in Figure 3.27. The labels A and B describe the first and second images of a frame pair. The

left-hand and right-hand images result from linearly and circularly polarised light respectively.

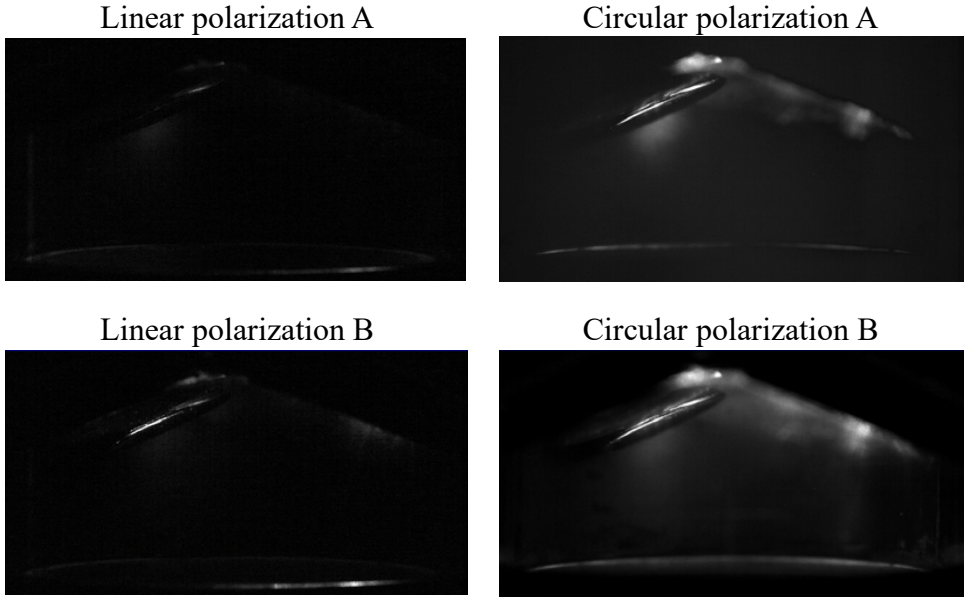

Figure 3.27 *Images showing the effect of the polarisation of the laser light on the background scatter.*

The intensity of the linearly polarised light in frame B is reduced by a third as the intensity of frame A is increased by a factor of three. This results in a frame pair with approximately equivalent intensities.

3.7 Summary

Particle image velocimetry is a complex technique that has been developed extensively over the past three decades [134]. This chapter provides a detailed description of the theory behind the technique and its practical setup. The system used to produce in-cylinder velocity measurements in the optical engine has also been summarised. The system is capable of capturing up to 6000 image pairs (limited by the camera memory) at up to 3.7 kframes/s at full resolution); the laser is capable of operating at 10 kHz and can provide pulses with variable time separation during a single cycle. LaVision DaVis 8.0 PIV software is used to acquire the raw images and perform the cross-correlation analysis for

the velocity calculation. In-house Matlab code is used for further analysis of the resulting vector fields.

Applying PIV to engines produces specific challenges that must be overcome in order to obtain high-quality, reliable data. Several challenges that have been discussed in this chapter include:

- Excessive scattered light from cylinder surfaces
- Inhomogeneous distribution of seeding particles during induction
- Optical distortion due to curved optical components

It was found that coating the cylinder head and rear surface of the quartz annulus with matt black paint was the most effective and robust method of reducing scatter from the images, therefore this was applied in the engine. The orientation of the pipe through which seeding particles are introduced to the intake flow was found to have a significant effect on the homogeneity of the seeding distribution on entry to the engine. Directing the flow of seeding particles away from the intake runner provided a more uniform distribution of particles, and so this has been implemented. The location of the camera was varied using trial-and-error to minimise any optical distortion introduced by the curved quartz annulus. A quarter-wave plate has also been installed in the beam path to convert the polarisation of the beams from linear to circular in order to reduce the difference in scatter between two frames.

The following chapter introduces novel methods quantifying differences between flow fields, especially those with large rotating structures commonly observed in the tumble plane of a modern GDI engine.

4 Quantitative Metrics for Comparison of In-Cylinder Flow Fields

4.1 Introduction

The ability to control the flow of a fluid is extremely important in many engineering applications; for example, the use of active surfaces to influence the boundary layer on an aircraft wing to maintain lift, or the design of the front wing of Formula 1 car to provide sufficient cooling to the braking systems, while also providing sufficient downforce. In IC engines, the intake system plays a crucial role in the determining the resulting in-cylinder fluid motion throughout the cycle [55]. As modern induction systems offer ever increasing flexibility of the valve lift profile, it is vital to understand the effect on resulting in-cylinder air motion to maximise the fuel economy benefits. In order to achieve this understanding, methods of quantifying the differences between flow fields are required.

In this chapter, several conventional methods that are used to compare flow fields are discussed, highlighting their use in engine research, which is primarily for the comparison of PIV measurements and CFD simulations. The relevance index (RI), a metric commonly used to assess vector alignment, is identified as a key tool used in quantifying differences between flow fields. Development of a new metric, the weighted relevance index (WRI), which builds on the existing relevance index to account for the local flow speed, is presented. Similarly, a metric for comparing flow speeds, known as the weighted magnitude index (WMI), is developed. The combination of the WRI and the WMI results in the Combined Magnitude and Relevance Index (CMRI), which is a metric that quantifies differences in both alignment and speed between vector fields with a single value. The

application of this metric to in-cylinder flow fields is demonstrated by investigating the number of cycles that are required to produce a representative mean flow field. The practical implementation of these metrics, including Matlab code, is also provided.

4.2 Methods of Comparing Vector Fields

A wide range of methods for quantifying the differences between planar flow fields have been developed. That said, qualitative comparisons are still common and remain a useful method of investigating trends [135][136]. However, manual inspection of the differences between flow fields is not practical for large datasets, and so quantitative metrics are preferred for robust comparisons.

The investigation of characteristic flow features has been a useful way of providing quantitative comparisons between flow fields, both simulated and experimental. Ameen *et al.* [137] compared both the mean and RMS velocity magnitudes along the axis of the intake jet to investigate the performance of LES simulations in matching PIV experiments. As well as the intake jet, Yang *et al.* [138], [139] identified the location of vortex centres and the direction of the flow in different regions of the cylinder as important criteria when comparing RANS and LES simulations with PIV experiments. In a similar way, Pera *et al.* [140] compared the radial and vertical velocity components along two horizontal lines at different in-cylinder locations in order to quantify the difference between LES simulations and PIV experiments. An example of these comparisons is shown in Figure 4.1. In contrast to selecting characteristic in-cylinder flow features, Van Dam *et al.* [141] calculated the differences between the mean velocity magnitudes and the standard deviations over the entire field of view to validate LES simulations of a GDI engine using experimental data.

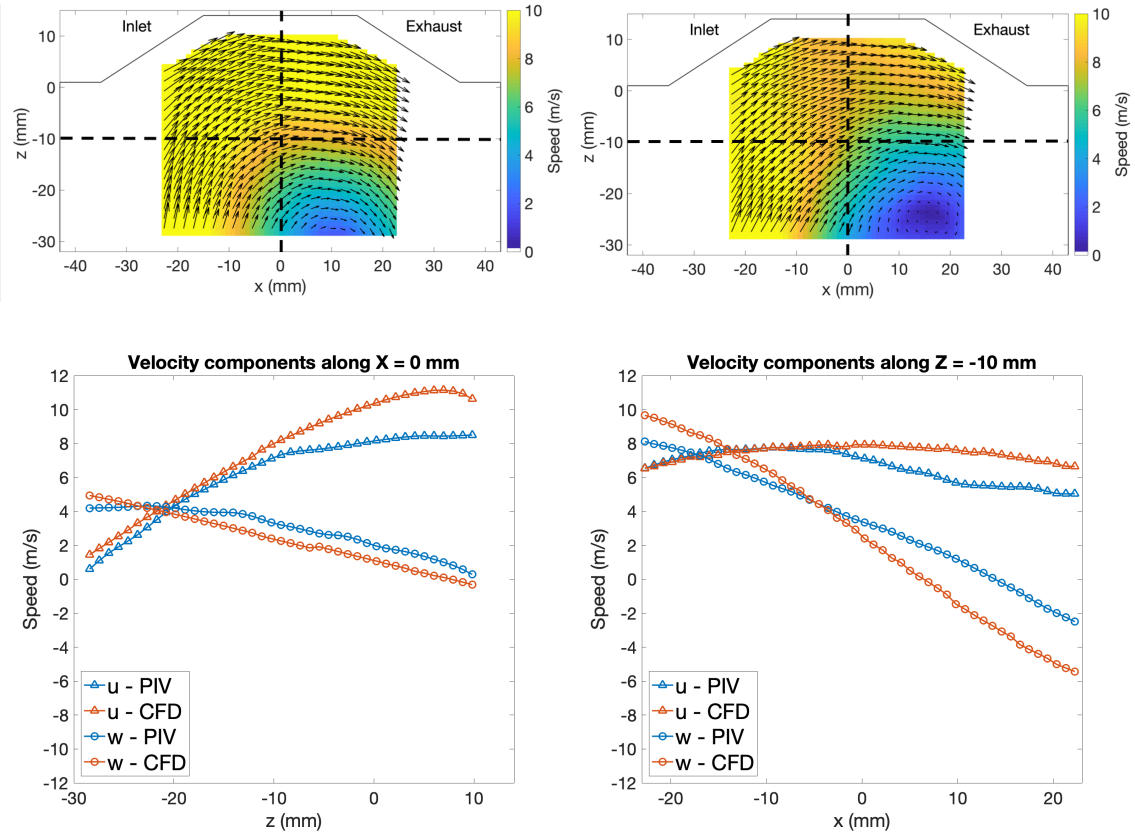

Figure 4.1 *An example of comparisons of the vertical and horizontal components of flow speed between experiment (top right) and simulation (top left) for a single flow field.*

In order to quantify the flow variability of both experiments and LES simulations, Van Dam *et al.* [142] introduced the Circular Standard Deviation (CSD). This quantity is claimed to be more appropriate for angular data than the regular standard deviation. In this way, variations in the direction of velocity components were separated from variations in the magnitude; a distinction that cannot be made by only comparing the RMS values of the velocity. This metric was also used to compare flow fields produced by sequential and parallel LES simulations [143].

A common metric for quantifying the differences in direction between two velocity vectors is the Relevance Index (RI), which was defined by Liu *et al.* [144]:

$$RI = \frac{(\boldsymbol{q_A} \cdot \boldsymbol{q_B})}{|\boldsymbol{q_A}||\boldsymbol{q_B}|} \tag{4.1}$$

where $(\boldsymbol{q_A}, \boldsymbol{q_B})$ denotes the dot product of vectors $\boldsymbol{q_A}$ and $\boldsymbol{q_B}$, and $|\boldsymbol{q_A}|$ denotes the magnitude of the vector $\boldsymbol{q_A}$.

The RI returns the cosine of the angle between two vectors, and so produces values that range from -1 for completely mis-aligned vectors and 1 for perfectly aligned vectors, as demonstrated in Figure 4.2. Therefore, the RI allows the difference in alignment between two vectors to be quantified by a single absolute value. This can be applied to a pair of velocity fields to produce a field of RI, which can be spatially averaged to obtain a single value that gives a measure of how closely two velocity fields are aligned. It has been used like this to directly compare simulated and measured flow fields [141], [145].

$\boldsymbol{q_A}$	$\boldsymbol{q_B}$	RI
→	→	1
→	↑ or ↓	0
→	←	-1

Figure 4.2 *The limits of the relevance index.*

An interesting use of the RI is to investigate the convergence of both simulated and experimental flow fields. Hu *et al.* [146] uses the RI (named the Structure Similarity Index) to find how many LES realisations are required to produce a representative mean for simulations of a turbulent, non-reacting jet. Similarly, Kuo *et al.* [147] used the RI to investigate the convergence of LES engine simulations by quantifying the variation of both

the mean and RMS velocity magnitude fields for ensemble averages of varying numbers of cycles.

The RI has also been used to quantify the differences in modes produced by Proper Orthogonal Decomposition (POD) of flow fields in a GDI engine by Chen *et al.* [148], [149]. It has also been applied to scalar fields such as the pixel intensity of spray images to investigate the variation in fuel spray characteristics [150], [151].

An alternative metric, the Magnitude Similarity Index (MSI) was defined by Hu *et al.* [146]:

$$MSI = 1 - \frac{|\boldsymbol{q}_\mathbf{A} - \boldsymbol{q}_\mathbf{B}|}{|\boldsymbol{q}_\mathbf{A}| + |\boldsymbol{q}_\mathbf{B}|} \tag{4.2}$$

It produces a value of 1 if the vectors are identical and 0 if the vectors are exactly opposite. Unlike the Relevance Index, the MSI accounts for differences in both alignment and magnitude between two vector fields due to the vector subtraction. This has been used by Van Dam *et al.* [143] and Ameen *et al.* [137] to directly quantify the differences between simulated and experimental flow fields. In a similar way to the RI, it has been used by Ameen *et al.* [152] to investigate the convergence of simulated scalar fields in a simulation of an n-dodecane fuel spray.

The metrics presented here provide useful methods of quantifying differences between specific flow features or the whole flow field in terms of vector alignment or magnitude. For analysis of in-cylinder flow measurements or simulations, the field data is commonly spatially averaged to reduce the volume of data for comparison. For this reason, it is essential that these metrics are sufficiently robust so that spatially averaged values are still a valuable method of comparison. It has been found that for flow fields with a strong rotational structure, such as the tumble flow setup in a modern DISI engine, the relevance

index can produce misleading results due to the effect of regions of low velocity near the vortex centre. The following sections discuss this effect and present two new metrics, the Weighted Relevance Index (WRI) and the Weighted Magnitude Index (WMI), that take into account the local velocities to produce robust metrics for comparisons of vector alignment and magnitude.

4.3 Weighted Relevance Index

4.3.1 Relevance index

As described in Section 4.2, the relevance index is a metric used to quantify the difference in alignment between two vectors. When comparing vector fields, the relevance index is usually computed for each vector to build up a scalar field of values between -1 and 1. It is worth noting the scale of the relevance index and what values indicate a 'good' match between vector fields; a value of 0.8 may seem close to unity and so the vectors are closely aligned. However, by using the inverse cosine function, a relevance index of 0.8 equates to a misalignment of approximately 40°. For comparison, values of 0.999 and 0.99 equate to misalignments of approximately 2.5° and 8° respectively.

Relevance index fields provide a map of the quality of the match in the alignment between two flow fields. For certain applications, it is necessary to quantify how similar a reference velocity field is to a large set of comparison velocity fields. In this case, it is not practical to manually search for the field that is the best match to the reference field, therefore the spatial average must be used. For example, in order to find the single cycle that is the best match to the mean cycle for a typical experiment that consists of 300 cycles, flow fields from each crank angle must be compared to the mean. If each cycle consists of measurements every 2 degrees crank angle during the compression stroke, the dataset for

comparison consists of 27 300 vector fields. Therefore, it is necessary to reduce the resulting relevance index fields to a single value by spatially averaging, defined by Equation 4.3.

$$\overline{RI} = \frac{1}{N}\sum_{i=1}^{N} \boldsymbol{RI}(i) \tag{4.3}$$

where $\boldsymbol{RI}(i)$ is a column vector of the relevance index field and N is the total number of values in the field.

4.3.2 Low velocity bias of the relevance index

The relevance index is an absolute metric; it simply quantifies the difference in angle between two vectors. This is a useful feature because it can be used across a wide range of applications and its value retains its significance. However, this is also a disadvantage in that it does not provide any information about the differences in magnitude between two vectors. Therefore, low-speed velocity vectors carry the same weight as those with high velocity. This can lead to potentially misleading results when comparing flow fields with a rotating flow structure such as a vortex.

The magnitudes of the velocity vectors near the centre of the vortex are typically small in comparison to the surrounding flow velocities. There is also a large velocity gradient as the direction of the flow reverses across the centre of the vortex. A consequence of this is that when two velocity fields with vortices are compared, only a small offset in the location of the centre of the vortices will result in a region of vectors becoming completely misaligned and having very low values of relevance index. This effect is demonstrated in Figure 4.3 with simple rotating flow fields created using Matlab.

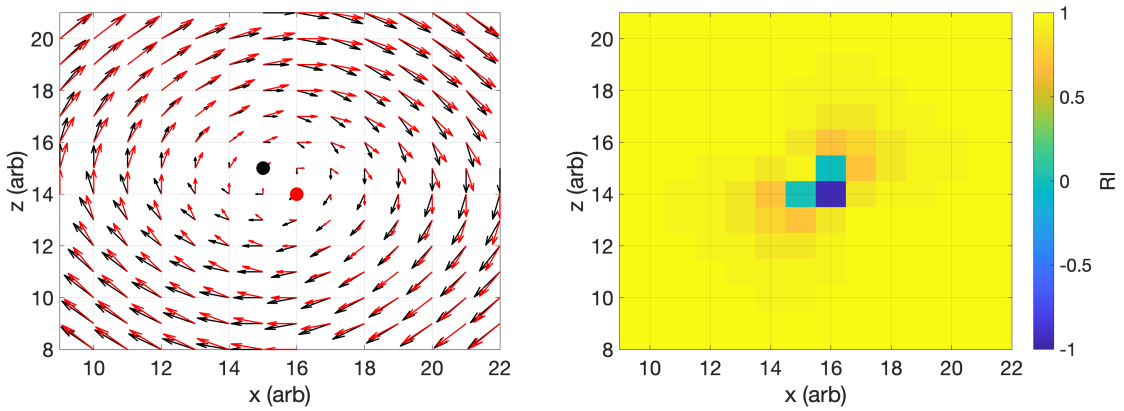

Figure 4.3 *An example demonstrating the calculation of the relevance index (right) for two identical flow fields except for an offset in the vortex centres (left).*

The left-hand image of Figure 4.3 shows plots of two identical rotating flow fields that are offset by one unit in both vertical and horizontal directions. The relevance index field, plotted on the right, clearly shows the large misalignment near the centre of the vortex where the flow velocities are low, even though the flow fields are well matched away from the vortex centres. Although this region of low relevance index only consists of a fraction of the total number of vectors in the field, it can have a significant effect on the spatially averaged value of relevance index as discussed later in this section.

Rotating flow structures are common in internal combustion engines in the form of large-scale tumble or swirl motion. Figure 4.4 shows two velocity fields measured during the compression stroke, plotted together to allow a visual comparison. The velocity fields (dataset A - black and dataset B - red) are ensemble averaged subsets of 150 cycles taken from a full dataset of 300 cycles, therefore they are very similar in structure with only a slight offset in the location of the tumble vortices (shown by the dots). The engine test conditions are provided in Table 4.1 and the PIV setup details are provided in Table 4.2.

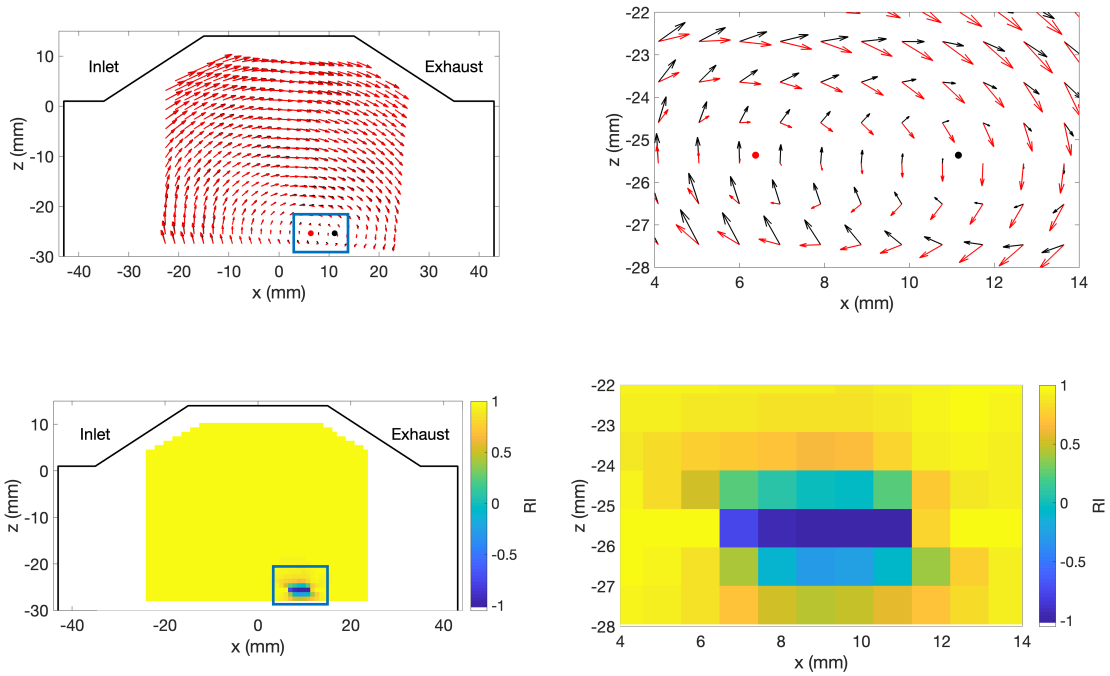

Figure 4.4 *Two datasets of measured flow fields (86°ca bTDC) plotted together (top) and the calculated relevance index field (bottom) with zoomed-in regions for clarity (right). The centres of the tumble vortices are shown by the coloured dots (dataset A – black, dataset B – red).*

Table 4.1 *Engine conditions for datasets A and B.*

Engine speed (RPM)	1500
MAP (bar)	0.42
Air temperature (°C)	35
Coolant temperature (°C)	18
IMOP (°ca aTDC gas exchange)	144
EMOP (°ca bTDC gas exchange)	121
Piston shape	C

Table 4.2 *PIV setup for datasets A and B.*

Timing of PIV measurements (°ca bTDC combustion)	180 - 0
Measurement increments (°ca)	2
Spatial resolution (mm)	1.96
Number of tests	4
Number of cycles measured per test	75
Total number of cycles	300

The view of the full flow field shows that the majority of the velocity vectors located far from the vortex centres are qualitatively well matched. The zoomed-in view shows the

relatively poor alignment of velocity vectors near the vortex centres. The corresponding relevance index field agrees and demonstrates that over 75% of the vector field is well matched with a relevance index over 0.99. However, there is a small region of misaligned vectors near the centre of the vortices with values of relevance index of approximately -1.

Figure 4.5 and Figure 4.6 show the effect that the low velocity region around the centres of the vortices has on the spatially averaged value of relevance index, $\overline{RI}$. Figure 4.5 shows the same relevance index field as that shown in Figure 4.4, however any values below zero have been removed. The removed region is solely due to the region surrounding the misaligned vortex centres.

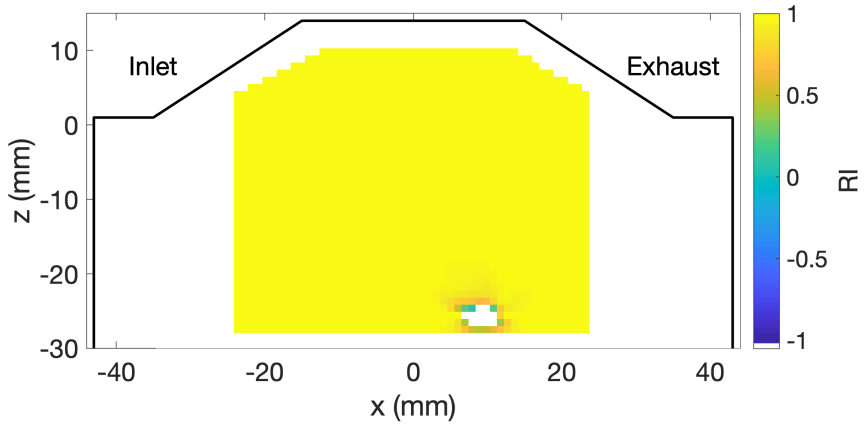

Figure 4.5 *The same relevance index field as that shown in Figure 4.4, with values less than zero removed.*

$\overline{RI}$ is recalculated and then converted into an equivalent angle using the inverse cosine function to give the average difference in angle between the two vector fields for every two crank angles in the compression stroke, shown in the bottom image of Figure 4.6.

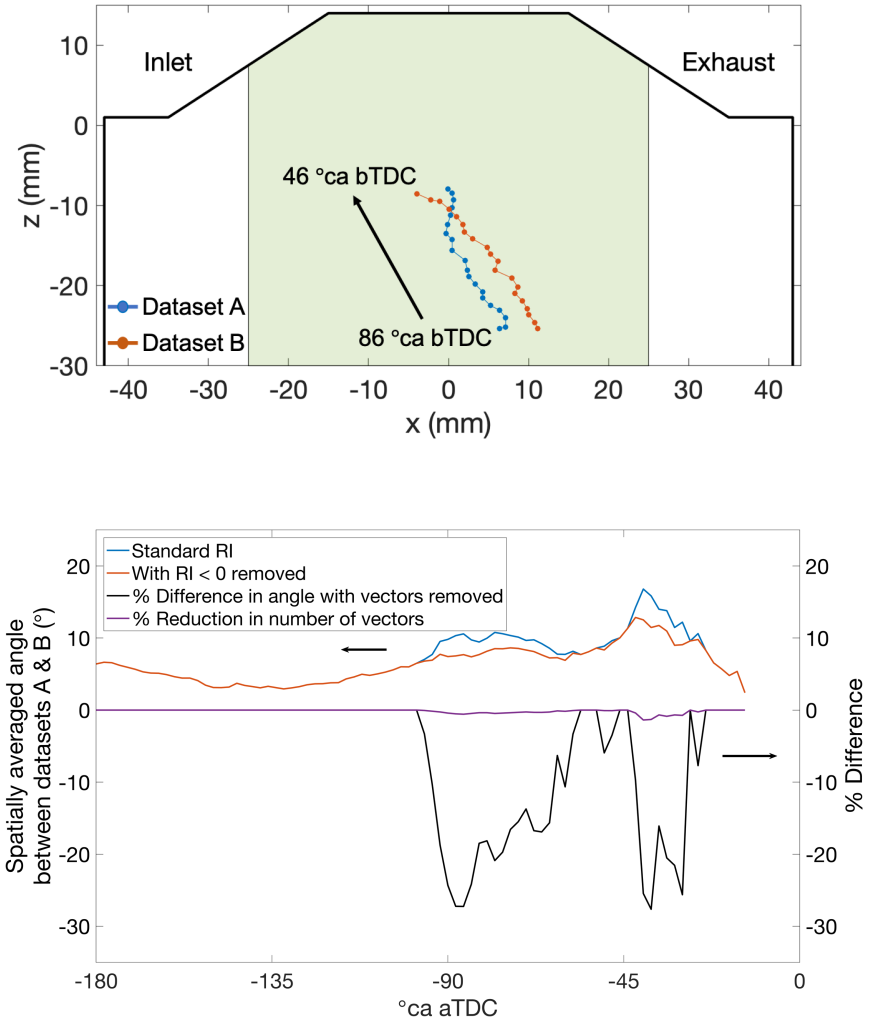

Figure 4.6 *The positions of the vortex centres of dataset A and B in the combustion chamber from 86°ca bTDC to 46°ca bTDC (top image) and plots of the equivalent misalignment angle calculated from $\overline{RI}$, with and without the RI < 0 vectors removed (blue and red lines). The corresponding percentage difference in angle is plotted on the right-hand axis (black line) with the percentage reduction in number of vectors (purple) (bottom image).*

The top image shows the positions of the vortex centres of the ensemble averaged flow fields of datasets A and B during the compression stroke. For each field, the vortex only appears in the field of view at 86°ca bTDC and is then hidden by the shaped piston crown around 46°ca bTDC. The blue and red lines in the bottom plot show the spatially averaged misalignment between the vector fields from datasets A and B, with and without the $RI < 0$ vectors removed. The purple line shows the percentage of vectors that are removed from the calculation and the black line shows the percentage difference between the

standard calculation of $\overline{RI}$ and that with the low values removed. This reveals that only 1% of the vectors causes a 30% difference in the spatially averaged value of the angle misalignment. Furthermore, for a given flow field in either dataset A or B, the removed vectors contribute less than 0.5% of the total kinetic energy. It is also worth noting that at the crank angles where the centres of the vortices are in similar positions (~ 52°ca bTDC), the difference in $\overline{RI}$ decreases to a minimum. This indicates that the region of low relevance index values has decreased in size as the vortex centres pass over each other.

Therefore, in order to produce a reliable spatially averaged value of relevance index, it is necessary to remove the low velocity bias inherent in analysing flows with rotating structures.

4.3.3 Development of the weighted relevance index

A way of removing the low velocity bias of the relevance index is to weight the relevance index by the normalised local velocity of the two fields. In this way, the misalignment penalty for regions of low velocity is reduced and its effect on the spatially averaged value of relevance index is also mitigated. A method of achieving this is provided in the following section.

For this section, a reference flow field is defined as $\boldsymbol{q}_A$ with components of velocity, $\boldsymbol{u}_A$ and $\boldsymbol{w}_A$, in the $\boldsymbol{x}$ and $\boldsymbol{z}$ directions respectively. $\boldsymbol{Q}_A$ is defined as the magnitude field of $\boldsymbol{q}_A$, such that $\boldsymbol{Q}_A = |\boldsymbol{q}_A| = \sqrt{\boldsymbol{u}_A{}^2 + \boldsymbol{w}_A{}^2}$. Similarly, a comparison field is defined as $\boldsymbol{q}_B$. Equation 4.4 defines the Weighted Relevance Index (WRI):

$$WRI(\boldsymbol{x}_i, \boldsymbol{z}_j) = \left(\frac{1 - \boldsymbol{RI}(\boldsymbol{x}_i, \boldsymbol{z}_j)}{2}\right) * \left(\frac{\boldsymbol{Q_A}(\boldsymbol{x}_i, \boldsymbol{z}_j)}{\text{median}(\boldsymbol{Q_A}(\boldsymbol{x}, \boldsymbol{z}))}\right) * \left(\frac{\boldsymbol{Q_B}(\boldsymbol{x}_i, \boldsymbol{z}_j)}{\text{median}(\boldsymbol{Q_B}(\boldsymbol{x}, \boldsymbol{z}))}\right) \quad (4.4)$$

Alignment penalty — **Velocity weighting factor Field A** — **Velocity weighting factor Field B**

where $RI(\boldsymbol{x}_i, \boldsymbol{z}_j)$ is the value of relevance index and $\boldsymbol{Q}_A(\boldsymbol{x}_i, \boldsymbol{z}_j)$ denotes the magnitude of the velocity field, $\boldsymbol{q}_A$, both at the ith $\boldsymbol{x}$ position and jth $\boldsymbol{z}$ position.

Perfect alignment between vectors is indicated by a value of zero and the value increases as the quality of match deteriorates. The alignment penalty (highlighted in green), involves rescaling the RI to shift the score for perfect alignment from 1 to 0, and complete misalignment from -1 to 1. This is necessary because the velocity weighting factors (highlighted in blue and red) tend to push the value of the WRI towards 0 for vectors with low velocity. In the original definition of the RI, with limits between -1 and 1, a value of 0 denotes a misalignment of 90°. However, the objective of the WRI is to artificially improve the quality of the match for low velocity vectors to reduce their effect on the spatially averaged value. Therefore, by rescaling the values of the RI, the velocity weighting factor boosts the value of the WRI for low velocity vectors even if there is poor alignment between them.

The function of the velocity weighting factors is to take into account the local velocity of the flow in both fields. In this way, if the magnitudes of the velocities in either field are small, the misalignment penalty is reduced, which results in a lower value of the WRI and a better alignment score for the vectors. The velocity weighting factors also amplify any

misalignment between high velocity vectors. Therefore, the metric penalises regions of the flows with high relative kinetic energy that are misaligned.

Figure 4.7 shows $\overline{RI}$ and $\overline{WRI}$ calculated during the compression stroke for the test conditions defined in Table 4.1. Firstly, the scale of $\overline{WRI}$ is very different to $\overline{RI}$ due to the nature of the velocity weighting. The plot of $\overline{RI}$ (blue line) shows that there are two main troughs in the relevance index; one that begins just before 90°ca bTDC as the tumble vortices of each field enters the field of view, and a very steep reduction just after 45°ca bTDC, when the tumble vortices have crossed paths and are moving apart. In contrast, the plot of $\overline{WRI}$ does not indicate a poor match (high score) when the tumble vortices first appear in the field of view around 90°ca bTDC. The reason for this is that the region of vector misalignment around the vortex centres does not affect $\overline{WRI}$ in the same way as $\overline{RI}$. There are opposite peaks for both $\overline{RI}$ and $\overline{WRI}$ at 42°ca bTDC, which indicate poor alignment for both metrics; these are due to mis-aligned velocity vectors located away from the centre of the tumble vortices, which affect both metrics.

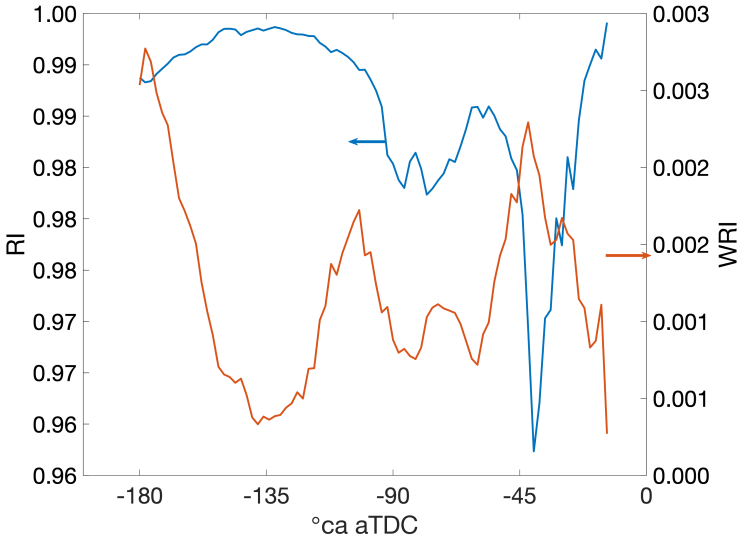

Figure 4.7 *Plots of $\overline{RI}$ (left axis) and $\overline{WRI}$ (right axis) during the compression stroke. Poor alignment is indicated by high values for $\overline{WRI}$ and low values for $\overline{RI}$.*

The denominator of each velocity weighting factor is the median flow speed in the corresponding field. This normalises the local velocity to the scale of the entire flow field. The median speed was selected over the maximum or mean velocity as it is less sensitive to anomalous values; this is demonstrated in Figure 4.8.

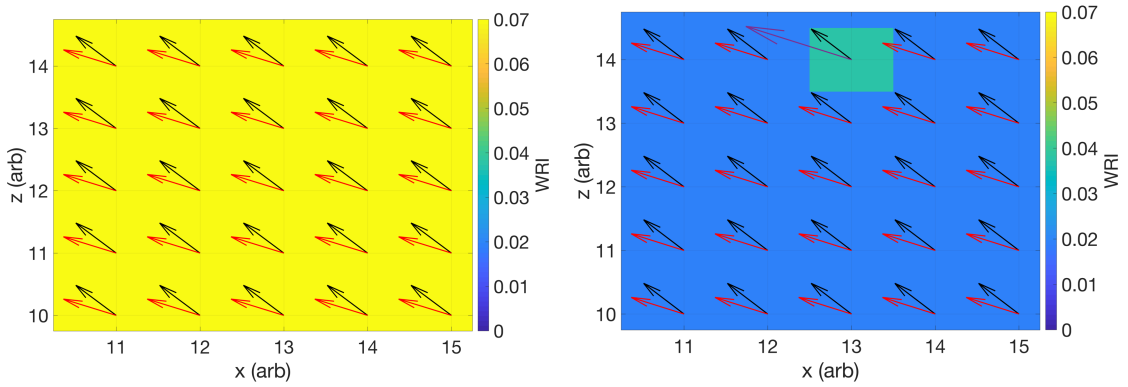

Figure 4.8 *Vector fields with a constant alignment offset overlaid on the weighted relevance index field using the maximum flow speed as the denominator for the velocity weighting factors, with (right) and without (left) an anomalous vector (shown in purple).*

Both images show a reference (red) and comparison (black) velocity field overlaid on the calculated *WRI* values between each vector field using the maximum flow speed as the denominator. For both examples there is a constant misalignment between the two vector fields, which results in the uniform value of *WRI* across the left-hand field. However, in the right-hand image, there is a single vector in the reference field that has double the speed of the surrounding vectors. If the denominator of the weighting factor was the maximum flow speed in each field, a single extreme vector could shift the normalisation for all the values in that field, as shown by the different background colour for the right-hand image. The single anomalous vector has a different value of *WRI* as its local velocity is higher, therefore it is penalised more strongly than the other vectors for the same misalignment, resulting in a higher value of *WRI*. To ensure the metric is more robust to anomalous vectors, the median velocity magnitude in each field is used as the denominator of the velocity weighting factors.

Figure 4.9 shows the updated *WRI* field for the same crank angle as the flow fields shown in Figure 4.4, with black and red circles indicating the centre of the vortices. The scale has been changed to reflect the new limits of the metric, however the colour scheme has been reversed to match that of Figure 4.4 (low values indicate good alignment for the WRI).

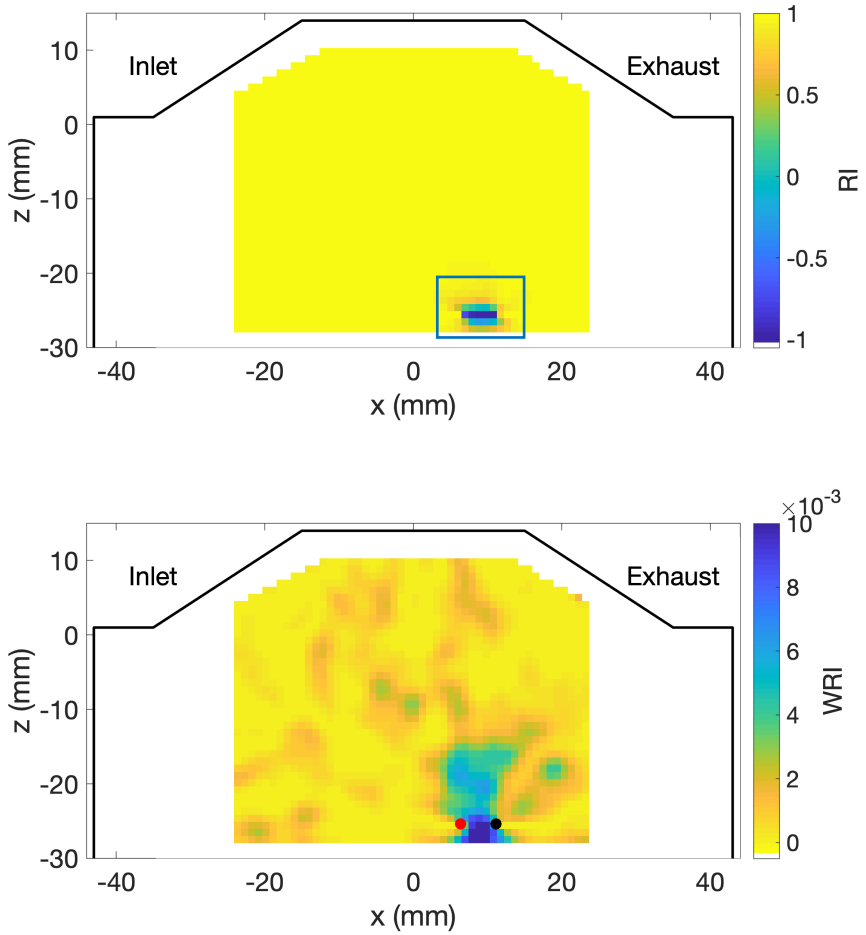

Figure 4.9 *WRI field (bottom) for the same velocity field shown in Figure 4.4 (top), with black and red circles denoting the centres of the vortices for dataset A and B respectively. The colour scale of Figure 4.4 has been reversed so that the background colours are consistent for each metric.*

In contrast to the field of *RI* shown in Figure 4.4, there are other regions of the flow fields that are being picked out as being misaligned, not just the region around the vortex centres. The highest values of *WRI*, indicating the worst matches between the flow fields, are located just below the vortex centres, where the flow speeds have increased sufficiently

from the vortex centres to be amplified by the velocity weightings. There is also a region above the vortex centres, which has relatively high values of *WRI*, but was ignored in the fields of relevance index. On inspection of the flow fields in Figure 4.4, these vectors are relatively well-aligned in comparison to those located below the vortex centres. However, due to their higher speeds, they are penalised more harshly.

4.4 Weighted Magnitude Index

When comparing flow fields, it is not only the direction of the flow that is important, but also its speed. As discussed in Section 4.3.1, the relevance index does not provide any information about the differences in the magnitude of two vectors. Therefore, it is necessary to define a metric that quantifies this difference.

The weighted magnitude index (WMI) for comparing reference velocity field, $\boldsymbol{q_A}$, to comparison velocity field, $\boldsymbol{q_B}$, is defined as:

$$WMI(x_i, y_i) = \frac{\left|\boldsymbol{Q}_A(\boldsymbol{x}_i, \boldsymbol{y}_j) - \boldsymbol{Q}_B(\boldsymbol{x}_i, \boldsymbol{y}_j)\right|}{\text{median}\left(\boldsymbol{Q}_A(\boldsymbol{x}, \boldsymbol{y}), \boldsymbol{Q}_B(\boldsymbol{x}, \boldsymbol{y})\right)} \tag{4.5}$$

where $\boldsymbol{Q}_A$ is defined in Section 4.3.3 as the magnitude field of $\boldsymbol{q_A}$.

For each location in a field, the metric calculates the absolute difference between the magnitudes of two vectors and normalises the result by the median flow speed in either field. Similarly to the WRI, the WMI gives a value of zero for vectors that have identical magnitudes and increases as the difference in flow speed increases.

The choice of the median velocity magnitude as the denominator is for the same reasons as those discussed in Section 4.3.3; the median velocity is a more robust value to normalise

the absolute difference between the local velocity magnitudes. Figure 4.10 shows an example of the WMI field comparing the flow fields of dataset A and B at 68°ca bTDC.

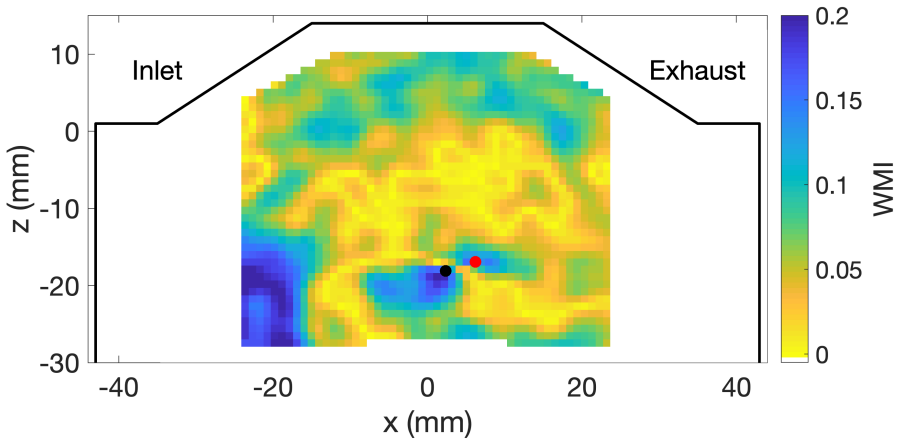

Figure 4.10 *A WMI field comparing datasets A and B at 68°ca bTDC.*

It is clear from Figure 4.10 that the scale of the *WMI* field is very different to that of the *WRI* fields. The apparent structure that is present in the field is due to the way in which the magnitudes of the velocity vectors vary spatially throughout the field; for example, during the transition from a region of fast to slow flow for the reference velocity field, at one point, its speed may match that of the comparison flow field very well. This results in structures that appear as 'lines' of well-matched flow speeds throughout the *WMI* field.

4.5 The Combined Magnitude and Relevance Index (CMRI)

4.5.1 Correlations between WRI and WMI

The objective of this work is to provide metrics that quantify the similarity of two vector fields. Vectors can vary in both direction and magnitude, therefore metrics that quantify the differences in alignment and magnitude have been developed in the previous sections. The spatially averaged metrics provide a single value that can be used to rank how similar comparison flow fields are to a reference field. However, these are applied separately. It is

not obvious that a flow field that is most similar to a reference flow field in terms of alignment will also be a good match in terms of magnitude. If this is the case, then either $\overline{WRI}$ or $\overline{WMI}$ can be used to find the flow field that is most similar to the reference. If not, then the metrics must be combined to take into account both alignment and magnitude.

To investigate the correlation between differences in alignment and magnitude, velocity fields for 1000 cycles from 270°ca bTDC to TDC in 10°ca increments were measured in 10 independent tests. Table 4.3 shows the engine conditions for these tests and Table 4.4 shows the PIV setup.

Table 4.3 *Engine conditions for the large dataset*

Engine speed (RPM)	1500
MAP (bar)	0.42
Air temperature (°C)	35
Coolant temperature (°C)	18
IMOP (°ca aTDC gas exchange)	144
EMOP (°ca bTDC gas exchange)	121
Piston	Flat

Table 4.4 *PIV setup for the large dataset*

Timing of PIV measurements (°ca bTDC combustion)	270 - 0
Measurement increments (°ca)	10
Number of tests	10
Number of cycles measured per test	100
Total number of cycles	1000

$\overline{WRI}$ and $\overline{WMI}$ were calculated for each cycle at all crank angles using the ensemble-averaged flow field of the whole dataset as the reference. In Figure 4.11, $\overline{WRI}$ and $\overline{WMI}$ for each cycle are plotted against each other for a single crank angle (190°ca bTDC). For both $\overline{WRI}$ and $\overline{WMI}$, a value of zero denotes a perfect match between two vector fields and a higher score implies a worse match.

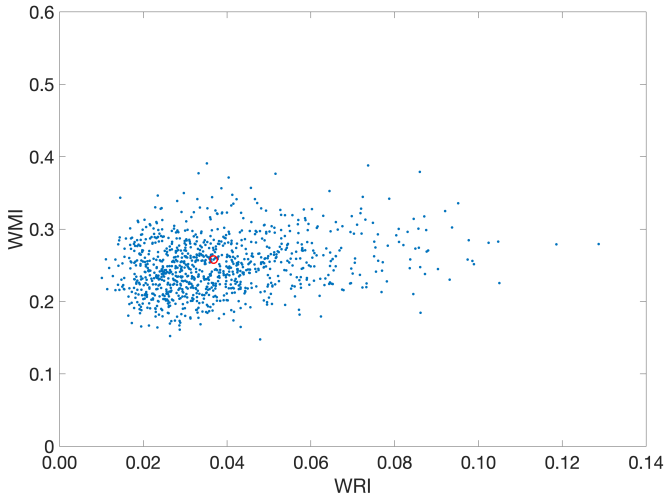

Figure 4.11 *Scatter plot of $\overline{WRI}$ against $\overline{WMI}$ for 1000 cycles at 190°ca bTDC for the test conditions shown in Table 4.2. The red circle shows the values of $\overline{WRI}$ and $\overline{WMI}$ for the individual cycle that best matches the mean cycle over all crank angles.*

There is no obvious correlation between $\overline{WRI}$ and $\overline{WMI}$, and this trend is consistent for all crank angles. The significant spread in values suggests that a flow field that matches well in terms of alignment, is not necessarily a good match in terms of magnitude. The red circle represents the value of $\overline{WRI}$ and $\overline{WMI}$ of the individual cycle that best matches the reference field for all crank angles. For this specific crank angle, there are cycles with better scores of both $\overline{WRI}$ and $\overline{WMI}$. Therefore, it is clear that some cycles may be more similar to the mean cycles at different points in the cycle; some may provide a good score of $\overline{WRI}$ (well-aligned) during the intake, which then deteriorates during the compression stroke.

From this analysis, it appears that there is no significant correlation between $\overline{WRI}$ and $\overline{WMI}$. Therefore, to find the cycle that is the best match to the mean cycle, both metrics must be taken into account. The next section discusses the combination of the WRI and WMI.

4.5.2 Combining the WRI and WMI

The objective of a combined metric is to produce a single value that provides an indication of the quality of the match of a comparison field to a reference field. This must include measures of the differences in both alignment and magnitude between the two vector fields. Potential methods of achieving this are the addition or multiplication of *WRI* and *WMI* fields. As both metrics range from 0 for a perfect match to a larger number for a poor match, the multiplication of the metrics will result in a perceived 'good' match (a value close to zero) when only one of the metrics has a value close to zero. However, the addition of the metrics will only result in a value close to 0 if both metrics have small values. Therefore, addition is the preferred operation for the combination of the WRI and WMI.

However, by inspecting the vector-wise distributions of *WRI* and *WMI* for a given flow field, it becomes clear that a simple addition of the metrics is not sufficient to produce a suitable combined metric. A vector-wise distribution for the flow field of a single cycle is shown in Figure 4.12.

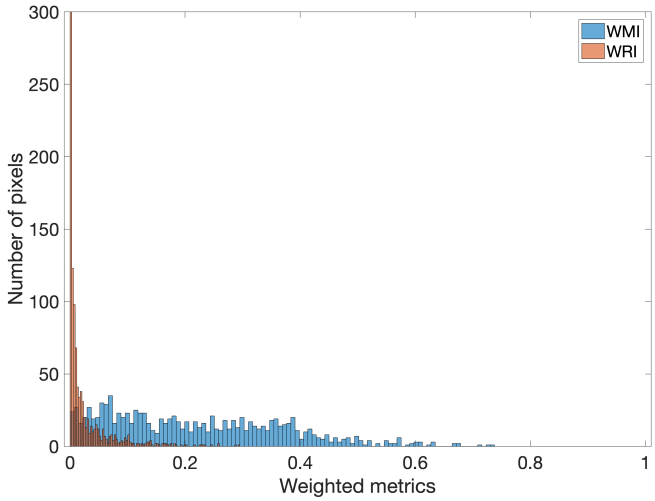

Figure 4.12 *Vector-wise distributions of WRI and WMI for an individual cycle at 70°ca bTDC for the test conditions given in Table 4.3.*

For a given flow field, the vector-wise distributions of *WRI* and *WMI* have very different ranges. The definition of the WRI causes the majority of values to have a narrow distribution around zero, with a maximum of approximately 0.3 for the example shown in Figure 4.12. However, the values of *WMI* are more widely spread, ranging from approximately 0 to 0.75. A consequence of this is that the values produced by the addition of the metrics are strongly weighted in favour of the WMI, resulting in a combined metric that only accounts for differences in magnitude. This effect is shown in Figure 4.13, which presents the comparison of an individual cycle to the mean cycle and fields of WRI, WMI and the addition of the two.

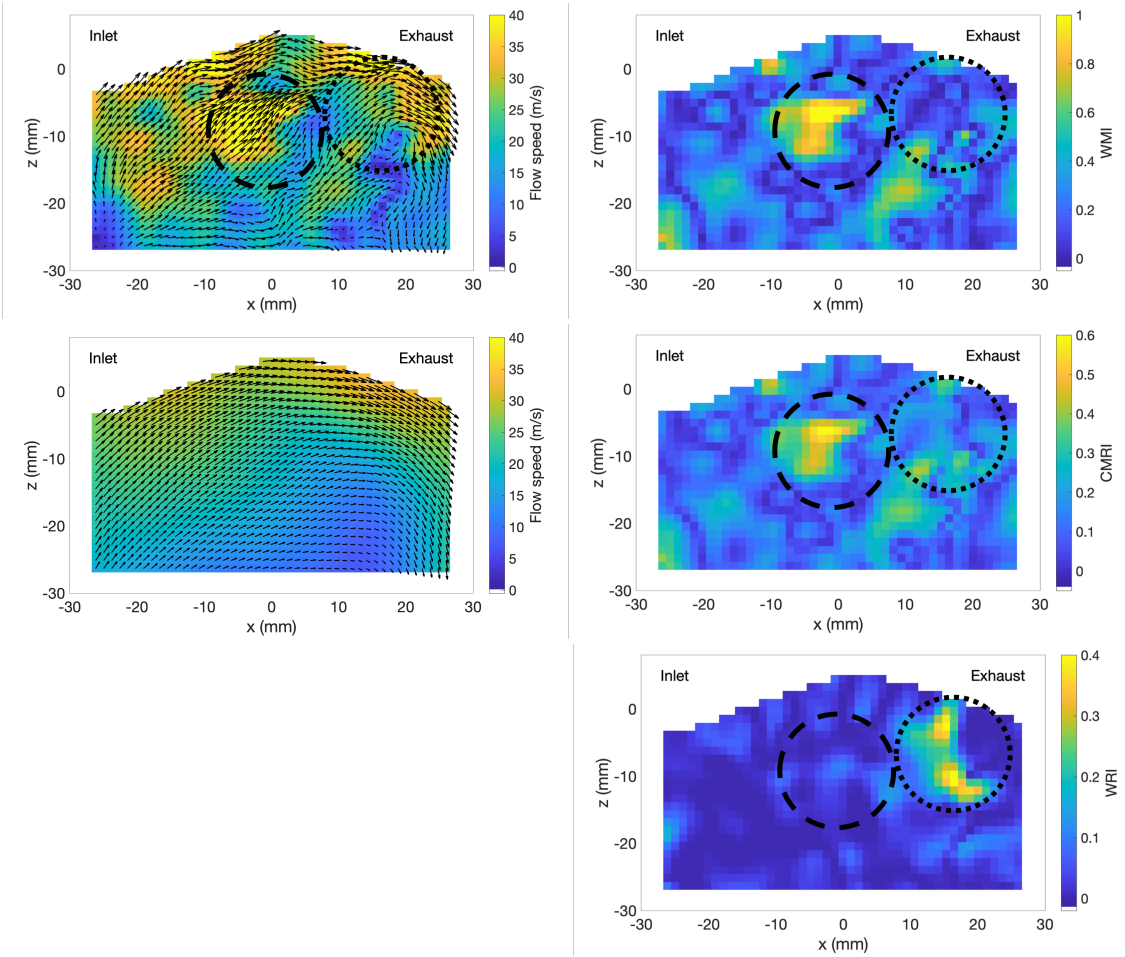

Figure 4.13 *Plots showing the comparison of an individual flow field (top left) to a reference mean field (bottom left). Fields of WRI (bottom right), WMI (top right) and their addition (centre right) are also presented. The dashed circle and dotted circle highlight regions of misalignment and poorly-matched magnitude that are visible in the fields of WRI and WMI, but the misalignment is not present in the combination.*

The individual cycle contains features that differ significantly from the mean flow field; the dashed circle highlights a region of flow that is aligned with the mean flow but is travelling at approximately twice the speed. A region of flow that is particularly poorly aligned with the mean flow is highlighted by the dotted circle. Both features appear in their respective metrics, however, only the region of high velocity appears in the combination of the metrics. This demonstrates how the simple addition of the two metrics does not include a significant contribution from the WRI.

In order to give the WRI equal weight when it is combined with WMI, the vector-wise distributions of the metrics must be normalised. The objective of this is to scale each metric so that the majority of values lie in the range from 0 to 1. In this way, the addition of the metrics will include contributions from both metrics, not just the WMI. Equation 4.6 shows the normalisation for a variable, $\boldsymbol{f}$, that represents the range of *WRI* and *WMI* values for a given dataset.

$$\boldsymbol{f}_{norm} = \frac{\boldsymbol{f} - f_{low}}{f_{high} - f_{low}} \tag{4.6}$$

where f_{low} and f_{high} are the values used to scale the majority of the values of $\boldsymbol{f}$ between 0 and 1.

If all the values of $\boldsymbol{f}$ are to be rescaled strictly between 0 and 1, then f_{low} and f_{high} are the minimum and maximum values of $\boldsymbol{f}$. For example, normalising *WRI* for all 1000 individual cycles at a given crank angle requires all 1000 *WRI* fields to be concatenated into a single vector, from which the minimum and maximum values can be found. However, to provide a robust normalisation, the minimum and maximum values are not used because a single pixel with an anomalous value of $\boldsymbol{f}$ will distort the scaling and reduce the effect of the

normalisation. Instead, the values of f_{low} and f_{high} are found using thresholds that ignore the most extreme values of the distribution. The lowest and highest 2% of all the values in the dataset are ignored in the scaling factor, resulting in 96% of the distribution being scaled between 0 and 1. Therefore, the lowest 2% are shifted to negative values and the highest 2% are greater than 1.

The left-hand plot of Figure 4.14 shows the original vector-wise distributions of the *WRI* and *WMI* for a single cycle (also shown in Figure 4.12) with lines showing the values that would be used for normalisation if the maximum values are used (solid lines) and threshold (98%) values are used (dashed lines). The lines for the lower 2% and minimum values have been omitted for clarity. The right-hand plot shows the normalised metrics, WRI_{norm} and WMI_{norm}, which have been rescaled with the threshold values.

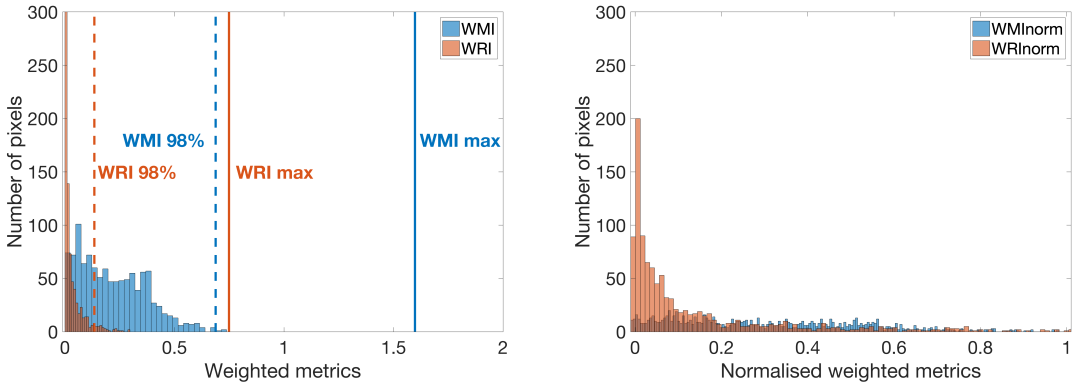

Figure 4.14 *Plots showing the original vector-wise distributions of WRI and WMI with lines showing the values that can be used for normalisation (left), and the normalised metrics ignoring the highest and lowest 2% for the rescaling (right).*

As seen in Figure 4.14, the normalied metrics now have similar ranges, which allows both metrics to contribute to the combined metric. This leads to the formal definition of the Combined Magnitude and Relevance Index (CMRI):

$$\boldsymbol{CMRI} = \frac{\boldsymbol{WRI}_{norm} + \boldsymbol{WMI}_{norm}}{2} \tag{4.7}$$

As the majority of the values of both WRI_{norm} and WMI_{norm} range between 0 and 1, their summation is divided by 2 so that the values of $CMRI$ lie within the same range. The effect of normalising the metrics before addition is shown in Figure 4.15, which presents the same comparisons as in Figure 4.13, with the exception that the normalised metrics are now plotted with a *CMRI* field.

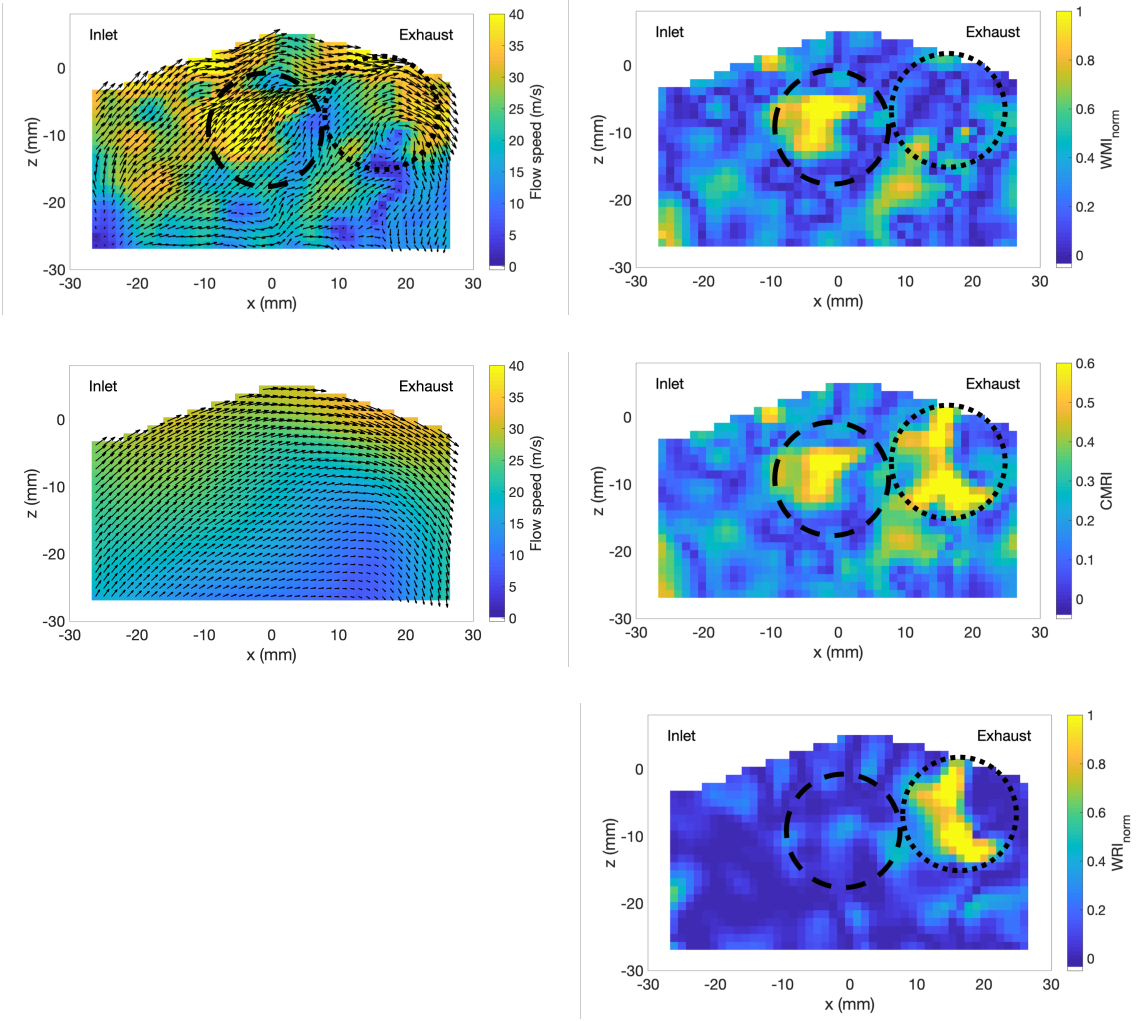

Figure 4.15 *An identical figure to Figure 4.13, showing the normalised metrics and the CMRI.*

Unlike in Figure 4.13, the *CMRI* now takes into account the poor alignment that appears in the normalised *WRI* field. By manipulating the distributions of *WRI* and *WMI* fields, the combined metric produces a field that reflects differences in both alignment and magnitude. This metric can be spatially averaged in order to find individual cycles that best match the mean in terms of both alignment and magnitude.

4.6 Application of the CMRI

For valid statistical analysis of flow field measurements, it is important to ensure that enough samples are acquired to accurately represent the mean flow field. Too few samples will result in large uncertainties in the resulting ensemble mean. For in-cylinder flow measurements, the recommended sample size ranges from hundreds to thousands of cycles [88]. The CMRI has been used to investigate how many cycles are required to produce a representative mean. The large dataset containing 1000 cycles was split into smaller subsets containing between 2 and 999 randomly selected cycles. The ensemble means of these subsets were then compared to the ensemble mean of the whole dataset using the CMRI. Figure 4.16 shows a plot of the mean spatially averaged CMRI at all crank angles for the comparison of the ensemble mean of each subset to the ensemble mean of the whole dataset.

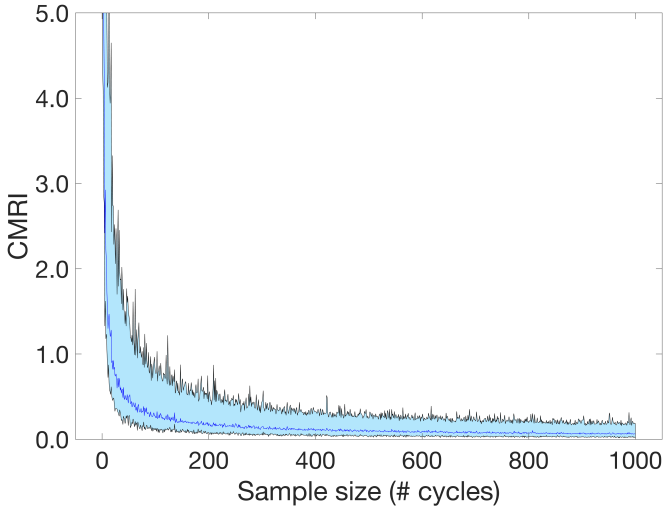

Figure 4.16 *A plot demonstrating the application of the CMRI to find the number of cycles required to produce a representative mean cycle. The blue line is the mean value of CMRI at all crank angles for each subset. The upper and lower bounds show the maximum and minimum values of CMRI at all crank angles for that subset.*

The value of CMRI drops rapidly as the number of cycles in each subset increases from 2 to 100. For subsets of greater than 100 cycles, there is very little change in the CMRI, which indicates that the ensemble mean flow fields for subsets of greater than 100 cycles are very similar to the ensemble mean of the whole dataset. It should be noted that this is not a universal result and the number of cycles required for a representative mean will depend on the test conditions. For this reason, 300 cycles was selected as a sufficient sample size to ensure statistical validity for each experiment in this thesis.

4.7 Practical Implementation of the Analysis Techniques

The code that implements the analysis techniques described in this chapter to calculate the WRI, WMI and CMRI has been written in Matlab. In order to complete the analysis, the velocity data is assumed to be in an appropriate format. For a single test, PIV velocity fields are measured over a range of crank angle degrees for a number of cycles, and each velocity component is stored in a multiple-dimensional array: u and w for the x and z directions

respectively. Each array has four dimensions to store the 2-dimensional velocity data for each crank angle and cycle; in Matlab format, an array *u* for the velocity data in the *x* – direction, is structured as '*u* (*x, y, crank angle, cycle*)'. This format is demonstrated in Figure 4.17.

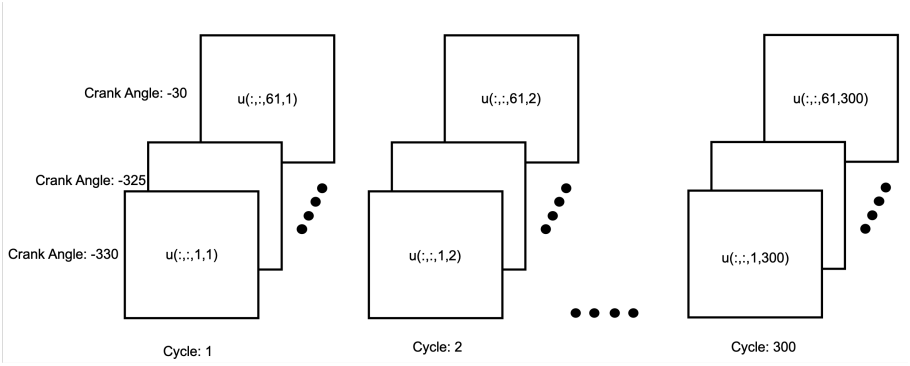

Figure 4.17 *An image depicting the format of storage arrays of velocity data.*

A number of functions are used for calculation of the WMI, WRI and CMRI:

WRI – calculateWRI.m

WMI –calculateWMI.m

CMRI – metric_scales.m and normalise_metric.m

The following sections demonstrate the use of these functions and an appendix includes the corresponding Matlab code.

4.7.1 Calculating the WRI

A function *calculateWRI.m* is used to calculate the WRI between two velocity fields. It requires 5 input arguments: *u* and *w* components of the velocity data for two velocity fields (*a_u, a_w* and *b_u, b_w*) and the corresponding mask array. The output is the WRI field showing the differences between the two input velocity fields. The code shown below demonstrates a possible use of the *calculateWRI*.m function, noting that the terms *'ca'* and

'cyc' denote the crank angle and cycle to be compared. This can be trivially inserted into a 'for' loop for automation over a whole dataset.

```
%% Implementation of the calculateWRI.m function

a_u = u_piv_field1(:,:,ca,cyc);
a_w = w_piv_field1(:,:,ca,cyc);

b_u = u_piv_field2(:,:,ca,cyc);
b_w = w_piv_field2(:,:,ca,cyc);

WRI_test(:,:,ca,cyc) = calculateWRI(a_u, a_w, b_u, b_w, mask(:,:,ca))
```

The *calculateWRI.m* function consists of three main parts:

- Calculating the difference in angle between two vectors.
- Calculating the magnitudes of each field and finding their median values.
- Calculating the WRI as given by Equation 4.4.

4.7.2 Calculating the WMI

In a similar way to the WRI, the WMI is calculated using a function *calculateWMI.m*, which is implemented with the same syntax as *calculateWMI.m* as shown below:

```
%% Implementation of the calculateWMI.m function

WMI_test(:,:,ca,cyc) = calculateWMI(a_u, a_w, b_u, b_w, mask(:,:,ca))
```

The *calculateWMI.m* function consists of two main parts:

- Calculate the magnitudes of each velocity field.
- Find the median magnitude of **both** fields and use this to normalise the difference between the two, as shown in Equation 4.5.

4.7.3 Calculating the CMRI

To calculate the CMRI, the WRI and WMI must already be available. As discussed in Section 4.5.2, the WRI and WMI must be normalised to ensure that their distributions are within the same range before they are combined to produce the CMRI. In order to achieve this, two functions are used: *metric_scales.m* and *normalise_metrics.m. Metric_scales.m* is used to find the specific values required to perform the normalisation of the WRI and WMI, which is then performed by *normalise_metrics.m*. After normalisation of both the WMI and WRI, the CMRI is calculated using Equation 4.7. The code below shows an example of the calculation of the CMRI.

```
%% Example code using metric_scales.m and normalise_metrics.m to calculate
the CMRI from values of WRI and WMI

% Creating vector that includes all values required for noralisation
WRI_allTests= [WRI_test1,WRI_test2,WRI_test3];
WMI_allTests= [WMI_test1,WMI_test2,WMI_test3];


% Selecting the upper and lower bounds for normlisation
pc_hi = 0.98;
pc_lo = 0.02;

% Use metric_scales.m to find the specific values to be used for
normalisation
[WRIscale_allTests_hi,WRIscale_allTests_lo] =
                              metric_scales(WRI_allTests,pc_hi,pc_lo);

[WMIscale_allTests_hi,WMIscale_allTests_lo] =
                              metric_scales(WMI_allTests,pc_hi,pc_lo);

% Use normalise_metric.m to normalise the WRI_test1 and WMI_test1 using
the values produced by metric_scales.m

WRI_norm_test1 (:,:,ca,cyc) = normalise_metric(WRI_test1(:,:,ca,cyc),…
WRIscale_allTests_hi,WRIscale_allTests_lo);


WMI_norm_test1(:,:,ca,cyc) = normalise_metric(WMI_test1(:,:,ca,cyc),…
WMIscale_allTests_hi,WMIscale_allTests_lo);

% Simply combine the normalised WRI and WMI to produce the CMRI
CMRI_test1(:,:,ca,cyc) =
            (WRI_norm_test1(:,:,ca,cyc) + WMI_norm_test1(:,:,ca,cyc))/2;
```

Three inputs are required for *metric_scales.m*; the first is a vector containing all the values that will be used in the comparison and hence, the normalisation. The two other inputs, *pc_hi* and *pc_lo*, dictate the range of the normalisation as demonstrated in Figure 4.14. This produces the specific values that will be used for the normalisation, which are then passed to *normalise_metrics.m* as input arguments.

The function *normalise_metrics.m* uses the outputs from *metric_scales.m* in addition to the original WRI or WMI values to produce the normalised metrics using Equation 4.6. After both the WRI and WMI have been normalised, the CMRI is calculated according to Equation 4.7. Although it is not shown here, all these metrics can be spatially averaged to produce a single value for a given field.

4.8 Summary

This chapter presents the development of two new metrics for quantifying the differences between vector fields; the weighted relevance index (WRI) and the weighted magnitude index (WMI). The weighted relevance index builds on the relevance index, which is used to quantify the misalignment of two vectors. A weighting factor based on the local velocity of the flow fields is introduced to remove low velocity biases, which arise near the centre of tumble vortices commonly present in DISI engines. The weighted magnitude index provides a measure of the difference in magnitude between two vectors. These quantities are typically calculated for a whole field and then spatially averaged to produce a single value, which can be used to rank how similar test flow fields are in relation to a reference flow field.

The WRI and WMI were applied to a sample of 1000 cycles to investigate any correlation between the two metrics. No obvious correlation was found, which leads to the conclusion that flow fields which are similar in terms of alignment are not necessarily similar in terms of flow speed for the conditions tested in this work. For this reason, a method of combining the WRI and WMI has been developed to produce a metric, known as the Combined Magnitude and Relevance Index (CMRI), which accounts for differences in both magnitude and alignment. The application of the CMRI has been demonstrated by investigating the number of cycles that are required to produce an ensemble mean flow field that is representative of the actual mean flow field. It was concluded that 300 cycles is a sufficient sample size for statistical validity and so this has been applied to all the experiments in this thesis.

The MATLAB implementation of these analysis techniques has been provided to aid the understanding of their practical use in quantifying differences between flow fields.

4.9 Appendix

calculateWMI.m

```
function [output] = calculateWRI(a_u,a_v,b_u,b_v,mask,varargin)


%% step 1 - calculate angular difference

% Find angle between U and V for each vector of first field
theta_aa=atan2(a_v(:,:),a_u(:,:));

% Find angle between U and V for each vector of second field
theta_bb=atan2(b_v(:,:),b_u(:,:));

% Calculate difference
thetaDiff=abs(theta_aa-theta_bb);

%% step 2 - calculate weighting factor

% Calculate magnitude of first velocity field
V_Mag_aa=(a_u(:,:).^2+a_v(:,:).^2).^0.5;


% Calculate magnitude of second velocity field
V_Mag_bb=(b_u(:,:).^2+b_v(:,:).^2).^0.5;

% Apply crank angle mask
V_Mag_aa= double( V_Mag_aa.*double(mask(:,:)));
V_Mag_bb= double( V_Mag_bb.*double(mask(:,:)));

% Calculate median velocity present in either field
V_mag_med_aa = nanmedian(V_Mag_aa(:));
V_mag_med_bb = nanmedian(V_Mag_bb(:));

%% step 3 – Calculate WRI according to Equation 1.8

penalty = (1/2)*(1-cos(thetaDiff))
                  .* (V_Mag_aa./V_mag_med_aa).*(V_Mag_bb./V_mag_med_bb);

% Apply mask to penalty
output= double(penalty.*double(mask(:,:)));

end
```

calculateWMI.m

```
function [output]= calculateWMI(a_u,a_v,b_u,b_v,mask,varargin)

%% Step 1 – Calculate magnitudes in each field

% Calculate magnitude of first velocity field
V_Mag_aa=(a_u(:,:).^2 + a_v(:,:).^2).^0.5;

% Calculate magnitude of second velocity field
V_Mag_bb=(b_u(:,:).^2 + b_v(:,:).^2).^0.5;
```

```
% Apply crank angle mask
V_Mag_aa= double( V_Mag_aa.*double(mask(:,:)));
V_Mag_bb= double( V_Mag_bb.*double(mask(:,:)));

%% Step 2 – Calculate median magnitudes of both fields and find the
normalized difference between the magnitudes of each field


% Calculate median velocity present in both fields
V_Mag_med = nanmedian([V_Mag_aa(:) ; V_Mag_bb(:)]);

% Calculate the difference in magnitudes normalised by the median
magnitude of both fields
VMagDiff=(abs((V_Mag_aa-V_Mag_bb))./V_Mag_med);

% Apply crank angle mask
VMagDiff= double( VMagDiff.*double(mask(:,:)));

% Assign output
output = VMagDiff;

end
```

metric_scales.m

```
function [metric_scale_hi, metric_scale_lo] =
                                metric_scales(metric_fullset,pc_hi,pc_lo)

% Sort values for full dataset into ascending order
metric_sort = sort(metric_fullset(:));

% Remove NaN values introduced by the digital mask
metric_sort_nonan = metric_sort(~isnan(metric_sort));

% Use this vector to define scaling limits for the normalization required
for the CMRI

metric_scale_hi =
            metric_sort_nonan(ceil(length(metric_sort_nonan)*pc_hi));

metric_scale_lo =
            metric_sort_nonan(floor(length(metric_sort_nonan)*pc_lo));
end
```

normalise_metrics.m

```
function [metric_norm] =
            normalise_metric(metric_old,metric_scale_hi,metric_scale_lo)

%% Scaling data so that metric_scale_hi and metric_scale_lo define new
boundaries for the metric (see Equation 1.11. Stretches the majority of
values over the range 0 to 1

metric_norm =
      (metric_old - metric_scale_lo)/(metric_scale_hi - metric_scale_lo);

end
```

5 Validation of CFD Simulations with PIV Using Quantitative Metrics

5.1 Introduction

Computational Fluid Dynamics (CFD) is now a standard tool used across a range of engineering disciplines from aerospace and automotive, to biomedical sciences and the petrochemical industry [85]. It involves the solution of mathematical models that represent physical processes using a numerical approach. Not only is it used to simulate the motion of fluids under certain conditions, it can also simultaneously provide 3-dimensional predictions of temperature, pressure and chemical composition. The improvement of computer hardware and cluster services in recent decades has resulted in the rapid development of CFD, enabling the completion of more complex simulations in less time.

There are many benefits associated with its use in the engineering design process; for example, the design of new combustion systems in the automotive industry. CFD simulations provide initial data that is used to guide the design and reduce the number of prototypes required, which reduces costs. CFD simulations can also provide data that is experimentally unobtainable due to physical constraints. Although engine test cells are still necessary, experimentation is expensive due to the high cost of the hardware and execution time.

The following section provides a brief overview of the methodology of CFD and the difficulties in simulating the complexities of an internal combustion engine.

5.1.1 Introduction to CFD

CFD involves the use of numerical algorithms to solve the governing equations that describe the physical nature of a flow under certain conditions. Before the numerical algorithms can be applied, the domain of the problem must first be defined, which usually involves the use of a digital solid model, before it is discretised into number of cells (known as meshing). The size of the cells defines the spatial resolution of the simulation and also dictates the computational cost; smaller cells result in a greater number of calculations that must be performed. The resolution of the mesh is known to have a significant effect on the accuracy of the simulation [85], therefore it is necessary to ensure that it is sufficiently fine to reach a converged solution. In simulations of engines, it is common to refine the grid around regions of interest, such as the valve curtain or spark plug. More recently, some CFD solvers dynamically refine the mesh during the simulation based on the local variation of certain variables [153].

After the domain has been meshed, solutions to the governing equations are calculated for each finite volume at each time step. The governing equations represent fundamental physical principles; conservation of mass, momentum and energy. For compressible, viscous flow, these are known as the Navier-Stokes equations and are provided in the conservative form:

Mass

$$\frac{\partial \rho}{\partial t} + \nabla.(\rho \boldsymbol{u}) = 0 \tag{5.1}$$

Momentum (x-direction)

$$\frac{\partial (\rho u)}{\partial t} + \nabla.(\rho u \boldsymbol{u}) = -\frac{\partial p}{\partial x} + \nabla.(\mu \nabla \mathrm{u}) + S_x \tag{5.2}$$

Energy

$$\frac{\partial (\rho e)}{\partial t} + \nabla.(\rho e \boldsymbol{u}) = -p\nabla.\boldsymbol{u} + \nabla.(\mathrm{k}\nabla \mathrm{T}) + \boldsymbol{\phi} + S_e \tag{5.3}$$

where ρ is the fluid density, $\boldsymbol{u}$ is the fluid velocity (such that $\boldsymbol{u} = u\,\mathbf{i} + v\,\mathbf{j} + w\,\mathbf{k}$), μ is the dynamic viscosity of the fluid, S_x accounts for body forces, e is the energy of the fluid, k is the thermal conductivity, T is the fluid temperature, $\boldsymbol{\phi}$ accounts for dissipation due to viscous effects, and S_e accounts for potential energy.

This is a set of coupled, non-linear equations that, as of yet, have no analytical solution. Therefore, for the most common CFD codes, the conservation equations are discretised for each finite volume and solved using advanced iterative methods.

It is known that the flow in an engine is highly turbulent, and that this turbulence plays a crucial role in mixture preparation and flame propagation [37]. The large-scale bulk motion, setup during the induction process, induces the formation of smaller turbulent eddies through the action of shear stresses resulting from the interaction between the intake jet and the in-cylinder gas. The formation of smaller eddies continues as the energy in the bulk flow feeds the turbulent motion, until it is dissipated as heat at the molecular level. This action encourages vigorous mixing, which transports fuel quickly throughout the combustion chamber, and interacts with the flame front, which increases the rate of combustion. Therefore, it is essential that the effect of turbulence is modelled by CFD simulations if they are to be used in the design of combustion systems. An inherent difficulty in the simulation (and measurement) of turbulence is the presence of a large range of temporal and spatial scales, which must be resolved to capture the true characteristics of the flow. There are a number of different approaches to turbulence modelling that are currently used by industry and researchers. The most common are Reynolds Averaged Navier-Stokes (RANS), Large Eddy Simulation (LES) and Direct Numerical Simulation

(DNS), which vary in their complexity and computational expense, as depicted in Figure 5.1.

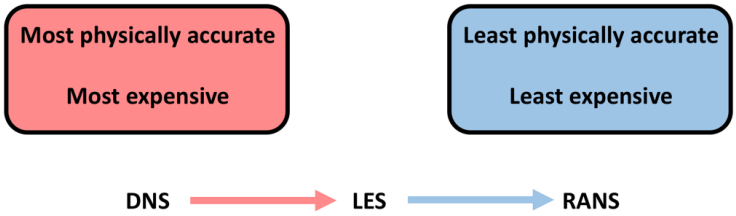

Figure 5.1 *Different approaches to turbulence modelling.*

5.1.2 Turbulence modelling

It is important to remember that CFD simulations are only as reliable as the mathematical models used to represent the underlying physical processes. In general, there is a compromise between computational time required and physical accuracy of the simulation. RANS has been widely used by industry as it requires the least time to complete a simulation and produces results that match experimental trends [139]. As the name suggests, the approach involves using Reynolds decomposition to separate the contributions of the mean flow and its fluctuations. By modifying Equation 5.2 and using this decomposition, extra terms, known as the Reynolds stresses, are produced that account for the effects of turbulent fluctuations on the mean flow. In order to solve for these new terms, a number of models have been developed, of which one of the most widely used is the k-ε model. This attempts to solve for the Reynolds stresses by investigating the mechanisms that affect the production and dissipation of the turbulent kinetic energy, k. This method also involves the introduction of a turbulent (or eddy) viscosity term that models all turbulent fluctuations in a similar fashion to viscous stresses on a Newtonian fluid. This term tends to eliminate the smaller length scales of fluid motion, leaving only the large-scale flow structures.

As a result of this approach, RANS simulations of engines are well suited to capturing the bulk flow motion and are the most economical in terms of computational resources. Despite its disadvantages, RANS simulations have been widely used for full simulations of combustion in DISI engines [154]–[158]. Furthermore, even though it is commonly thought that RANS simulations should produce a converged result [83], some studies have shown this is not necessarily the case, and that cycle-by-cycle variations and even stochastic processes such as combustion knock can be modelled using RANS [159]–[161].

In an attempt to reduce the reliance on simplified models to predict turbulence, LES uses a different approach; a spatial filter is applied to the Navier-Stokes equations in order to retain a larger range of flow scales that are directly resolved. In a similar way to RANS, any flow scales smaller than the filter must be modelled. More detailed information on the theory of LES is provided in [85], [162]. Although LES simulations are considerably more expensive than those produced using RANS [163], the improvements in the performance of computational hardware has resulted in increased popularity of the use of LES for engine simulations [83], [88], [164]–[166]. Its ability to more accurately capture the random nature of the in-cylinder flow has led to its use in the characterisation of cycle-by-cycle variations in DISI engines [167]–[170]. In order to demonstrate the differences between RANS and LES simulations, Figure 5.2 shows plots of OH from simulations of a reacting diesel fuel spray using RANS and LES. The differences in the spatial resolution of the flame are clear; for the RANS simulation, the flame has very smooth features in contrast to the complex shape of the LES simulation due to the resolved turbulent motion.

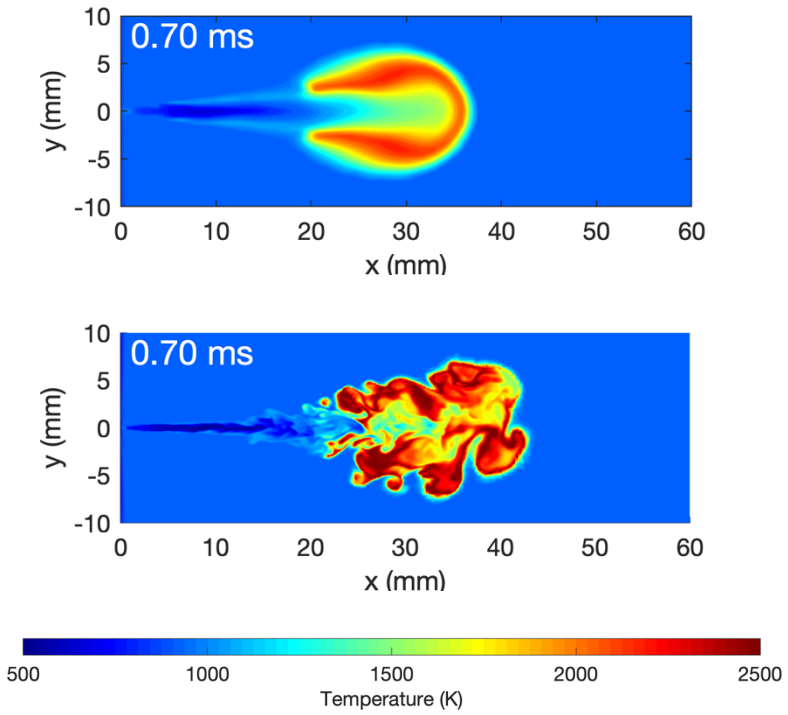

Figure 5.2 *Plots of OH comparing RANS (top) and LES (bottom) simulations of a reacting diesel fuel spray (reproduced with permission from* [171]*).*

If the spatial filter used for LES is decreased in size until all flow scales are resolved directly, this is known as Direct Numerical Simulation. This approach does not require any sub-grid models to simulate turbulent effects and so produces the most physically accurate results. However, the extreme computational effort required to perform such simulations for in-cylinder flows, means that it is limited only to research applications [172].

5.1.3 Validation of CFD

As discussed in Chapter 4, effective validation of CFD simulations is essential to ensure their effective use in engineering applications. For validation of in-cylinder flow field simulations, PIV is the most common experimental tool. In this chapter, the methods outlined in Chapter 4, the WRI, WMI and CMRI, are used to quantify the differences between in-cylinder flow simulations and measurements in the optical engine.

5.2 Experimental Setup

For this work, in-cylinder flow fields were measured using high-speed PIV for three test conditions that are related to a production engine load map. The test conditions have also been simulated using a commercially available CFD software package, StarCD. It must be noted that the simulations were completed by engineers at Jaguar Land Rover, and are not the work of the author. The following sections describe the test conditions, PIV setup and simulation setup. For more detailed information on the optical engine and PIV system, refer to Chapters 2 and 3.

5.2.1 Engine operating conditions

Three conditions, named T1, T2 and T8, have been selected from the load map of an engine calibration in order to compare measurements and simulations for realistic conditions. Table 5.1 provides the details of the conditions.

Table 5.1 *Engine conditions.*

	T1	T2	T8
Engine speed (RPM)	1500	1500	1750
Manifold Air Pressure (kPa)	80	95	96
Air volume flowrate (l/s)	1.57	3.65	3.40
Intake air temperature (°C)	45	45	45
Coolant temperature (°C)	23	23	23
Inlet maximum valve lift (mm)	6.3	6.8	6.1
Inlet valve opening/closing (°ca aTDC gas exchange)	-33 / 101	-30 / 117	-23 / 112
Exhaust valve opening/closing (°ca aTDC gas exchange)	-217 / 51	-243 / 25	-219 / 49

Figure 5.3 shows the valve lift profiles and in-cylinder pressure traces for each condition. For T1 and T2, the engine speed is 1500 rpm and for T8, it is increased to 1750 rpm. T1 is throttled slightly, whereas T2 and T8 are almost wide-open throttle. The air temperature

and coolant temperature were held constant for each condition at 45 °C and 23 °C respectively.

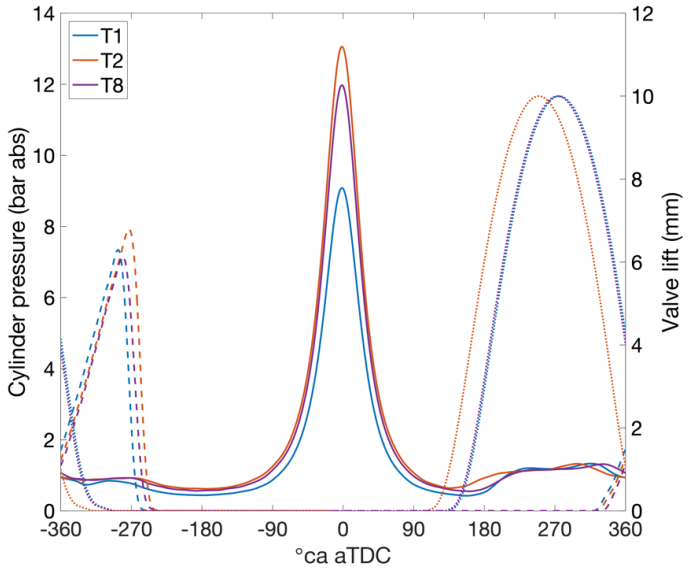

Figure 5.3 *Plots showing the inlet and exhaust valve profiles (dashed and dotted lines) and the mean in-cylinder pressure traces for T1 (blue), T2 (orange) and T8 (purple).*

This study only considers motored flow; therefore, the spark plug has been replaced with a brass blank to reduce background scatter for the PIV measurements. A transparent acrylic annulus was used to provide optical access to combustion chamber and a quartz piston insert was used to provide access for the laser sheet. Piston C was used for all tests.

5.2.2 PIV setup

Table 5.2 provides details of the PIV experiment for all the test conditions.

Table 5.2. *Details of the PIV setup for all conditions.*

Range of recorded CAD (°ca bTDC combustion)	330 – 30
Measurement increments (°ca)	5
Number of cycles	300
Number of runs per test	3
Spatial resolution (mm)	1.96
Vector resolution (mm)	0.98
Field of view (mm^2)	40 × 45

The field of view of the PIV measurements and a schematic of the PIV timings are shown in Figure 5.4.

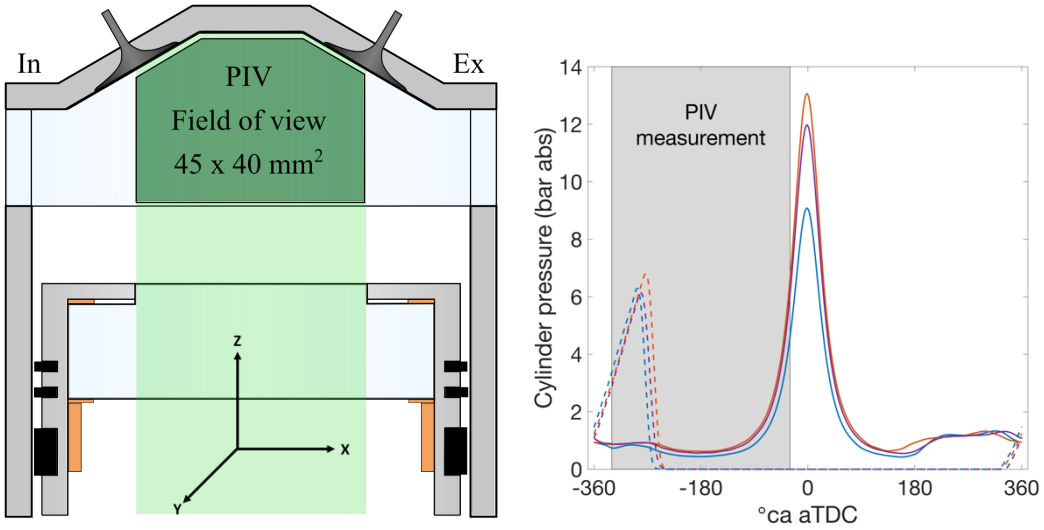

Figure 5.4 *Plots showing the field of view and coordinate system (left) and the timings (right) for the PIV measurements.*

PIV measurements were made every 5°ca from 330°ca bTDC (relative to combustion TDC) to 30 °ca bTDC to capture both the induction process and the compression stroke. Measurements near TDC were unavailable due to the piston crown features blocking the scattered light from the oil droplets. The measurement plane was located 1 mm towards the front of the engine from the central tumble plane (y = -1 mm using the coordinate system in Figure 5.4). This reduced the large amount of scattered laser light from the tip of the fuel injector affecting the measurement region.

For each test condition, the optimal seeding density was obtained using an iterative process. Similarly, the optimal dt values for each crank angle were found through trial-and-error to ensure that the maximum displacement of droplets between frames was less than a quarter of the width of an interrogation window (32 × 32 pixels).

5.2.3 Numerical setup

A commercially available CFD package, StarCD, was used for the RANS simulations of the optical engine. These simulations were setup and performed by engineers at Jaguar Land Rover and the resulting data was passed to Oxford for further processing and comparison. A solid model of the combustion system is produced using Computational Aided Design (CAD) software and provides the correct geometry for the simulation. This model is then discretised into a finite number of nodes, known as a 'mesh'. The mesh provides the points at which the governing equations are solved at each timestep, and so dictates the spatial resolution of the simulation The computational domain for the simulations is shown in Figure 5.5.

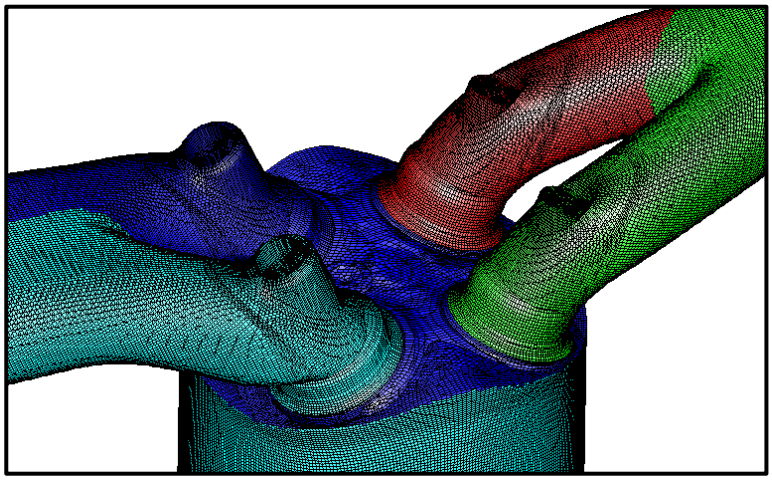

Figure 5.5 *An image of the computational domain used for the RANS simulations.*

In order to initiate the simulation, initial and boundary conditions must be specified; wherever possible engine measurements have been used to provide these. At the intake and exhaust ports, crank-angle resolved dynamic pressure measurements were used as inputs. Steady state temperature measurements were used as initial conditions at these locations. For components where temperature measurements were unavailable, assumptions were made; for example, the temperatures of the inlet and exhaust valves were assumed to be the

same as the cylinder head, which was controlled by the temperature of the coolant. The measured mass flow of air entering the engine was also used as an input boundary condition, as well as the valve lift profiles measured during engine operation. Figure 5.6 shows examples of the pressure measurements at the inlet and exhaust ports that are used as boundary conditions for the simulations. Also shown are the measured inlet and exhaust valve lifts.

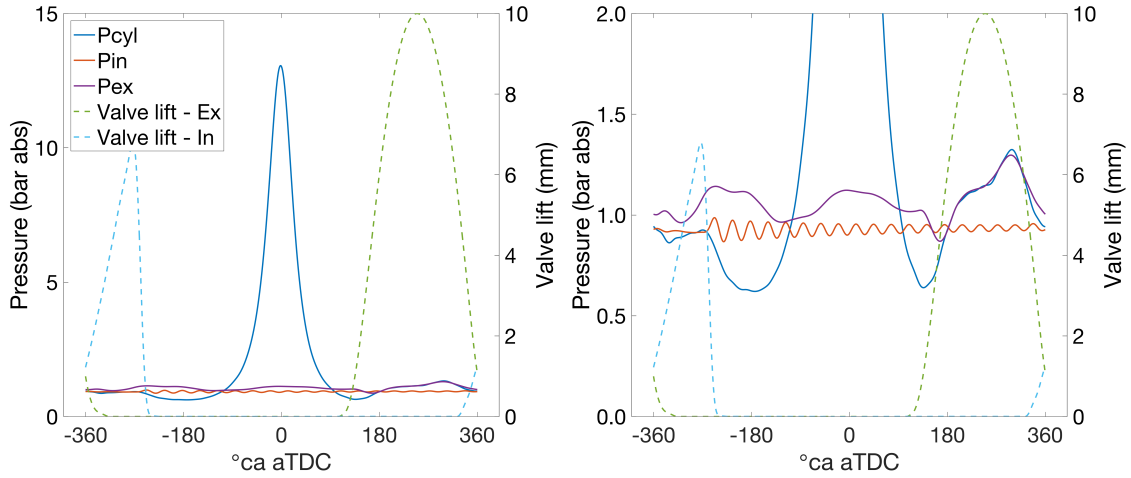

Figure 5.6 Plots demonstrating a selection of pressure measurements used as the boundary conditions for the simulations. The solid lines indicate pressure measurements and the dashed lines indicate valve lift measurements. A zoomed plot is shown on the right to highlight the dynamic pressure measurements at the inlet and exhaust ports.

In general, the mesh had a minimum cell size of 0.7 mm, which was reduced to 0.3 mm for the valve curtain area as shown in Figure 5.7. As a result, each simulation contained approximately 3.25 million cells. The timestep for the simulation remained constant at 0.1°ca. Turbulence was modelled using the standard RNG (Renormalised Group) k-ε model and a modified Angelberger model was used to model heat transfer.

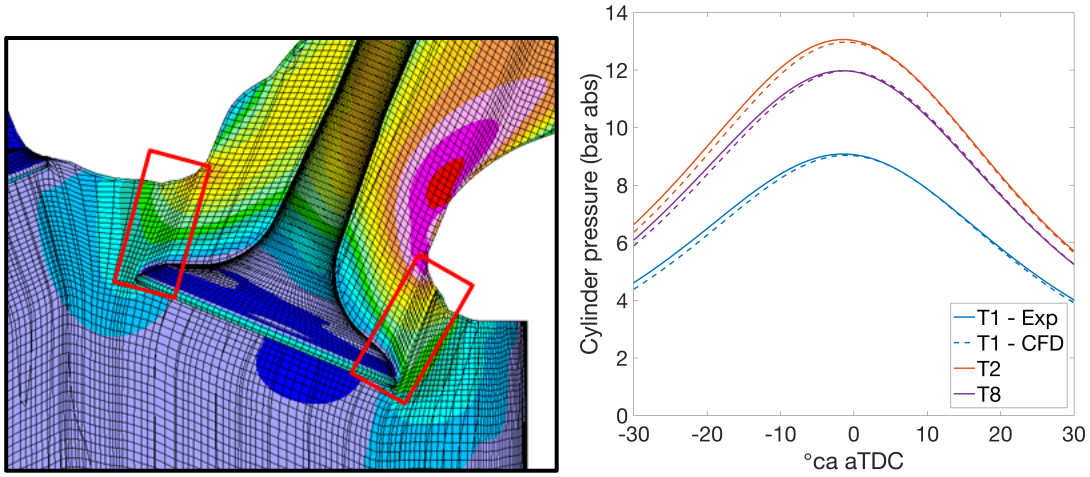

Figure 5.7 *An image highlighting the reduced cell size around the valve curtain (left) and a plot comparing the measured and simulated pressure traces (right).*

The measured and simulated pressure traces are shown in Figure 5.7. In order to match the simulated in-cylinder pressure with the measurements, the crevice length (defined as the distance between the top land and the top piston ring) was varied for each condition. This is an attempt to take into account the loss of mass in the experiments due to blow-by past the piston rings by changing the compression ratio. There was no further tuning of the physical models.

5.2.4 Post-processing of CFD results

CFD simulations provide a three-dimensional, three-component velocity field, which must be reduced to a planar field in order to directly compare with PIV results. Firstly, it was ensured that the geometric origin of the simulations and the PIV measurements were identical. Two-component CFD vectors from the plane of interest (y = -1 mm) were then extracted onto a grid that had twice the spatial resolution of the PIV measurement grid. The resulting CFD vector field was linearly interpolated before it was mapped directly onto the PIV measurement grid. As result of this process, both simulated and measured flow fields

were located on identical spatial grids, which is necessary for the analysis methods. An example of a CFD flow field mapped onto a PIV measurement grid is shown in Figure 5.8.

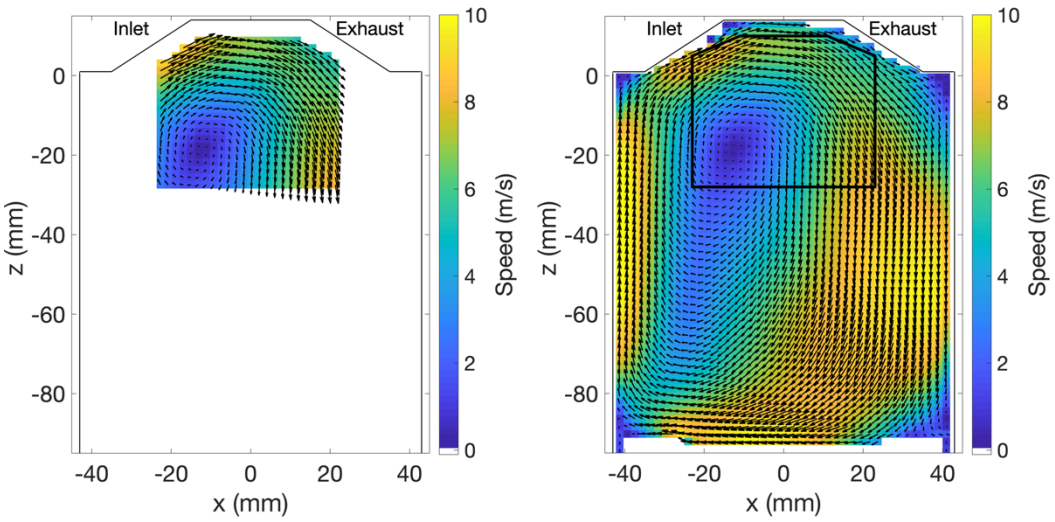

Figure 5.8 *Example of a simulated flow field (right) mapped onto the PIV measurement grid (left). The black box in the right-hand image shows the field of view of the PIV measurement.*

The PIV flow fields used for the validation of the RANS simulations are ensemble averages of 300 cycles recorded in three sets of 100 cycles. Section 4.6 discusses experimental results that demonstrate that 300 cycles is a conservative number of cycles required to produce a representative mean cycle.

It should be noted that both PIV and CFD vector fields were processed with an identical digital mask to remove vectors from regions obscured by the inlet valves and piston. Due to the different valve profiles, the most conservative mask (for test condition T2) was used for all conditions to ensure that the same number of vectors are compared between conditions. All mean flow fields plotted in the following section show every second vector for clarity. Any velocity fields of individual cycles show all vectors to retain the small variations in the flow.

5.3 Results and Discussion

This section demonstrates how the quantitative metrics described in Chapter 4 can be used to identify differences between simulated and measured flow fields. A number of differences identified by the metrics are then explored in more detail using conventional methods of comparison to evaluate the performance of the metrics.

5.3.1 Initial investigation using the CMRI, WRI and WMI

Figure 5.9 shows plots of the spatially averaged CMRI throughout the cycle for all three test conditions, which provide initial comparisons between simulated and measured flow fields. Low values of CMRI indicate a better match between flow fields than higher values.

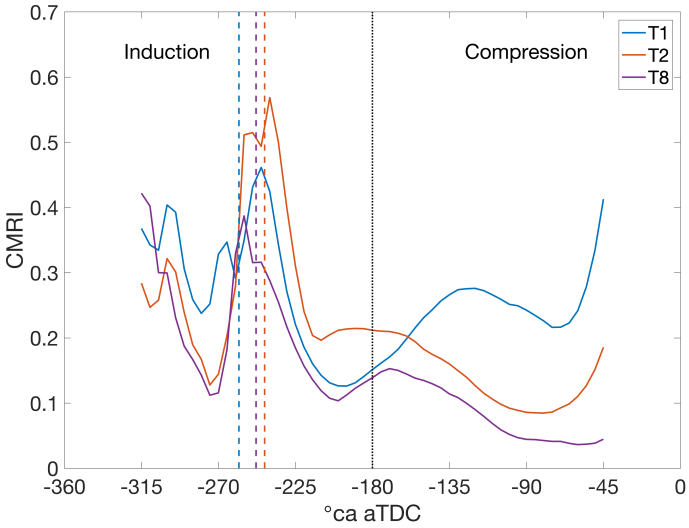

Figure 5.9 *Plots of the spatially-averaged CMRI showing the differences between simulated and measured flow fields in terms of alignment and magnitude. The dashed lines show the timing of IVC for each condition. Low values denote a better match between flow fields.*

There are a number of features that can be highlighted from this plot; firstly, there are peaks in the CMRI that occur at approximately 240 °ca bTDC for all the test points. Shortly after BDC, the CMRI for T2 and T8 decreases to a minimum during the compression stroke. In contrast, the CMRI for T1 increases significantly until approximately 115°ca bTDC. After a local minimum at 70°ca bTDC, the match between CFD and PIV flow fields for T1

deteriorates rapidly, whereas there are only small changes in the quality of the match between CFD and PIV flow fields for T2 and T8.

The plots of the CMRI allow regions of interest to be easily identified in the comparisons between flow fields. As it accounts for differences in both alignment and magnitude of the velocity fields, further analysis of the WRI and WMI is required to decouple their contributions to the CMRI. Figure 5.10 shows plots of the normalised WRI and WMI for all conditions.

Inspecting the plots of WRI and WMI separately provides more information about the nature of the features identified by the CMRI (Figure 5.9). For example, by examining the plot of the WRI, it is clear that the peaks in the plots of the CMRI at 240°ca bTDC for all conditions are due to a misalignment of the flow fields, rather than a difference in magnitude. Furthermore, the plots of the WMI reveal a number of peaks that correspond to the inlet valve closing period for each condition. These peaks are also visible in the plot of the CMRI; however, it is less clear due to the contribution of the WRI at around 240°ca bTDC. The increase in the CMRI for T1 during the compression stroke from BDC to 115°ca bTDC appears to be a combination of both a misalignment and difference in magnitude between simulated and measured vector fields. After this timing, the WMI decreases, whereas the WRI increases rapidly. Three features identified by the metrics are listed below and discussed in more detail in the following sections:

- Peaks in the WMI during inlet valve closing
- Peaks in the WRI for all conditions at 240°ca bTDC
- Increase in all metrics during the compression stroke for T1

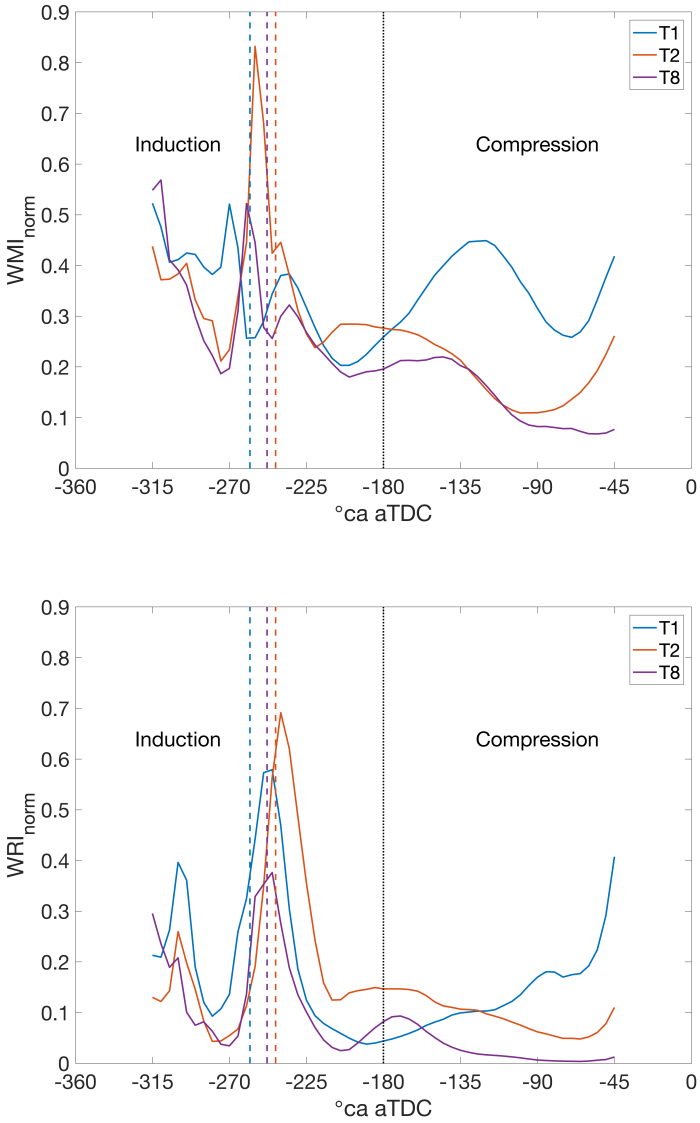

Figure 5.10 *Plots of the spatially averaged WRI (top) and WMI (bottom) showing the differences between simulated and measured flow fields in terms of magnitude and alignment separately. The coloured dashed lines show the timing of IVC for each condition.*

5.3.2 Peaks in the WMI during inlet valve closing

Figure 5.10 shows distinct peaks of the WMI at timings that correspond to the period of inlet valve closing for each condition. To investigate the origin of these peaks, fields of the WMI for each condition at the respective timings of the peaks of the WMI are displayed in Figure 5.11. The peaks occur at 270°ca bTDC, 255°ca bTDC and 260°ca bTDC for T1, T2

and T8 respectively, and both simulated and measured flow fields are overlaid on fields of WMI.

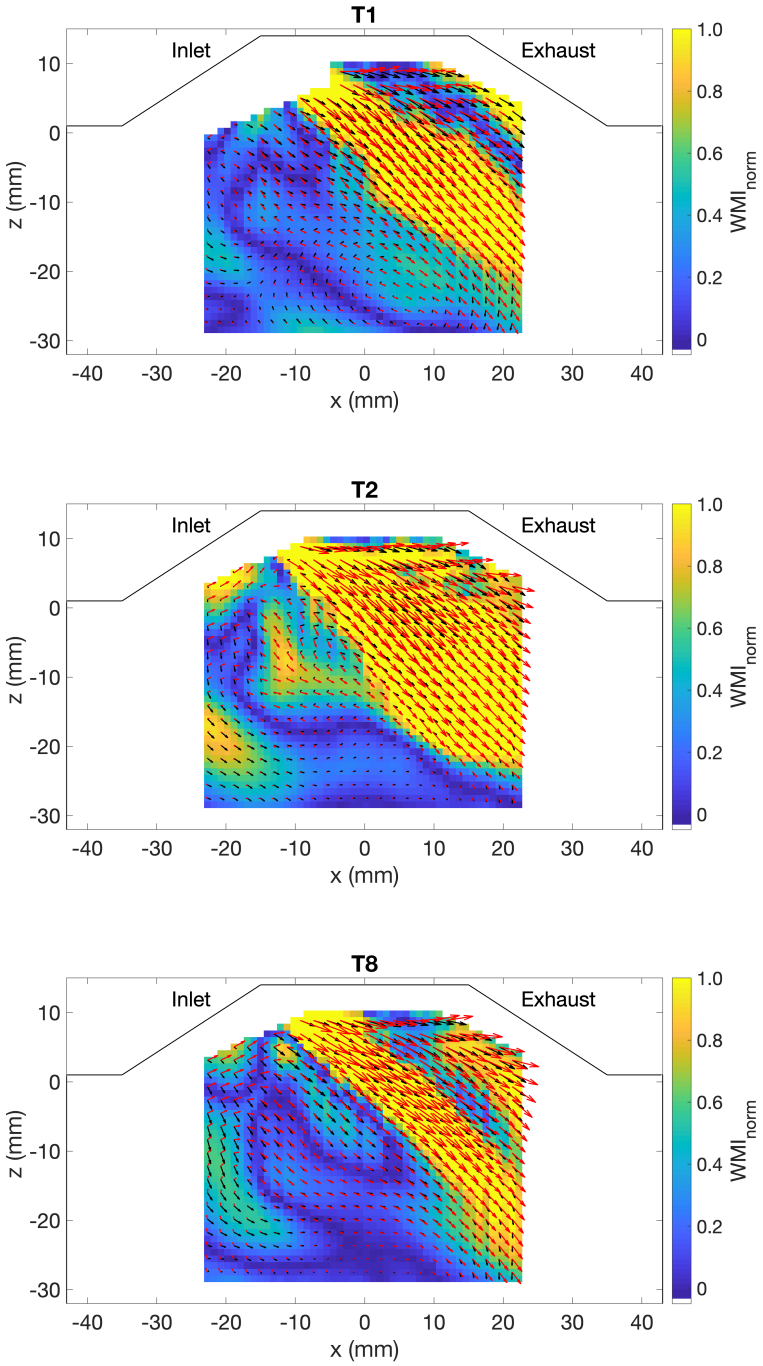

Figure 5.11 *Fields of the WMI at the locations of the peaks shown in Figure 5.10. T1 - 270°ca bTDC, T2 - 255°ca bTDC and T8 - 260°ca bTDC. The overlaid black and red arrows show the PIV and CFD vector fields respectively.*

As the valves are closing, for each condition there is a high-speed jet from the inlet valve entering the combustion chamber for all conditions. In this region, there are relatively high values of the WMI between the two flow fields. On inspection of the velocity vectors, it is clear that the simulations predict higher velocities in the jet than the PIV results for all conditions, which leads to high values of the WMI. Although there are differences in the velocities on the inlet side of the field of view, they are relatively small compared to those in the jet and so result in small values of the WMI.

The higher momentum of the simulated intake flow results in the intake jet penetrating further into the cylinder than the experimental results. This can be seen in the lower, right-hand side of the field of view, where the simulated flow field persists in the direction of the inlet jet. In contrast, the PIV flow fields begin to turn towards the centre of the cylinder due to a loss of momentum. It is worth noting that the PIV flow fields are averages of 300 individual cycles, therefore any variations in the intake flow will smoothed out. There are indeed individual PIV cycles for which the magnitude of the velocity in the intake jet is more similar to that simulated by CFD, as shown in Figure 5.12.

Figure 5.12 shows flow fields of the simulated cycle, mean PIV cycle and an individual cycle at 270°ca bTDC for T1. The colour scales in the plots of the simulated cycle (top) and the mean PIV cycle (bottom) reflect what is shown in the fields of the WMI field in Figure 5.11; the simulated flow speed is considerably greater and the intake jet penetrates further into the combustion chamber at this crank angle in comparison to the mean PIV cycle. The maximum velocity predicted by CFD is 125 m/s, whereas the maximum velocity of the mean PIV flow field is only 74 m/s. However, inspection of the flow field of cycle 199 (Figure 5.12, middle) shows that an individual cycle can have significantly higher

flow speeds than the PIV mean cycle. The maximum velocity of this cycle is approximately 45% faster than the mean PIV cycle at 108 m/s and the jet penetrates further into the cylinder, in a similar way to the simulated flow field.

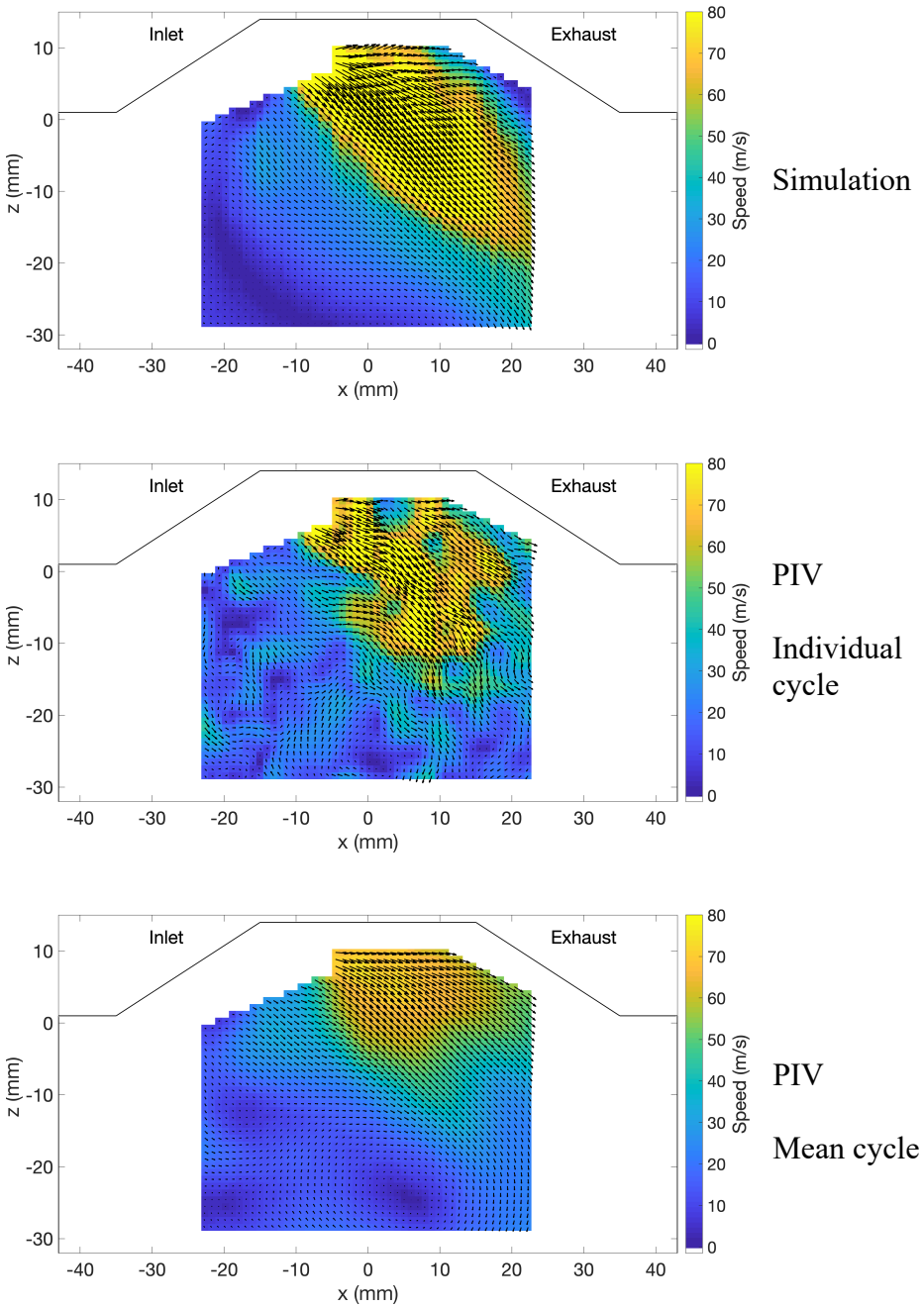

Figure 5.12 *Flow fields demonstrating comparisons of an individual cycle (middle) that best matches the simulated RANS flow field (top) in terms of flow speed for T1. The mean PIV flow field is also shown (bottom). Every velocity vector has been plotted to retain the detail of the fluctuation in the flow field of the individual cycle.*

One metric that is commonly used to assess the performance of engines is the tumble ratio (TR), as defined in Section 3.5. This definition produces a single value that is positive for a velocity field that has a clockwise rotational direction for the coordinate system used in this study. The tumble ratio is dependent on the magnitude of the velocity vectors, their direction and their location in relation to the centre of mass. Figure 5.13 shows plots of TR for all three conditions, with dotted lines marking the timings of peak valve lift and valve closing.

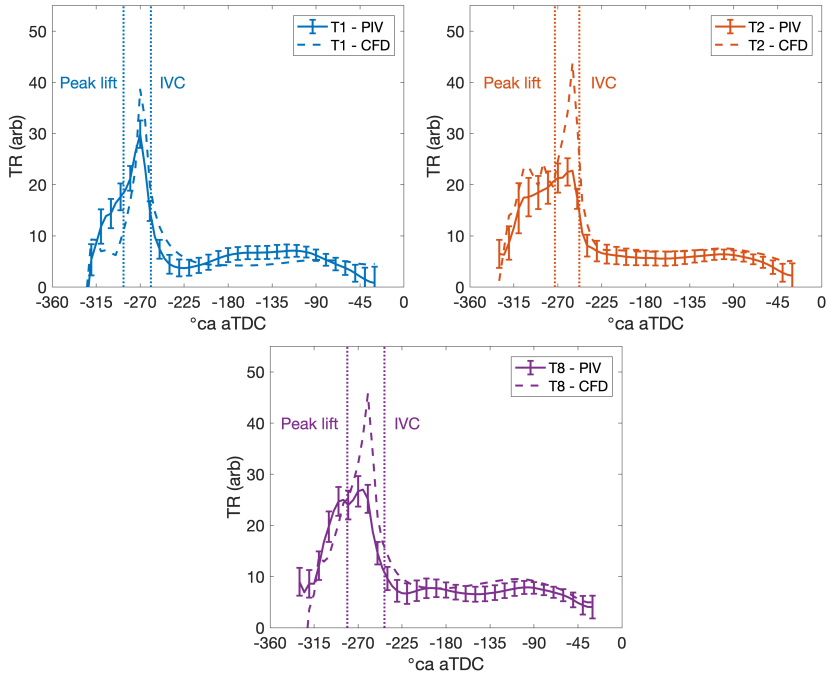

Figure 5.13 *Plots of tumble ratio (TR) for T1, T2 and T8. The dotted lines mark the timings of peak valve lift and valve closing. Markers of ± 1 standard deviation for the TR are shown for every 10th crank angle of the PIV flow fields.*

The main difference between the CFD and PIV results in Figure 5.13 is the large peak in the simulated TR values that occurs during the valve closing period for all conditions. These peaks correspond directly to the peaks of the spatially averaged WMI identified in Figure 5.10, which leads to the conclusion that the difference in TR between PIV and CFD is due to differences in the speed of the intake jet, as discussed previously.

It is evident that the difference in TR between CFD and PIV is significantly higher for T8 and T2 than for T1. On inspection of the CFD flow fields in Figure 5.11 (red arrows), the high-speed flow of the intake jet for T2 and T8 fills the entire upper, right-hand side of the field of view. In contrast, the CFD flow field for T1 has a stagnant region near the exhaust side of the cylinder head. This appears as a high value of the WMI because there are large differences between PIV and CFD velocity magnitudes in this region, as the PIV results do not have this region of slow flow. However, the stagnant region in the simulation results in a reduced value of TR, which agrees more closely with experiment, even though there is a difference in the structure of the flow fields. This is an example of how the detail in the flow fields can be lost through the use of spatially averaged conventional metrics, from which differences in the flow are inferred.

5.3.3 Peaks in the WRI at 240°ca bTDC

Dominant peaks at 240°ca bTDC in the plots of the CMRI (Figure 5.9) also feature in the plots of the WRI, shown in Figure 5.10 (top). These peaks occur for all conditions; however, they are noticeably larger for T1 and T2 in comparison to T8. It is worth noting that at this timing, the inlet valve has closed for all conditions. To investigate the cause of such differences in the flow fields between CFD and PIV, Figure 5.14 presents fields of the WRI for each condition at 240°ca bTDC with overlaid simulated and measured vector fields.

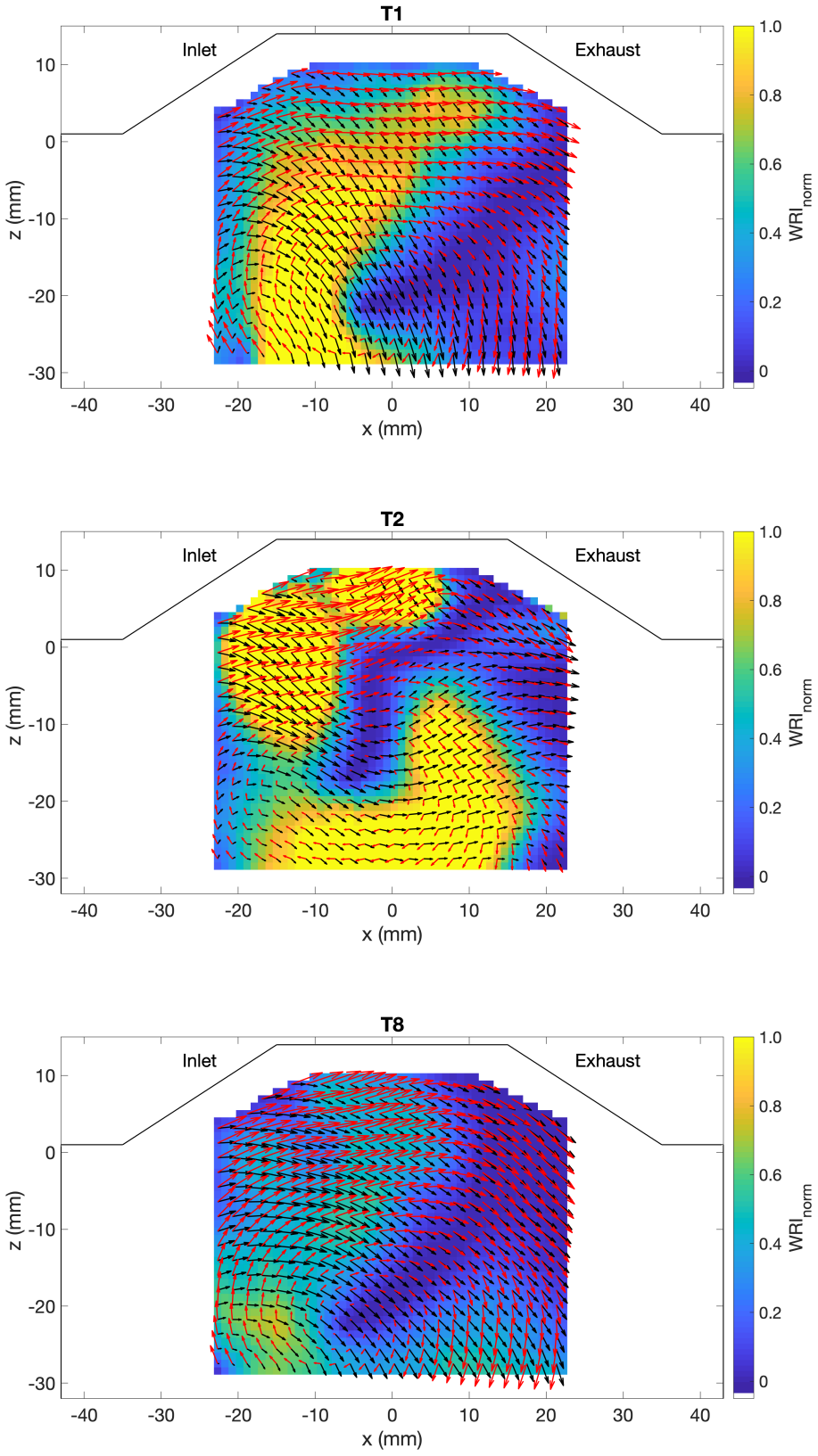

Figure 5.14 *. Fields of the WRI at 240°ca bTDC for T1, T2 and T8. The overlaid black and red arrows show the PIV and CFD vector fields.*

As expected from the spatially averaged results, the WRI fields demonstrate that there is a significantly greater misalignment between the simulated and experimental flow fields for T1 and T2, than for T8. It is interesting to note that, for all conditions, the simulations predict a very similar velocity field after IVC. Whereas, in contrast, the mean PIV flow fields for each condition display distinct differences. The simulated results show that after IVC, a strong tumble flow is setup for all conditions with some variation in the location of the main tumble vortex. Similarly, the experimental flow fields for T1 and T8 reveal a strong clockwise tumble motion. Although the main PIV tumble vortex is not visible in the experimental field of view at this time, by inspecting the direction of the vectors, it can be inferred that the tumble vortex for these points is located beyond the lower left-hand corner of the field of view. Relative to its corresponding simulation, there appears to be a greater offset between the location of the vortex centre for T1 than that of T8, which results in a greater misalignment for velocity vectors of greater magnitude. As discussed previously, the definition of the WRI penalises misaligned, high-speed vectors more than low-speed vectors. Around the centre of the CFD tumble vortex for both T1 and T8, the values of the WRI are relatively low, but as the distance from the vortex centre increases there is an increase in the weighting of the misalignment in the calculation of the WRI. The predicted and measured tumble vortices are closer for T8 than for T1; therefore, far away from the vortex centre, the high-speed vectors are more closely aligned, resulting in a lower WRI. In contrast, for T1, the offset between the tumble vortices is relatively large, which results in some high-speed velocity vectors 180 degrees misaligned and high values of the WRI.

The measured flow field for T2 has a distinctly different structure to those of T1 and T8. Instead of a large-scale tumble motion, there is a region of low velocity flow in the centre of the combustion chamber that interrupts the tumbling motion and results in large

differences in alignment between simulated and measured flow fields. On further analysis of the PIV flow fields, this feature appears for all conditions, but is dependent on the timing of IVC. For example, IVC for T1 occurs earlier than T2 and T8 (see Table 5.1 for details), therefore this feature appears earlier in the flow fields for T1. Figure 5.15 shows the evolution of the measured in-cylinder flow for T2 for a number of measurements after IVC.

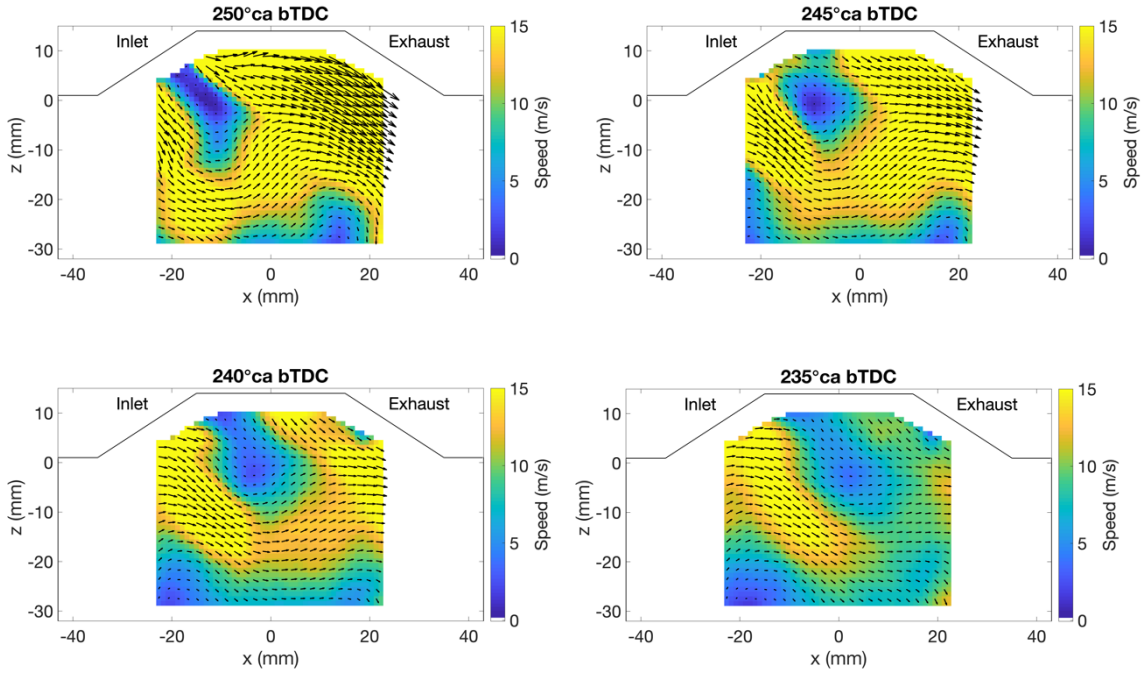

Figure 5.15 *Mean PIV velocity fields showing the evolution of the flow field for T2 from 250°ca bTDC to 235°ca bTDC (IVC occurs at 243°ca bTDC).*

IVC for T2 occurs at 243°ca bTDC, hence the flow field at 250°ca bTDC shows the flow field as the inlet valve is closing. The region of slow flow is initially located near the inlet valve. The flow fields at 245°ca bTDC, 240°ca bTDC and 235°ca bTDC show how the region of slow flow moves towards the exhaust and grows, directing the main tumble motion towards the centre of the cylinder. This is in contrast to the simulations, which predict that the tumbling flow follows the boundary of the cylinder head directly after IVC.

The origin of the region of the slow flow remains unclear; however, it could be due to out-of-plane motion and it could also be related to the spike in WMI discussed in the Section 5.3.2. For these test conditions, the inlet valves close very quickly, with a duration of approximately 30°ca between peak lift and the valve closing. In this time, the area through which the air is flowing decreases rapidly, which results in a burst of high velocity gas entering the chamber just before the valve closes. This region of high velocity gas is predicted by CFD and is what causes the spikes in tumble ratio as discussed in Section 5.3.2. However, similar spikes are not seen in the plots of measured tumble ratio, but small peaks do appear for T1 and T2 in plots of spatially averaged flow speed (shown in Figure 5.17 in Section 5.3.4). The measured intake jet is slower than the prediction, and so the detail is lost in the spatial average. Due to the three-dimensional annular shape of inlet jet as it enters the combustion chamber past the valve, a section cuts through the central tumble plane where the PIV measurement is made. This high velocity gas travelling straight through the measurement plane appears as a region of low velocity in the PIV flow fields. It disrupts the tumbling motion and deflects the bulk flow away from the cylinder head towards the centre of the combustion chamber. However, this is not the case for the CFD simulation, which predicts a uniform tumbling motion. This effect leads to the misalignment between the flow fields for some time after IVC for each condition, as captured by the WRI.

5.3.4 Increase in all metrics for T1 during the compression stroke

The plot of the spatially averaged CMRI (Figure 5.9) shows that the difference between simulated and measured flow fields for T1 increases during the compression stroke until approximately 115°ca bTDC. The opposite is true for T2 and T8, for which the match improves during the same period. The plots of the WRI and WMI (Figure 5.10) confirm

that over this period, the differences in both alignment and magnitude contribute to the increase in the CMRI.

Figure 5.16 shows plots of the WRI and WMI for T1 at 115°ca bTDC, as well as the corresponding CFD and PIV velocity fields. The PIV and CFD velocity fields in Figure 5.16 (c) and (d) show that the simulation underestimates the speed of the measured flow. The main tumble vortex for the PIV flow field is located near the bottom right-hand corner of the field of view, whereas the vortex centre for the simulated flow field is below the bottom edge of the field of view. These differences in the flow fields give rise to the increases in the WRI and WMI, and subsequently, the CMRI. The plot of the WRI shown in Figure 5.16 (a) shows a region of higher values slightly to the left of the PIV tumble vortex. This is due to misaligned vectors with relatively high velocities. At the centre of the PIV tumble vortex, the WRI values are low.

The plot of the WMI in Figure 5.16 (b) shows a region of high values on the inlet side of the measurement region. This corresponds to the region of biggest difference between flow speeds shown in Figure 5.16 (c) and (d), where the measured flow speeds are approximately double those predicted by CFD. The value of the WMI reduces towards the right-hand side of the field of view as the absolute differences in magnitude are small compared to the overall flow speeds in the measurement region.

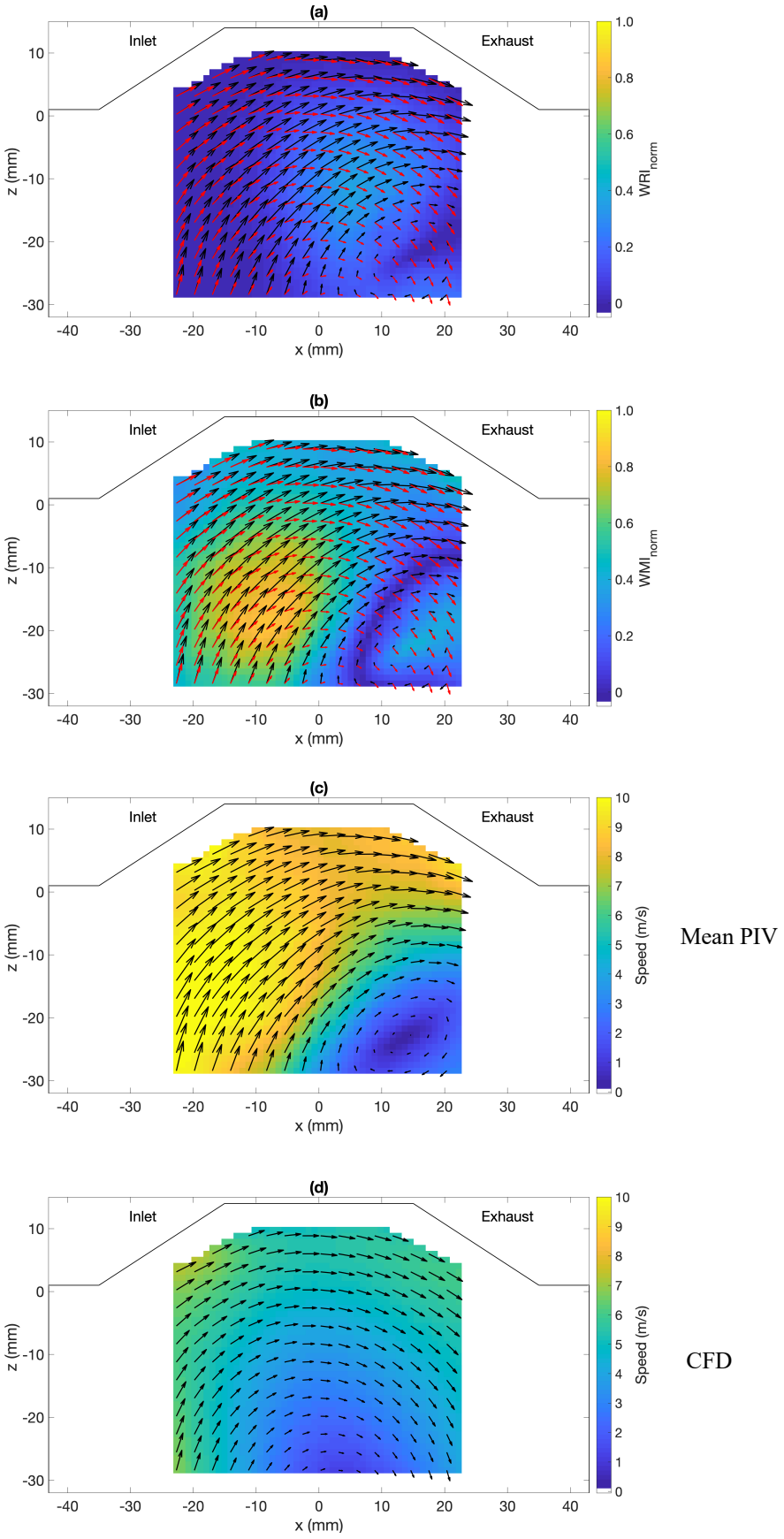

Figure 5.16 Plots of the WRI (a), WMI (b), and corresponding velocity fields for PIV (c) and CFD (d) for T1 at 115°ca bTDC (peak in the CMRI). The overlaid black and red arrows show the PIV and CFD vector fields respectively.

A conventional method of investigating the magnitude differences between simulated and experimental flow fields is the spatially averaged flow speed. This is plotted for all conditions in Figure 5.17.

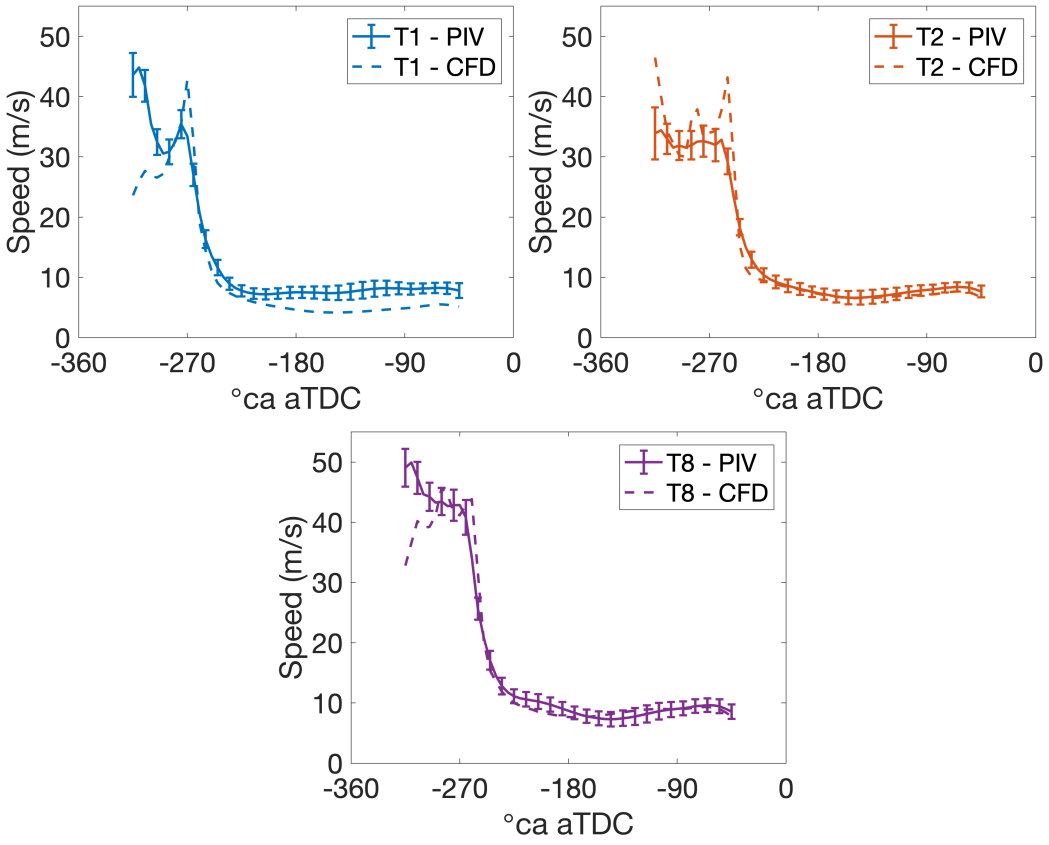

Figure 5.17 *Plots of spatially averaged velocity magnitude for PIV experiments (solid) and CFD simulations (dashed) for T1, T2 and T8. Markers show 1 standard deviation for every 10th crank angle for the PIV measurements.*

It is evident that the simulated flow speeds during the compression stroke for T2 and T8 are very well matched to the experimental results. However, there is a noticeable difference for T1, where the PIV flow speed is underpredicted by CFD. The simulated results suggest that the different inlet conditions for T1 result in a significant difference in the flow fields, not only in terms of flow speed, but also flow structure. Figure 5.18 shows the predicted locations of the main tumble vortex for each condition from 250°ca bTDC to TDC. By 250°ca bTDC, which is after IVC for T1 and just before IVC for T2 and T8, the bulk tumble

motion has been generated by the intake jet. For all conditions, the overall motion of the tumble centres follows a spiralling path that starts near the centre of the cylinder before being transported downwards and towards the intake by the action of the piston, and then upwards towards the exhaust side during the compression stroke, before finishing near the centre of the combustion chamber at TDC Although, the general trajectories of the tumble vortices are similar, there is a distinct difference for T1 in comparison to T2 and T8, which are almost overlapping during the compression stroke. The location of the vortex centre for T1 is similar to that of T2 at 250°ca bTDC, however the paths quickly diverge as the tumble vortex for T2 follows that of T8 in moving downwards with the piston. In contrast, the vortex centre for T1 does not travel towards the piston with T2 and T8 but remains higher in the cylinder for longer. As a result, the flow structure for T1 is considerably different to that of T2 and T8 early in the compression stroke.

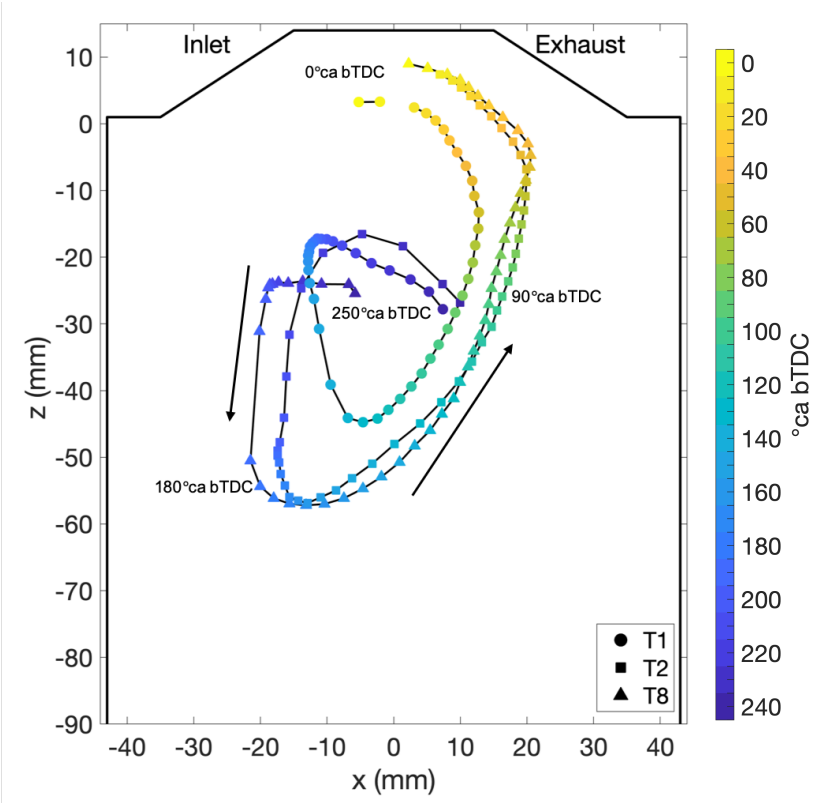

Figure 5.18 *Plots of the location of the main tumble vortices for the simulated flow fields from 250°ca bTDC to TDC, values every 5°ca.*

Due to the velocity weightings in the definitions of the WRI and WMI, and their normalisation to produce the CMRI, the final value that ranks the quality of the match between two velocity fields is only relative to the data that is used in the comparisons. Therefore, to put the results into perspective, Figure 5.19 shows equivalent plots to Figure 5.16, for T8, which has the lowest value of the CMRI (best match) at 115°ca bTDC. It is clear from the velocity fields in Figure 5.19 (c) and (d), that there is qualitatively very good agreement between the simulated and experimental results in terms of both magnitude and alignment. The black vectors are difficult to see as they are overlaid on the fields of WRI and WMI, which have very low values due to the well-matched flow fields. As a result, the spatially averaged values of the WRI and WMI, and CMRI are low, which demonstrates that the metrics can be used to quantitatively rank comparisons of flow fields.

Although there some differences between the measured flow fields of T1, T2 and T8 in terms of local flow speed, the flow structure is similar between the three test points. Comparison of Figure 5.16 (c-d) and Figure 5.19 (c-d) shows the differences between the measured and simulated flow fields for T1 and T8 at 115°ca bTDC; the measured flows are qualitatively similar, albeit with small differences in vortex location and flow speeds due to the different inlet conditions. However, there are significant differences in terms of flow speed and structure for the simulated flow fields, which are picked out by the CMRI.

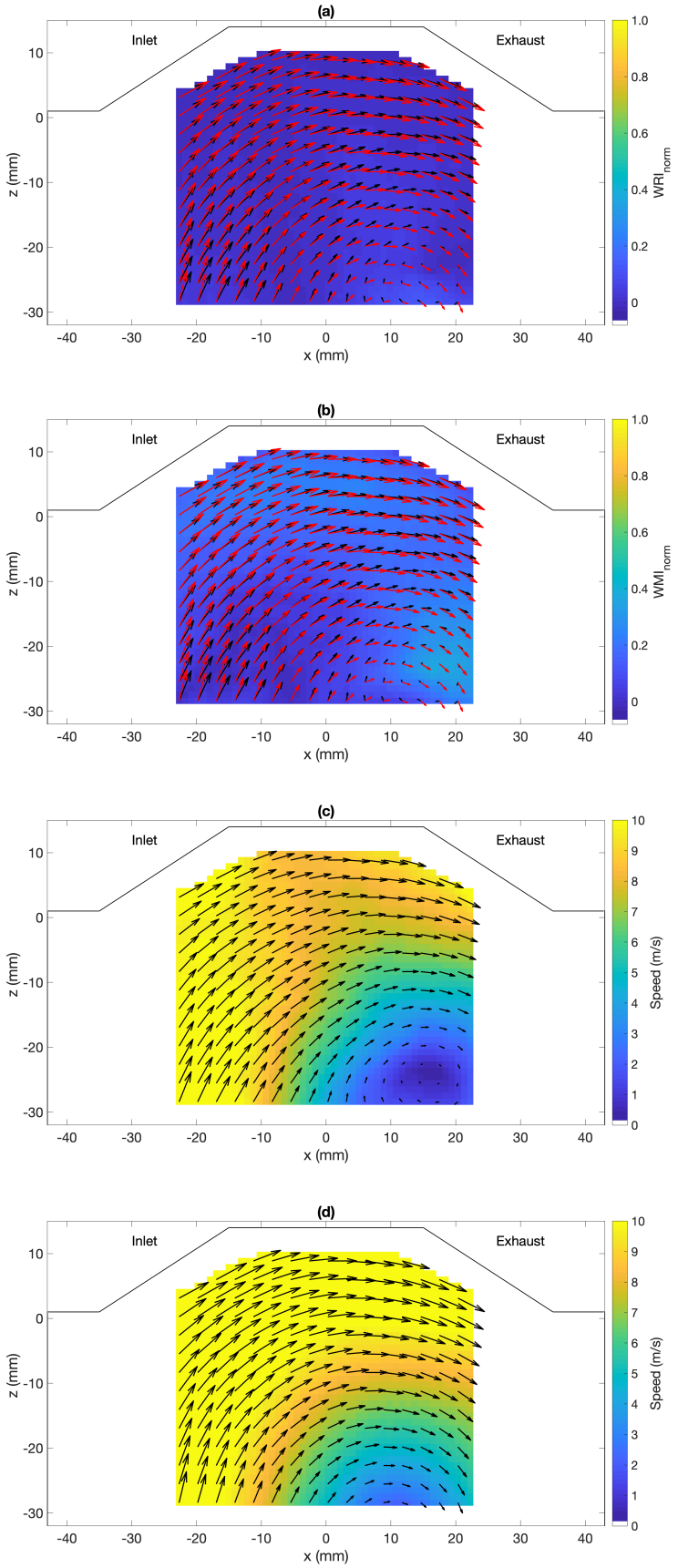

Figure 5.19 *Plots of the WRI (a), WMI (b) and corresponding velocity fields for PIV (c) and CFD (d) for T8 at 115°ca bTDC (lowest value of the CMRI). The overlaid black and red arrows show the PIV and CFD vector fields respectively.*

5.4 Comparisons of Individual Cycles

Up to this point the quantitative metrics have been used to directly compare the simulated flow field and the mean PIV flow field. However, calculation of the mean PIV flow field inherently removes the small-scale velocity fluctuations that are present in the flow fields of individual cycles. Although RANS simulations involve the solution of averaged equations and so do not resolve the smaller length scales, there may be an individual cycle that is a better representation of the simulated flow structure than the mean PIV field. It would be interesting to know where the CFD simulation lies within the distribution of the measured cycles. This may be especially important in the simulation of firing cycles where the RANS simulation only produces one cycle, from which no information can be gained about the variability of combustion. By comparing the CFD to individual cycles, it is possible to determine whether the simulation is predicting a flow field that is similar to an individual cycle that has resulted in fast or slow combustion. This could have a significant effect on the design of a new combustion system.

By calculating the CMRI between each individual cycle and the single simulated cycle, it is possible to rank the cycles based on how similar they are to the CFD in terms of flow speed and alignment. This makes it possible to select the individual cycle that is most similar to the simulation. An example of this process is shown in Figure 5.20, which displays flows fields at 90°ca bTDC for the simulated cycle, the mean PIV cycle, and the individual cycles that are most similar (cycle 9) and most different (cycle 115) to the simulation for T2 during the compression stroke.

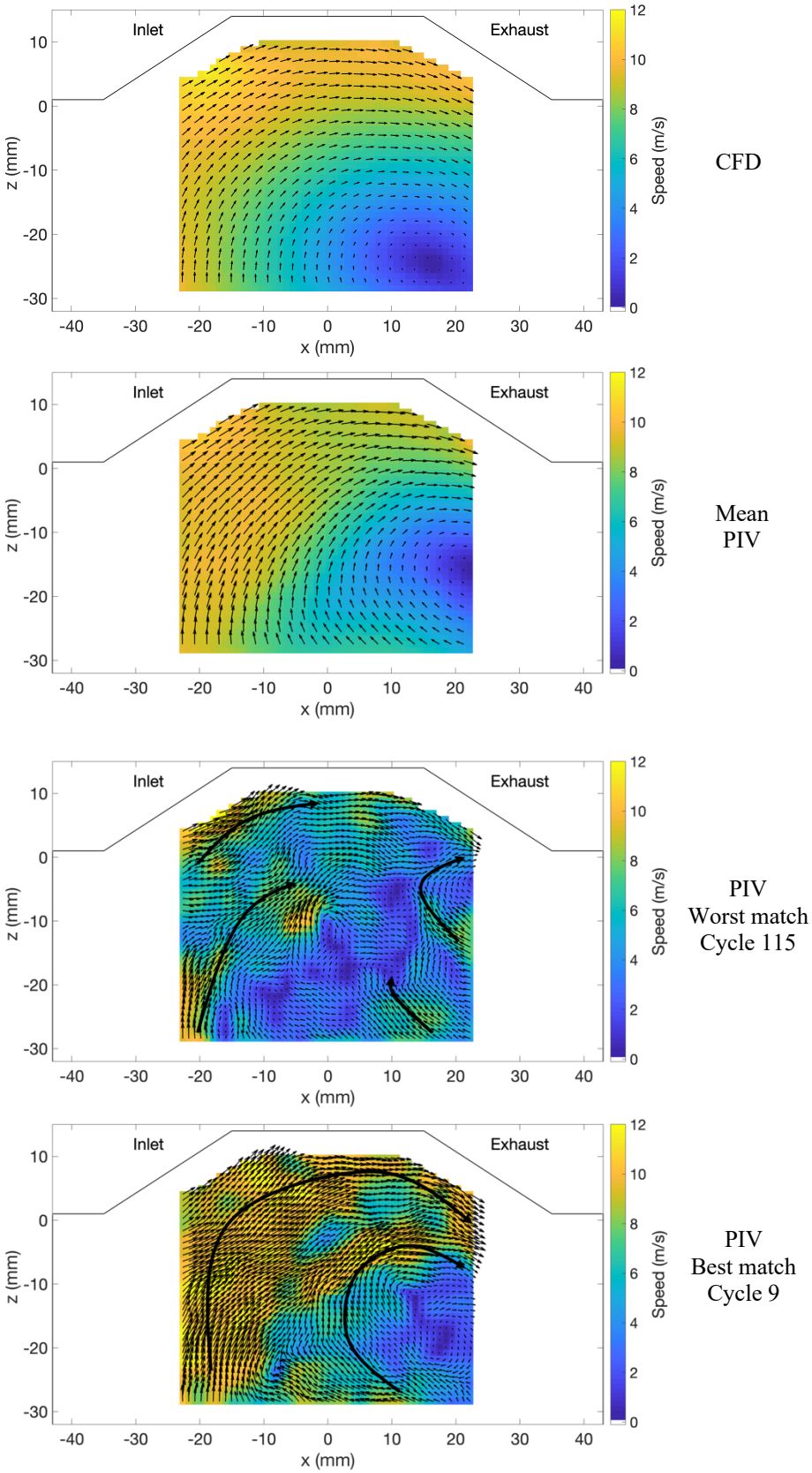

Figure 5.20 *Plots demonstrating the use of the quantitative metrics in comparing individual cycles (worst match - lower middle and best match - bottom) to the simulated cycle (top) and mean PIV cycle (upper middle). Flow fields are for T2 at 90°ca bTDC and the best and worst matches correspond to cycles 9 and 115 respectively. The overlaid black arrows indicate the overall flow motion. For the individual cycles, every vector is plotted to show the small-scale variation.*

Qualitatively, the simulated flow field and mean PIV flow field are well matched, with the simulation predicting slightly higher flow speeds. This reflects the spatially averaged flow speeds plotted in Figure 5.17, where the simulated flow speed lies within the variation of the measurements. In contrast, there is a noticeable difference between the simulated flow field and that of cycle 115; although there is an overall clockwise tumble motion, it is much less coherent than the simulation. The flow on the inlet side of the combustion chamber has significantly lower velocity and there is a region of relatively slow velocities in the centre of the field of view.

The flow field of cycle 9 is qualitatively a much better match to the simulation than cycle 115. Although the small-scale variation in the velocity vectors is clearly present, the overall flow structure is matched well in terms of speed and direction. The differences between the individual cycles and the simulated cycles are highlighted by the fields of *CMRI* in Figure 5.21.

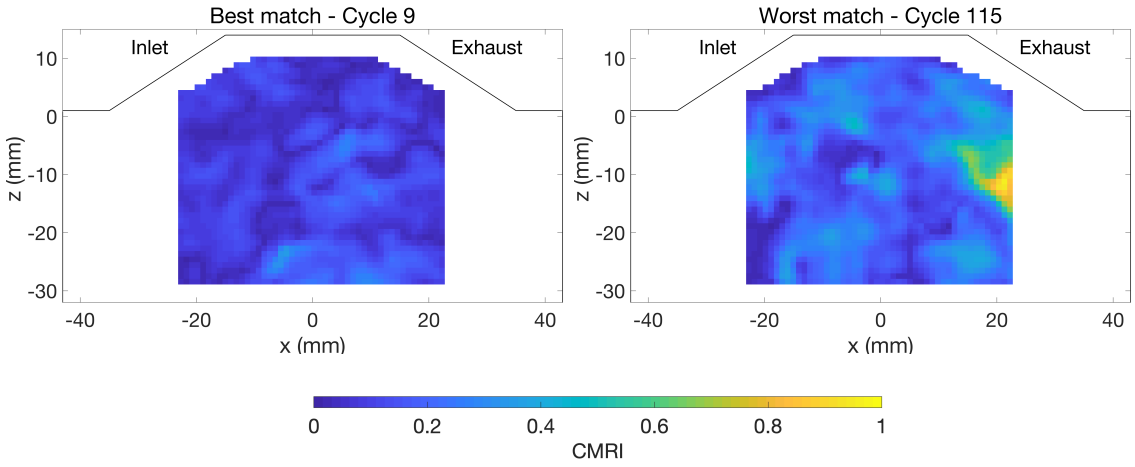

Figure 5.21 *Fields of the combined index (CMRI) quantifying the differences between cycles 9 (left) and 115 (right) (shown in Figure 5.20) and the simulated flow field at 90°ca bTDC. A low value of CMRI indicates a closer match between the individual flow field and the simulation.*

As expected, comparison of individual cycles results in the presence of smaller structures in the fields of *CMRI*, in contrast to the comparisons between the mean PIV cycle and the simulation shown in Figure 5.16. In Figure 5.21, it is clear that the field of *CMRI* for

cycle 9 is generally darker than that of cycle 115, which indicates a closer match to the simulated flow field. The main difference between cycle 115 and the simulation is highlighted by a yellow region on the right-hand edge of the field of view. On inspection of the flow fields in Figure 5.20, this patch of high *CMRI* is due to a region of flow in cycle 115 that is directed in almost the opposite direction to that of the simulation, travelling at similar velocities.

Figure 5.22 demonstrates the differences between the simulated and measured flow fields, including the mean flow field and cycles 9 and 115, by plotting histograms of the flow speed at each spatial location.

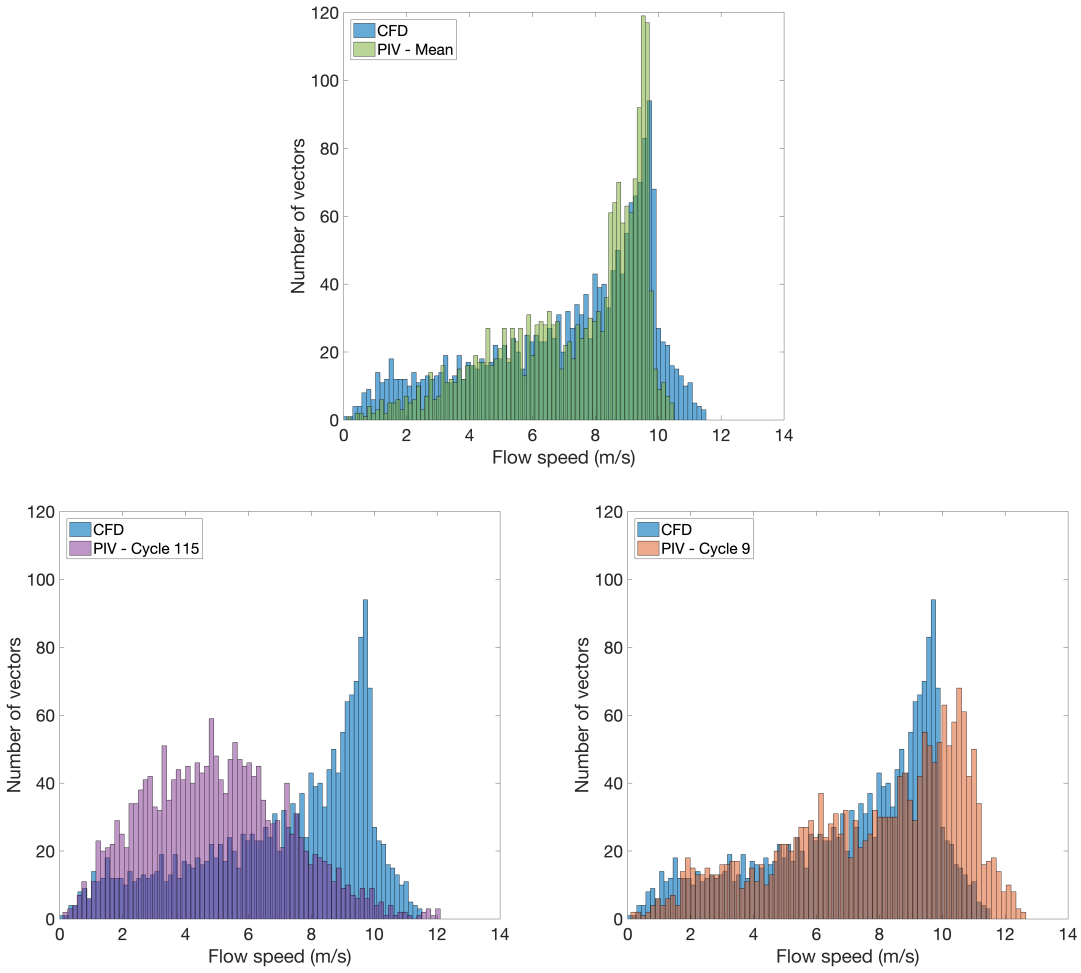

Figure 5.22 *Histograms comparing the flow speeds throughout the field of view for the flow fields shown in Figure 5.20.*

Although, the distribution of flow speeds for the mean PIV flow field has a similar shape to that of the simulation, the highest flow speeds are approximately 1.5 m/s slower. The distribution for cycle 115, which was the worst match to the simulation in terms of CMRI, is almost the opposite to that of the simulation; there is a broad peak at lower speeds, which reflects what is seen in the corresponding flow field. The shape of the distribution of cycle 9 is similar to that of the simulation; however, it is shifted to higher speeds, indicating a faster flow. Using the distributions of flow speeds alone might provide misleading results, as there is no spatial information about the location or direction of the flow vectors; it is possible that a flow field could have a very similar distribution of flow speeds but with a very different structure. However, these cycles have been selected using metrics that account for alignment and flow speed, hence there is confidence that a cycle with a well-matched distribution of flow speeds, is also similar in terms of flow structure.

5.5 Summary

In this chapter, novel metrics for quantifying the differences between vector fields have been used to validate RANS simulations of a DISI optical engine with high-speed PIV measurements. The normalised WRI and WMI, as well as the CMRI have been used to quantitatively compare the simulations and measurements for three different test conditions, T1, T2 and T8, which represent three points on the load map of a production engine.

The engine speed was 1500 rpm for T1 and T2, and 1750 rpm for T8. T1 was partially throttled, in contrast to T2 and T8, which were run at almost full throttle. The valve lift profiles varied between the test conditions. Experimental data were used as boundary conditions for the simulations, which were performed by engineers at Jaguar Land Rover.

Spatially averaged values of the WRI, WMI and CMRI provided insights into global differences between the simulations and measurements; the main differences of which were identified as:

- An overprediction of the speed of the intake jet during the valve closing period.
- A distinct region of slow flow that appears near the intake valve directly after IVC for all test conditions is observed in the mean PIV flow fields, but not predicted by the RANS simulations. The cause of this is thought to be out-of-plane motion from a burst of high velocity gas through the inlet valves during IVC.
- For a single test condition (T1), the RANS simulations underestimate the flow speeds and predict a different flow structure during the compression stroke than those of T2 and T8. In contrast, the PIV measurements suggest that the flow structures for all conditions are similar, although there are differences in flow speeds.

Although this study demonstrates the use of the WRI, WMI and CMRI for quantitative validation of CFD simulations, the metrics can be used to compare any vector fields. It was also noted that the use of mean PIV flow fields for comparison with RANS must be treated with caution, as the inherent variation in the measured flow fields is not considered. For this reason, the metrics were also used to determine how similar the flow fields of individual cycles are to the CFD simulations. It was found that there are individual cycles that differ significantly the mean PIV cycle. This could be important when validating CFD that is used in the design of future combustion systems.

6 The Effect of In-Cylinder Flow Motion on Combustion

6.1 Introduction

In-cylinder flow motion plays a vital role in mixture preparation and has been highlighted as one of the main causes of cycle-by-cycle variations in SI engines [39]. The complex interaction between the fuel spray and the in-cylinder bulk motion can have a strong influence on the homogeneity of the air-fuel mixture at the time of ignition, especially for stratified mode operation (see Chapter 1), and has been found to be a significant source of cyclic variation [165], [173]–[180]. Furthermore, the flow structure near the spark plug at the time of ignition also has a strong effect on the initial flame growth due its interaction with the spark plasma [71], [81], [181] and the subsequent convection of the early flame kernel [61], [182]–[190]. The turbulent nature of the flow not only causes distortion of the spark channel, affecting the timing and location of ignition, but it also interacts with the resulting flame kernel by wrinkling its surface, increasing its surface area and the rate of combustion. The bulk flow dictates the direction in which the flame is convected, which can either encourage or suppress flame growth; if the flame is transported quickly towards a flammable region of air-fuel mixture, combustion can proceed rapidly. However, excessive heat losses due to contact between the flame and the spark electrodes or cylinder walls may result in quenching and poor combustion performance. The period of initial flame growth that dictates the phasing of combustion is known to occur before the pressure rise due to combustion is observed on the in-cylinder pressure trace [191], therefore optical and numerical methods have been used to study its importance as a source of cyclic variation.

A range of optical diagnostic techniques have been used simultaneously to investigate in detail the effect of in-cylinder motion on combustion. Peterson *et al.* [192], [193] used high-speed PIV, Mie scattering and Planar Laser Induced Fluorescence (PLIF) to investigate the complex interactions between the in-cylinder flow field, fuel spray and resulting fuel distribution on combustion performance of a GDI engine in stratified mode. One of the main causes of partial burn cycles and misfires was slow flame propagation due to strong flow velocities that transport the flame kernel away from the flammable mixture. Additional studies simultaneously combined dual-plane OH-LIF and stereoscopic PIV to provide a detailed description of the three dimensional flame transport in a SI engine under homogeneous, stoichiometric conditions [194], [195]. A combination of high-speed PIV, spray imaging and flame imaging was used by Zeng *et al.* [196] to investigate the combustion performance of a GDI engine operated in stratified mode with E70 fuel. It was possible to link the flow direction and kinetic energy in a region near the cylinder head to the spray angle and subsequent combustion performance. High kinetic energy in this region combined with a less collapsed spray resulted in a high burn rate, whereas cycles with the opposite flow characteristics resulted in partial burns. In additional work, Zeng *et al.* [197] performed similar tests on the same engine, focussing on the use of intake-generated swirl to reduce cyclic variability. It was found that increased swirl ensured that the early flame kernel was consistently transported towards one spray plume that straddled the spark plug, which resulted in a more repeatable flame propagation. Without swirl, the spark plasma was randomly stretched either side of the spark plug, interacting with either spray plume and leading to higher variability in the direction of flame propagation, which occasionally resulted in partial burning cycles. A downside to the introduction of strong swirling flow was found to be an increase in soot emissions [198]. Subsequent tests using simultaneous PIV measurements, IR imaging and flame imaging revealed that the combination of swirl

and tumble resulted in an asymmetric distribution of the fuel vapour before combustion, which correlated spatially with soot luminosity. This series of work highlights the complexities of the interactions between the in-cylinder flow motion and fuel spray, and their effect on combustion performance.

Most commonly flow measurements are made using planar PIV at a single location in the combustion chamber, which is typically the central tumble plane or a slice of the swirl plane near the firing deck. However, work completed by Bode *et al.* [199], [200] investigated the effect of the three dimensional field on cycle-by-cycle variation in combustion performance in a stratified charge GDI engine. The first study used two high-speed lasers to measure flow fields in the central tumble plane and one mid-valve plane quasi-simultaneously. It built on work competed previously by Stiehl *et al.* [173], [174] which discovered that variations in the intake-generated tumble flow were the cause for variations in the second injection of a triple injection strategy. Bode *et al.* [199] used statistical correlation analysis to demonstrate links between regions of the flow and variations in IMEP, with maximum values resulting from flows that favoured early flame propagation. These regions of flow could be tracked back through the cycle to the mid-valve measurement plane. Krüger *et al.* [86] demonstrated how this analysis can be used in the design of new combustion systems by combining the experimental data with simulated CFD data to produce an updated intake geometry that resulted in reduced variation in the in-cylinder flow motion. In their second study, Bode *et al.* [200] improved the setup by using an acousto-optical-deflector to measure three tumble planes quasi-simultaneously (central and two mid-valve planes). Similarly, the focus of the work was cycle-by-cycle variations, however in this case, the engine was operated under lean homogeneous mode and used a tumble flap in the intake system to vary the in-cylinder tumble motion. The same statistical correlation analysis was

applied to the velocity fields from all three planes and it was found that increased tumble motion resulted in more favourable flow near the spark plug, transporting the early flame kernel towards the centre of the cylinder. This was due to a more central tumbling motion across all three measurement planes, in contrast to the low tumble case where the main tumble vortex was distorted and more variable.

Combining optical diagnostics with pressure-based measurements have been used frequently to explore the effects of the in-cylinder flow fields on combustion. A common method is to analyse the combustion performance of many cycles and sort them according to certain criteria such as peak pressure, angle of peak pressure, IMEP or burn durations calculated from heat release analysis (e.g. CA10, CA50, etc.). This allows slow-burning and fast-burning cycles to be selected for further analysis using optical methods in order to find correlations between local parameters, such as the in-cylinder flow speeds, and global, pressure-derived parameters. A thorough conditional analysis was performed by Schiffman *et al.* [201] in an attempt to find the main causes for cycle-by-cycle variations in a research optical SI engine operating in homogeneous mode using propane or methane as the fuel. High-speed PIV measurements were combined with in-cylinder pressure measurements and flame-imaging to correlate combustion indicators (CA10 and IMEP) with 416 metrics for a large range of test conditions. A pre-screening process reduced the number of metrics to the seven most significant before a multivariate statistical analysis was used to find which parameters were the leading factors affecting the early burn rate, characterised by CA10. Among the most important factors affecting the burn rate were the magnitude and direction of the velocity field, and the shear strength near the spark plug at the time of ignition. The parameter with the greatest effect on CA10 was found to be the time taken for transition from a laminar to turbulent flame, as estimated by OH* flame imaging. This typically

occurs before the in-cylinder pressure transducer detects a rise in pressure due to combustion (< CA01), and so highlights the importance of the ignition event and its effect on subsequent combustion. Zeng *et al.* [202] extended this study by studying the effect of in-cylinder flow on the delay from laminar to turbulent flame propagation using PIV and flame imaging in the swirl plane. Their conclusions agreed with [201] as they found that local flow conditions near the spark at the time of ignition correlated with CA10, with favourable conditions resulting in the flame travelling symmetrically through the combustion chamber. In a less extensive study than [201], Truffin *et al.* [203] used conditional analysis to investigate the leading causes of cycle-by-cycle variations using LES simulations of a homogeneous charge SI engine using propane as the fuel. One stable condition (stoichiometric mixture) and two unstable conditions (lean mixture and nitrogen dilution) were simulated and validated with experiment, before a multivariate statistical analysis was performed to find the leading causes of cyclic variation. They found that the direction and magnitude of the flow near the spark was one of the leading causes of variability in flame ignition and subsequent combustion variability.

Rather than focussing on the flow near the spark plug, Ding *et al.* [204] used a combination of Particle Tracking Velocimetry (PTV), PLIF and flame imaging to investigate the effect of in-cylinder flow speeds and fuel distribution on combustion in a small region near the surface of the piston in a PFI engine using iso-octane under stoichiometric conditions. Using conditional analysis, a region of flow near the piston surface was found to correlate with the peak pressure, which was used here as a proxy for burn rate. High velocity flows parallel to the surface of the piston resulted in faster combustion. The expanding flame then caused acceleration of these flows near the piston, which was found to have a dramatic effect on the boundary layer.

In this work, the effect of in-cylinder flow motion is investigated using a combination of pressure-based analysis, high-speed planar PIV measurements and flame imaging. Pressure-based combustion indicators are used to split the data into fast and slow burning cycles before a thorough investigation of the in-cylinder flow fields is performed to quantify links between flow-derived quantities and combustion performance.

6.2 Experimental Setup

Table 6.1 outlines the operating condition that has been used to investigate the effect of in-cylinder flow on combustion. For this, high-speed planar PIV was used to measure in-cylinder velocity fields under motored and fired operation. Simultaneous high-speed measurements of in-cylinder, inlet and exhaust pressures were recorded to monitor repeatability of conditions for each test.

6.2.1 Engine operating conditions

Figure 6.1 shows plots of the pressure traces and valve lifts for motored and fired operation.

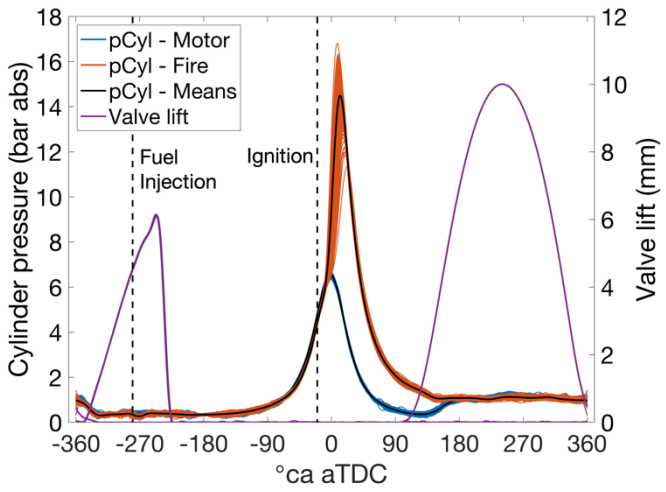

Figure 6.1 *Plots of the cylinder pressure traces for motored and fired operation. Inlet and exhaust valve lifts are also shown. All coloured lines are individual cycles to show the experimental variation and the black lines indicate mean values.*

Table 6.1 shows the engine operating conditions for the firing test.

Table 6.1 *Engine operating conditions.*

Engine speed (RPM)	1000
Manifold Air Pressure (kPa)	38
Air volume flowrate (L/s)	1.03
Intake air temperature (°C)	45
Coolant temperature (°C)	23
Inlet valve opening/closing (°ca aTDC gas exchange)	15 / 135
Inlet maximum valve lift (mm)	6.1
Exhaust valve opening (°ca aTDC gas exchange)	468 / 16
Fuel	Iso-octane
Injection pressure (bar)	200
Injection timing (°ca bTDC combustion)	280
Injection duration (ms)	0.61
Spark timing (°ca bTDC combustion)	20
λ	1.0
Average IMEPn (bar)	1.63
COV_{IMEPn} (%)	2.57
Average P_{max} (bar)	14.6
COV_{Pmax} (%)	6.32

Iso-octane at 200 bar was injected during the induction process at 280°ca bTDC to provide a homogeneous mixture. The engine was throttled, resulting in a manifold air pressure of 0.38 bar and an average peak pressure of 14.6 bar. The COV_{IMEPn}, an indicator of combustion stability, was 2.57%, which is within the acceptable limits typically set by automotive manufacturers. A test condition with low values of IMEP was chosen to preserve the quartz components; although rated to a peak pressure of 60 bar, they have been known to fail under much lower peak pressures. As discussed in Chapter 5, for the PIV measurements, a conservative estimate of the number of cycles required to produce a representative mean flow field is 300. Therefore, 300 cycles have been recorded in 3 tests

of 100 cycles each. Figure 6.2 shows a plot of net IMEP for the whole dataset, highlighting each test run.

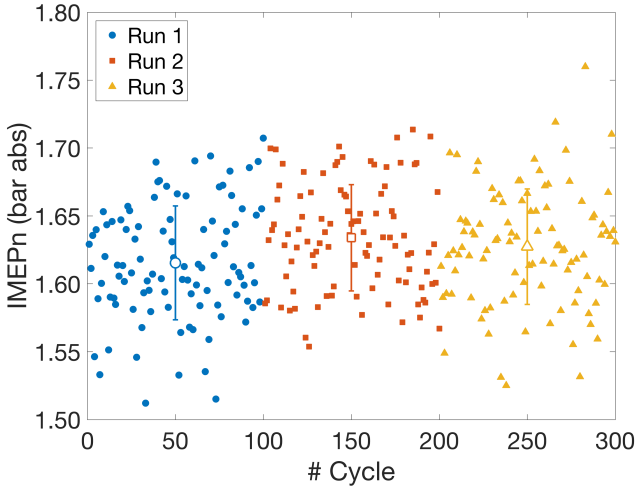

Figure 6.2 *Plots of net IMEP for300 cycles split into 3 independent runs of 100 cycles each. The mean for each test run is also shown displaying ± 1 standard deviation.*

6.2.2 PIV setup

Details of the PIV setup for these tests are shown in Table 6.2. See Chapter 3 for the general setup of the PIV system in the tumble plane.

Table 6.2 *Details of the PIV setup for all conditions.*

Range of recorded CAD (°ca bTDC combustion)	330 – 35
Number of cycles	300
Spatial resolution (mm)	1.96
Vector resolution (mm)	0.98
Field of view (mm^2)	45 × 40

Figure 6.3 shows the field of view in the combustion chamber for the PIV measurements and a schematic of the PIV measurement timings.

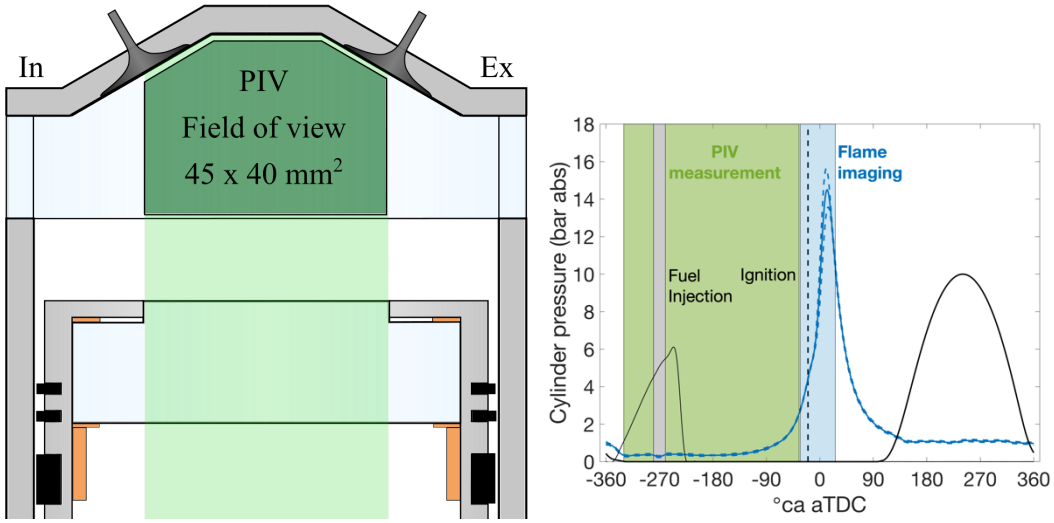

Figure 6.3 *Example of the PIV field of view for all measurements (left) and a schematic of the PIV measurement timing (right). For fired operation, the PIV measurements were not recorded during fuel injection (highlighted by the grey region) due to the large amount of scattered light from the laser sheet impacting liquid fuel droplets. The timings of flame imaging are highlighted by the blue region.*

Velocity measurements were made under both motored and fired operation. For fired operation, PIV measurements were unavailable during fuel injection, from 280 to 265 °ca bTDC. During this period, the scattered light from the seeding particles is overpowered by the large amount of scattered light from the liquid fuel droplets. The d*t* was optimised iteratively for each crank angle, ensuring that the maximum particle displacement was less than 8 pixels (1/4 of the 32 × 32 pixel interrogation window). The processing procedure is described in Chapter 3.

6.2.3 Flame imaging

Flame images were captured using a high-speed CMOS camera (Photron FastCam PCI-1024) at an acquisition frequency of 6 kHz, resulting in an image every 1°ca from 33°ca bTDC to 26°ca aTDC. The schematic shown in Figure 6.4 demonstrates the imaging setup for capturing flame images.

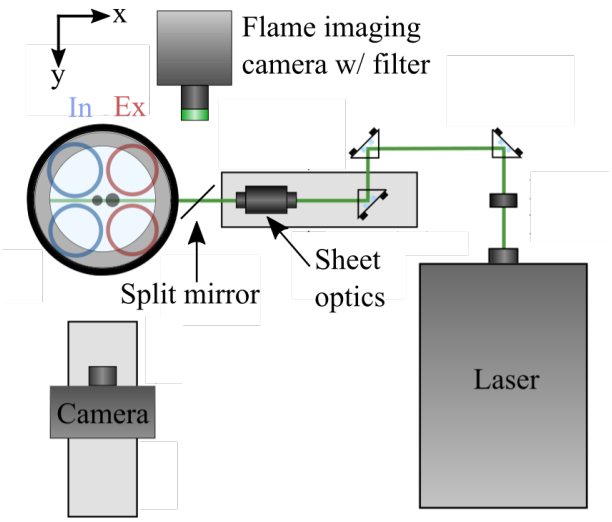

Figure 6.4 *Schematic of the imaging setup used for the simultaneous combustion imaging and PIV measurements.*

.

Flame images were captured from below the combustion chamber using the 45° mirror and quartz piston window. As the PIV laser also enters the combustion chamber from this direction, a split mirror was required to reflect the light from combustion onto the second camera, while also allowing the PIV laser sheet to safely pass. The laser sheet impacted the cylinder head along the central tumble plane, which resulted in a very strong reflection that is directly imaged by the flame imaging camera. In order to prevent damage to the camera sensor, a filter was used to reduce the intensity of the scattered laser light, which resulted in images of low intensity. The camera was triggered by a TTL pulse from the engine ETCS system, which was logged to ensure synchronicity between the PIV and pressure measurements.

The general schematic for processing the combustion images is shown in Figure 6.5. A background image is subtracted from the raw image to remove any scatter present from the impacting laser sheet. The image is then masked to remove regions that are blocked by the piston. An adaptive thresholding method is used to binarise the flame and identify its boundary, which is then smoothed using a Gaussian filter. The resulting mask is then

reapplied to the background subtracted image and overlays are added to show the progress of the flame in the combustion chamber.

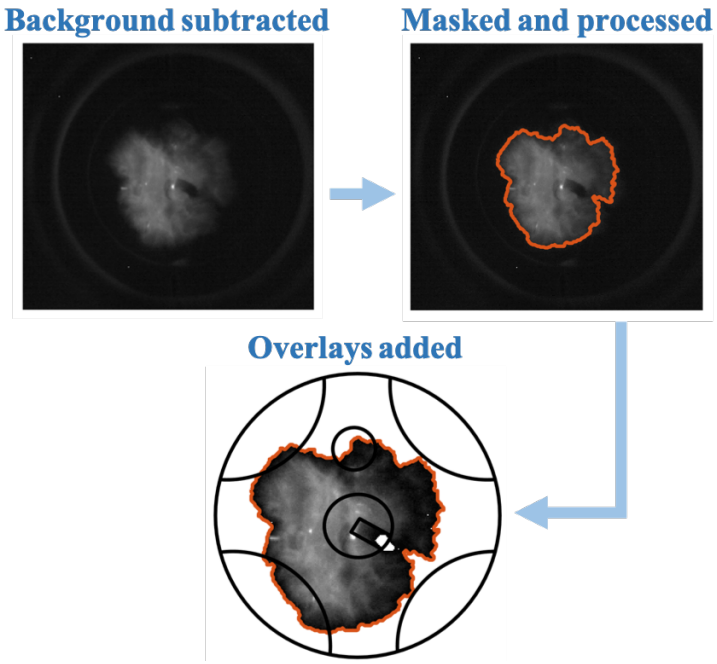

Figure 6.5 *A schematic demonstrating the processing of the flame images used in the following analysis.*

6.3 Results and Discussion

The objective of this work is to investigate the effect of the in-cylinder flow on the rate of combustion by combining pressure-based combustion indicators, in-cylinder velocity measurements and flame imaging. Before the fired results are presented, the differences between the flow fields under motored operation and those with fuel injection and combustion are discussed.

6.3.1 The effect of fuel injection and combustion on in-cylinder flow structure

For the velocity measurements under motored and fired operation, the boundary conditions were held constant. However, for the firing case, the in-cylinder conditions are likely to be

different due to fuel injection and the presence of exhaust gas residuals in the combustion chamber during induction. Furthermore, the temperature of the bulk gas temperature is higher by approximately 100 K, as indicated by previous thermometry measurements in this engine [77]. Figure 6.6 shows plots of ensemble averaged, spatially averaged mass-specific kinetic energy (defined in Chapter 3) of the flow throughout the cycle with markers indicating the mean ± 1 standard deviation for both motored and fired conditions. This is a useful global parameter to determine large differences in the flow speeds between tests, however it does not provide any information about differences in flow structure.

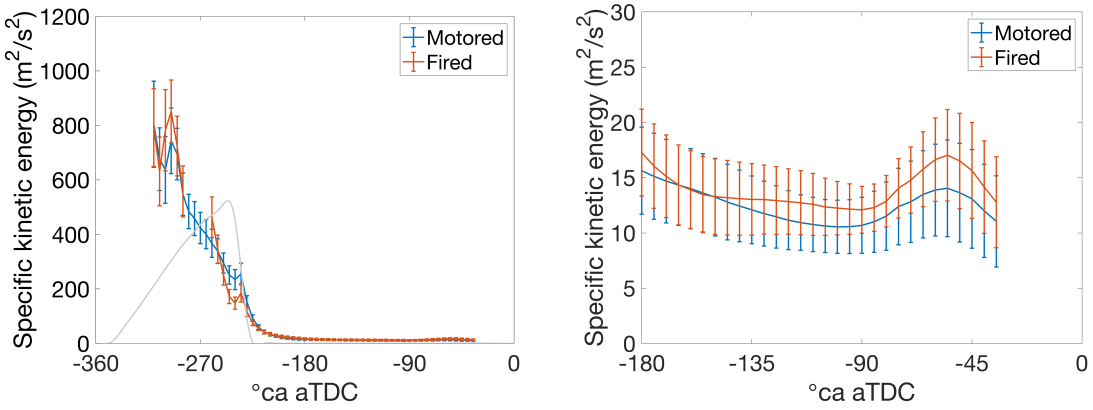

Figure 6.6 *Plots of the ensemble averaged, spatially averaged kinetic energy for all cycles under motored and fired operation. Due to the large difference in flow velocities throughout the cycle, the compression stroke is aslo shown in detail on the right. Markers indicate ±1 standard deviation about the mean. Valve lift is shown to highlight the higher flow velocities due to the high-speed intake jet.*

The left-hand plot also shows the valve lift trace to highlight the period where the inlet valves are open. For both motored and fired cases, the flow velocities are significantly higher while the inlet valves are open, due to the presence of the intake jet. For PIV measurements immediately after the opening of the inlet valve, the distribution of seeding particles is highly variable as there has not been sufficient time for the oil droplets to be transported throughout the field of view. Therefore, the velocity measurements from 330°ca bTDC to 315°ca bTDC have been omitted.

The fuel spray prevented velocity measurements from 280°ca bTDC to 265°ca bTDC for the firing cases. As discussed previously, any differences in flow kinetic energy between the two cases are due to the effects of combustion and/or fuel injection. Therefore, it would be useful to separate these effects by measuring the flow fields with fuel injection only. However, this experiment was performed for a different test condition using a similar valve lift profile, and it was found that the fuel condenses and forms dense clouds that prevent PIV measurements for a considerable portion of the cycle. This is demonstrated in Figure 6.7, which shows plots of the in-cylinder pressure trace and a raw image of the condensation cloud.

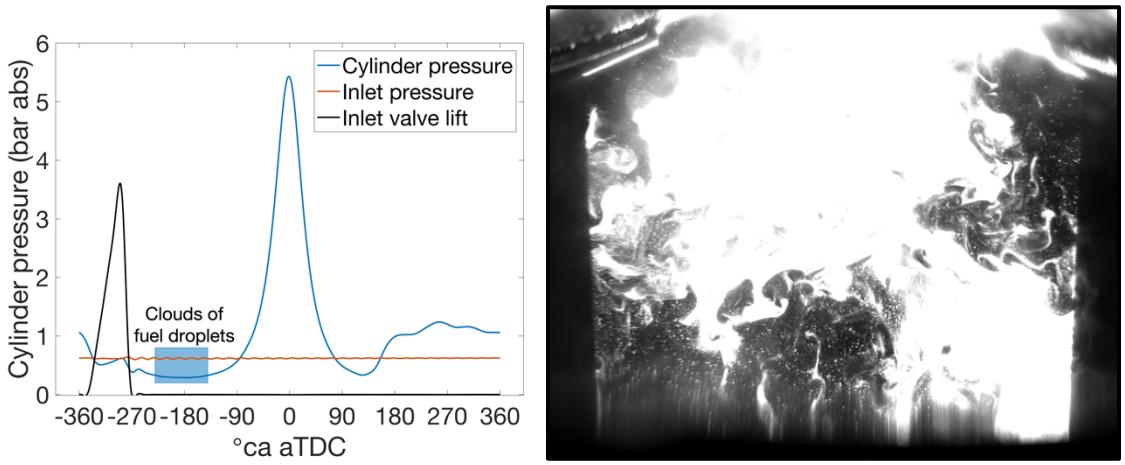

Figure 6.7 *Plots of the mean in-cylinder and intake pressures (top) and an example of a raw image of the condensed fuel clouds due to the effect of early inlet valve closing (right).*

As the inlet valve closes during the induction stroke, the in-cylinder pressure decreases to a minimum value of 0.285 bar due to the downward motion of the piston. The reduction in pressure and temperature in the cylinder causes dense clouds of fuel to condense, which scatter the laser light much more strongly than the oil droplets and so prevent any velocity measurements for a considerable duration of the cycle. This phenomenon did not appear during fired operation as in-cylinder temperatures are approximately 100 K higher [77].

On inspection of the plots of spatially-averaged kinetic energy in Figure 6.6, there is a noticeable difference in the flow kinetic energy between the motored and fired cases directly after fuel injection. However, at 285°ca bTDC, immediately before fuel injection, the kinetic energy of both flows is almost equal. This suggests that the difference immediately after fuel injection is due to the influence of the spray. The kinetic energy of the flow for fired operation is initially greater than for motored operation, but then decreases at a faster rate as the valve closes. To investigate any spatial differences between motored and fired operation, the ensemble averaged flow fields at 260 and 255°ca bTDC are shown in Figure 6.8.

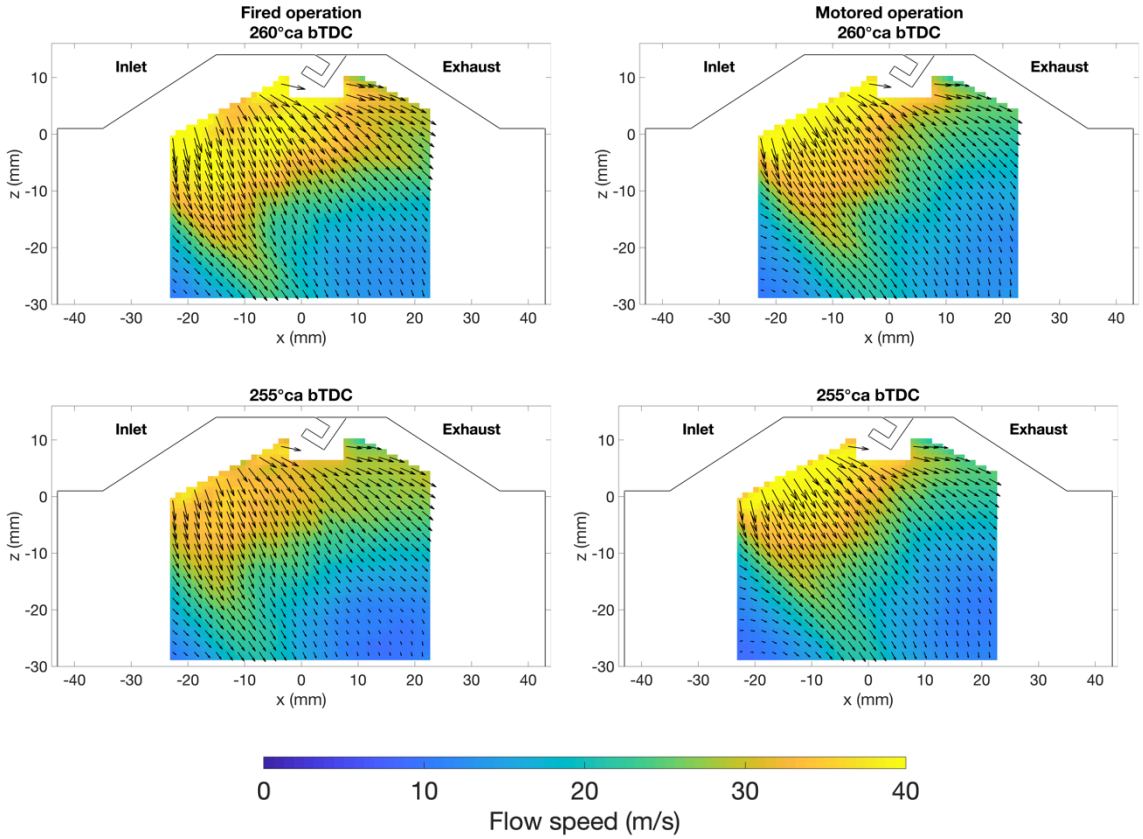

Figure 6.8 *Ensemble averaged flow fields for both fired (left) and motored (right) operation at 260 and 255°ca bTDC demonstrating similar flow structures after fuel injection.*

There are no obvious differences in flow structure between fired and motored operation, which is dominated mainly by the intake jet with the flow angled from the inlet valves to

the bottom right of the field of view. Fuel injection appears to only have an effect on the magnitude of the flow velocity, which is initially greater for fired operation, but rapidly dissipates.

For both motored and fired cases, as the valves closes, there is a sudden increase in kinetic energy at 235°ca bTDC this is due to a small pocket of high-speed gas that enters the combustion chamber due to the short duration of the valve closing period, also seen for similar valve lift profiles in Chapter 5. Throughout the remainder of the induction stroke, the kinetic energy of the flow in the field of view decreases. The plot on the right-hand side of Figure 6.6 focusses on the compression stroke, as this is hidden in the left-hand image due to the difference in ranges of flow speeds between the induction and compression strokes. By the latter stages of the compression stroke, the differences in kinetic energy between motored and fired operation that were observed directly after fuel injection have largely disappeared. For the fired case, the flow kinetic energy is slightly greater than that of the motored case, but it lies within the variation of the motored dataset. Work investigating the effect of fuel injection on in-cylinder flow by Chen *et al.*[205] and Zhuang *et al.*[206] also found that direct injection of fuel early in the cycle does not result in significant differences in the in-cylinder flow field by the end of compression.

To demonstrate the general flow structure for fired operation, Figure 6.9 shows a selection of ensemble-averaged flow fields from throughout the compression stroke.

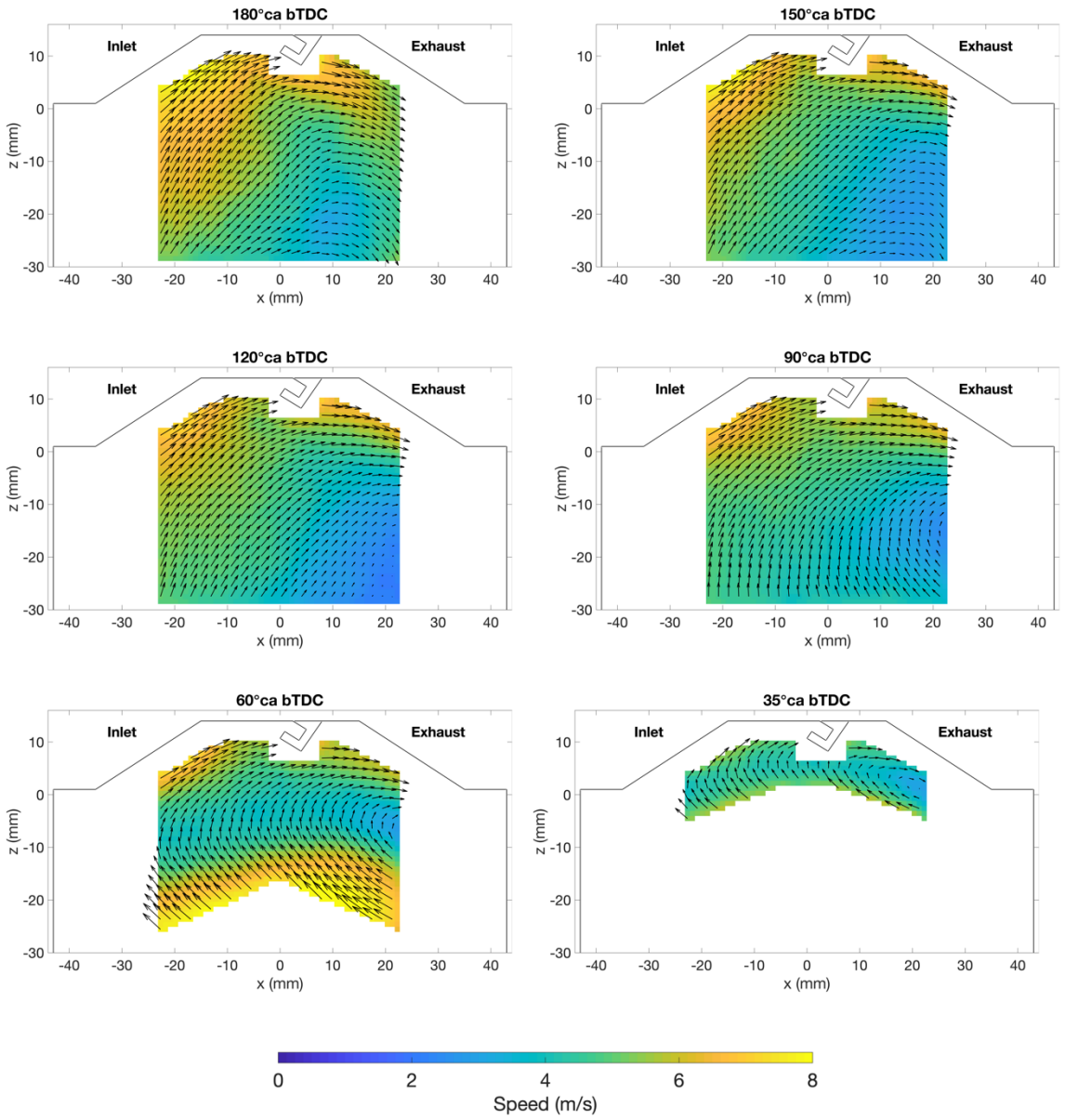

Figure 6.9 *Vector fields showing the flow development after the inlet valve has closed for fired operation. Every other vector has been plotted for clarity.*

A strong tumbling motion is set up by the induction process and as the cycle progresses, the tumble vortex moves from the inlet to the to the exhaust side of the field of view. By 90°ca bTDC, it has started to move upwards as the piston travels towards the cylinder head. At 35°ca bTDC, the digital mask applied during PIV post-processing has removed the regions of the field of view where the piston feature has blocked the scattered light from the oil droplets. It is worth noting that the laser sheet is located in the central tumble plane and enters the combustion chamber through the flat piston window, midway between the

piston features. Therefore, the vectors that appear to be coming from the solid surface of the piston feature, are in reality located in the central tumble plane where the lower region of the sheet has been blocked from view by the piston. At this time, the mean flow fields possess a clockwise rotating motion with the bulk flow travelling across the spark plug from the inlet to exhaust.

Although inspection of mean flow fields is a useful way of observing the general flow structure for given inlet conditions, for investigation into cyclic variation, a more detailed analysis of the flow fields of individual cycles is required.

6.3.2 The effect of in-cylinder flow on combustion

General flow characterisation

As discussed in Section 6.1, a common method for identifying flow features that influence combustion involves the combination of flow field analysis and in-cylinder pressure measurements. The in-cylinder pressure trace provides an independent method of identifying cycles that differ in terms of rate of combustion, which can then be used to perform conditional analysis on the velocity measurements. One of the simplest pressure-derived combustion indicators is the angle at which peak pressure occurs, and this has been used in this work to identify fast and slow burning cycles.

In a first attempt to identify important flow features that affect combustion, it is useful to take the extremes of the dataset and search for noticeable differences between the corresponding flow fields. This provides a starting point from which to investigate statistically significant flow features that influence the rate of combustion. The left-hand plot in Figure 6.10 shows in-cylinder pressure traces for all 300 cycles (grey lines), two of

the fastest and slowest burning cycles (blue lines and red lines) as indicated by the angle of peak pressure, and the cycles with the highest (purple line) and lowest (yellow line) spatially averaged kinetic energy throughout the compression stroke. The right-hand plot shows the corresponding spatially averaged kinetic energy.

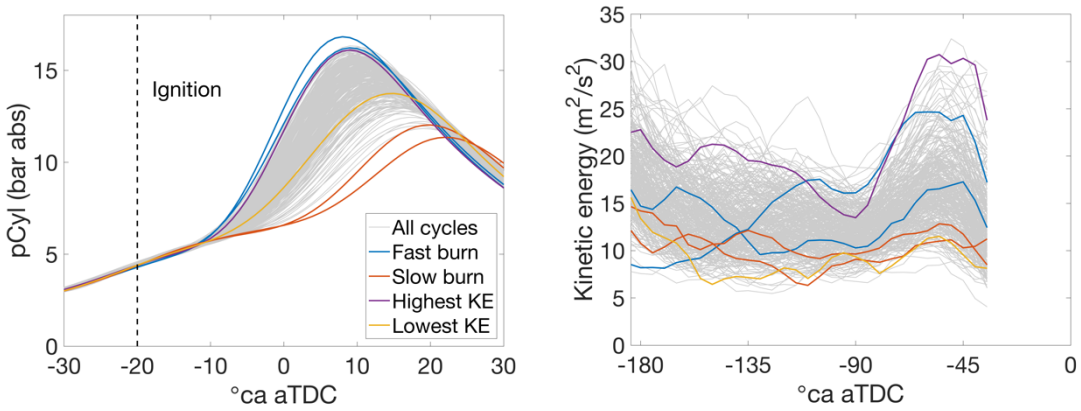

Figure 6.10 *Plots of in-cylinder pressure (left) and spatially averaged kinetic energy (right) for the two cycles with the fastest combustion (blue lines), slowest combustion (red lines), and the cycles with the highest (purple line) and lowest kinetic energy (yellow line).*

The right-hand plot in Figure 6.10 shows the considerable variation in the flow kinetic energy for the whole dataset. It is clear that cycles with the highest kinetic energy near the end of the compression stroke do not necessarily result in the fastest combustion. Although the two slow burning cycles both appear to have lower kinetic energy throughout the compression stroke, one of the fast burning cycles has comparable kinetic energy at 35°ca bTDC. The cycle for which the flow has the highest kinetic energy throughout compression is one of the fastest burning, and the cycle with the lowest kinetic energy is relatively slow burning.

Although kinetic energy is a useful metric for indicating the activity of the in-cylinder flow, it provides no spatial information about the location of the kinetic energy in the combustion chamber. An important feature of the flow fields is the magnitude and direction of the velocity vectors in relation to the spark plug at the time of ignition. Figure 6.11 shows

vector plots of the in-cylinder flow field at 35°ca bTDC (15°ca before ignition) for the same cycles shown in Figure 6.10.

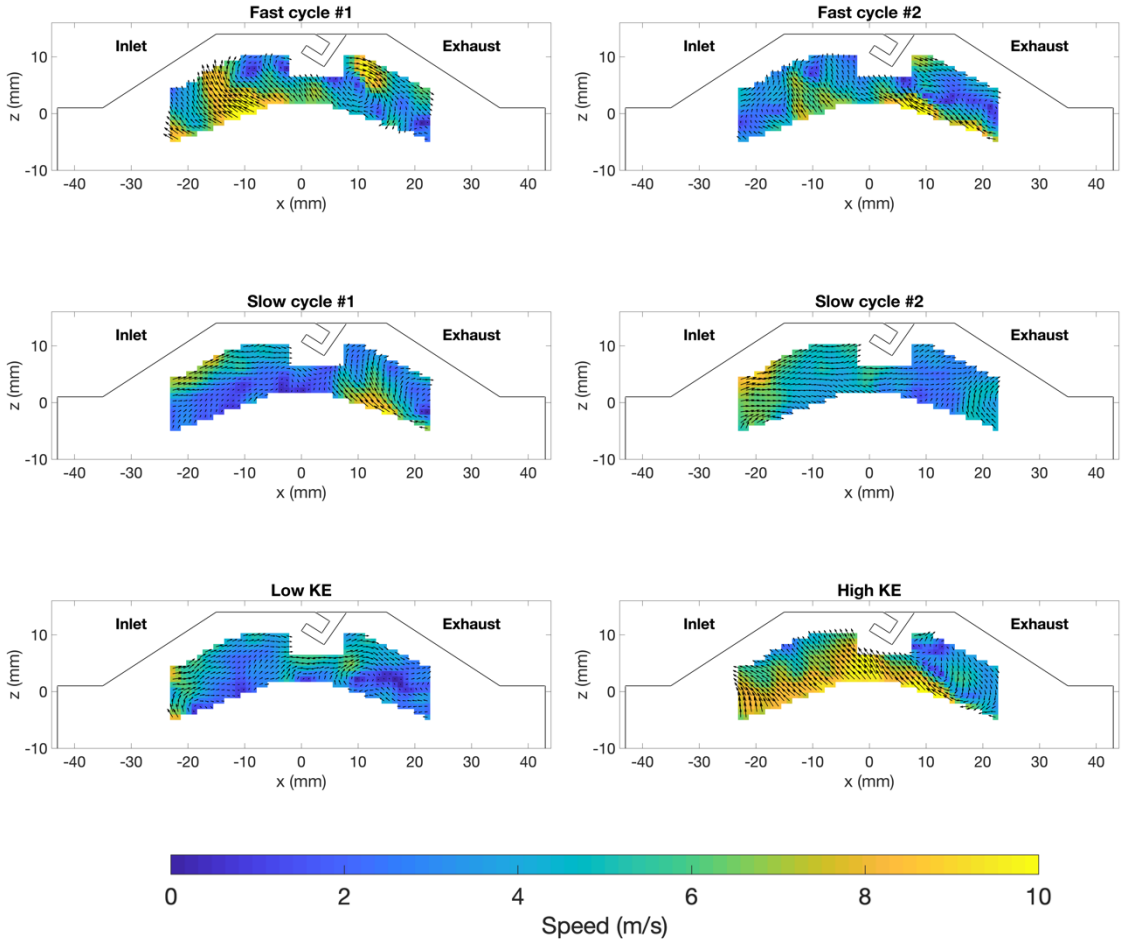

Figure 6.11 *Plots of the in-cylinder flow fields for the two cycles with the fastest combustion (top), slowest combustion (middle) and the cycles with the highest and lowest kinetic energy (bottom) at 35°ca bTDC, 15°ca before ignition.*

The flow fields reflect the plots of spatially averaged kinetic energy with the slow burning cycles containing flow speeds that are 20% slower on average than the fast burning cycle with high kinetic energy (Fast cycle #1). The flow speed of other fast burning cycle (Fast cycle #2) is very similar to that of the slow burning cycles, however the flow structure near the spark plug is significantly different; for the fast burning cycle, the flow is directed towards the inlet port. In contrast, the flow of the slow burning cycles is travelling parallel to the cylinder head from inlet to exhaust, across the spark plug. Similar features can also

be seen for the other fast burning cycle and the cycles with the highest and lowest kinetic energy, corresponding to relatively fast and slow rates of combustion.

Conditional analysis

Inspecting individual cycles at either extreme of the dataset in terms of rate of combustion maximises the opportunity of observing flow features that influence combustion. However, due to the nature of cyclic variation in DISI engines (as seen in the pressure trace and spatially averaged kinetic energy in Figure 6.10), meaningful conclusions can only be drawn from statistical analysis of the whole dataset. For this reason, the following analysis reduces the dataset of 300 cycles into 3 subsets of 30 cycles each, which represent the fastest and slowest 10% in terms of burn rate as well as the most average 10%, denoted here as 'medium burn'. Figure 6.12 shows these subsets using the in-cylinder pressure trace overlaid on all the cycles of the dataset.

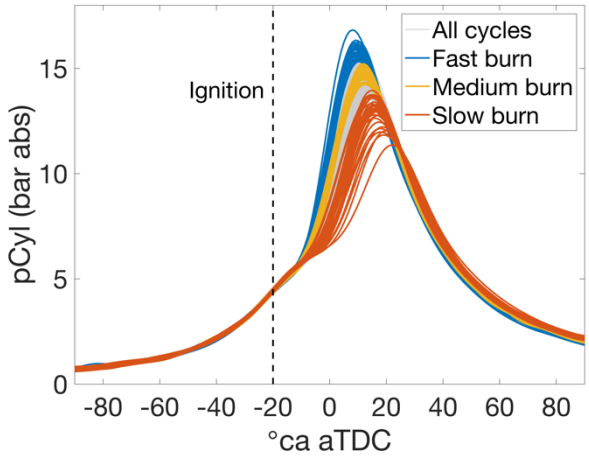

Figure 6.12 *Plots showing the cycles selected for the conditional analysis of the velocity measurements using the angle of peak pressure as an indicator of the rate of combustion.*

In the same way, the corresponding velocity measurements are reduced into subsets of fast, medium and slow burning cycles. Ensemble averages and associated statistics of flow-derived parameters can be calculated and compared, as shown in the left-hand plot of Figure 6.13, which displays ensemble averages of the kinetic energy for fast, medium and

slow burning cycles on a background of all individual cycles and their ensemble mean. The right-hand plot shows how the peak pressure, which can be treated as an indicator for the rate of combustion, is related to the spatially averaged kinetic energy, averaged throughout the compression stroke.

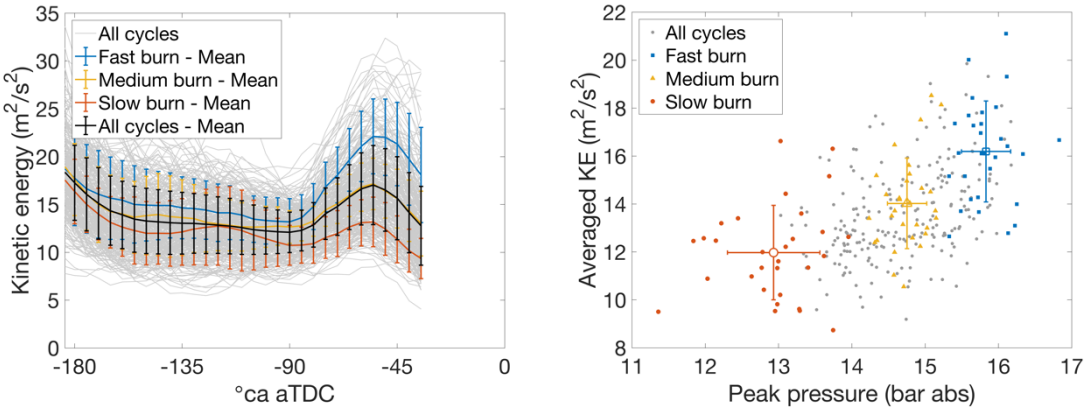

Figure 6.13 *Plots showing the spatially averaged kinetic energy (left) of in-cylinder flows for the ensemble averages of 30 fast burning cycles (blue line), 30 slow burning cycles (red line), 30 cycles with average burn rates (yellow line) and the average of all cycles (black line). On the right, mean kinetic energy of the conditioned datasets are plotted against peak pressure. Markers indicate 1 standard deviation of the mean.*

On inspection of both plots, there appears to be a trend indicating that cycles with higher kinetic energy later in the compression stroke result in a faster burn rate, and the opposite for cycles with lower kinetic energy. It is also worth noting that the ensemble average of the kinetic energy for the cycles with the medium burn rate agrees well with the ensemble average of all cycles, which indicates that the mean of the medium burn subset is representative of the mean of the whole dataset. Furthermore, the fact that there is a transition from fast to medium to slow burning cycles in terms of spatially averaged kinetic energy suggests that there is link between burn rate and in-cylinder flow. However, it is clear from the right-hand plot, that there is no statistically valid correlation between kinetic energy and peak pressure on an individual cycle basis, which suggests that kinetic energy alone is not the only factor involved in dictating the rate of combustion. As discussed previously, the location and direction of regions of flow with high kinetic play an important

role in ignition and the development of the early flame. Therefore, in order to determine features of the flow that influence the rate of combustion, the spatial information of the flow fields must be considered. Figure 6.14 shows the progression of the ensemble-averaged flow fields for fast and slow burning cycles from 65°ca bTDC to 35°ca bTDC.

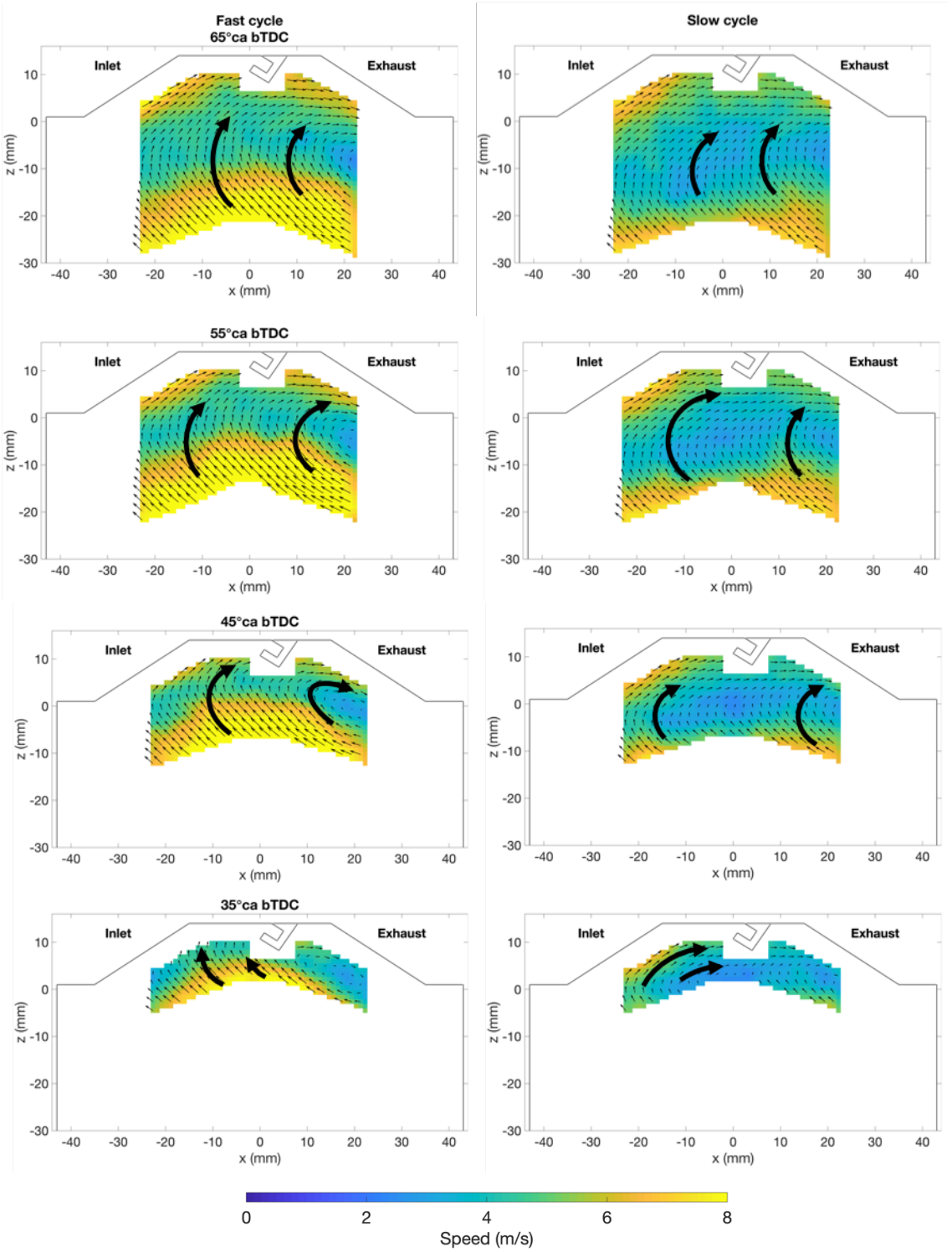

Figure 6.14 *Plots showing the progression of the mean in-cylinder flow fields of 30 fast burning cycles (left) and 30 slow burning cycles (right) from 65°ca bTDC to 35°ca bTDC.*

Comparison of the two sets of flow fields reveals that the difference in kinetic energy is due to a region of relatively fast flow located just above the piston, which is directed upwards towards the inlet valves. Although the flow in this region has a similar direction for the slow burning cycles at 65°ca bTDC, it is approximately 3-4 m/s slower in comparison to the flow field of the fast burning cycles. This region of fast flow persists until the final measurement at 35°ca bTDC, where it remains angled away from the spark plug, towards the inlet valves. In contrast, the flow above the piston for the slow burning cycles has less momentum and by 35°ca bTDC has been rotated clockwise by the large-scale tumble motion so that it is directed towards the spark plug.

6.3.2.1 Flow field analysis using the WRI and WMI

Figure 6.14 demonstrates that there are significant differences between the ensemble averaged flow fields of fast and slow burning cycles. Therefore, investigating regions of the flow that are most different between the two flow fields could provide indicators of what flow features have the greatest influence on the rate of combustion. The quantitative metrics introduced in Chapter 4, the Weighted Relevance Index (WRI) and the Weighted Magnitude Index (WMI), provide a method of determining regions of the flow fields that are the most different in terms of flow direction and magnitude, which can then be investigated in more detail. The method used for this analysis is demonstrated in Figure 6.15, and involves obtaining a mask from the values of the WRI and WMI that exceed a certain threshold for the comparison between the ensemble averaged fast and slow burning subsets. The left-hand plot shows flow fields for the fast and slow burning cycles overlaid on top of each other, and the corresponding WMI as the background. As shown previously in Figure 6.14, the flow above the piston is considerably faster for the fast burning mean cycle, which results in higher values of the WMI. Close to the cylinder head

and spark plug, the velocity vectors, although misaligned, have similar magnitudes and low values of the WMI as a result. A mask is generated by selecting a threshold for the metric (1.2 in this case), and any vector that exceeds this value is then used to define the mask. The right-hand plot shows the corresponding mask generated from the WMI at this crank angle (50°ca bTDC). This process is then repeated for each crank angle and the result is a set of masks for the WMI and WRI, which are used to extract regions of the flow fields from individual cycles in order to assess their effect on combustion.

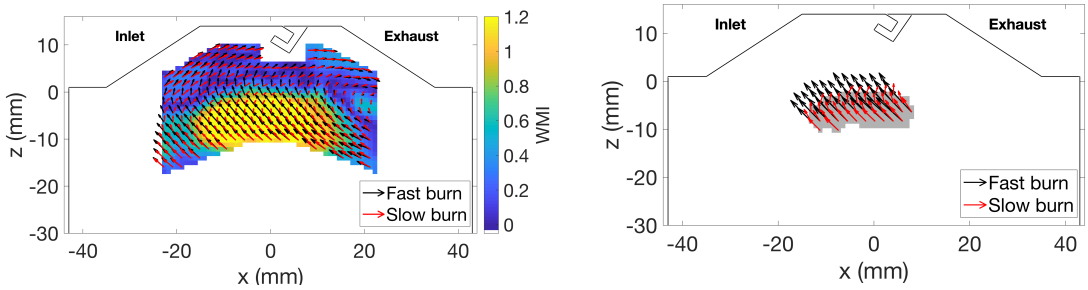

Figure 6.15 *Plot of the normalised WMI between the ensemble averaged flow fields for fast and slow burning cycles (left) and a plot of the resulting mask using a threshold value of 1.2 for the WMI (right). Vectors have been enlarged to aid visualisation.*

Figure 6.16 shows the masks (grey regions) generated by the WRI and WMI from 60°ca bTDC to 35°ca bTDC, which is the range of crank angles that will be analysed in detail as there is the largest difference in both magnitude and alignment between the ensemble averaged flow fields of fast and slow burning cycles. It can be seen that the masks extract different regions of the flow throughout this crank angle range. The mask generated from the magnitude comparison highlights a region of flow located immediately above the piston where there is a noticeably higher velocity for the cycles with faster combustion. This region of fast flow persists throughout the compression stroke until the final measurement at 35°ca bTDC. In contrast, the mask generated from the alignment metric initially highlights a region that is located centrally in the field of view, which then grows in size and, by 35°ca bTDC, occupies the whole inlet-side of the combustion chamber.

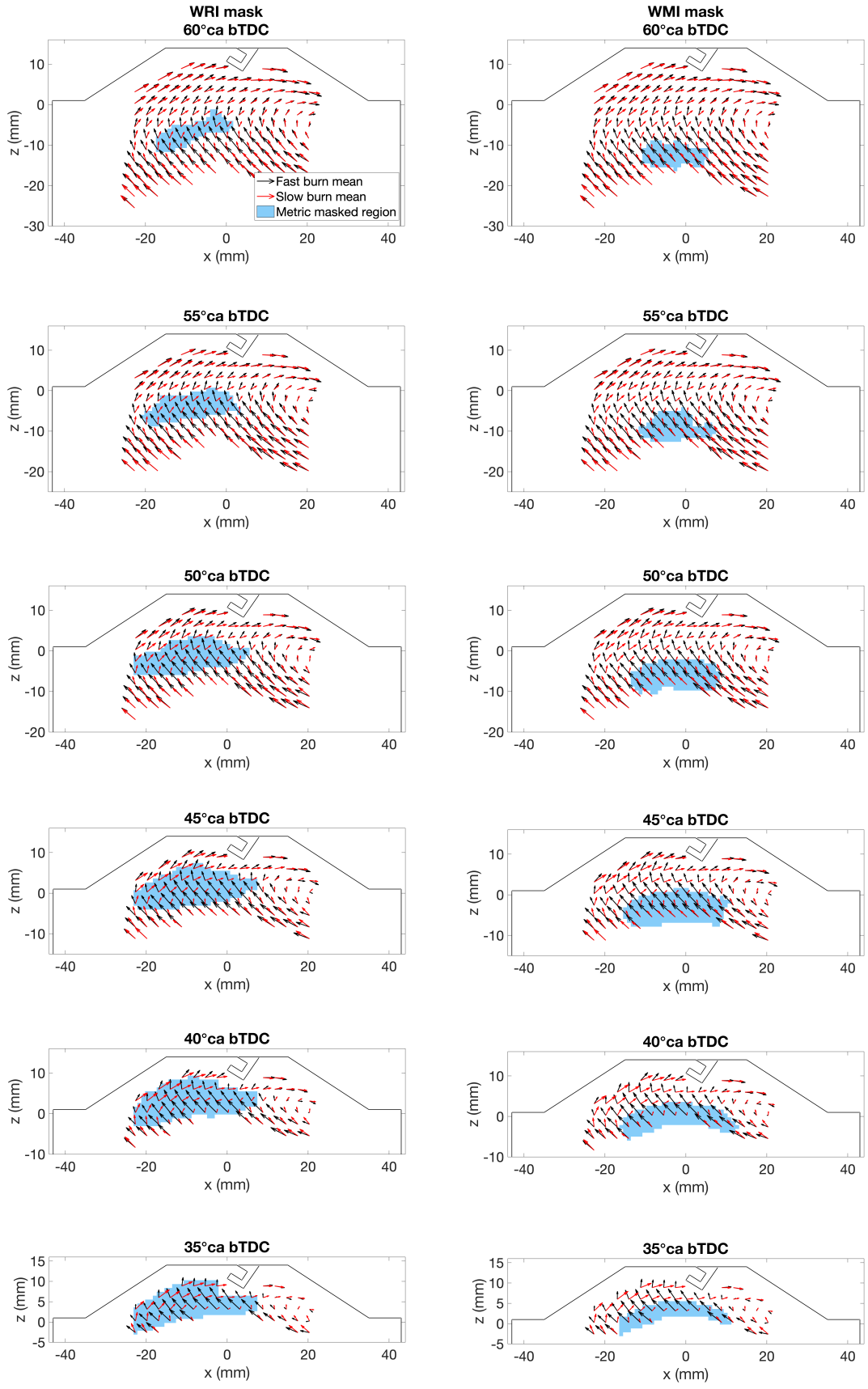

Figure 6.16 *Plots displaying the masks determined by the WRI (left) and WMI (right), which are used to select regions of the flow that will be investigated in more detail. Every third vector shown for clarity.*

Figure 6.17 demonstrates how the masked regions are used to compare different flow fields. After the masks have been applied to the conditioned subsets, the vectors that lie within the masked region are then spatially averaged to produce a single vector that represents the mean direction and magnitude of that region of flow. The mean vectors are then ensemble averaged within the conditioned subsets to produce an average vector, which can then be compared for fast, medium and slow burning subsets. The statistical variation of the magnitude and direction of the vectors are also calculated and plotted as wedges of variation, displaying ± 1 standard deviation in both direction and magnitude.

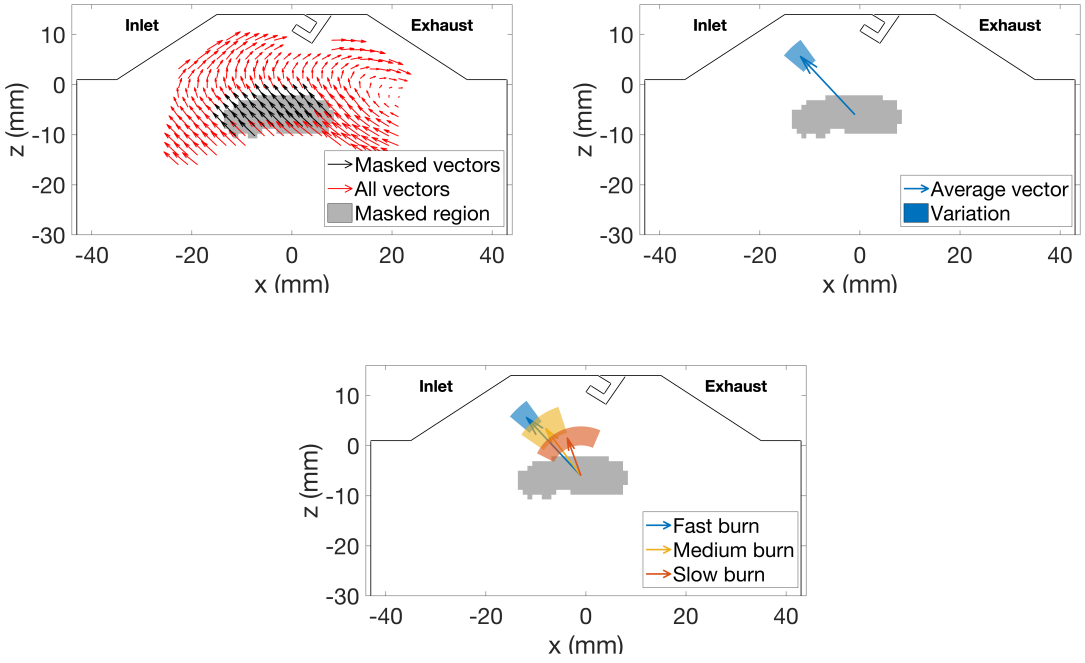

Figure 6.17 *Plots demonstrating the process of producing average vectors from a masked region of the flow fields: highlighting the regions that exceed the threshold (top left), spatially averaging the masked vectors to produce a single flow vector a given flow field, and finally ensemble averaging all mean vectors in a subset of fast, medium and slow burning cycles to produce a representative flow vector and the variation (in this case, ± 1 standard deviation for flow magnitude and direction).*

Analysis of ensemble averaged flow vectors

Figure 6.18 and Figure 6.19 show the results of this analysis for both the WMI and WRI masks from 60°ca bTDC to 35°ca bTDC. On inspection of both figures, it is apparent that there is a consistent trend for all the crank angles shown, and both sets of masks; there is a

progression in terms of flow direction from the fast burning cycles to the medium burning cycles, and finally to the slow burning cycles. This trend was also present in the plots of kinetic energy and indicates that there is a link between the rate of combustion and the flow characteristics captured by these masked regions. As well as the vectors of the subsets, the ensemble mean flow vector of the whole dataset is also plotted with its variation. In general, the mean vector of the medium burn subset is very similar to that of the whole dataset, although the variation is larger for the whole dataset than that of the medium burn subset. This indicates that the mean flow vector of the medium burn cycles is a good representation of the mean of the whole dataset, in contrast to the fast and slow burning subsets, which are considerably different.

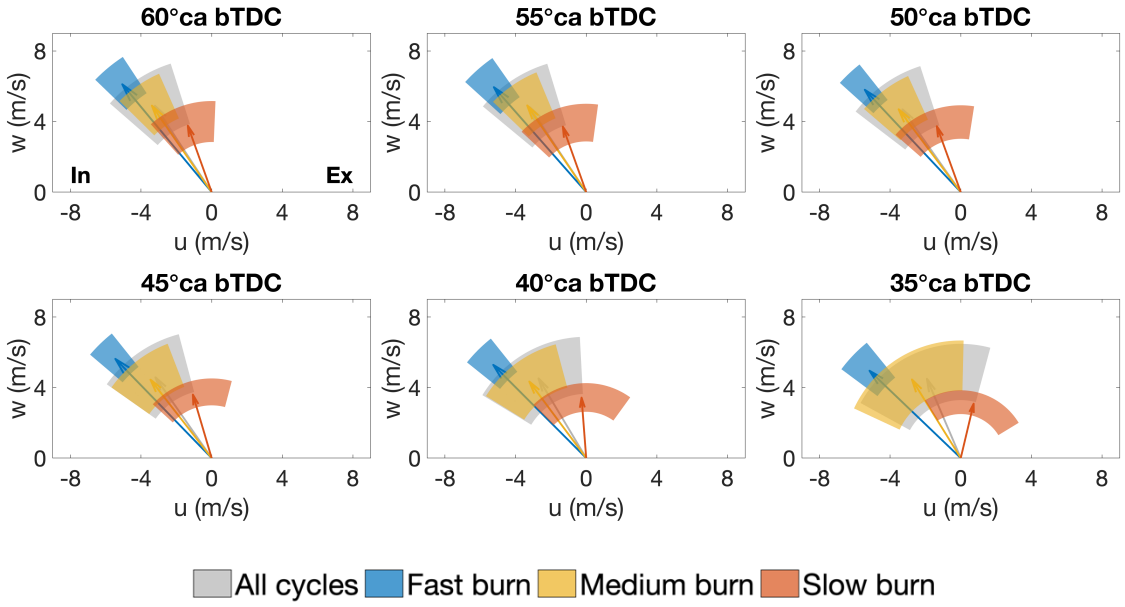

Figure 6.18 *Plots of ensemble averaged flow vectors for regions masked by the WMI (shown in Figure 6.16), for fast (blue), medium (yellow), slow (red) burning subsets, and all cycles (grey). The coloured wedges denote ± 1 standard deviation of flow magnitude and direction for each subset. Negative* ***u*** *is directed towards the inlet and positive* ***u*** *is directed towards the exhaust.*

The plots for the WMI masked region from 60°ca bTDC to 45°ca bTDC, highlight a region of flow immediately above the piston where, on average, there is a highly directed volume of gas with high velocity that is travelling towards the inlet side of the cylinder head for the

fast burning subset. In contrast to the slow burning subset, the average flow speed is approximately double, and the standard deviation in flow direction is over 3 times lower. The highly directional nature of the flow in this region for the fast burning cycles remains for all crank angles, with only small changes in the directional variation. The average direction of the flow vectors for slow burning cycles is initially similar to that of the fast and medium cycles at 60°ca bTDC, however the flow is progressively rotated clockwise by the tumbling flow entering the field of view near the cylinder head on the inlet side. By 35°ca bTDC, the average direction and speed of the flow for slow burning cycles is notably different to that of fast burning cycles, as it is angled towards the exhaust valves with approximately half the speed. Although the flow vector for medium burning cycles lies in between the two extremes, it is angled more closely to the fast burn subset, which suggests that the flow angles of the whole dataset are skewed towards those of the fast burning cycles. The variation in flow direction for all subsets except that of the fast burning cycles increases for each crank angle, indicating that fast burning cycles tend to have more a repeatable flow feature in this region during compression.

The plots shown in Figure 6.19 present the results of the conditional analysis using the WRI as a mask, which extracts a different region of the field of view in comparison to the WMI mask (refer to Figure 6.16 for details).

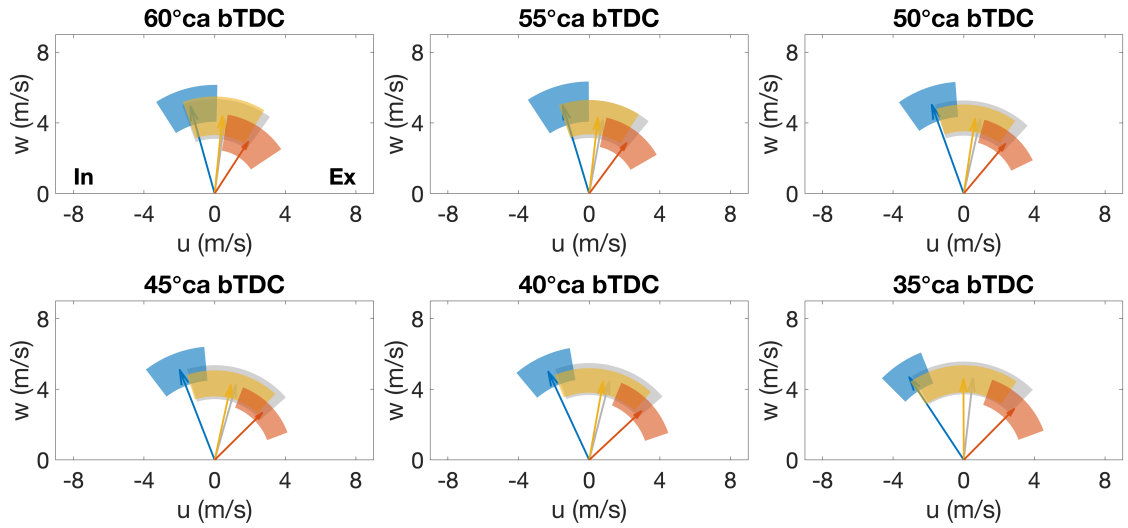

Figure 6.19 *Plots of ensemble averaged flow vectors for regions masked by the WRI (shown in Figure 6.16) for fast (blue), medium (yellow) and slow (red) burning subsets, and all cycles. The coloured wedges denote ± 1 standard deviation of flow magnitude and direction for each subset.*

This region is located approximately midway between the piston surface and the cylinder head, on the inlet-side of the combustion chamber. In this region, the flow for the fast burning cycles tends to be directed towards the inlet valve due to the volume of high-speed gas located above the piston. Meanwhile, flow for the slow burning cycles tends to be directed more towards the spark plug, due to the influence from the high-speed tumbling flow entering the field of view from the inlet side of the combustion chamber. The difference in flow direction between the fast and slow burning subsets increases during the compression stroke, with almost a 90° separation in flow angle by 35°ca bTDC. These plots lead to a similar conclusion as that of the WMI masked data; the flow for fast burning cycles tends to have higher speeds and be directed away from the spark plug, in contrast to that of slow burning cycles, which is slower and angled towards the spark plug and exhaust valves.

Analysis of individual flow vectors

Analysis of the conditionally averaged vectors reveals that there are significant differences between the flow features that are present for fast and slow burning cycles. However, the wedges of variations show that there is considerable spread in both flow direction and magnitude within the conditional averages. Therefore, it would be interesting to investigate the relationship between the flow field and combustion on a cycle-by-cycle basis.

Figure 6.20 and Figure 6.21 show plots of the spatially averaged flow vectors of the individual cycles from the which the ensemble averages were calculated for the plots in Figure 6.18 and Figure 6.19. The top-left plot in Figure 6.20 shows the pressure traces of all cycles in the 300-cycles dataset, as well as the subsets of fast and slow burning cycles, and both the fastest (purple line) and slowest (cyan line) burning cycles. The corresponding flow vectors using the WMI mask are displayed in the adjacent three plots for crank angles 55°ca bTDC, 45°ca bTDC and 35°ca bTDC to investigate the significant increase in flow angle variation observed in the ensemble averaged vectors.

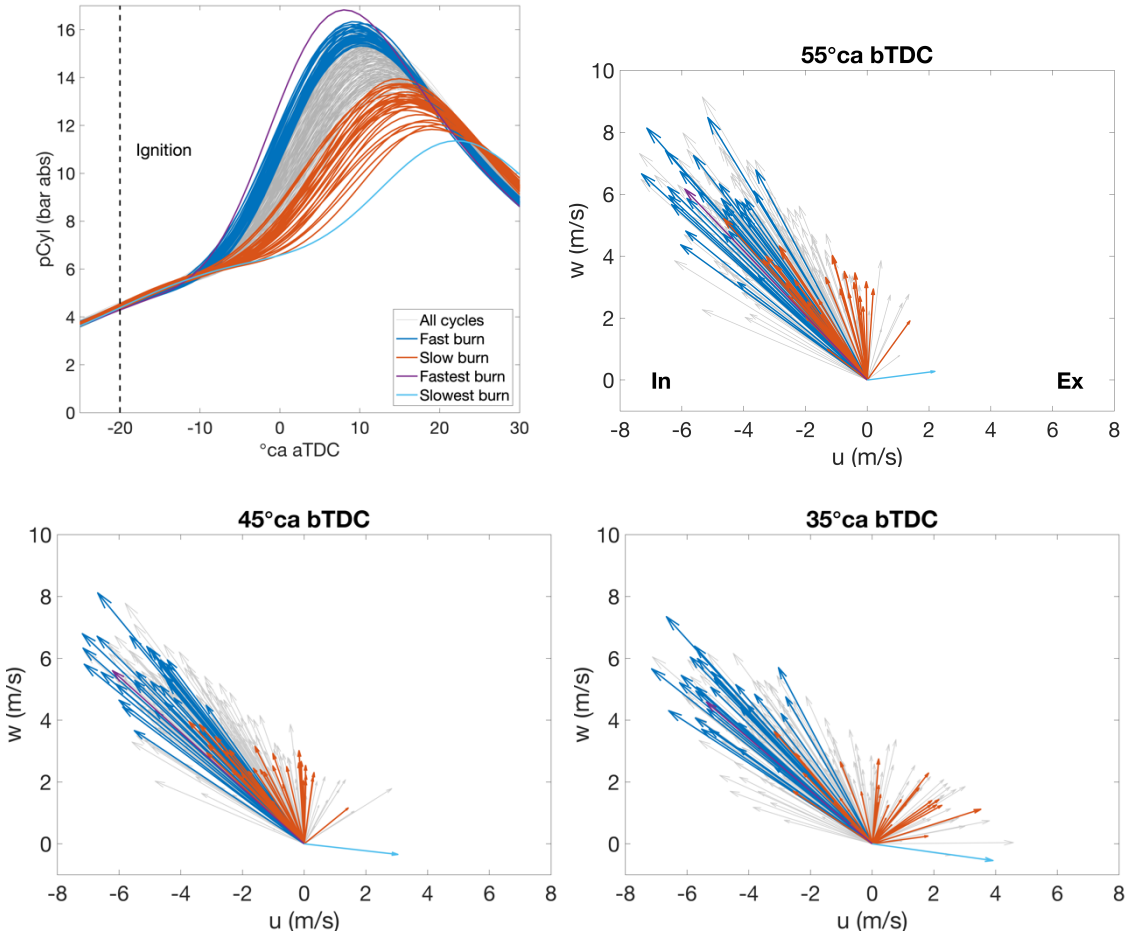

Figure 6.20 *Plots of the spatially averaged flow vectors for individual cycles using the WMI mask for a sequence of crank angles: 55°ca bTDC (top right), 45°ca bTDC (bottom left) and 35°ca bTDC (bottom right). The plot of the pressure trace (top left) indicates the fast and slow burning subsets (blue and orange lines), the fastest and slowest burning cycles (purple and light blue), as well as all cycles in the 300-cycle dataset (light grey). This colour scheme applies to all these plots and those in Figure 6.21.*

As expected, the tends that were observed in the ensemble averaged flow vectors are reflected by the individual cycles; fast burning cycles tend to have a region of flow with high velocity, directed towards the inlet valves. However, the plots of individual vectors demonstrate the considerable variation in flow fields throughout the whole dataset. At 55°ca bTDC, all flow vectors of the fast burning subset are directed towards the inlet valve. Surprisingly, several flow vectors from the slow burning subset lie among the distribution of vectors from the fast burning subset. The rest are much slower and are directed vertically upwards and towards the right. From 45 to 35°ca bTDC, the spread of slow burning vectors

increases substantially, although a number of vectors remain indistinguishable from those of fast burning cycles. There is also a large number of flow vectors from the remaining 80% of the dataset that fall within the distributions of both the fast and slow burning cycles, which result in 'normal' combustion. The vectors for the fastest and slowest burning cycles both behave as expected. The plots of individual WRI-masked flow vectors from 45 to 35°ca bTDC are shown in Figure 6.21.

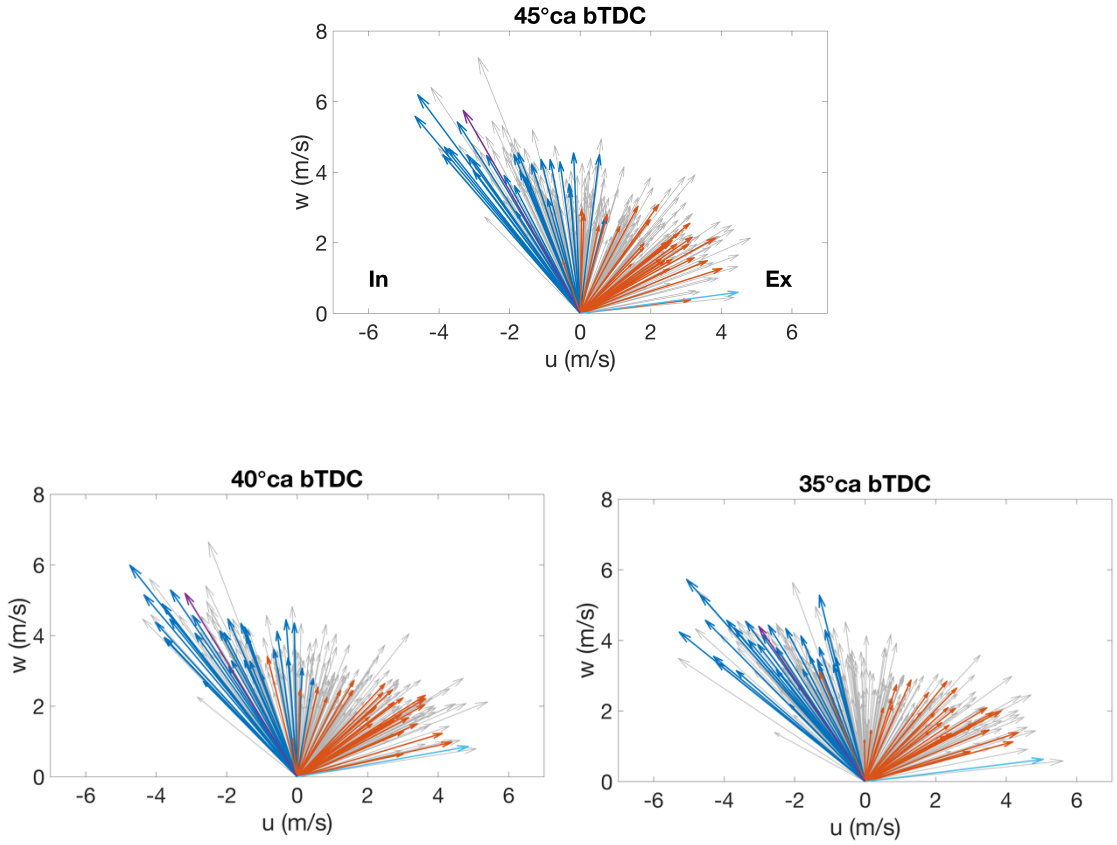

Figure 6.21 *Plots of the spatially averaged flow vectors for individual cycles using the WRI mask for a sequence of crank angles: 45°ca bTDC (top right), 40°ca bTDC (bottom left) and 35°ca bTDC (bottom right). The colour scheme is the same as that given in Figure 6.20.*

There is a clear separation between the majority of flow vectors from the fast and slow burning subsets for each crank angle. At 35°ca bTDC in particular, apart from a single anomalous flow vector for a slow burning cycle, there is an almost binary split between the fast and slow burning subsets. The masked region at this crank angle covers the whole left-

hand side of the field of view, therefore the flow vectors for the fast burning cycles are directed towards the inlet valves whereas the vectors of the slow burning cycles are angled towards the spark plug and exhaust valves. Similar to the WMI-masked plots, the flow vectors for the fastest and slowest cycles follow the trends of the ensemble averaged results.

6.3.3 Flame imaging analysis

To investigate the effect of the in-cylinder flow field on early flame propagation, a high-speed camera was used to image the flame every crank angle from 33°ca bTDC to 26°ca aTDC. Spark ignition occurred at 20°ca bTDC, therefore the motion and growth of the flame kernel was captured. The processing procedure for the flame images, described in Section 6.2.3, removes the background and extracts the contour of the flame. From these contours, metrics that quantify the growth of the flame such as the flame area and centroid location can be calculated. These metrics will be used to discuss the cyclic variation in flame development.

Figure 6.22 shows examples of the flame progression for the fastest and slowest burning cycles (cycles 73 and 145 respectively), alongside plots of mass fraction burnt (MFB) derived from the in-cylinder pressure trace using the Rassweiler and Withrow method[207], as outlined in Chapter 2 . The direction of the bulk tumble motion at the spark plug is shown as well as the location of the PIV measurement to aid orientation (see Figure 6.4 for more details). It should be noted that due to the limited field of view through the 45 mm diameter quartz piston crown, the flame imaging analysis can only be performed up until the point where any part of the flame reaches the edge of the field of view. The flame will continue to grow after this time, however the edge of the flame can no longer be tracked.

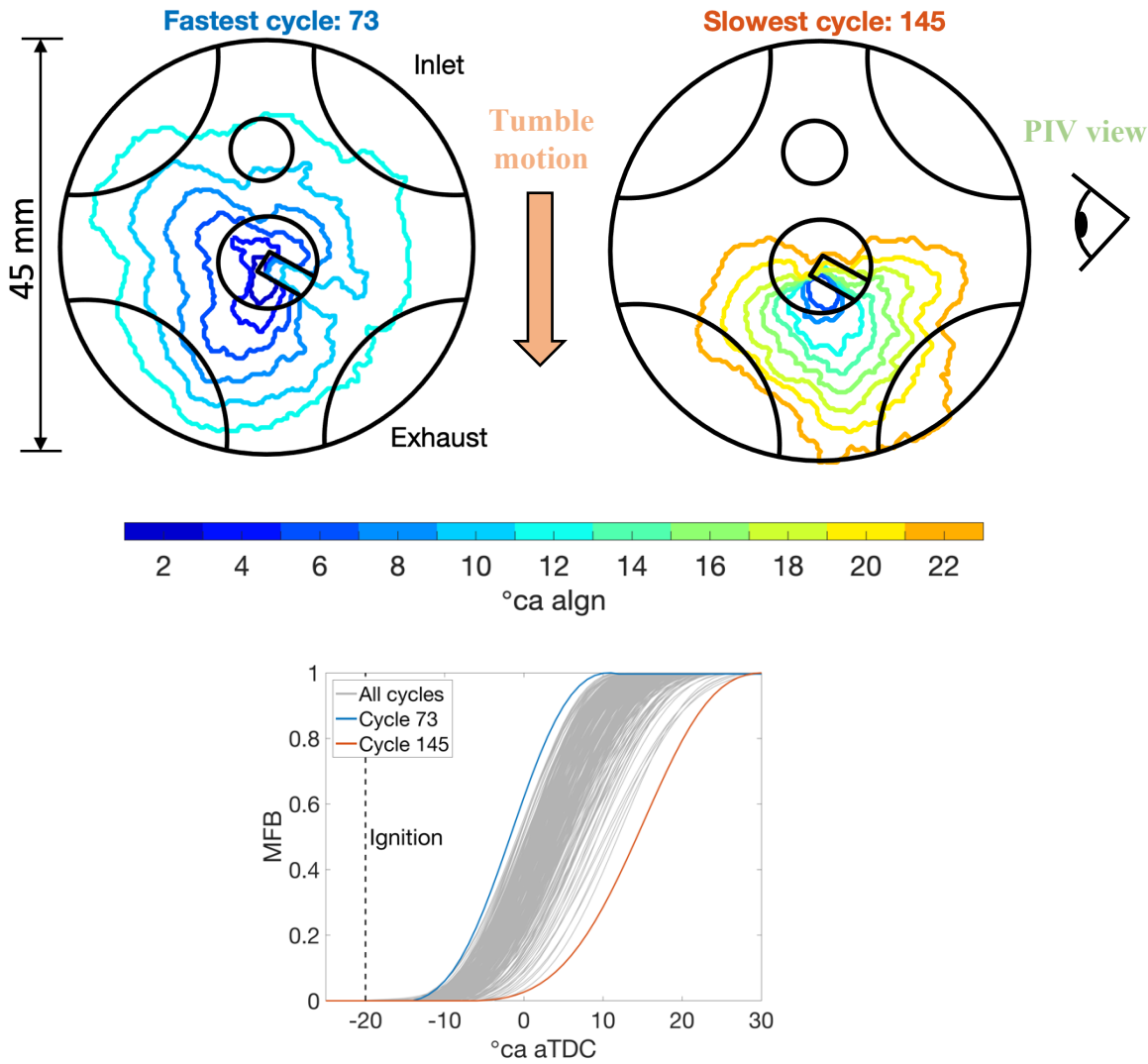

Figure 6.22 *Flame contours showing the growth of the flame after spark ignition for the cycles with the fastest (cycle 73,top left) and slowest (cycle 145,top right) combustion. The colours denote the crank angle at which each flame contour occurs in relation to the spark timing (20°ca bTDC). Plots of mass fraction burnt (bottom) demonstrate the difference in burn rate indicated by in-cylinder pressure measurements.*

The flame contours indicate a number of differences between the two cycles; the flame for the fast-burning cycle appears only 1 crank angle degree after ignition, which is 4 degrees before the flame is detected for the slow burning cycle. When the flame does appear from behind the spark plug ground electrode in the slow burning cycle, it remains close to the spark plug for a longer duration than the fast burning cycle. Heat transfer from the flame to the spark plug electrodes is a known cause of flame quenching and could be the cause of this delayed flame growth.

The flame structures are also significantly different between the two cycles. For the fast burning cycle, after the flame has been initiated, it grows rapidly in all directions, spreading throughout the combustion chamber. In contrast, the flame for the slow burning cycle grows asymmetrically towards the exhaust valves. At the time it reaches the edge of the field of view, only a small fraction of the flame has travelled towards the inlet valves. From the raw images, the flame only reaches the limit of the field of view on the inlet side of the combustion chamber 39°ca after ignition, in comparison to 17°ca for the fastest burning cycle.

There are clear differences between the initial flame growth and its subsequent development for the fastest and slowest individual cycles. To investigate if similar flame structures appear for the whole dataset, this analysis must be applied to all cycles. Figure 6.23 shows plots of the normalised flame area for all cycles alongside the mass fraction burnt derived from the pressure trace. The flame area is calculated by binarizing the processed flame image and summing the number of pixels in the resulting region. The summation is then normalised by the total number of pixels in the field of view to produce a value that indicates the flame coverage.

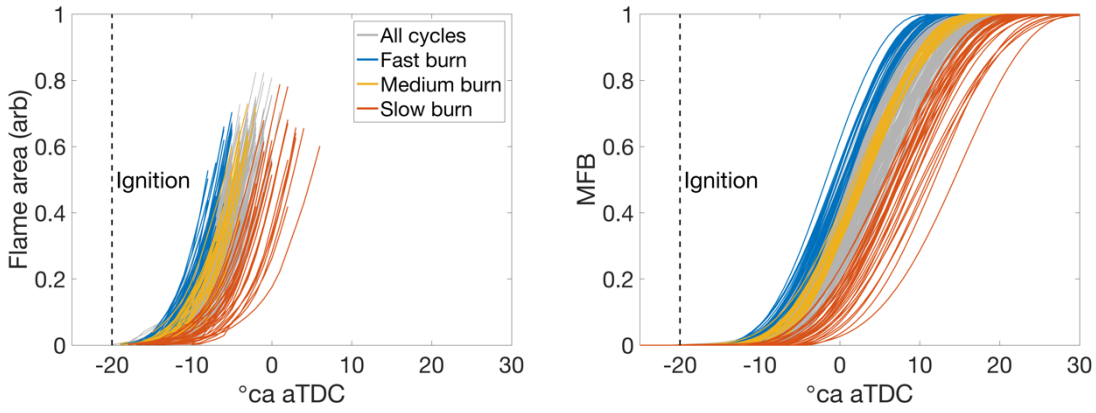

Figure 6.23 *Plots of the normalised flame area calculated from the combustion images (left) and the mass fraction burnt (MFB) for all cycles. All cycles are plotted in grey and the subsets of fast (blue lines), medium (yellow lines) and slow (red lines) burning cyces, as defined previously, are also highlighted.*

As discussed previously, the flame image processing is only valid until the flame reaches the edge of the field of view. Therefore, the curves of flame area in the left-hand plot appear to end abruptly at different crank angles for each cycle. The subsets of fast, medium and slow burning cycles, as defined by the angle of peak pressure, are also highlighted in both plots. It is clear that the period of rapid flame growth occurs earlier for fast burning cycles in comparison to slow burning cycles. This agrees well with the pressure-derived calculations of MFB, demonstrated by the correlation between the crank angle of 10% MFB (CA10) and the crank angle at which the flame occupies 20% of the field of view, shown in Figure 6.24.

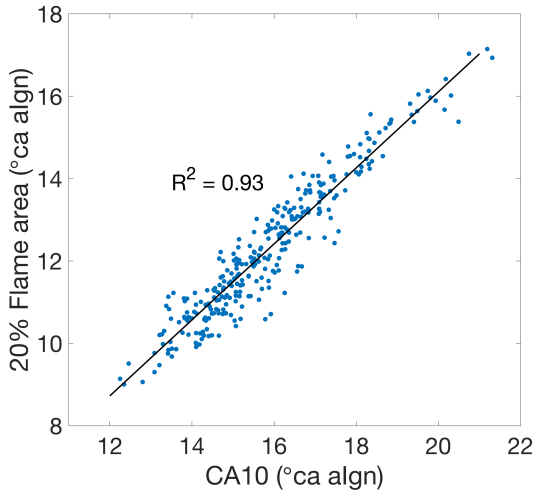

Figure 6.24 *Scatter plot of the angle of 10% MFB (CA10) against the angle at which the flame area occupies 20% of the the field of view. The line of best fit and R^2 value are also shown.*

Due to the reduced field of view through the quartz piston, it is only possible to track the initial flame development. Therefore, it is difficult to compare the growth rate of the fully developed flame using the optical measurements. In order to investigate whether the slow burning cycles result from slow initial flame growth or a slow fully developed flame, pressure-derived calculations of mass fraction burnt are used. Figure 6.25 plots CA10, an indicator of the early flame growth, and CA10-90, which is an indicator of the growth rate of the fully developed flame. The dataset has been sorted in ascending order using CA10 to emphasise any trends.

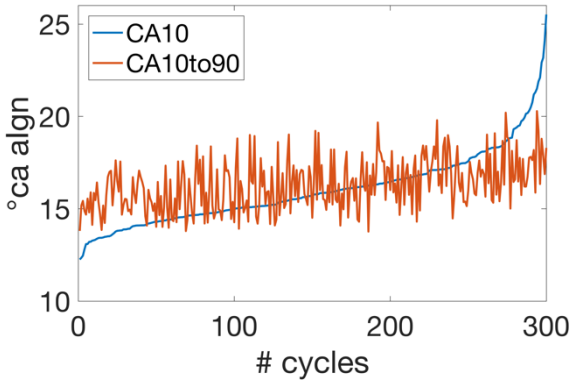

Figure 6.25 *Plots of CA10 and CA10-90for the whole dataset, sorted by CA10.*

The plot of CA10 demonstrates the variation in early flame growth for all cycles, with 13°ca difference between the extremes of the dataset. In contrast to the relatively large range of CA10, the plot of CA10-90 remains almost constant for all cycles, albeit with fluctuations from cycle to cycle. This indicates that the variation observed in the burn rates throughout the dataset is primarily due to the early flame development, which is captured by the flame imaging setup.

Plots of normalised flame area in Figure 6.23 indicate that there is a wide range of flame growth rates for all cycles, therefore it is worth investigating whether there are repeatable flame structures that indicate poor combustion performance. The flame contours for the slowest burning cycle, shown in Figure 6.22, revealed a strong asymmetric flame growth towards the exhaust valve in contrast to the flame of the fastest cycle, which spread rapidly in all directions. To investigate if these features are common among the whole dataset, the flame images were separated into subsets corresponding to the rate of combustion, in the same way as the velocity data in Section 6.3.2. The flame images within each subset are then used to build up maps showing the frequency of occurrence of the location of the flame. The frequency is normalised by the total number of cycles in the subset to give values that range between 0 and 1. Figure 6.26 shows maps of presence probability of the flame for the subsets with the 30 of the fastest and slowest burning cycles.

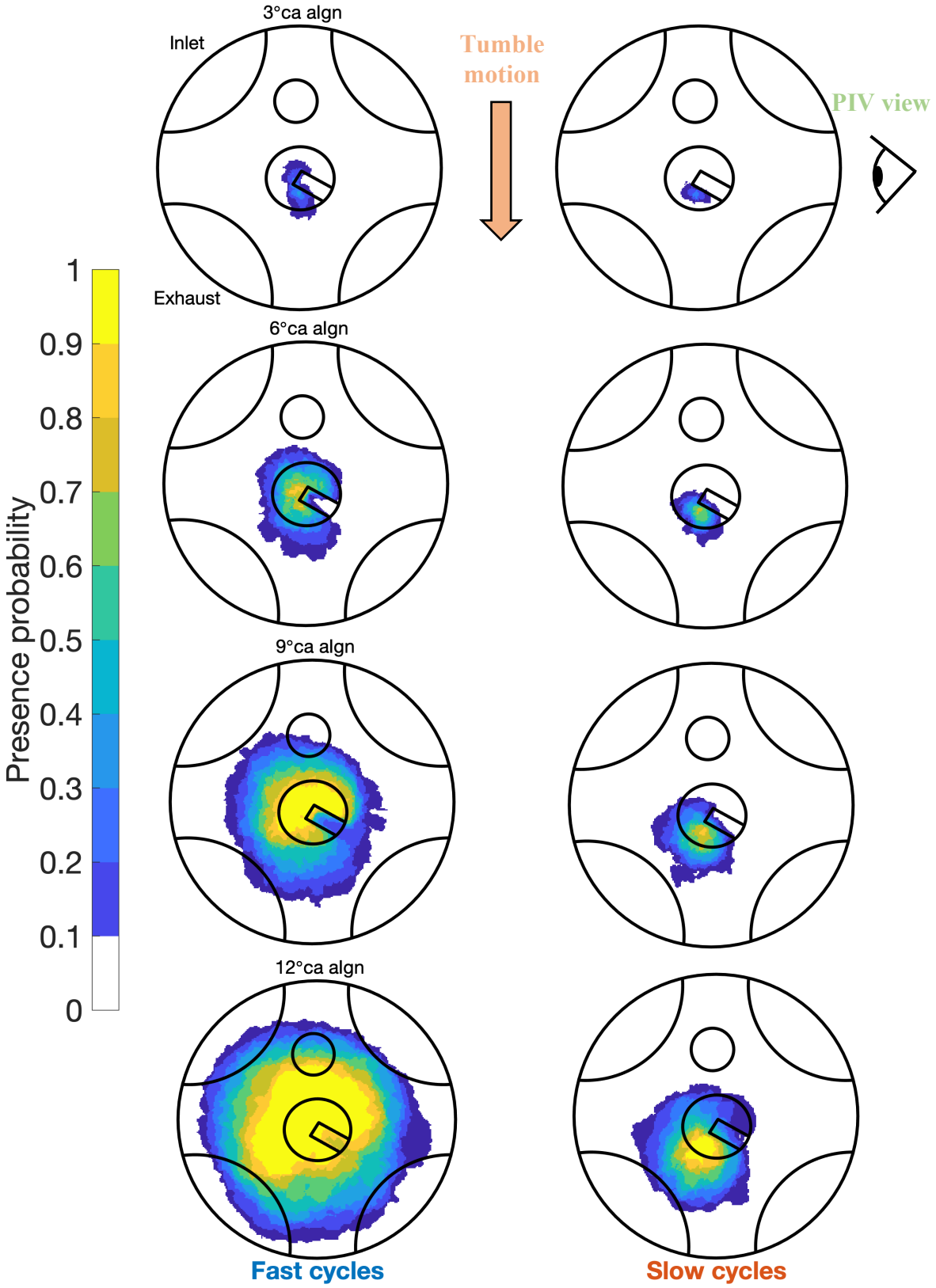

Figure 6.26 *Plots showing the flame presence probability for a number of crank angles for the 30 fastest (left) and slowest (right) cycles. A value of 1 indicates that the flame is present at the location for all the cycles in the subset. The orientation of the cylinder head is the same as that shown in Figure 6.22.*

These plots indicate that the observed differences between the flame structures of the fastest and slowest burning cycles are consistent with those that are present for the corresponding subsets. By 3°ca after ignition, there is already a difference between the two subsets, with a higher proportion of fast burning cycles moving away from the spark plug. The difference between the 2 subsets increases with crank angle as the flames of the fast burning subset grow faster than those of the slow burning subset. By 9°ca after ignition, the contour indicating 10-20% presence probability is already greater than the same contour for the slow burning subset at 12°ca.

Not only is the rate of flame growth different between the subsets, but there are also significant differences between the spatial locations of the flames. Similar to the fastest burning individual cycle, the flames of the fast burning subset tend to grow in a more uniform manner, spreading throughout the combustion chamber in all directions. It is also interesting to note that by 9°ca after ignition, 90-100% of the flames of the fast burning cycles have moved towards the inlet valves. This is even more apparent by 12°ca after ignition, where a large proportion of the 90-100% presence probability contour is located closer to the inlet side of the combustion chamber. However, the opposite is true for the subset of slow burning cycles; the presence probability contours indicate that, by 12°ca after ignition, most of the flames have grown towards the exhaust valves. Shortly after 12°ca after ignition, the flame of the fastest burning cycle reaches the limit of the field of view, however the fastest of the slow burning cycles only reaches the limit by 18°ca after ignition. Therefore, Figure 6.27 shows plots of the flame presence probability for 15°ca and 18°ca after ignition. These emphasise that the flames of slow burning cycles tend to move towards the exhaust side of the combustion chamber.

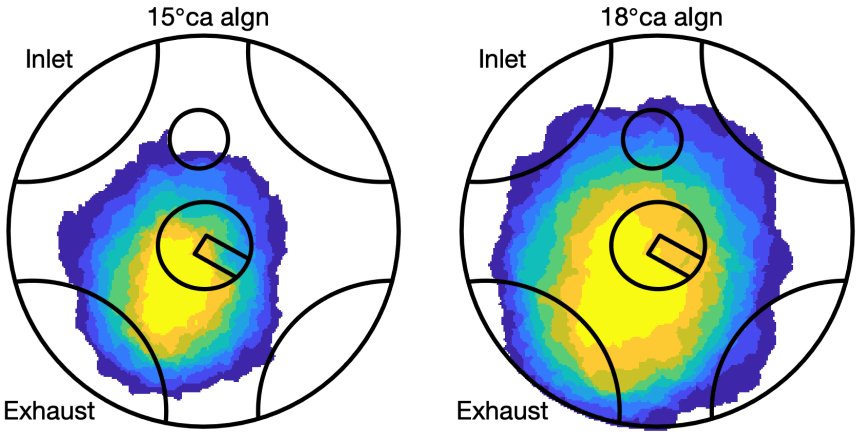

Figure 6.27 *Plots of flame presence probability at 15°ca and 18°ca for the subset of slow burning cycles, where the flames reach the limit of the field of view. The scale and orientation are the same as the images shown in Figure 6.26.*

A potential cause of flame propagation that results in poor combustion performance is the in-cylinder motion prior to ignition. In Section 6.3.2, analysis of the conditionally averaged velocity data revealed that there are significant differences in the flow fields of fast and slow burning cycles; Figure 6.18 and Figure 6.19 both show average flow vectors that indicate that the flow for cycles with rapid combustion tends to be directed towards the inlet valve, whereas for slow burning cycles, the flow is directed towards the spark plug and exhaust valves. The individual flow vectors, shown in Figure 6.20 and Figure 6.21, also show this and reveal the considerable variation for the whole dataset. These trends agree with the observations of the flame transportation towards the exhaust valves for slow burning cycles, and towards the inlet valves for the fast burning cycles. Figure 6.28 shows the distribution of flame centroids throughout the combustion chamber for all cycles at the crank angle at which the flame occupies 20% of the field of view. The flame centroids for the fast and slow burning cycles are also highlighted.

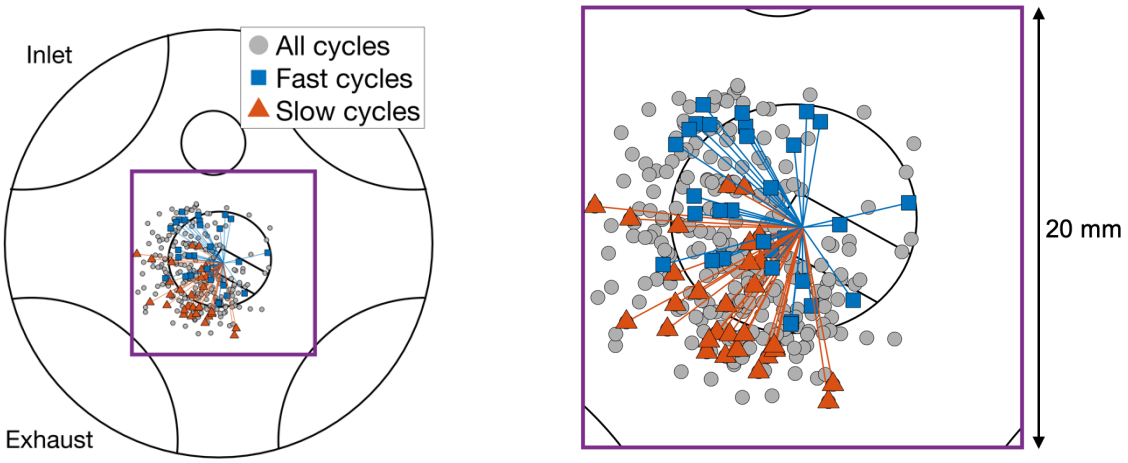

Figure 6.28 *Plots showing the locations of the flame centroids at the crank angle at which the flame occupies 20% of the field of view. All cycles are shown by grey circles, the fast burning subset by blue squares and the slow burning subset by red triangles. The purple box is enlarged for the image on the right to show the centroid positions in more detail.*

This plot shows the large variation in the movement of the flames for the all cycles in the dataset. The distribution of flame centroids appears skewed to the front of the engine (left of the plot), which could indicate flow motion in the swirl direction. The ground strap of the spark plug could also be inhibiting the motion of the flame towards the rear of the engine (right of the plot). As suggested by the plots of flame presence probability in Figure 6.26, flame centroids of 25 of the 30 slow burning cycles are transported towards the exhaust valves. That said, there are many flames that are located further towards the exhaust valves that result in faster combustion. The distribution of flame centroids for fast burning cycles is more uniform than that of slow burning cycles, with 60% located closer to the inlet valves. The more evenly distributed flame centroids reflect the more uniform growth of the flames for fast burning cycles in comparison to the highly asymmetric flame progression for slow burning cycles

To investigate the correlation between the translation and growth of the flame, and the in-cylinder motion on cycle-by-cycle basis, the fluid velocity and flame displacement are compared in a common directional component, the x-direction. Figure 6.29 shows a plot of flame centroid displacement relative to the spark plug in the x-direction (from inlet to

exhaust) at 11°ca after ignition against the *u*-component of the in-cylinder velocity, spatially averaged using the WRI mask at 35°ca bTDC (also shown in Figure 6.29, top). The size and colour of the markers, and the vectors, indicate the normalised flame area.

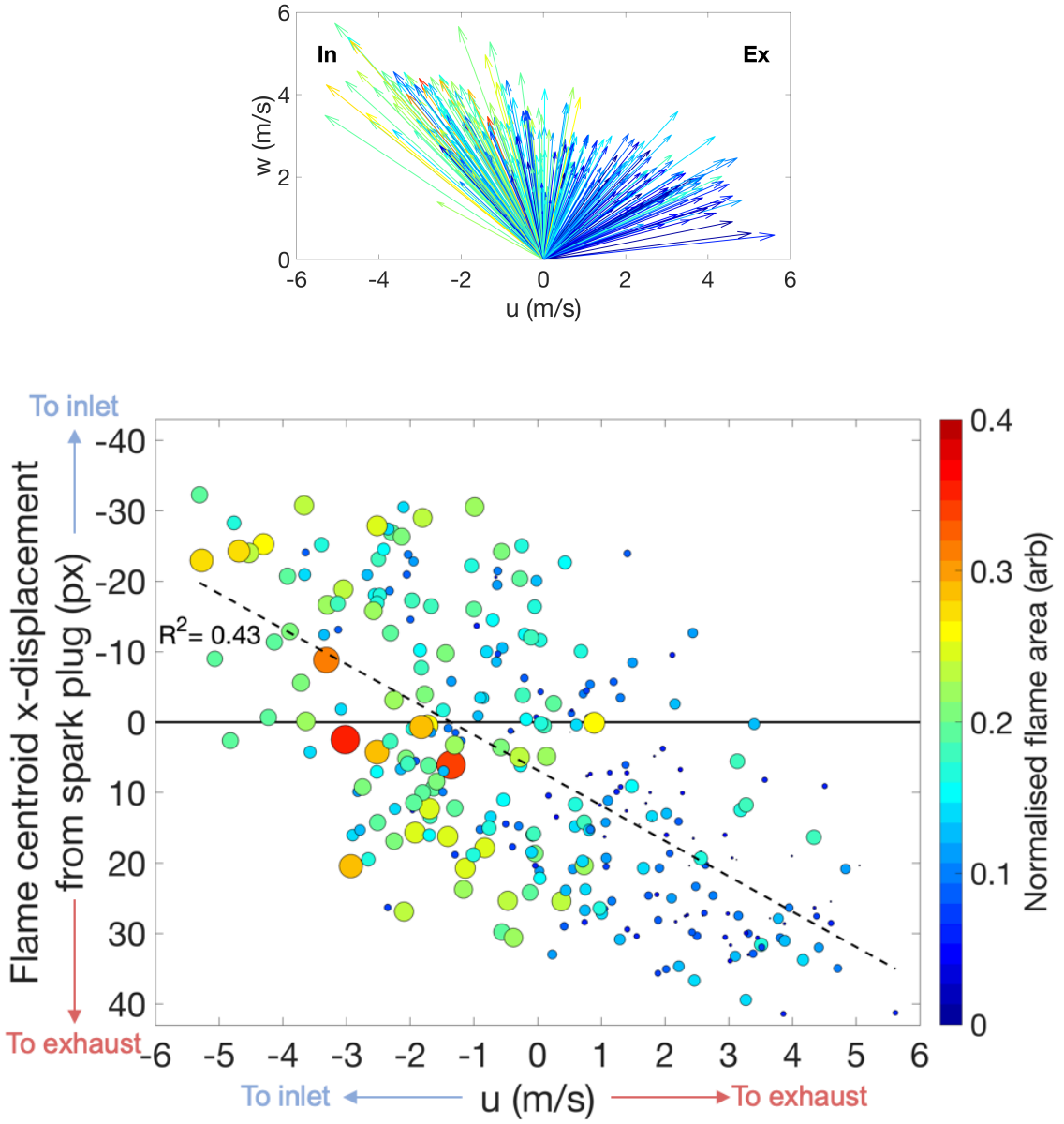

Figure 6.29 *Plot showing the displacements of the flame centroids in the x-direction (relative to the spark location) for all cycles at 11°ca after ignition against the u-component of the spatially averaged, WRI-masked velocity vector at 15°ca bTDC (bottom). The size and colour of the markers denote the normalised flame area. Shown above are the spatially averaged flow vectors in the WRI-masked region at 35°ca bTDC with the colour scale indicating flame growth at 11°ca after ignition. The direction of the y-axis is the same as the plot of flame centroids in Figure 6.28.*

The distribution of the sizes of the markers reveals that, in general, the flame growth is slower for positive values of *u* (towards the exhaust valve). Ensemble averaged and

individual vector plots in Figure 6.19 and Figure 6.21 indicated that the flow for slow burning cycles tends to be angled towards the spark plug. As these flow vectors were selected using the pressure-derived combustion indicator, which was shown to correlate well with the optical flame growth indicator, it is not surprising that these vectors lead to slow flame growth. That said, the conditioned subset of slow burning cycles used the extremes of the dataset; Figure 6.29 indicates that the link between flame growth and flow direction is not limited only to the extremes of the fast and slow burning cycles, but applies in general to the whole dataset. Furthermore, inspection of the vector plot reiterates this finding that the vast majority of vectors angled to the right (positive values of u) are coloured dark blue, indicating slow flame growth. A negative u-component, or a vector directed away from the spark plug, towards the inlet valve, tends to result in fast flame growth rates, as indicated by the relatively large proportion of larger markers.

The line of best fit is plotted to indicate the correlation between the location of the flame centroid in the x-direction in relation to the spark plug, and the u-component of velocity in the region masked by the WRI. The general trend suggests that as the flow direction switches from inlet to exhaust, the flame moves as expected. However, the R^2 value of 0.43 does not indicate a strong correlation and there are a number of outliers that appear to suggest the opposite of the general trend. There are a number of reasons why this could be the case; although the in-cylinder flow is three-dimensional, the PIV measurements are made in a single plane in the centre of the cylinder, therefore there is no knowledge of the swirl velocities in the region of the spark plug. Even though there is a dominant tumble motion for this engine, out-of-plane velocities could have a significant effect on the motion of the flame and its development. For this analysis, the flow vectors have been spatially averaged over regions of the field of view by using metrics to quantify the greatest

differences between fast and slow burning cycles. Within these regions, there could be considerable variation of the velocity vectors that is hidden by the spatial average. For example, it is possible for a small eddy to be present within the region, which would affect the spatial average. Furthermore, flame imaging is a line-of-sight measurement and so any flame motion in the z-direction is unknown.

6.4 Summary

The work in this chapter has investigated the effect of in-cylinder flow motion on the cyclic variation of combustion by using simultaneous high-speed PIV measurements and flame imaging. Velocity measurements were made from 330°ca to 35°ca bTDC in increments of 5°ca, capturing both the induction and compression processes. A high-speed camera was used to capture images of the flame every crank angle degree until 26°ca aTDC, by which time the flame had reached the edge of the field of view for all cycles. The angle of peak pressure was used to condition the velocity measurements for fast and slow burning cycles. Ensemble averages of the flow fields for the fastest and slowest 10% (30) of cycles were then compared using the quantitative metrics, the WRI and WMI (defined in Chapter 4). This analysis identified regions of the flow with the greatest differences in terms of alignment and magnitude, which were then converted into masks and applied to the flow fields of the whole dataset. Spatial averages of these masked flow fields were then used to find flow features that influence combustion performance.

Analysis of the combustion-conditioned, ensemble averaged flow vectors revealed that there are significantly difference flow features present for fast and slow burning cycles:

- The WMI-masked flow vectors demonstrate a region of highly directed, fast flow directly above the piston that is twice as fast for fast burning cycles in comparison to slow burning cycles.
- For fast burning cycles, this fast region of flow is directed towards the inlet valve at 60°ca bTDC and remains as such over the range of crank angles. For the slow burning cycles, however, the region of the flow is rotated clockwise by the tumble motion towards the spark plug and exhaust valves throughout the latter stages of compression.
- The WRI-masked flow fields reveal significant differences between the fast and slow burning cycles in a different region to the WMI, with flow directions towards the inlet and spark plug respectively.
- By 35°ca bTDC, the average flow direction is almost 90 degrees different between fast and slow burning cycles.

Analysis of the corresponding individual flow vectors reflects the results of the ensemble averaged analysis, and also demonstrates the large variation present for all cycles. The WRI-masked flow vectors show that there is almost a binary split between fast and slow burning cycles at 35°ca bTDC, with all the flow vectors for fast burning cycles directed towards the inlet valves, and all but one of the vectors for slow burning cycles directed towards the spark plug.

Analysis of the flame images revealed that the flames of fast burning cycles tend to grow rapidly in all directions, in comparison to those of the slow burning cycles that appear to move towards the exhaust valves. Direct comparison of the u-component of the velocity vector for the WRI-masked region at 35°ca bTDC and the displacement of the flame

centroid in the *x*-direction revealed a weak link between the flame position and flow direction. However, there is a trend for the whole dataset that indicates that poor combustion results from flow motion that is directed towards the exhaust valves. Rapid flame development was found to result from vectors that are directed towards the inlet valve.

An interesting addition to this work would be to investigate the origins of the differences in in-cylinder motion that influence combustion. For the current PIV setup, the fast region of flow located above the piston appears from the exhaust side of the field of view during the compression stroke. However, it is very difficult to track this pocket of high-speed gas back in time without observing the flow motion for the whole cylinder. Determining the cause of this distinct flow feature could aid the design of future combustion systems.

7 Conclusions and Future Work

This chapter provides a summary of the work included in this thesis and a number of suggestions for future research.

7.1 Summary

The objective of this project was to develop an optical engine test facility that can provide valuable in-cylinder velocity measurements to aid the validation of CFD simulations performed by engineers at Jaguar Land Rover and also provide insight into the performance of the Ingenium combustion system. Chapter 1 provides an overview of the current challenges facing the automotive industry, as well as a brief summary of the operation of DISI engines. The optical engine and auxiliary systems used in this work have been outlined in Chapter 2. A range of optical access is offered via a selection of cylinder liners including a full steel barrel, a full quartz barrel, and a short steel barrel with a quartz annulus. The top surface of the liners has a curved profile to provide uninterrupted views of the fuel injector and spark plug. The intake system has been designed to provide a wide range of operating conditions including boosting and a continuously variable valve lift system. This facility ensures that a broad range of optical diagnostics can be applied; in this work, a high-speed Particle Image Velocimetry (PIV) system has been installed and commissioned.

Chapter 3 provides the general theory of the PIV technique and outlines the system that has been installed on the optical engine. The system is capable of providing planar flow field measurements at a rate of 3.7 kHz at full resolution (1280 × 800 pixels) and a total of 6000 frame pairs in single test. The sheet optics and camera are both mounted on motorised

translation stages to allow quick and simple alignment of the sheet in the combustion chamber. The timing delay between the laser pulses can be varied throughout the cycle to account for variation in flow speeds and improve the dynamic range of the measurements. Application of PIV in an optical engine results in some specific challenges that must be addressed to ensure the quality of the results. One of the main issues is the excessive scattered light from the reflective surfaces of the cylinder head and walls. A number of methods have been investigated to reduce the scattered light, including matt black paint, fluorescent paint with appropriate optical filters, and varying the polarisation of the laser light. Fluorescent paint was found to be promising in terms of scatter reduction; however, it must be sufficiently robust to withstand the energy in the focussed laser sheet. Matt black paint proved to be the most effective and robust method of reducing scatter from the pent-roof and cylinder walls. A quarter-wave plate was used to convert the polarisation of the laser light from linear to circular in order to equalise the scatter from the cylinder head and improve the contrast of the particle images.

Chapter 4 provides a summary of existing methods that are used to quantify the differences between flow fields, both experimental and simulated. The relevance index (RI) is identified as a useful tool that provides an absolute measure of the similarity between two flow fields in terms of alignment. However, by definition it does not account for the magnitudes of the velocity vectors, therefore regions of mis-aligned, low-speed vectors carry the same weight as mis-aligned, high-speed vectors. This can lead to misleading spatially averaged results for flows with rotating structures such as those present in modern DISI engines designed for large-scale tumble motion. The relevance index was modified to produce a new metric, the Weighted Relevance Index (WRI), that accounts for the local flow velocities. In this way, mis-aligned vectors with high kinetic energy are penalised

more than those with low kinetic energy. Similarly, a metric named the Weighted Magnitude Index (WMI), has been developed to quantify differences in flow speed between two velocity fields. A combined metric that accounts for both alignment and magnitude was found to be a useful tool for comparing flow fields, therefore the Combined Magnitude and Relevance Index (CMRI) was developed. An example of its application is investigating how many cycles are required to produce a representative mean flow field. A large dataset of 1000 cycles was split into smaller subsets that ranged in size from 2 to 999 randomly sampled cycles and then compared with the mean of the whole dataset. It was found that 300 cycles is a conservative estimate for the number of cycles required to produce a representative mean.

The metrics developed in Chapter 4 are applied in Chapter 5 to compare experimental flow fields and those predicted by CFD RANS simulations for three different test conditions over a range of engine speeds and loads. The metrics were able to determine a number of differences between the measured and simulated flow fields:

- The simulations consistently predicted higher intake jet velocities during the induction process, as the valve is closing.
- For all conditions, the simulations failed to predict a region of low-speed flow that develops near the cylinder as the intake valve closes, which then affects the structure of the subsequent tumble flow. This is thought to be a region of the flow with high out-of-plane velocities due to the intake jet cutting through the measurement plane.
- For a single test point, T1, the differences between the simulated and measured flow fields increased throughout the compression stroke. This is in contrast to the other two test points, T2 and T8, which are very well matched. The CFD simulation for

T1 predicted a delayed motion of the tumble vortex in comparison to T2 and T8, which resulted in a different flow structure during the compression stroke.

These results highlight the advantages of the newly developed metrics over conventional metrics in exposing differences between flow fields that could potentially be hidden by spatially averaging, which is necessary for comparisons of large datasets.

All these comparisons have been made between a RANS simulation and ensemble averaged PIV measurements. The CMRI has also been used to investigate if there are flow fields of individual cycles that better match the simulated flow field than the ensemble average PIV flow field. It was found that there are indeed individual cycles that differ significantly from the mean PIV cycle and the simulation. In contrast, some individual cycles were found to be similar to the simulation, even though they include small-scale structure not present in the simulated flow fields due to the nature of the RANS method.

Chapter 6 investigates the effect of the in-cylinder flow field on cycle-by-cycle variations in combustion. Flow field measurements were made every 5°ca throughout the induction and compression strokes until 15°ca before ignition. In-cylinder pressure measurements were used to conditionally sample the cycles to form subsets of the 10% fastest burning, 10% medium burning and 10% slowest burning cycles. This conditioning was also applied to the flow field measurements in order to investigate any flow features that significantly influence combustion variation. The WRI and WMI were used to find the regions of greatest difference between the ensemble averages of the fast and slow burning subsets. The greatest difference in alignment between the two subsets tended to be a region of flow located at the inlet side of the engine, which was directed towards the inlet valve for the

fast burning cycles, and the spark plug for the slow burning cycles. The region determined by the WMI was located directly above the piston, where the flow tended to be significantly faster for fast burning cycles in comparison to slow burning cycles. These regions were then used to mask the flow fields of the whole dataset in order to produce a single vector for each cycle that represented the flow direction and magnitude in the masked region. Although, there was considerable variation in the spread of vectors for the whole dataset, trends indicated that flow directed towards the spark plug at 15°ca before ignition resulted in lower burn rates. In contrast, flows with higher velocity directed towards the cylinder head approximately 30°ca before ignition, resulted in faster combustion.

Synchronous broadband imaging of the flame agrees with these conclusions; not only do the flames of slow burning cycles appear to remain near the spark plug for longer in comparison to those of fast burning cycles, but they also tend to grow asymmetrically towards the exhaust valves. In contrast, the flames of fast burning cycles travel more uniformly in all directions, filling the field of view more quickly. Although the flow analysis and combustion imaging suggest that flows directed towards the spark plug 15°ca before ignition result in slower combustion, there was no strong correlation between the displacement of the early flame centroids and the flow velocity.

7.2 Future work

Throughout the course of this work, a number of areas for future work have been identified and are discussed here.

All the flow measurements in this work were taken in the central tumble plane. Although the intake system of this engine is designed to produce a strong tumble motion, the in-

cylinder flow is highly three-dimensional. Therefore, it would be interesting to measure the flow in other planes such as the swirl and cross-tumble. The piston crown features prevented measurements past 30°ca bTDC in this work, however, viewing through the transparent piston crown for the swirl plane would not be affected in the same way. Synchronous flow measurements and combustion imaging could be captured across TDC to investigate the effect of flow structures at the time of ignition, and the influence of the flame itself on the surrounding flow field. This would be particularly useful for further validation of CFD simulations.

In this work, comparisons were made between RANS simulations and ensemble-averaged PIV flow fields. The comparison of individual cycles to the simulations was also briefly discussed, and it was found that it is possible for the flow field of an individual cycle to better match the simulation than the ensemble average flow field. However, due to the nature of RANS simulations, which use averaged equations, it is unclear how appropriate it is to use individual cycles as validation. Further investigation into methods of improving the validation process for CFD simulations using individual cycles would be useful and particularly important for simulations of combustion.

The metrics defined in Chapter 4 were able to extract regions for the flow that were considerably different between fast and slow burning cycles. In particular, there was a region of fast flow located above the piston surface that appeared to result in a faster burn rate. A useful addition to this work would be to investigate a robust method of determining the origin of these fast pockets of gas. Identifying the source of differences in the flow fields would provide useful information to aid the design of future combustion systems.

It would be interesting to add to the work of Chapter 7 by investigating the link between the rate of combustion and turbulence. In this work, the effect of the bulk flow on the rate of combustion was investigated. However, turbulence is known to have a significant effect on the rate of flame growth, therefore it would be interesting to analyse the current dataset in further detail in an attempt to correlate turbulent flow parameters with pressure-based combustion indicators or flame-imaging data. For flows in engines, it is not trivial to separate in-cylinder turbulence and cyclic variation of the bulk flow. However, there are methods involving temporally and spatially filtering data to separate the contributions of turbulence from the bulk flow. Furthermore, the current PIV system provides in-cylinder flow measurements with a spatial resolution of 1.96 mm, which is sufficiently fine to resolve the integral length scale in engines.

8 References

[1] D. Kodjak, “Policies to Reduce Fuel Consumption, Air Pollution, and Carbon Emissions from Vehicles in G20 Nations,” *ICCT - Briefing Paper*, 2015. Available:http://www.theicct.org/sites/default/files/publications/ICCT_G20-briefing-paper_Jun2015_updated.pdf. [Accessed: 28-Aug-2016].

[2] ACEA, “The Automobile Industry Pocket Guide,” 2019. Available:https://www.acea.be/uploads/publications/ACEA_Pocket_Guide_2018-2019.pdf. [Accessed: 21-Apr-2019].

[3] SMMT, “SMMT Motor Industry Facts 2018,” 2018. Available:https://www.smmt.co.uk/wp-content/uploads/sites/2/SMMT-Motor-Industry-Facts-June-2018.pdf. [Accessed: 21-Apr-2019].

[4] Z. Yang and A. Bandivadekar, “2017 Global Update: Light-Duty Vehicle Greenhouse Gas and Fuel Economy Standards,” *ICCT - Report*, 2017. Available:http://www.theicct.org/sites/default/files/publications/2017-Global-LDV-Standards-Update_ICCT-Report_23062017_vF.pdf. [Accessed: 21-Apr-2019].

[5] IPCC, “Global Warming of 1.5°C,” *Summary for Policymakers*, 2018. Available: http://www.ipcc.ch/report/sr15/. [Accessed: 18-Oct-2018].

[6] EEA, “Greenhouse Gas Emissions from Transport,” *Indicator Assessment*, 2018. Available:https://www.eea.europa.eu/data-and-maps/indicators/transport-emissions-of-greenhouse-gases/transport-emissions-of-greenhouse-gases-11. [Accessed: 07-May-2019].

[7] P. Mock, “CO2 Emission Standards for Passenger Cars and Light-Commercial Vehicles in the European Union,” *ICCT Policy Update*, 2019. Available:https://www.theicct.org/sites/default/files/publications/EU-LCV-CO2-2030_ICCTupdate_20190123.pdf. [Accessed: 21-Apr-2019].

[8] U. Tietge, “CO2 emissions from new passenger cars in the EU : Car manufacturers’ performance in 2017,” *ICCT - Briefing Paper*, 2018. Available:https://www.theicct.org/sites/default/files/publications/EU_manufacturers_performance_CO2_20180712.pdf. [Accessed: 21-Apr-2019].

[9] Transport for London, “Ultra Low Emission Zone,” 2019. Available:https://tfl.gov.uk/modes/driving/ultra-low-emission-zone. [Accessed: 30-Apr-2019].

[10] Department for Transport, “Vehicle Licensing Statistics: Annual 2018,” *Statistical Release*, 2019. Available:https://assets.publishing.service.gov.uk/government/uploads/system/uploads/attachment_data/file/794736/vehicle-licensing-statistics-2018.pdf. [Accessed: 21-Apr-2019].

[11] ICCT, “European Vehicle Market Statistics - Pocketbook 2018/2019,” 2019. Available:https://www.theicct.org/sites/default/files/publications/ICCT_Pocketbook_2018_Final_20190408.pdf. [Accessed: 21-Apr-2019].

[12] GFEI, IEA, and ICCT, “Fuel Economy in Major Car Markets : Technology and Policy Drivers 2005-2017,” *Working Paper*, 2019. Available:https://www.theicct.org/sites/default/files/publications/GFEI_WP19_Final_V3_Web.pdf. [Accessed: 21-Apr-2019].

[13] U. Tietge (ICCT), S. Díaz, P. Mock, A. Bandivadekar, J. Dornoff, and N. Ligterink (TNO), “From Laboratory to Road - A 2018 update of official and ‘Real-World’ fuel consumption and CO2 values for passenger cars in Europe,” *ICCT - White Paper*, 2019. Available:https://www.theicct.org/sites/default/files/publications/Lab_to_Road_2018_fv_20190110.pdf. [Accessed: 21-Apr-2019].

[14] U. Tietge (ICCT) *et al.*, “From Laboratory to Road - A 2015 update of official and ‘Real-World’ fuel consumption and CO2 values for passenger cars in Europe,” *ICCT - White Paper*, 2015. Available:https://www.theicct.org/sites/default/files/publications/ICCT_LaboratoryToRoad_2015_Report_English.pdf. [Accessed: 17-May-2016].

[15] SMMT, “New Car CO2 Report 2018,” 2018. Available:https://www.smmt.co.uk/wp-content/uploads/sites/2/SMMT-New-Car-Co2-Report-2018-artwork.pdf. [Accessed: 22-Apr-2019].

[16] J. German, “Hybrid vehicles: Trends in Technology Development and Cost Reduction,” *ICCT - Technical Brief*, 2015. Available:https://www.theicct.org/sites/default/files/publications/ICCT_TechBriefNo1_Hybrids_July2015.pdf. [Accessed: 17-May-2016].

[17] R. Reeves *et al.*, “Electric Vehicles: Driving the Transition,” *House of Commons - Business, Energy and Industrial Strategy Committee: 14th Report of Session 2017-2019*, 2018. Available:https://publications.parliament.uk/pa/cm201719/cmselect/cmbeis/383/383.pdf. [Accessed: 22-Apr-2019].

[18] U. Tietge, P. Mock, N. Lutsey, and A. Campestrini, “Comparison of Leading Electric Vehicle Policy and Deployment in Europe,” *ICCT - White Paper*, 2016. Available:http://www.theicct.org/sites/default/files/publications/ICCT_EVpolicies-Europe-201605.pdf. [Accessed: 22-Apr-2019].

[19] Ofgem, “Implicatins of the transition to Electric Vehicles,” *Future Insights Series*, 2018. Available:https://www.ofgem.gov.uk/ofgem-publications/136142. [Accessed: 22-Apr-2019].

[20] BP, “BP Statistical Review of World Energy,” 2018. Available:https://www.bp.com/content/dam/bp/business-sites/en/global/corporate/pdfs/energy-economics/statistical-review/bp-stats-review-2018-full-report.pdf. [Accessed: 21-Apr-2019].

[21] Deloitte, “New market. New entrants. New challenges. Battery Electric Vehicles,” *Strategic Report*, 2018. Available:https://www2.deloitte.com/content/dam/Deloitte/uk/Documents/manufacturing/deloitte-uk-battery-electric-vehicles.pdf. [Accessed: 22-Apr-2019].

[22] National Grid, “Future Energy Scenarios,” 2018. Available:http://fes.nationalgrid.com/media/1363/fes-interactive-version-final.pdf. [Accessed: 21-Apr-2019].

[23] A. Joshi, “Review of Vehicle Engine Efficiency and Emissions,” SAE Technical Paper 2019-01–0314, 2019, DOI: 10.4271/2019-01-0314.

[24] M. Bassett, J. Hall, T. Cains, M. Underwood, R. Wall, and B. G. Richards, "Dynamic Downsizing Gasoline Demonstrator," *SAE Int. J. Engines*, 10(3):884–891, 2017, DOI: 10.4271/2017-01-0646.

[25] Y. Wada, K. Nakano, K. Mochizuki, and R. Hata, "Development of a New 1.5L I4 Turbocharged Gasoline Direct Injection Engine," SAE Technical Paper 2016-01–1020, 2016, DOI: 10.4271/2016-01-1020.

[26] J. Kargul, M. Stuhldreher, D. Barba, C. Schenk, S. Bohac, and J. Mcdonald, "Benchmarking a 2018 Toyota Camry 2.5-Liter Atkinson Cycle Engine with Cooled-EGR," SAE Technical Paper 2019-01–0249, 2019, DOI: 10.4271/2019-01-0249.Abstract.

[27] N. Yoshida, "Development of New I4 2.5L Gasoline Direct Injection Engine," SAE Technical Paper 2019-01–1199, 2019, DOI: 10.4271/2019-01-1199

[28] G. Doornbos, S. Hemdal, and D. Dahl, "Reduction of Fuel Consumption and Engine-out NO x Emissions in a Lean Homogeneous GDI Combustion System, Utilizing Valve Timing and an Advanced Ignition System," SAE Technical Paper 2015-01–0776, 2015, DOI: 10.4271/2015-01-0776.

[29] K. Clasen, L. Koopmans, and D. Dahl, "Homogeneous Lean Combustion in a 2lt Gasoline Direct Injected Engine with an Enhanced Turbo Charging System," SAE Technical Paper 2018-01–1670, 2018, DOI: 10.4271/2018-01-1670.

[30] C. Schenk and P. Dekraker, "Potential Fuel Economy Improvements from the Implementation of cEGR and CDA on an Atkinson Cycle Engine," SAE Technical Paper 2017-01–1016, 2017, DOI: 10.4271/2017-01-1016.

[31] K. Hwang *et al.*, "Development of New High-Efficiency Kappa 1.6L GDI Engine," SAE Technical Paper 2016-01-0667, 2016, DOI: 10.4271/2016-01-0667.

[32] M. Choi, D. B. Roth, and D. Jakiela, "Synergies of Cooled External EGR, Water Injection, Miller Valve Events and Cylinder Deactivation for the Improvement of Fuel Economy on a Turbocharged-GDI Engine; Part 2, Engine Testing," SAE Technical Paper 2019-01–0242, 2019, DOI: 10.4271/2019-01-0242

[33] Mazda, "Mazda Reveals All New Mazda 3," *Press Release*, 2018. Available:https://insidemazda.mazdausa.com/press-release/mazda-reveals-all-new-mazda3/. [Accessed: 30-Apr-2019].

[34] J. Borée and P. C. Miles, *In-Cylinder Flow - Encyclopedia of Automotive Engineering Encyclopedia of Automotive Engineering*. John Wiley & Sons, 2014. DOI: 10.1002/9781118354179

[35] R. H. Stanglmaier, M. J. Hall, and R. D. Matthews, "Fuel-Spray / Charge-Motion Interaction within the Cylinder of a Direct-Injected , 4-Valve , SI Engine," SAE Technical Paper 980155, 1998, DOI: 10.4271/980155.

[36] J. B. Heywood, *Internal Combustion Engine Fundamentals*. New York: McGraw-Hill Education, 1988. ISBN: 9781260116106

[37] R. Stone, *Introduction to Internal Combustion Engines*. Basingstoke: Palgrave Macmillan, 2012, ISBN: 9780230576636

[38] J. L. Lumley, *Engines - An Introduction*. Cambridge University Press, 1999, ISBN: 9781139175135

[39] N. Ozdor, M. Dulger, and E. Sher, "Cyclic Variability in Spark Ignition Engines A Literature Survey," SAE Transactions 940987, 1994, DOI: 10.4271/940987

[40] D. L. Reuss, "Cyclic Variability of Large-Scale Turbulent Structures in Directed and Undirected IC Engine Flows," SAE Technical Paper 2000-01–0246, 2000, DOI: 10.4271/2000-01-0246.

[41] T. Justham, S. Jarvis, A. Clarke, C. P. Garner, G. K. Hargrave, and N. A. Halliwell, “Simultaneous study of intake and in-cylinder IC engine flow fields to provide an insight into intake induced cyclic variations,” *J. Phys. Conf. Ser.*, 45(1):146–153, 2006, DOI: 10.1088/1742-6596/45/1/019.

[42] T. Justham, S. Jarvis, C. P. Garner, G. K. Hargrave, A. Clarke, and D. Richardson, “Single Cylinder Motored SI IC Engine Intake Runner Flow Measurement Using Time Resolved Digital Particle Image Velocimetry,” SAE Technical Paper 2006-01–1043, 2006, DOI: 10.4271/2006-01-1043.

[43] H. Ruhland, T. Lorenz, J. Dunstheimer, A. Breuer, and M. Khosravi, “A Study on Charge Motion Requirements for a Class-Leading GTDI Engine,” SAE Technical Paper 2017-24–0065, 2017, DOI: 10.4271/2017-24-0065.

[44] R. Ogink and A. Babajimopoulos, “Investigating the Limits of Charge Motion and Combustion Duration in a High-Tumble Spark-Ignited Direct-Injection Engine,” *SAE Int. J. Engines*, 9(4):2129–2141, 2016, DOI: 10.4271/2016-01-2245.

[45] Y. Yoshihara, K. Nakata, D. Takahashi, T. Omura, and A. Ota, “Development of High Tumble Intake-Port for High Thermal Efficiency Engines,” SAE Technical Paper 2016-01–0692, 2016, DOI: 10.4271/2016-01-0692.

[46] P. Adomeit, M. Jakob, S. Pischinger, A. Brunn, and J. Ewald, “Effect of Intake Port Design on the Flow Field Stability of a Gasoline DI Engine,” SAE Technical Paper 2011-01–1284, 2011, DOI: 10.4271/2011-01-1284.

[47] B. Khalighi, “Intake-Generated Swirl and Tumble Motions in a 4-Valve Engine with Various Intake Configurations-Flow Visualization and Particle Tracking Velocimetry,” SAE Technical Paper 900059, 1990, DOI: 10.4271/900059

[48] T. Wang, D. Liu, B. Tan, G. Wang, and Z. Peng, “An investigation into in-cylinder tumble flow characteristics with variable valve lift in a gasoline engine,” *Flow, Turbul. Combust.*, 94(2):285–304, 2015, DOI: 10.1007/s10494-014-9562-4.

[49] D. Liu, T. Wang, M. Jia, and G. Wang, “Cycle-to-cycle variation analysis of in-cylinder flow in a gasoline engine with variable valve lift,” *Exp. Fluids*, 53(3):585–602, 2012, DOI: 10.1007/s00348-012-1314-4.

[50] I. Bücker, D. Karhoff, M. Klaas, and W. Schröder, “Engine In-Cylinder Flow Control via Variable Intake Valve Timing,” SAE Technical Paper 2013-24–0055, 2013, DOI: 10.4271/2013-24-0055.

[51] J. W. G. Turner *et al.*, “The HOTFIRE Homogeneous GDI and Fully Variable Valve Train Project - An Initial Report,” SAE Technical Paper 2006-01–1260, 2006, DOI: 10.4271/2006-01-1260.

[52] J. W. G. Turner, M. D. Bassett, R. J. Pearson, G. Pitcher, and K. J. Douglas, “New Operating Strategies Afforded by Fully Variable Valve Trains,” SAE Technical Paper 2004-01–1386, 2004, DOI: 10.4271/2004-01-1386.

[53] P. A. Stansfield *et al.*, “Unthrottled Engine Operation using Variable Valve Actuation : The Impact on the Flow Field , Mixing and Combustion Reprinted From : Diesel Injection SI Engine Technology,” SAE Technical Paper 2007-01–1414, 2007.

[54] D. Cleary and G. Silvas, “Unthrottled Engine Operation with Variable Intake Valve Lift , Duration , and Timing,” SAE Technical Paper 2007-01–1282, 2007, DOI: 10.4271/2007-01-1282

[55] C. Arcoumanis and J. H. Whitelaw, “Fluid Mechanics of internal combustion engines - a review,” *Proc. Inst. Mech. Eng. Part C*, 201(1):57–74, 1986, DOI: 10.1017/CBO9780511794353.

[56] S. B. Pope, *Turbulent Flows*. Cambridge: Cambridge University Press, 2000, ISBN: 9780511840531

[57] C. Arcoumanis, Z. Hu, C. Vafidis, and J. Whitelaw, "Tumbling Motion: A Mechanism for Turbulence Enhancement in Spark-Ignition Engines," SAE Technical Paper 900060, 1990, DOI: 10.4271/900060

[58] M. Reeves, M. J. Haste, C. P. Garner, and N. A. Halliwell, "Barrel swirl breakdown in spark-ignition engines: insights from particle image velocimetry measurements," *Proc. Inst. Mech. Eng. Part D-Journal Automob. Eng.*, 213(D6):595–609, 1999, DOI: Doi 10.1243/0954407991527134.

[59] H. Zhao, *Advanced Direct Injection Combustion Engine Technologies and Development*. Cambridge: Woohead Publishing Limited, 2010, ISBN: 9781845697440

[60] A. Taylor, "Science review of internal combustion engines," *Energy Policy*, 36:4657–4667, 2008, DOI: 10.1016/j.enpol.2008.09.001.

[61] J. E. T. Rimmer, E. J. Long, C. P. Garner, G. K. Hargrave, D. Richardson, and S. Wallace, "The Influence of Single and Multiple Injection Strategies on In-Cylinder Flow and Combustion within a DISI Engine," SAE Technical Paper 2009-01–0660, 2009, DOI: 10.4271/2009-01-0660.

[62] C. Schwarz, E. Schünemann, B. Durst, J. Fischer, and A. Witt, "Potentials of the Spray-Guided BMW DI Combustion System," SAE Technical Paper 2006-01–1265, 2006.

[63] F. Zhao, M. C. Lai, and D. L. Harrington, "Automotive spark-ignited direct-injection gasoline engines," *Prog. Energy Combust. Sci.*, 25(5):437–562, 1999, DOI: 10.1016/S0360-1285(99)00004-0.

[64] F. Leach, T. Knorsch, C. Laidig, and W. Wiese, "A Review of the Requirements for Injection Systems and the Effects of Fuel Quality on Particulate Emissions from GDI Engines," SAE Technical Paper 2018-01–1710, 2018, DOI: 10.4271/2018-01-1710.

[65] W. F. Piock, B. Befrui, A. Berndorfer, and G. Hoffmann, "Fuel Pressure and Charge Motion Effects on GDi Engine Particulate Emissions," *SAE Int. J. Engines*, 8(2):2015-01–0746, 2015, DOI: 10.4271/2015-01-0746.

[66] E. Stevens and R. Steeper, "Piston Wetting in an Optical DISI Engine : Fuel Films, Pool Fires , and Soot Generation," SAE Technical Paper 2001-01–1203, 2001, DOI: 10.4271/2001-01-1203

[67] R. N. Fansler, T. D., Reuss, D. L., Sick, V., & Dahms, "Invited Review: Combustion instability in spray-guided stratified-charge engines: A review," *Int. J. Engine Res.*, 16(3):260–305, 2015, DOI: 10.1177/1468087414565675

[68] P. C. Miles, "History and Evolution of Optically Accessible Research and Their Impact on Our Undestanding of Engine Combustion," Proceedings of the ASME 2014 Internal Combustion Engine Division Fall Technical Conference ICEF2014-5701, 2014, DOI: 10.1115/ICEF2014-5701

[69] H. Zhao, *Laser Diagnostics and Optical Measurements Techniques in Internal Combustion Engines*. SAE International, 2012, ISBN: 978-0768057829

[70] V. Sick, "High speed imaging in fundamental and applied combustion research," *Proc. Combust. Inst.*, 34(2):3509–3530, 2013, DOI: 10.1016/j.proci.2012.08.012.

[71] C. Fajardo and V. Sick, "Flow field assessment in a fired spray-guided spark-ignition direct-injection engine based on UV particle image velocimetry with sub crank angle resolution," *Proc. Combust. Inst.*, 31(2):3023–3031, 2007, DOI: 10.1016/j.proci.2006.08.016.

[72] V. Sick, M. C. Drake, and T. D. Fansler, "High-speed imaging for direct-injection gasoline engine research and development," *Exp. Fluids*, 49(4):937–947, 2010, DOI: 10.1007/s00348-010-0891-3.

[73] M. C. Drake and D. C. Haworth, “Advanced gasoline engine development using optical diagnostics and numerical modeling,” *Proc. Combust. Inst.*, 31(1):99–124, 2007, DOI: 10.1016/j.proci.2006.08.120.

[74] C. Schulz and V. Sick, “Tracer-LIF diagnostics: Quantitative measurement of fuel concentration, temperature and fuel/air ratio in practical combustion systems,” *Prog. Energy Combust. Sci.*, 31(1):75–121, 2005, DOI: 10.1016/j.pecs.2004.08.002.

[75] B. Williams *et al.*, “Multi-Component Quantitative PLIF: Robust Engineering Measurements of Cyclic Variation in a Firing Spray-Guided Gasoline Direct Injection Engine,” SAE Technical Paper 2008-01–1073, 2008, DOI: 10.4271/2008-01-1073.

[76] S. Einecke, C. Schulz, V. Sick, A. Dreizler, R. Schießl, and U. Maas, “Two-Dimensional Temperature Measurements in an SI Engine Using Two-Line Tracer LIF,” SAE Technical Paper 982468, 1998, DOI: 10.4271/982468

[77] B. Scott, C. Willman, B. Williams, P. Ewart, R. Stone, and D. Richardson, “In-Cylinder Temperature Measurements Using Laser Induced Grating Spectroscopy and Two-Colour PLIF,” *SAE Int. J. Engines*, 10(4):2191–2201, 2017, DOI: 10.4271/2017-24-0045.

[78] B. Peterson, E. Baum, B. Böhm, V. Sick, and A. Dreizler, “High-speed PIV and LIF imaging of temperature stratification in an internal combustion engine,” *Proc. Combust. Inst.*, 34(2):3653–3660, 2013, DOI: 10.1016/j.proci.2012.05.051.

[79] T. Fansler and S. E. Parrish, “Spray Measurement Technology: A Review,” *Meas. Sci. Technol.*, 26:012002, 2015, DOI: 10.1088/0957-0233/26/1/012002.

[80] B. Böhm, C. Heeger, R. L. Gordon, and A. Dreizler, “New perspectives on turbulent combustion: Multi-parameter high-speed planar laser diagnostics,” *Flow, Turbul. Combust.*, 86(3–4):313–341, 2011, DOI: 10.1007/s10494-010-9291-2.

[81] R. N. Dahms, M. C. Drake, T. D. Fansler, T. W. Kuo, and N. Peters, “Understanding ignition processes in spray-guided gasoline engines using high-speed imaging and the extended spark-ignition model SparkCIMM. Part A: Spark channel processes and the turbulent flame front propagation,” *Combust. Flame*, 158(11):2229–2244, 2011, DOI: 10.1016/j.combustflame.2011.03.012.

[82] A. Dreizler and B. Böhm, “Advanced laser diagnostics for an improved understanding of premixed flame-wall interactions,” *Proc. Combust. Inst.*, 35(1):37–64, 2015, DOI: 10.1016/j.proci.2014.08.014.

[83] D. C. Haworth, “Large-Eddy Simulation of In-Cylinder Flows,” *Oil Gas Sci. Technol.*, 54(2):175–185, 1999, DOI: 10.2516/ogst:1999012.

[84] D. C. Haworth, “A Review of Turbulent Combustion Modeling for Multidimensional In-Cylinder CFD,” SAE Technical Paper 2005-01–0993, 2005, DOI: 10.4271/2005-01-0993.

[85] H. Versteeg and W. Malalasekera, *An Introduction to Computational Fluid Dynamics: The Finite Volume Method*. Harlow, London: Pearson Education Ltd, 2007, ISBN: 9788131720486

[86] C. Krüger, J. Schorr, F. Nicollet, J. Bode, A. Dreizler, and B. Böhm, “Cause-and-effect chain from flow and spray to heat release during lean gasoline combustion operation using conditional statistics,” *Int. J. Engine Res.*, 18(1–2):143–154, 2017, DOI: 10.1177/1468087416686721.

[87] C. Lacour and C. Pera, “An Experimental Database Dedicated to the Study and Modelling of Cyclic Variability in Spark-Ignition Engines with LES,” SAE Technical Paper 2011-01–1282, 2011, DOI: 10.4271/2011-01-1282.

[88] E. Baum, B. Peterson, B. Böhm, and A. Dreizler, "On theValidation of LES Applied to Internal Combustion Engine Flows: Part 1: Comprehensive Experimental Database," *Flow, Turbul. Combust.*, 92(1–2):269–297, 2014, DOI: 10.1007/s10494-013-9468-6.

[89] M. Baumann, F. Di Mare, and J. Janicka, "On the validation of large eddy simulation applied to internal combustion engine flows part II: Numerical analysis," Flow, Turbulence and Combustion 299–317, 2014, DOI: 10.1007/s10494-013-9472-x.

[90] P. Schiffmann, S. Gupta, D. Reuss, V. Sick, X. Yang, and T. W. Kuo, "TCC-III Engine Benchmark for Large-Eddy Simulation of IC Engine Flows," *Oil Gas Sci. Technol.*, 71(3), 2016, DOI: 10.2516/ogst/2015028.

[91] D. A. Sunnarborg, "Quick Release Engine Cylinder," US Patent 6158406, 2000.

[92] F. W. Bowditch, "A New Tool for Combustion Research A Quartz Piston Engine," SAE Technical Paper 610002, 1961.

[93] A. W. Roughton, "Resolved Spatially Turbulence Measurements in Internal Combustion Engines Using Flying Hot-Wire Velocimetry," Thesis, University of Cambridge, 1989.

[94] P. C. Stainback and K. A. Nagabushana, "Review of Hot-Wire Anemometry Techniques and the Range of their Applicability for Various Flows," *J. Fluids Eng. Trans. ASME*, 167:93–133, 1993.

[95] C. Tropea, "Laser Doppler Anemometry: Recent Developments and Future Challenges," *Meas. Sci. Technol.*, 6:605, 1995, DOI: 10.1088/0957-0233/6/6/001

[96] P. O. Witze, "A Critical Comparsion of Hot-Wire Anemometry and Laser Doppler Velocimetry for I. C. Engine Applications," SAE Technical Paper 800132, 1979, DOI: 10.4271/800132

[97] K. Kikuchi and O. Mochizuki, "Micro-PIV (micro particle image velocimetry) visualization of red blood cells (RBCs) sucked by a female mosquito," *Meas. Sci. Technol.*, 22:064002, 2011, DOI: 10.1088/0957-0233/22/6/064002.

[98] J. Bosbach, M. Kuhn, and C. Wagner, "Large scale particle image velocimetry with helium filled soap bubbles," *Exp. Fluids*, 46(3):539–547, 2009, DOI: 10.1007/s00348-008-0579-0.

[99] A. K. Prasad, "Stereoscopic particle image velocimetry," *Exp. Fluids*, 29(2):103–116, 2000.

[100] Q. Gao, H. Wang, and G. Shen, "Review on development of volumetric particle image velocimetry," *Chinese Sci. Bull.*, 58(36):4541–4556, 2013, DOI: 10.1007/s11434-013-6081-y.

[101] M. R. Maxey and J. J. Riley, "Equation of motion for a small rigid sphere in a nonuniform flow," *Phys. Fluids*, 26(4):883, 1983, DOI: 10.1063/1.864230.

[102] R. Mei, "Velocity fidelity of flow tracer particles," *Exp. Fluids*, 22(1):1–13, 1996, DOI: 10.1007/BF01893300.

[103] R. J. Adrian and J. Westerweel, *Particle Image Velocimetry*. Cambridge: Cambridge University Press, 2011, ISBN: 0521440084

[104] A. Melling, "Tracer particles and seeding for particle image velocimetry," *Meas. Sci. Technol.*, 8:1406–1416, 1997, DOI: 10.1088/0957-0233/8/12/005.

[105] M. Raffel, C. E. Willert, S. T. Wereley, and J. Kompenhans, *Particle Image Velocimetry: A Practical Guide*. Berlin: Springer, 2007, ISBN: 978-3-319-68851-0

[106] C. Willert, S. Moessner, and J. Klinner, "Pulsed Operation of High Power Light Emitting Diodes for Flow Velocimetry," *8th Int. Symp. Part. Image Velocim. - PIV09*, 2009.

[107] C. Willert, B. Stasicki, J. Klinner, and S. Moessner, "Pulsed operation of high-power light emitting diodes for imaging flow velocimetry," *Meas. Sci. Technol.*, 21:075402, 2010, DOI: 10.1088/0957-0233/21/7/075402.
[108] A. A. Aguirre-Pablo, M. K. Alarfaj, E. Li, J. F. Hernandez-Sanchez, and S. T. Thoroddsen, "Tomographic Particle Image Velocimetry using Smartphones and Colored Shadows," *Nat. Sci. Reports*, 7(1):3714, 2017, DOI: 10.1038/s41598-017-03722-9
[109] C. E. Willert and M. Gharib, "Digital particle image velocimetry," *Exp. Fluids*, 10(4):181–193, 1991, DOI: 10.1007/BF00190388
[110] R. Hain, C. J. Kahler, and C. Tropea, "Comparison of CCD , CMOS and intensified cameras," *Exp. Fluids*, 42(3):403–411, 2007, DOI: 10.1007/s00348-006-0247-1.
[111] J. Westerweel, "Fundamentals of digital particle image velocimetry," *Meas. Sci. Technol.*, 8:1379–1392, 1997, DOI: 10.1088/0957-0233/8/12/002.
[112] O. Pust, "PIV: Direct Cross-Correlation compared with FFT-based Cross-Correlation," *Proc. 10th Int. Symp. Appl. Laser Tech. to Fluid Mech.*, 2000.
[113] R. D. Keane and R. J. Adrian, "Theory of cross-correlation analysis of PIV images," *Appl. Sci. Res.*, 49(3):191–215, 1992, DOI: 10.1007/BF00384623.
[114] A. K. Prasad, R. J. Adrian, C. C. Landreth, and P. W. Offutt, "Effect of Resolution on the Speed and Accuracy of Particle Image Velocimetry Interrogation," *Exp. Fluids*, 13(2–3):105–116, 1992, DOI: 10.1007/BF00218156
[115] J. Westerweel, "Efficient detection of spurious vectors in particle image velocimetry data," *Exp. Fluids*, 16(3–4):236–247, 1994, DOI: 10.1007/BF00206543.
[116] J. Westerweel and F. Scarano, "Universal outlier detection for PIV data," *Exp. Fluids*, 39(6):1096–1100, 2005, DOI: 10.1007/s00348-005-0016-6.
[117] LaVision GmbH, "Laser Timing Stabilizer Product Manual," Gottingen, 2016.
[118] R. D. Keane and R. J. Adrian, "Optimization of particle image veIocimeters. Part I: Double pulsed systems," *Meas. Sci. Technol.*, 1:1202–1215, 1990, DOI: 10.1088/0957-0233/1/11/013
[119] F. Scarano and M. L. Riethmuller, "Iterative multigrid approach in PIV image processing with discrete window offset," *Exp. Fluids*, 26(6):513–523, 1999, DOI: 10.1007/s003480050318.
[120] F. Scarano and M. L. Riethmuller, "Advances in iterative multigrid PIV image processing," *Exp. Fluids*, S051–S060, 2000, DOI: 10.1007/s003480070007.
[121] J. Westerweel, D. Dabiri, and M. Gharib, "The effect of a discrete window offset on the accuracy of cross-correlation analysis of digital PIV recordings," *Exp. Fluids*, 23(1):20–28, 1997, DOI: 10.1007/s003480050082.
[122] J. Westerweel, "On velocity gradients in PIV interrogation," *Exp. Fluids*, 44(5):831–842, 2008, DOI: 10.1007/s00348-007-0439-3.
[123] H. T. Huang, H. E. Fiedler, and J. J. Wang, "Limitation and improvement of PIV - Part I: Limitation of conventional techniques due to deformation of particle image patterns," *Exp. Fluids*, 15(4–5):168–174, 1993, DOI: 10.1007/BF00189883.
[124] H. T. Huang, H. E. Fiedler, and J. J. Wang, "Limitation and improvement of PIV - Part II: Particle image distortion, a novel technique," *Exp. Fluids*, 15(4–5):263–273, 1993, DOI: 10.1007/BF00223404.
[125] F. Scarano, "Iterative image deformation methods in PIV," *Meas. Sci. Technol.*, 13:R1–R19, 2002, DOI: 10.1088/0957-0233/13/1/201
[126] K. Jambanuthan, X. Y. Ju, B. N. Dobbins, and S. Ashforth-Frost, "An improved cross correlation technique for particle image velocimetry," *Meas. Sci. Technol.*, 6:507–514, 1995, DOI: 10.1088/0957-0233/6/5/012
[127] LaVision, "Personal communication," 2017.

[128] P. Abraham, D. Reuss, and V. Sick, “High-Speed Particle Image Velocimetry Study of In-Cylinder Flows with Improved Dynamic Range,” SAE Technical Paper 2013-01–0542, 2013, DOI: 10.4271/2013-01-0542.
[129] CD-Adapco, “STAR-CD Methodolgy Manual,” 2015.
[130] D. L. Reuss, M. Megerle, and V. Sick, “Particle-image velocimetry measurement errors when imaging through a transparent engine cylinder,” *Meas. Sci. Technol.*, 13:1029–1035, 2002, DOI: 10.1088/0957-0233/13/7/309
[131] E. Paterna, P. Moonen, V. Dorer, and J. Carmeliet, “Mitigation of surface reflection in PIV measurements,” *Meas. Sci. Technol.*, 24:057003, 2013, DOI: 10.1088/0957-0233/24/5/057003.
[132] T. Lee, “PIV study of near-field tip vortex behind perforated Gurney flaps,” *Exp. Fluids*, 50(2):351–361, 2011, DOI: 10.1007/s00348-010-0933-x.
[133] H. Nobach and E. Bodenschatz, “Limitations of accuracy in PIV due to individual variations of particle image intensities,” *Exp. Fluids*, 47(1):27–38, 2009, DOI: 10.1007/s00348-009-0627-4.
[134] R. J. Adrian, “Twenty years of particle image velocimetry,” *Exp. Fluids*, 39(2):159–169, 2005, DOI: 10.1007/s00348-005-0991-7.
[135] R. de O. A. Coelho, C. A. G. Junior, R. B. R. Da Costa, R. L. Franco, and R. M. Valle, “High-speed PIV Validation for CFD Simulation of Steady Flow Through a Single Cylinder Research Engine,” SAE Technical Paper 2015-36–0298, 2015, DOI: 10.4271/2015-36-0298.
[136] A. G. S. Raj, J. M. Mallikarjuna, and G. Venkitachalam, “Analysis of In-Cylinder Air Motion in a DI Diesel Engine with Four Different Piston Bowl Configuration - A CFD and PIV Comparison,” *SAE Int. J. Engines*, 6(4):1978–1983, 2013, DOI: 10.4271/2013-01-2786.
[137] M. M. Ameen, X. Yang, T. Kuo, and S. Som, “Using LES to simulate cycle-to-cycle variability during the gas exchange process,” Proceedings of the ASME 2017 Internal Combustion Fall Technical Conference ICEF2017-3591, 2017, DOI: 10.1115/ICEF20173591.
[138] X. Yang, S. Gupta, T. Kuo, and V. Gopalakrishnan, “RANS and LES of IC Engine Flows – A Comparative Study,” Proceedings of the ASME 2013 Internal Combustion Engine Division Fall Technical Conference ICEF2013-19043, 2013, DOI: 10.1115/ICEF2013-19043.
[139] X. Yang, S. Gupta, T.-W. Kuo, and V. Gopalakrishnan, “RANS and Large Eddy Simulation of Internal Combustion Engine Flows—A Comparative Study,” *J. Eng. Gas Turbines Power*, 136:051507, 2014, DOI: 10.1115/1.4026165.
[140] C. Pera and C. Angelberger, “Large Eddy Simulation of a Motored Single-Cylinder Engine Using System Simulation to Define Boundary Conditions: Methodology and Validation,” SAE Technical Paper 2011-01–0834, 2011, DOI: 10.4271/2011-01-0834.
[141] N. Van Dam, M. Sjöberg, and S. Som, “Large-Eddy Simulations of Spray Variability Effects on Flow Variability in a Direct-Injection Spark-Ignition Engine under Non-Combusting Operating Conditions,” SAE Technical Paper 2018-01–0196, 2018, DOI: 10.4271/2018-01-0196.
[142] N. Van Dam and C. Rutland, “Understanding In-Cylinder Flow Variability Using Large Eddy Simulations,” Proceedings of the ASME 2015 Internal Combustion Engine Division Fall Technical Conference ICEF2015-1103, 2015, DOI: 10.1115/ICEF2015-1103.

[143] N. Van Dam, W. Zeng, M. Sjöberg, and S. Som, "Parallel Multi-cycle LES of an Optical Pent-roof DISI Engine under Motored Operating Conditions," Proceedings of the ASME 2017 Internal Combustion Fall Technical Conference ICEF2017-3603, 2017, DOI: 10.1115/ICEF2017-3603.

[144] K. Liu and D. C. Haworth, "Development and Assessment of POD for Analysis of Turbulent Flow in Piston Engines," SAE Technical Paper 2011-01–0830, 2011, DOI: 10.4271/2011-01-0830.

[145] T. Wang, W. Li, M. Jia, D. Liu, W. Qin, and X. Zhang, "Large-eddy simulation of in-cylinder flow in a DISI engine with charge motion control valve: Proper orthogonal decomposition analysis and cyclic variation," *Appl. Therm. Eng.*, 75:561–574, 2015, DOI: 10.1016/j.applthermaleng.2014.10.081.

[146] B. Hu, S. Banerjee, K. Liu, and Q. Xue, "Large Eddy Simulation of a Turbulent Non-Reacting Spray Jet," Proceedings of the ASME 2015 Internal Combustion Engine Division ICEF2015-1033, 2015, DOI: 10.1115/ICEF2015-1033.

[147] T. W. Kuo, X. Yang, V. Gopalakrishnan, and Z. Chen, "Large Eddy Simulation (LES) for IC Engine Flows," *Oil Gas Sci. Technol.*, 69(1):61–81, 2014, DOI: 10.2516/ogst/2013127.

[148] H. Chen, D. L. Reuss, D. L. Hung, and V. Sick, "A practical guide for using proper orthogonal decomposition in engine research," *Int. J. Engine Res.*, 14(4):307–319, 2013, DOI: 10.1177/1468087412455748.

[149] H. Chen, M. Xu, and D. L. S. Hung, "Analyzing In-cylinder Flow Evolution and Variations in a Spark-Ignition Direct-Injection Engine Using Phase-Invariant Proper Orthogonal Decomposition Technique," SAE Technical Paper 2014-01–1174, 2014, DOI: 10.4271/2014-01-1174.

[150] H. Chen, D. L. S. Hung, M. Xu, H. Zhuang, and J. Yang, "Proper orthogonal decomposition analysis of fuel spray structure variation in a spark-ignition direct-injection optical engine," *Exp. Fluids*, 55:1703, 2014, DOI: 10.1007/s00348-014-1703-y.

[151] H. Chen, D. L. S. Hung, M. Xu, and J. Zhong, "Analyzing the Cycle-To-Cycle Variations of Pulsing Spray Characteristics By Means of the Proper Orthogonal Decomposition," *At. Sprays*, 23(7):623–641, 2013, DOI: 10.1615/AtomizSpr.2013007851.

[152] M. M. Ameen, Y. Pei, and S. Som, "Computing Statistical Averages from Large Eddy Simulation of Spray Flames," SAE Technical Paper 2016-01–0585, 2016, DOI: 10.4271/2016-01-0585.

[153] P. K. Senecal, E. Pomraning, K. J. Richards, and S. Som, "Grid-Convergent Spray Models for Internal Combustion Engine Computational Fluid Dynamics Simulations," Proceedings of the ASME 2012 Internal Combustion Engine Division Fall Technical Conference ICEF2012-92043, 2012, DOI: 10.1115/1.4024861.

[154] R. Scarcelli, N. Matthias, and T. Wallner, "Numerical Investigation of Combustion in a Lean Burn Gasoline Engine," SAE Technical Paper 2013-24–0029, 2013, DOI: 10.4271/2013-24-0029.

[155] R. Scarcelli, N. S. Matthias, and T. Wallner, "Numerical and experimental analysis of ignition and combustion stabilty in EGR dilute GDI operation," Proceedings of the ASME 2014 Internal Combustion Engine Division Fall Technical Conference Internal Combustion Engine Division ICEF2014-5607, 2014, DOI: 10.1115/ICEF2014-5607

[156] X. Yang, A. Solomon, and T.-W. Kuo, “Ignition and Combustion Simulations of Spray-Guided SIDI Engine using Arrhenius Combustion with Spark-Energy Deposition Model,” SAE Technical Paper 2012-01–0147, 2012, DOI: 10.4271/2012-01-0147.

[157] E. Pomraning, K. Richards, and P. K. Senecal, “Modeling Turbulent Combustion Using a RANS Model, Detailed Chemistry, and Adaptive Mesh Refinement,” SAE Technical Paper 2014-01–1116, 2014, DOI: 10.4271/2014-01-1116.

[158] N. Salman, E. Pomraning, M. Raju, R. Reese, S. D. Givler, and P. K. Senecal, “Gasoline Combustion Modeling of Direct and Port-Fuel Injected Engines using a Reduced Chemical Mechanism,” SAE Technical Paper 2013-01–1098, 2013, DOI: 10.4271/2013-01-1098.

[159] P. K. Senecal, E. Pomraning, R. Scarcelli, K. Richards, T. Wallner, and J. Sevik, “Cycle-to-Cycle Variations in Multi-Cycle Engine RANS Simulations,” SAE Technical Paper 2016-01–0593, 2016, DOI: 10.4271/2016-01-0593.

[160] D. Probst, E. Pomraning, R. Scarcelli, P. K. Senecal, and K. Richards, “The Observation of Cyclic Variation in Engine Simulations When Using RANS Turbulence Modeling,” Proceedings of the ASME 2014 Internal Combustion Engine Division Fall Technical Conference ICEF2014-5605, 2014, DOI: 10.1115/icef2014-5605.

[161] E. Corti, S. Falfari, C. Forte, S. Fantoni, and G. M. Bianchi, “A RANS CFD 3D Methodology for the Evaluation of the Effects of Cycle By Cycle Variation on Knock Tendency of a High Performance Spark Ignition Engine,” SAE Technical Paper 2014-01–1223, 2014, DOI: 10.4271/2014-01-1223.

[162] C. J. Rutland, “Large-eddy simulations for internal combustion engines - A review,” *Int. J. Engine Res.*, 12(5):421–451, 2011, DOI: 10.1177/1468087411407248.

[163] C. K. Blomberg, K. Boulouchos, Y. M. Wright, L. Zeugin, M. Bolla, and S. S. Pandurangi, “Modeling Split Injections of ECN ‘Spray A’ Using a Conditional Moment Closure Combustion Model with RANS and LES,” *SAE Int. J. Engines*, 9(4):2107–2119, 2016, DOI: 10.4271/2016-01-2237.

[164] D. Goryntsev, A. Sadiki, and J. Janicka, “Towards Large Eddy Simulation of Spray Combustion in Direct Injection Spark Ignition Engine,” SAE Technical Paper 2011-01–1884, 2011, DOI: 10.4271/2011-01-1884.

[165] D. Goryntsev, A. Sadiki, and J. Janicka, “Investigation of Fuel-Air Mixing in DISI Engine using LES,” SAE Technical Paper 2011-01–1886, 2011, DOI: 10.4271/2011-01-1886.

[166] B. Enaux *et al.*, “Large Eddy Simulation of a Motored Single-Cylinder Piston Engine: Numerical Strategies and Validation,” *Flow, Turbul. Combust.*, 86(2):153–177, 2011, DOI: 10.1007/s10494-010-9299-7.

[167] S. Buhl *et al.*, “A Combined Numerical and Experimental Study of the 3D Tumble Structure and Piston Boundary Layer Development During the Intake Stroke of a Gasoline Engine,” *Flow, Turbul. Combust.*, 98(2):579–600, 2017, DOI: 10.1007/s10494-016-9754-1.

[168] V. Granet, O. Vermorel, C. Lacour, B. Enaux, V. Dugué, and T. Poinsot, “Large-Eddy Simulation and experimental study of cycle-to-cycle variations of stable and unstable operating points in a spark ignition engine,” *Combust. Flame*, 159(4):1562–1575, 2012, DOI: 10.1016/j.combustflame.2011.11.018.

[169] A. Robert, S. Richard, O. Colin, L. Martinez, and L. De Francqueville, “LES prediction and analysis of knocking combustion in a spark ignition engine,” *Proc. Combust. Inst.*, 35(3):2941–2948, 2015, DOI: 10.1016/j.proci.2014.05.154.

[170] O. Vermorel, S. Richard, O. Colin, C. Angelberger, A. Benkenida, and D. Veynante, "Towards the understanding of cyclic variability in a spark ignited engine using multi-cycle LES," *Combust. Flame*, 156(8):1525–1541, 2009, DOI: 10.1016/j.combustflame.2009.04.007.

[171] X. Fang, R. Ismail, M. H. Davy, and J. Camm, "Numerical Studies of Combustion Recession on ECN Diesel Spray A," Proceedings of the ASME 2018 Internal Combustion Fall Technical Conference ICEF2018-9597, 2018, DOI: 10.1115/icef2018-9597.

[172] M. Schmitt, C. E. Frouzakis, A. G. Tomboulides, Y. M. Wright, and K. Boulouchos, "Direct numerical simulation of the effect of compression on the flow, temperature and composition under engine-like conditions," *Proc. Combust. Inst.*, 35(3):3069–3077, 2014, DOI: 10.1016/j.proci.2014.06.097.

[173] R. Stiehl, J. Bode, J. Schorr, C. Krüger, A. Dreizler, and B. Böhm, "Influence of intake geometry variations on in-cylinder flow and flow–spray interactions in a stratified direct-injection spark-ignition engine captured by time-resolved particle image velocimetry," *Int. J. Engine Res.*, 17(9):983–997, 2016, DOI: 10.1177/1468087416633541.

[174] R. Stiehl, J. Schorr, C. Krüger, A. Dreizler, and B. Böhm, "In-cylinder flow and fuel spray interactions in a stratified spray-guided gasoline engine investigated by high-speed laser imaging techniques," *Flow, Turbul. Combust.*, 91(3):431–450, 2013, DOI: 10.1007/s10494-013-9500-x.

[175] Sebastian H. R. Müller, Stefan Arndt, and Andreas Dreizler, "Analysis of the In-Cylinder Flow Field / Spray Injection Interaction within a DISI IC Engine Using High-Speed PIV," SAE Technical Paper 2011-01-1288 , 2011, DOI: 10.4271/2011-01-1288.

[176] M. Zhang, M. Xu, and D. L. S. Hung, "Simultaneous two-phase flow measurement of spray mixing process by means of high-speed two-color PIV," *Meas. Sci. Technol.*, 25(9):095204, 2014, DOI: 10.1088/0957-0233/25/9/095204.

[177] B. Peterson and V. Sick, "Simultaneous flow field and fuel concentration imaging at 4.8 kHz in an operating engine," *Appl. Phys. B Lasers Opt.*, 97:887–895, 2009, DOI: 10.1007/s00340-009-3620-y.

[178] B. Peterson, E. Baum, C. P. Ding, D. Michaelis, A. Dreizler, and B. Böhm, "Assessment and application of tomographic PIV for the spray-induced flow in an IC engine," *Proc. Combust. Inst.*, 36(3):3472–3475, 2017, DOI: 10.1016/j.proci.2016.06.114.

[179] D. Goryntsev, A. Sadiki, M. Klein, and J. Janicka, "Large eddy simulation based analysis of the effects of cycle-to-cycle variations on air-fuel mixing in realistic DISI IC-engines," *Proc. Combust. Inst.*, 32(2):2759–2766, 2009, DOI: 10.1016/j.proci.2008.06.185.

[180] D. Frieden and V. Sick, "Investigation of the Fuel Injection, Mixing and Combustion Processes in an SIDI Engine using Quasi-3D LIF Imaging," SAE Technical Paper 2003-01–0068, 2003, DOI: 10.4271/2003-01-0068.

[181] R. Dahms, T. D. Fansler, M. C. Drake, T. W. Kuo, A. M. Lippert, and N. Peters, "Modeling ignition phenomena in spray-guided spark-ignited engines," *Proc. Combust. Inst.*, 32(2):2743–2750, 2009, DOI: 10.1016/j.proci.2008.05.052.

[182] P. G. Aleiferis, A. M. K. P. Taylor, K. Ishii, and Y. Urata, "The nature of early flame development in a lean-burn stratified-charge spark-ignition engine," *Combust. Flame*, 136(3):283–302, 2004, DOI: 10.1016/j.combustflame.2003.08.011.

[183] O. Pajot and C. Mounaïm-Rousselle, “Instantaneous Flow Field Effects on the Flame Kernel in S.I.Engine by Simultaneous Optical Diagnostics,” SAE Technical Paper 2000-01–1796, 2000, DOI: 10.4271/2000-01-1796.
[184] Y. Shekhawat *et al.*, “An Experimental and Simulation Study of Early Flame Development in a Homogeneous-charge Spark-Ignition Engine,” *Oil Gas Sci. Technol.*, 72(5):1–18, 2017, DOI: 10.2516/ogst/2017028.
[185] M. Buschbeck, N. Bittner, T. Halfmann, and S. Arndt, “Dependence of combustion dynamics in a gasoline engine upon the in-cylinder flow field , determined by high-speed PIV,” *Exp. Fluids*, 53:1701–1712, 2012, DOI: 10.1007/s00348-012-1384-3.
[186] A. Cairns and C. G. W. Sheppard, “Cyclically Resolved Simultaneous Flame and Flow Imaging in a SI Engine,” SAE Technical Paper 2000-01–2832, 2000, DOI: 10.4271/2000-01-2832.
[187] B. Johansson, “Cycle to Cycle Variations in S.I. Engines - The Effects of Fluid Flow and Gas Composition in the Vicinity of the Spark Plug on Early Combustion,” SAE Technical Paper 962084, 1996, DOI: 10.4271/962084.
[188] M. K. Le, T. Furui, A. Nishiyama, and Y. Ikeda, “Application of High-Speed PIV Diagnostics for Simultaneous Investigation of Flow Field and Spark Ignited Flame inside an Optical SI Engine,” *SAE Int. J. Engines*, 10(3):2017, 2017, DOI: 10.4271/2017-01-0656.
[189] C. Mounaim-Rousselle *et al.*, “Experimental characteristics of turbulent premixed flame in a boosted Spark-Ignition engine,” *Proc. Combust. Inst.*, 34(2):2941–2949, 2013, DOI: 10.1016/j.proci.2012.09.008.
[190] C. Pera, V. Knop, and J. Reveillon, “Influence of flow and ignition fluctuations on cycle-to-cycle variations in early flame kernel growth,” *Proc. Combust. Inst.*, 35(3):2897–2905, 2015, DOI: 10.1016/j.proci.2014.07.037.
[191] G. T. Kalghatgi, “Early flame development in a spark-ignition engine,” *Combust. Flame*, 60(3):299–308, 1985, DOI: 10.1016/0010-2180(85)90035-5.
[192] B. Peterson, D. L. Reuss, and V. Sick, “On the ignition and flame development in a spray-guided direct-injection spark-ignition engine,” *Combust. Flame*, 161(1):240–255, 2014, DOI: 10.1016/j.combustflame.2013.08.019.
[193] B. Peterson, D. L. Reuss, and V. Sick, “High-speed imaging analysis of misfires in a spray-guided direct injection engine,” *Proc. Combust. Inst.*, 33(2):3089–3096, 2011, DOI: 10.1016/j.proci.2010.07.079.
[194] B. Peterson, E. Baum, A. Dreizler, and B. Böhm, “An experimental study of the detailed flame transport in a SI engine using simultaneous dual-plane OH-LIF and stereoscopic PIV,” *Combust. Flame*, 202:16–32, 2019, DOI: 10.1016/j.combustflame.2018.12.024.
[195] B. Peterson, E. Baum, B. Böhm, and A. Dreizler, “Early flame propagation in a spark-ignition engine measured with quasi 4D-diagnostics,” *Proc. Combust. Inst.*, 35(3):3829–3837, 2015, DOI: 10.1016/j.proci.2014.05.131.
[196] W. Zeng, M. Sjöberg, and D. L. Reuss, “Combined effects of flow/spray interactions and EGR on combustion variability for a stratified DISI engine,” *Proc. Combust. Inst.*, 35(3):2907–2914, 2015, DOI: 10.1016/j.proci.2014.06.106.
[197] W. Zeng, M. Sjöberg, D. L. Reuss, and Z. Hu, “The role of spray-enhanced swirl flow for combustion stabilization in a stratified-charge DISI engine,” *Combust. Flame*, 168:166–185, 2016, DOI: 10.1016/j.combustflame.2016.03.015.
[198] W. Zeng, M. Sjöberg, D. L. Reuss, and Z. Hu, “High-speed PIV, spray, combustion luminosity, and infrared fuel-vapor imaging for probing tumble-flow-induced asymmetry of gasoline distribution in a spray-guided stratified-charge DISI engine,” *Proc. Combust. Inst.*, 36(3):3459–3466, 2017,

DOI: 10.1016/j.proci.2016.08.047.
[199] J. Bode, J. Schorr, C. Krüger, A. Dreizler, and B. Böhm, "Influence of three-dimensional in-cylinder flows on cycle-to-cycle variations in a fired stratified DISI engine measured by time-resolved dual-plane PIV," *Proc. Combust. Inst.*, 36(3):3477–3485, 2017, DOI: 10.1016/j.proci.2016.07.106.
[200] J. Bode, J. Schorr, C. Krüger, A. Dreizler, and B. Böhm, "Influence of the in-cylinder flow on cycle-to-cycle variations in lean combustion DISI engines measured by high-speed scanning-PIV," *Proc. Combust. Inst.*, 37(4):4929–4936, 2018, DOI: 10.1016/j.proci.2018.07.021.
[201] P. Schiffmann, D. L. Reuss, and V. Sick, "Empirical investigation of spark-ignited flame-initiation cycle-to-cycle variability in a homogeneous charge reciprocating engine," *Int. J. Engine Res.*, 19(5):491–508, 2018, DOI: 10.1177/1468087417720558.
[202] W. Zeng, S. Keum, T. W. Kuo, and V. Sick, "Role of large scale flow features on cycle-to-cycle variations of spark-ignited flame-initiation and its transition to turbulent combustion," *Proc. Combust. Inst.*, 37(4):4945–4953, 2018, DOI: 10.1016/j.proci.2018.07.081.
[203] K. Truffin, C. Angelberger, S. Richard, and C. Pera, "Using large-eddy simulation and multivariate analysis to understand the sources of combustion cyclic variability in a spark-ignition engine," *Combust. Flame*, 162(12):4371–4390, 2015, DOI: 10.1016/j.combustflame.2015.07.003.
[204] C. P. Ding, B. Peterson, M. Schmidt, A. Dreizler, and B. Böhm, "Flame/flow dynamics at the piston surface of an IC engine measured by high-speed PLIF and PTV," *Proc. Combust. Inst.*, 37(4):4973–4981, 2018, DOI: 10.1016/j.proci.2018.06.215.
[205] H. Chen, H. Zhuang, D. L. Reuss, and V. Sick, "Influence of Early and Late Fuel Injection on Air Flow Structure and Kinetic Energy in an Optical SIDI Engine," SAE Technical Paper 2018-01–0205, 2018, DOI: 10.4271/2018-01-0205.
[206] H. Zhuang, V. Sick, and H. Chen, "Impact of Fuel Sprays on In-Cylinder Flow Length Scales in a Spark-Ignition Direct-Injection Engine," *SAE Int. J. Engines*, 10(3):752–766, 2017, DOI: 10.4271/2017-01-0618.
[207] G. M. Rassweiler and L. Withrow, "Motion Pictures of Engine Flames Correlated with Pressure Cards," SAE Technical Paper 380139, 1938, DOI: https://doi.org/10.4271/380139.